UNIVERSITY OF SOUTHAMPTON

Faculty of Engineering and the Environment

Aeronautics, Astronautics and Computational Engineering

Aerodynamic Noise of High-speed Train Bogies

by

Jianyue Zhu

Thesis for the degree of Doctor of Philosophy

June 2015

UNIVERSITY OF SOUTHAMPTON

ABSTRACT

FACULTY OF ENGINEERING AND THE ENVIRONMENT

Aeronautics, Astronautics and Computational Engineering

Thesis for the degree of Doctor of Philosophy

AERODYNAMIC NOISE OF HIGH-SPEED TRAIN BOGIES

Jianyue Zhu

For high-speed trains, aerodynamic noise becomes significant when their speeds exceed 300 km/h and can become predominant at higher speeds. Since the environmental requirements for railway operations will become tighter in the future, it is necessary to understand the aerodynamic noise generation and radiation mechanism from high-speed trains by studying the flow-induced noise characteristics to reduce such environmental impacts. The aim of this thesis is to investigate the flow behaviour and the corresponding aeroacoustic mechanisms from high-speed trains, especially around the bogie regions. Since the prediction of the flow-induced noise in an industrial context is difficult to achieve, this study focuses on scale models with increasing complexity. The aerodynamic and aeroacoustic behaviour of the flow past an isolated wheelset, two tandem wheelsets, a simplified bogie and the bogie inside the cavity with and without the fairing as well as considering the influence of the ground are investigated at a scale 1:10. A two-stage hybrid method is used consisting of computational fluid dynamics and acoustic analogy. The near-field unsteady flow is obtained by solving the Navier-Stokes equations numerically through the delayed detached-eddy simulation and the source data are applied to predict the far-field noise signals using the Ffowcs Williams-Hawkings acoustic analogy. All simulations were run with fully structured meshes generated according to the guidelines based on a grid independence study on a circular cylinder case. Far-field noise radiated from the scale models was measured in an open-jet anechoic wind tunnel. Good agreement is achieved between numerical simulations and experimental measurements for the dominant frequency of tonal noise and the shape of the spectra. Numerical results show that turbulent flow past the isolated wheelset is dominated by three-dimensional vortices. Vortex shedding around the axle is the main reason for the tonal noise generation with the dominant peak related to the vortex shedding frequency. The noise directivity shows a typical dipole pattern. Moreover, for both the tandem-wheelset and the simplified bogie cases, the unsteady flow developed around them is characterized by the turbulent eddies with various scales and orientations including the coherently alternating shedding vortices generated from the upstream axles. The vortices formed from the upstream geometries are convected downstream and impinge on the downstream bodies, generating a turbulent wake

behind the objects. Vortex shedding and flow separation as well as interaction around the bodies are the key factors for the aerodynamic noise generation. The radiated tonal noise corresponds to the dominant frequencies of the oscillating lift and drag forces from the geometries. The directivity exhibits a distinct dipole shape for the noise radiated from the upstream wheelset whereas the noise directivity pattern from the downstream wheelset is multi-directional. Compared to the wheelsets, the noise contribution from the bogie frame is relatively small. Furthermore, when the bogie is located inside the bogie cavity, the shear layer developed from the cavity leading edge has a strong interaction with the flow separated from the upstream bogie and cavity walls. Thus a highly irregular and unsteady flow is generated inside the bogie cavity due to the considerably strong flow impingement and interaction occurring there. Unlike the isolated bogie case, noise spectra from the bogie inside the cavity are broadband and a lateral dipole pattern of noise radiation is generated. The noise prediction based on the permeable surface source is formulated and programmed using the convective Ffowcs Williams-Hawkings method. Results show that the bogie fairing is effective in reducing the noise levels in most of the frequency range by mounting a fairing in the bogie area; and for the bogie inside the bogie cavity with the ground underneath, the far-field noise level is increased due to more flow interactions around the geometries and the ground reflection effect.

Contents

1 Introduction 1

1.1 Background 1

1.2 Research Objectives 3

1.3 Structure of Thesis 3

2 Literature Review 5

2.1 Aeroacoustic Research on High-speed Trains 5

2.1.1 Bogie 6

2.1.2 Pantograph 10

2.1.3 Pantograph recess 11

2.1.4 Inter-coach spacing 12

2.1.5 Nose of power car 13

2.1.6 Rear power car 14

2.1.7 Coach wall surfaces 14

2.1.8 Ventilators, louvres and cooling fans 15

2.1.9 Concluding remarks 16

2.2 Theory on Aerodynamic Noise Prediction using Acoustic Analogy 16

2.2.1 General sound sources 17

2.2.2 Lighthill's theory: acoustic analogy 17

2.2.3 Curle's theory: effect of solid boundaries 21

2.2.4 Ffowcs Williams-Hawkings method: effect of source motion 22

2.2.5 Theory of vortex sound 25

2.3 Numerical Methods for Aeroacoustics 25

2.3.1 Direct computation methods 26

2.3.2 Integral methods based on acoustic analogy 27

2.3.3 Empirical methods 30

2.4 Experimental Techniques for Aerodynamics and Aeroacoustics 31

2.4.1 Wind-tunnel measurements 31

2.4.2 Field and on-board measurements 35

2.5 Summary 36

3 Research Description 37

3.1 Research Outline 37

3.2 Numerical Approach 38

3.2.1 Computational mesh generation 39

3.2.2 CFD solution process 40
3.2.3 Far-field noise prediction 47
3.2.4 Post-processing of simulation results 48
3.3 Experimental Arrangement 50
3.4 Summary 51
4 Circular Cylinder 52
4.1 Experimental Study in Literature 52
4.2 Numerical Setup 54
4.3 Grid Sensitivity Study 57
4.4 Aerodynamic Results 59
4.4.1 Properties of the DDES model 59
4.4.2 Instantaneous flow field and time-dependent forces 60
4.4.3 Mean flow characteristics 65
4.4.4 Surface pressure spectra 67
4.4.5 Divergence of Lamb vector 68
4.5 Aeroacoustic Results 69
4.5.1 Acoustic spectra computation and verification 69
4.5.2 Acoustic directivity 71
4.6 Summary 72
5 Isolated Wheelset 73
5.1 Wheelset Geometry 73
5.2 Numerical Setup 74
5.3 Aerodynamic Results from Simulation 77
5.3.1 Properties of the DDES model 77
5.3.2 Instantaneous flow field and time-dependent forces 78
5.3.3 Lift and drag coefficients 84
5.3.4 Divergence of Lamb vector 86
5.4 PIV Experiment versus Numerical Simulation 87
5.4.1 PIV experiment 87
5.4.2 Numerical simulation corresponding to PIV experiment 90
5.5 Aeroacoustic Results 93
5.5.1 Acoustic spectra computation 94
5.5.2 Experimental verification 96
5.5.3 Acoustic directivity 99
5.6 Likely Effect of Simplified Wheels 101
5.7 Summary 105
6 Tandem Wheelsets and Simplified Bogie 107
6.1 Flow Structure of Tandem Circular Cylinders 107
6.2 Numerical Setup 108

6.3 Aerodynamic Results 110
6.3.1 Instantaneous flow field 110
6.3.2 Lift and drag coefficients 118
6.3.3 Wall pressure fluctuations 121
6.3.4 Divergence of Lamb vector 122
6.4 Aeroacoustic Results 123
6.4.1 Acoustic spectra computation 124
6.4.2 Experimental verification 126
6.4.3 Acoustic directivity 129
6.5 Summary 133
7 Simplified Bogie inside Bogie Cavity 135
7.1 Geometry of Bogie Cavity without and with the Fairing 135
7.2 Numerical Setup 136
7.3 Aerodynamic Results 137
7.3.1 Instantaneous flow field 137
7.3.2 Fluctuating force coefficients 145
7.3.3 Wall pressure fluctuations 149
7.4 Aeroacoustic Results 150
7.4.1 Acoustic spectra computation 150
7.4.2 Acoustic directivity 152
7.5 Bogie inside Bogie Cavity with Ground underneath 153
7.5.1 Instantaneous flow structure 155
7.5.2 Acoustic spectra and directivity 156
7.6 Summary 158
8 Influence of Bogie Fairing and Ground on Sound Generation Based on Convective FW-H Formulation 160
8.1 FW-H Acoustic Analogy and Kirchhoff Approach 161
8.2 Permeable Data Surface for FW-H Method 161
8.3 Convective FW-H Equation 162
8.4 Numerical Method for Solving the Convective FW-H Equation 166
8.4.1 Thickness noise 168
8.4.2 Loading noise 171
8.4.3 Wind-tunnel case 171
8.5 Numerical Algorithm for Noise Prediction 172
8.5.1 Comparison of retarded time method and advanced time approach 172
8.5.2 Spatial interpolation 174
8.5.3 Numerical implementation 174
8.5.4 Numerical verification 175
8.6 Influence of Bogie Fairing on Sound Generation 179

8.7 Influence of Ground on Sound Generation 183
8.8 Summary 185
9 Conclusions and Future Work 186
9.1 Conclusions 186
9.1.1 Isolated wheelset 187
9.1.2 Tandem wheelsets and simplified bogie 187
9.1.3 Simplified bogie inside bogie cavity 188
9.2 Future Work 188
9.2.1 Aerodynamic noise predication for high-speed train in reality 189
9.2.2 Numerical simulation and computational modelling 189
References 191

List of figures

1.1 $L_{\mathrm{Aeq,tp}}$ measured at 25 m from TGV-A (∇, □, ◇), TGV-Duplex (○, △) and Thalys (+) [9] 2

2.1 Sketch of main aeroacoustic sources from high-speed trains 5
2.2 Noise source maps of front power car from TGV Duplex at 350 km/h in 4 kHz 1/3 octave band [24] 6
2.3 Comparison of noise source maps of the leading car from ICE3 between wind-tunnel and full-scale tests [25] 7
2.4 Iso-surfaces of the instantaneous λ_2 criterion [27] 8
2.5 Instantaneous velocity and pressure fields around leading bogie [28] 9
2.6 A low-noise pantograph [30] 11
2.7 Single arm pantograph [29] 11

3.1 Lateral microphone positions for measurements on vehicles with constant speed [87] 49

4.1 Arrangement of cylinder in test section of wind tunnel [93] 53
4.2 Two-dimensional sketch of computational domain with the cylinder 54
4.3 Structured mesh generated around the cylinder 55
4.4 Instantaneous y^+ distributions around the cylinder surface 56
4.5 Delayed detached-eddy simulation model properties 60
4.6 Contours of instantaneous streamwise velocity fields 61
4.7 Contours of instantaneous spanwise vorticity fields 61
4.8 Iso-surfaces of the instantaneous normalized Q criterion 62
4.9 Time-history of lift and drag coefficients (part) 63
4.10 Power spectral density of lift and drag coefficients 63
4.11 Power spectral density of pressure at the wake position of cylinder 64
4.12 Streamwise mean velocity field (CFD simulation) 66
4.13 Streamwise mean velocity field (PIV experiment) [101] 66
4.14 Mean wall shear stress around the cylinder 67
4.15 Mean pressure coefficient on the cylinder surface 67
4.16 Spectrum of pressure on the cylinder top surface 68

4.17 Visualization of the divergence of the Lamb vector 69
4.18 Spectra comparisons of the radiated noises 71
4.19 Noise directivity for the cylinder (calculation) 72

5.1 Simplifying of wheelset model 74
5.2 Isolated wheelset model (1:10 scale, dimensions in millimetre) 75
5.3 Sketch of the computational domain with the isolated wheelset (not to scale) 76
5.4 Structured mesh generated around the wheelset 77
5.5 Delayed detached-eddy simulation model properties ($\theta = 60^0$) 78
5.6 Contours of instantaneous velocity magnitude in horizontal plane through centre of wheelset (bottom view) 79
5.7 Contours of instantaneous spanwise vorticity fields in vertical planes through centre of wheel and axle (side views) 79
5.8 Contours of instantaneous spanwise vorticity fields in vertical planes through corner of wheel and axle (side views) 80
5.9 Mean streamlines around the wheel of the wheelset 81
5.10 Iso-surfaces of the instantaneous normalized Q criterion 82
5.11 Power spectral density of pressure at wheelset wake positions 83
5.12 Time-history of lift and drag coefficients (part) 84
5.13 Power spectral density of lift and drag coefficients (isolated wheelset) 86
5.14 Power spectral density of lift and drag coefficients (isolated axle and isolated wheel) 86
5.15 Visualization of the divergence of the Lamb vector in horizontal plane through centre of wheelset (bottom view) 87
5.16 Schematic diagram of the 7'×5' wind tunnel layout and the PIV experimental setup 88
5.17 Front view of the PIV experimental setup of isolated wheelset case 89
5.18 Streamwise mean velocity field (PIV experiment) 89
5.19 Sketch of the computational domain with the wheelset (not to scale) 90
5.20 Streamwise mean velocity field (CFD simulation) 91
5.21 Comparisons of streamwise and vertical mean velocity profiles at x/D=0.6 91
5.22 Iso-surfaces of the instantaneous normalized Q criterion 92

5.23 Sketch of receiver locations 93
5.24 Spectra of acoustic pressure at far-field receivers (U_∞=30 m/s) 95
5.25 Spectra of acoustic pressure at receiver 3 96
5.26 Experimental setup in the anechoic chamber 97
5.27 Background noise for a mean stream flow speed of 30 m/s (top receiver) 98
5.28 Comparisons of spectra of far-field sound from simulations and experiments 98
5.29 Noise directivity from rotating and nonrotating wheelsets 100
5.30 Noise directivity for rotating and non-rotating wheelsets (streamwise *x*-*y* plane) 101
5.31 Three-dimensional noise directivity for a rotating wheelset (centre of directivity pattern corresponds to 40 dB) 101
5.32 Idealized wheel and detailed wheel models (1:10 scale) 102
5.33 Iso-surfaces of the instantaneous normalized Q criterion (isometric view) 102
5.34 Mean streamlines around the isolated wheel 103
5.35 Power spectral density of lift and drag coefficients 104
5.36 Noise directivity from non-rotating isolated wheels and wheelset 105

6.1 Simplified bogie model (1:10 scale, dimensions in millimetre) 108
6.2 Sketch of the computational domain (not to scale) 109
6.3 Structured mesh topology around the bogie 109
6.4 Contours of instantaneous velocity magnitude in horizontal plane through centre of wheelset (bottom views) 111
6.5 Contours of instantaneous velocity magnitude in vertical plane through axle mid-span (side views) 112
6.6 Iso-surfaces of the instantaneous normalized Q criterion (tandem wheelsets) 113
6.7 Iso-surfaces of the instantaneous normalized Q criterion (simplified bogie) 114
6.8 Contours of the instantaneous spanwise vorticity fields in a vertical plane (side views) 116
6.9 Power spectral densities of pressure at bogie wake positions 118
6.10 Power spectral densities of lift coefficients 120
6.11 Power spectral densities of drag coefficients 120

6.12 Wall pressure fluctuation level of the simplified bogie 122
6.13 Visualization of the divergence of the Lamb vector in horizontal plane through centre of wheelset (bottom views) 123
6.14 Sketch of receiver locations in the *z-y* plane..... 124
6.15 Spectra of acoustic pressure on far-field receivers (U_∞=30 m/s) 126
6.16 Experimental setup in the anechoic chamber 127
6.17 Background noise for a mean stream flow speed of 30 m/s (top receiver) 127
6.18 Comparisons of far-field noise spectra between simulation and experiment 128
6.19 Noise directivity of front and rear wheelsets in vertical *z-y* plane 130
6.20 Noise directivity of front and rear wheelsets in horizontal *x-z* plane ... 130
6.21 Three-dimensional noise directivity for front and rear wheelsets of simplified bogie (centre of directivity pattern corresponds to 50 dB) 131
6.22 Noise directivity of front and rear half-bogies in vertical *z-y* plane 132
6.23 Three-dimensional noise directivity for bogie (starting at 50 dB) 133
6.24 Noise directivity of whole geometry in vertical *x-y* plane 133

7.1 Models of simplified bogie inside the cavity..... 136
7.2 Sketch of the computational domain of bogie cavity case without fairing (not to scale) 137
7.3 Contours of instantaneous velocity magnitude in horizontal plane through centre of wheelset (bottom view)..... 138
7.4 Contours of instantaneous velocity magnitude in vertical plane through axle mid-span (side views)..... 139
7.5 Iso-surfaces of the instantaneous normalized Q criterion (case without fairing)..... 140
7.6 Iso-surfaces of the instantaneous normalized Q criterion (case with fairing) 141
7.7 Contours of the instantaneous spanwise vorticity fields in a vertical plane for bogie without fairing 143
7.8 Power spectral densities of pressure at bogie wake positions for bogie cavity case without fairing..... 145
7.9 Power spectral densities of lift coefficients 147
7.10 Power spectral densities of drag coefficients..... 147

7.11 Power spectral densities of side force coefficients 147
7.12 Power spectral densities of force coefficients of the bogie-inside-cavity cases 148
7.13 Wall pressure fluctuation level of inner bogie surfaces inside the cavity 149
7.14 Wall pressure fluctuation level of outer bogie surfaces inside the cavity 150
7.15 Spectra of acoustic pressure on far-field receivers (bogie inside bogie cavity without fairing) 151
7.16 Comparisons of spectra of acoustic pressure on far-field receivers 151
7.17 Three-dimensional noise directivity radiated from bogie surfaces inside the cavity (centre of directivity pattern corresponds to 40 dB) 153
7.18 Two-dimensional noise directivity radiated from bogie surfaces inside the cavity 153
7.19 Model of simplified bogie inside the cavity with ground underneath... 154
7.20 Sketch of the computational domain of bogie inside the cavity with ground underneath (not to scale)..... 154
7.21 Iso-surfaces of the instantaneous normalized Q criterion for the case with ground underneath 155
7.22 Contours of the instantaneous spanwise vorticity fields in a vertical plane for the case with ground underneath (axle mid-span, side view) 156
7.23 Comparison of spectra of acoustic pressure on far-field receivers (cases without fairing) 156
7.24 Three-dimensional noise directivity radiated from bogie surfaces inside the cavity (centre of directivity pattern corresponds to 40 dB) 157
7.25 Two-dimensional noise directivity radiated from bogie surfaces inside the cavity (cases without fairing) 158

8.1 Geometric interpretation of emission 166
8.2 Comparisons of time history of sound pressure between analytical and predicted solutions..... 176
8.3 Comparisons of noise directivity between analytical and predicted solutions..... 177

8.4 Sketches of permeable surfaces used for wheel test case 179
8.5 Comparisons of spectra of far-field sound pressure 179
8.6 Sketch of porous surfaces used for FW-H integration (top view, not to scale) 180
8.7 Comparisons of far-field noise spectra in bogie cavity case without fairing 181
8.8 Comparisons of far-field noise prediction from permeable surface (fairing effect) 183
8.9 Comparisons of far-field noise prediction from permeable surface (ground effect, cases without fairing) 184

List of tables

2.1 Noise characteristics of aerodynamic noise sources of KTX-Sancheon at a speed of 300 km/h (dB(A), center frequency of 500 Hz bandwidth) [23] 6

4.1 Overview of the mesh size and timestep size for grid independence study 57
4.2 Summary of computations with different mesh and time resolutions 58
4.3 Root-mean-square and mean values of lift and drag coefficients 63

5.1 Root-mean-square and mean values of aerodynamic force coefficients (isolated wheelset) 85

6.1 Root-mean-square and mean values of aerodynamic force coefficients (simplified bogie) 119

7.1 Root-mean-square and mean values of aerodynamic force coefficients (bogie-inside-cavity case without the fairing) 146

DECLARATION OF AUTHORSHIP

I, Jianyue Zhu

declare that the thesis entitled

Aerodynamic Noise of High-speed Train Bogies

and the work presented in the thesis are both my own, and have been generated by me as the result of my own original research. I confirm that:

- this work was done wholly or mainly while in candidature for a research degree at this University;
- where any part of this thesis has previously been submitted for a degree or any other qualification at this University or any other institution, this has been clearly stated;
- where I have consulted the published work of others, this is always clearly attributed;
- where I have quoted from the work of others, the source is always given. With the exception of such quotations, this thesis is entirely my own work;
- I have acknowledged all main sources of help;
- where the thesis is based on work done by myself jointly with others, I have made clear exactly what was done by others and what I have contributed myself;
- parts of this work have been published and submitted as given in the list of publications.

Signed: ……

Date:……

List of Publications

Journal Publications

- J.Y. Zhu, Z.W. Hu, D.J. Thompson. Flow simulation and aerodynamic noise prediction for a high-speed train wheelset. International Journal of Aeroacoustics, 2014, 13(7&8): 533-552.
- J.Y. Zhu, Z.W. Hu, D.J. Thompson. Flow behaviour and aeroacoustic characteristics around a simplified high-speed train bogie (submitted to Journal).
- J.Y. Zhu, Z.W. Hu, D.J. Thompson. On the effect of a fairing on the flow and flow-induced noise behaviour around a simplified high-speed train bogie (submitted to Journal).
- J.Y. Zhu, Z.W. Hu, D.J. Thompson. Flow and flow-induced noise behaviour of a simplified high-speed train bogie inside the bogie cavity with ground underneath (draft).

Conferences

- J.Y. Zhu, Z.W. Hu, D.J. Thompson. Analysis of aerodynamic and aeroacoustic behaviour of a simplified high-speed train bogie. Proceedings of the 11th International Workshop on Railway Noise, Sweden, September 2013; Notes on Numerical Fluid Mechanics and Multidisciplinary Design, 126: 489-496, 2015.
- J.Y. Zhu, Z.W. Hu, D.J. Thompson. Analysis of flow and aerodynamic noise behaviour of a simplified high-speed train bogie inside the bogie cavity. High Speed Rail: Celebrating Ambition, University of Birmingham, December 2014.

Acknowledgements

Foremost, I would like to thank my supervisors Dr. Zhiwei Hu and Prof. David Thompson for their guidance, encouragement and patience during all the time of this study.

Many thanks go to Prof. Neil Sandham and Dr. Gwenael Gabard for their suggestions on the first and upgrade reviews of this research.

Thanks to Koen for help in post-processing of simulated data and Eduardo for the assistance in the experimental measurements.

Helpful discussions with Ryu, Toni, Simone, Michael, Patrick, Yusik, Wen, Kangping, Xiaowan, Jinqiu and Shuangli are appreciated.

My thanks extend to MSc students Mano, David, Kyuha, Alexis and Samuel for the experimental setup preparation and wind tunnel testing.

The numerical simulations were performed on the Iridis3 and Iridis4 clusters managed by University of Southampton. The research studentship provided by University of Southampton is gratefully appreciated.

Finally, I thank my parents for their invaluable encouragement. And thank you Guoqiao and Huayan. Love and support from you accompany me every day.

Definitions and abbreviations

Greek Symbols

α_j	Weight coefficient
$\delta(f)$	Dirac delta function
δ_{ij}	Kronecker delta
Δ	Grid spacing
ρ	Density
ρ'	Density perturbation
ξ	Isoparametric element coordinate
η	Isoparametric element coordinate
τ_{ij}	Stress Tensor
τ	Retarded time (emission time)
τ_e	Source time
μ	Dynamic viscosity
ν	Kinematic viscosity
$\tilde{\nu}$	Modified turbulent kinematic viscosity
ν_t	Turbulent kinematic viscosity
κ	Kármán constant
Ω_{ij}	Mean rate-of-rotation tensor

Alphanumeric Symbols

c_0	Speed of sound
C_D	Drag coefficient, $\frac{D_f}{(1/2)\rho_0 U_0^2 DL}$
C_L	Lift coefficient, $\frac{L_f}{(1/2)\rho_0 U_0^2 DL}$
C_p	Pressure coefficient, $\frac{p-p_\infty}{(1/2)\rho_0 U_0^2}$
d	Wall distance
$\tilde{d}$	Length scale
D	Diameter

D_f	Drag force
f	Frequency
$f(\mathbf{x},t)$=0	Function describing the source surface
f_{v1}	Damping coefficient
$H(f)$	Heaviside function
$\|J\|$	Jacobian determinant
l	Typical length scale
L	Length
l_j	Unit outward normal
L_f	Lift force
L_p	Sound pressure level
M	Free stream Mach number, U_0/c_0
M_r	Source Mach number in radiation direction
$\hat{\mathbf{n}}$	Unit outward normal vector
N_i	Interpolation functions
P	Pressure
P_{ij}	Compressive stress tensor
p'	Fluctuating pressure
p_e	Effective sound pressure level
p_{ref}	Reference acoustic pressure (=20 μPa)
Q	Volume flow rate
Q	Q criterion (second invariant of the velocity gradient)
Q	Sound source strength
$\mathbf{r}$	Radiation vector ($\mathbf{r}=\mathbf{x}-\mathbf{y}$)
$\mathbf{R}$	Radiation distance vector
R^*	Emission distance
Re	Reynolds number, $U_0 D/\nu$
R_{m}	Garrick triangle distance
S	Surface area
S_{ij}	Mean strain rate tensor
$\|S_{ij}\|$	Magnitude of the strain rate tensor
St	Strouhal number, fD/U_0

T	Period
t	Time
T_{ij}	Lighthill stress tensor
U, V, W	Cartesian components of velocity
U_i	Mean velocity
u_i'	Fluctuating velocity
u_i, v_i	Flow velocity component
U_∞	Freestream velocity
U_0	Freestream velocity
V	Integration volume
W_i	Quadrature weight coefficients
x_i	Cartesian coordinates
$\mathbf{x} = (x_1, x_2, x_3)$	Observer position
$\mathbf{y} = (y_1, y_2, y_3)$	Source position
y^+	Dimensionless first-cell spacing
$\bar{\square}^2$	Convective wave operator
∇	Gradient operator

Superscript

$\bar{}$	Mean value
$'$	Fluctuation value
$+$	Non-dimensional parameter in wall units

Subscript

0	Ambient freestream quantities
i, j	Vector component in fixed reference frame
n	Projection in the normal direction
∞	Freestream quantities

Abbreviations

BANC	Benchmark problems for Airframe Noise Computations
CAA	Computational Aeroacoustics

CFD	Computational Fluid Dynamics
CFL	Courant-Friedrichs-Lewy
COP	Coherent Output Power
DES	Detached-Eddy Simulation
DDES	Delayed Detached-Eddy Simulation
DLR	Deutsches Zentrum für Luft- und Raumfahrt (German Aerospace Center)
DNS	Direct Numerical Simulation
FFT	Fast Fourier Transform
FW-H	Ffowcs Williams-Hawkings
ICE	Inter City Express (German high speed train)
ISO	International Organization for Standardization
ISVR	Institute of Sound and Vibration Research
KTX	Korean Train eXpress
LBM	Lattice-Boltzmann method
LES	Large Eddy Simulation
N-S	Navier-Stokes
OASPL	Overall Sound Pressure Level
PIMPLE	merged PISO-SIMPLE
PISO	Pressure-Implicit Split Operator
PIV	Particle Image Velocimetry
POS	Paris-Ostfrankreich-Süddeutschland (German for Paris, Eastern France, Southern Germany)
PSD	Power Spectral Density
RANS	Reynolds-Averaged Navier-Stokes
RMS	Root-mean-square
RTRI	Railway Technical Research Institute (Japan)
S-A	Spalart-Allmaras
SIMPLE	Semi-Implicit Method for Pressure-Linked Equations
SNCF	Société Nationale des Chemins de Fer français (French National Railway Corporation)

SPL	Sound Pressure Level
TGV	Train à Grande Vitesse (French high speed train)
TKE	Turbulent Kinetic Energy
URANS	Unsteady Reynolds-Averaged Navier-Stokes

Chapter 1

Introduction

1.1 Background

High-speed railways are being developed rapidly around the world. Normally the peak running speed of a high-speed train is capable of reaching over 300 km/h. As the running speed of a high-speed train increases, the aerodynamic noise generation increases and becomes the dominant noise source [1].

Since early in the last century, theoretical studies of aerodynamic noise have been focused extensively on the problems of noise from aircraft, especially jet engines, which led to the development of aeroacoustics as a subarea of aerodynamics to study flow-induced noise. Recently, with the significant reductions of the aerodynamic noise from modern high-bypass ratio aero-engines, the efforts are directed toward the airframe noise reduction, particularly during approach and landing conditions. Using computational tools, including computational fluid dynamics (CFD) and computational aeroacoustics (CAA) methods, and experimental measurement techniques, many studies have been carried out over the last few decades regarding the development of source mechanism descriptions, noise prediction capabilities and noise reduction technologies of flow-induced noise, particularly in aerospace engineering for landing gear and airframes [2-8].

The flow speeds applying to landing gear during take-off and approach-to-landing are between 250 km/h and 400 km/h, making the aeroacoustic problem quite similar to that of high-speed trains [9]. However, by comparison with a jet engine and airframe structure, a train has a relatively low flow velocity but quite large

dimensions (particularly in length) and it is necessary to consider the ground effect on the aerodynamic behaviour. For high-speed trains, many studies have shown that aerodynamic noise becomes significant when their speeds exceed 300 km/h and can become predominant at higher speeds or with the reduction of the rolling noise [1,9-12]. No further global reduction of high-speed train noise can be achieved if the aerodynamic noise is not reduced. A transition speed represents the change from the dominance of rolling noise to that of aerodynamic noise. This speed is not well defined but is currently thought to lie between 300 and 400 km/h as shown in Figure 1.1 [9].

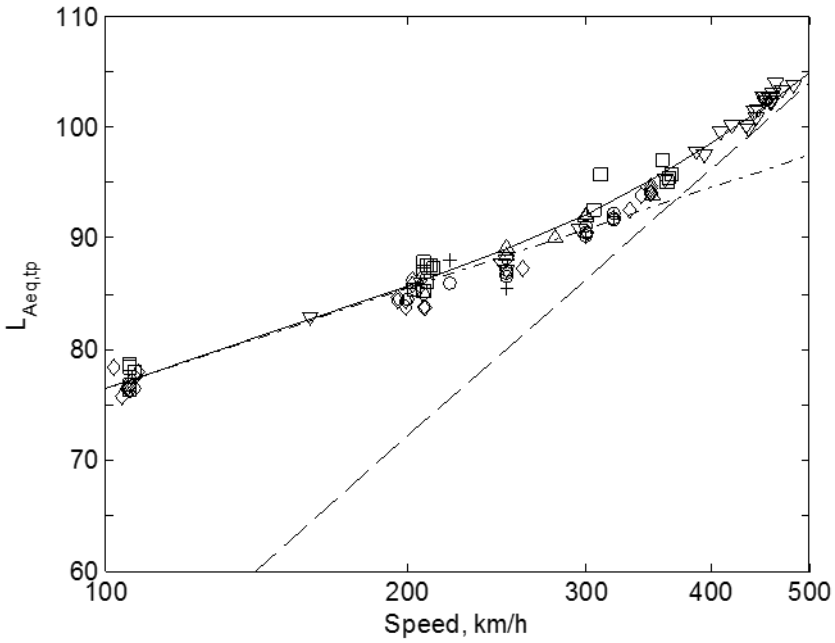

Figure 1.1: $L_{Aeq,tp}$ measured at 25 m from TGV-A (∇, □, ◇), TGV-Duplex (○, △) and Thalys (+) [9]. – · – · Straight line with slope of $30 \log_{10} V$ to represent rolling noise; – – – straight line with slope of $80 \log_{10} V$ to represent aerodynamic noise; — total noise.

Due to more stringent certification rules and increased sensitivity of the community, environmental requirements for railway operations are expected to become tighter in the future. In particular, annoyance due to railway noise has to be taken into account in the expansion of new high-speed line projects. Much work has been done on railway rolling noise. The reduction of rolling noise has reached a stage where theoretical models are quite mature and a number of research and demonstration projects have been carried out to show that low-noise vehicles and tracks can be designed [9,13]. However by comparison, the

generation of aerodynamic noise from high-speed trains is less well understood, especially in terms of theoretical analyses of source generation and noise prediction. Significant progress has been made in the understanding of the aerodynamic phenomena associated with high-speed trains [14-20]. By contrast, the aerodynamic noise from high-speed train requires further attention. It is evident that a good understanding of the sound sources and their physical characteristics is essential to find good solutions to control the aerodynamic noise.

1.2 Research Objectives

This research aims to investigate the aerodynamic noise generating mechanism from the scale models with increasing complexity around high-speed train bogie region and to see the differences between the various cases. The emphases are put on the flow separation and vortex interaction between each component of the configurations and the corresponding mechanisms of aerodynamic noise generation. Numerical simulations are compared with experimental measurements. The influences of the bogie fairing and the ground effect on the noise generation and radiation are analysed numerically.

1.3 Structure of Thesis

The rest of the thesis is organized as follows:

Chapter 2 presents an overview of previous studies on aerodynamic noise in high-speed trains followed by a review of the fundamental principles of aeroacoustics theory based on acoustic analogy and a general description of aerodynamic noise prediction methods including numerical and experimental techniques.

According to the literature survey, the research methodology used for this study is addressed in Chapter 3, giving an overall description of the research outline and describing the computational approaches and the experimental methods applied here.

Chapter 4 focuses on the flow and flow-induced noise behaviour of a circular cylinder case in which the grid independence study is performed, and then the benchmark for simulation setup and mesh resolution requirement are discussed. The numerical simulations on the different scale models with increasing complexity from a high-speed train bogie area are investigated in Chapters 5 to 7, which include the cases of an isolated wheelset (Chapter 5), the tandem wheelsets as well as a simplified bogie (Chapter 6), and the simplified bogie inside the bogie cavity with and without the fairing as well as considering the ground underneath (Chapter 7). The aerodynamic noise generated from the solid integration surfaces using acoustic analogy method is computed for these geometries. Noise predictions of some cases are verified by comparison with experimental measurements in an anechoic open-jet wind tunnel.

Based on the convective Ffowcs Williams-Hawkings formulation, an aerodynamic noise prediction code is implemented in Chapter 8. Using the unsteady flow data obtained from CFD calculations, the aerodynamic noise generated from the cases of bogie inside the bogie cavity is calculated from a permeable integration surface using the acoustic analogy method to investigate the influence of the bogie fairing and the ground on the noise generation and sound radiation.

Finally, the conclusions are summarized and future work is proposed in Chapter 9 based on the findings from this research.

Chapter 2

Literature Review

This chapter presents an introduction on the previous studies of aerodynamic noise in high-speed trains, followed by the fundamental principles of aerodynamic noise prediction techniques based on the acoustic analogy method. Different approaches using numerical simulation and experimental measurement for aeroacoustics are reviewed thereafter.

2.1 Aeroacoustic Research on High-speed Trains

The main aeroacoustic sources on conventional high-speed trains identified by different studies are the bogie, the pantograph, the recess of the pantograph, the inter-coach spacing, the nose of the power car, the coach wall surfaces, the rear power car, the louvres and the cooling fans [9,10,11,21,22], as sketched in Figure 2.1. They will be discussed individually below. In general, it is found that for these various sources, the aerodynamic noises are generated by flow passing over the structural elements and by turbulent flow itself. As an example, the Korean high-speed train (Korean Train eXpress, KTX) pass-by noise was measured at a speed of 300 km/h using the microphone array. Based on the noise map, the bogies, pantograph and inter-coach gaps were found to be the main noise sources as shown in Table 2.1 [23].

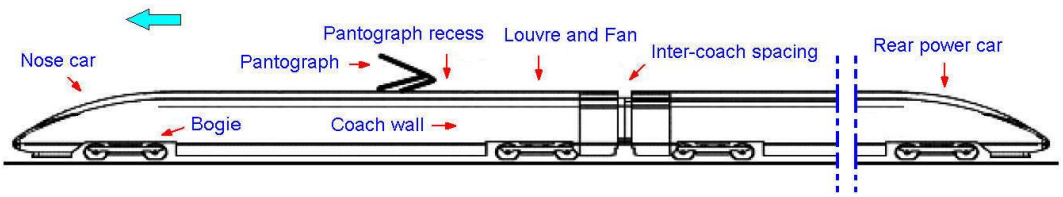

Figure 2.1: Sketch of main aeroacoustic sources from high-speed trains

	500 Hz	1000 Hz	1500 Hz	2000 Hz	2500 Hz	3000 Hz
Leading bogie	77	75	72	68	64	62
Rear bogie	76	77	73	67	66	63
Pantograph	70	73	71	66	68	65
Pantograph recess	67	70	68	65	63	62
Inter-coach spacing	68	63	68	62	66	62

Table 2.1: Noise characteristics of aerodynamic noise sources of KTX-Sancheon at a speed of 300 km/h (dB(A), center frequency of 500 Hz bandwidth) [23]

2.1.1 Bogie

High-speed train bogies are complex structures containing many components exposed to flow with little or no streamlining. The aerodynamic noise produced from the bogie area has been estimated to be around 15 dB larger than that from the pantograph regarding the noise contribution to the overall noise of the whole train [9].

Identification of bogie aerodynamic sources was investigated with on-board measurements using the COP (coherent output power) technique in [21]. It was shown that the coherent source mechanisms from the bogie area were more complex than the acoustic radiation behaviour of the inter-coach spacing and hard to recognize. Thus, the bogie could not be modelled by a single noise source and should be considered as several uncorrelated acoustic sources. Other sources located near the upstream and downstream wheels radiated efficiently in the frequency range 500-1000 Hz.

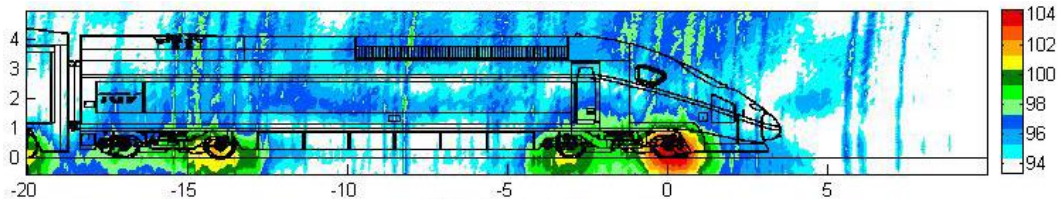

Figure 2.2: Noise source maps of front power car from TGV Duplex at 350 km/h in 4 kHz 1/3 octave band [24]

Using a star-shaped microphone array, the noise source maps from a TGV (*train à grande vitesse*, French high-speed train) Duplex at 300 km/h were presented in [9]. It was found that the leading bogie was the main noise source from the front power car over the frequency range 250-1250 Hz; the lower part of the cab door contributed to the noise in the 500 and 630 Hz bands; and the wheels appeared to be the main source at higher frequencies above 2 kHz. Further characterization of these sources at 350 km/h was carried out by SNCF (*société nationale des chemins de fer français*, French national railway corporation) [24]. It can be seen clearly from Figure 2.2 that a strong noise source is located at the leading bogie area, particularly around the front wheelset region. Since the rolling noise from each wheel is very similar, more aerodynamic noise is generated around the leading bogie due to the unsteady airflow passing through the large surface shape variations and discontinuities around the leading bogie area. Therefore, significant aerodynamic noise is generated in the leading bogie region due to a large number of flow separations and interactions with high-level turbulence developed there.

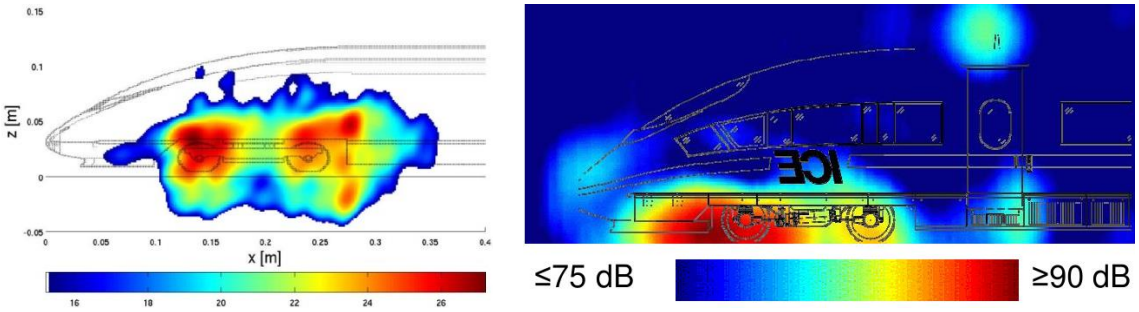

(a) 20 kHz 1/3 octave band of the wind tunnel measurement at 40 m/s

(b) 0.8 kHz 1/3 octave band of the field measurement at 92 m/s

Figure 2.3: Comparison of noise source maps of the leading car from ICE3 between wind-tunnel and full-scale tests [25]

To locate the main sources of noise in the bogie area and to characterize the unsteady sources, an experiment was carried out using a 1:25 scale model of an ICE3 (inter city express, German high-speed train) in the aeroacoustic wind tunnel Brunswick (AWB) of DLR (*Deutsches Zentrum für Luft- und Raumfahrt*, German aerospace centre) [25]. Figure 2.3 compares the noise source maps of a leading car from the ICE3 between wind-tunnel and full-scale tests. The bogie section in the model was less detailed and the train surface was smooth. A

microphone array consisting of 143 microphones was positioned outside the flow in the open-jet wind tunnel. The interest was focused on the cavities of the bogies and the gaps between the vehicles. Based on these measurements, modifications for noise reduction were applied and the noise maps from the bogie area were obtained. It should be noted that in the case of the wind-tunnel measurement, the geometry of the bogie was simplified and there was no wheel-rail interaction, thus no rolling noise took place. Moreover, there was no moving ground beneath the train. Nevertheless, the results matched qualitatively, making sense to conduct aeroacoustic measurement of trains in wind tunnels.

Another way to understand the flow behaviour is to carry out numerical simulations through modelling the turbulent viscous flow. A global relation between turbulence reduction and subsequent aerodynamic noise reduction has been found in [26]. Six shape modifications around the bogie area between the trailer vehicles, which is also the inter-car region in a TGV RESEAU train using articulated Jakobs bogies, have been simulated by CFD using the RANS (Reynolds-averaged Navier-Stokes) approach to identify the main turbulence production source. The configurations with the most successful turbulence reduction were tested in an anechoic wind tunnel to validate the flow calculation and investigate the expected aerodynamic noise reduction.

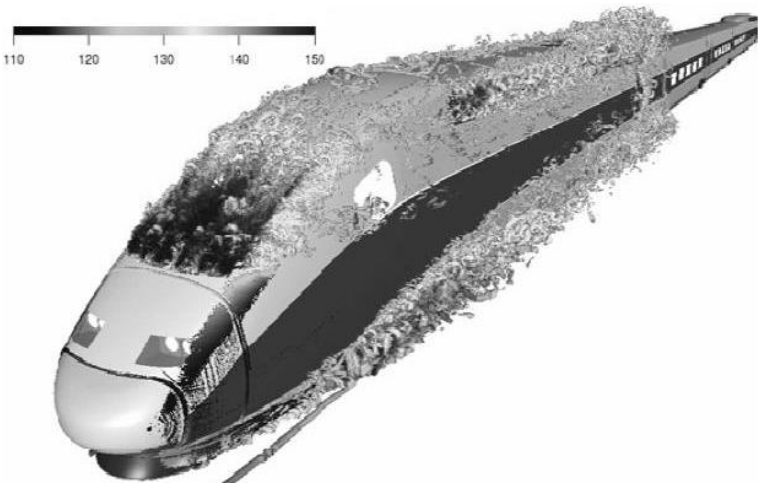

Figure 2.4: Iso-surfaces of the instantaneous λ_2 criterion [27]

Numerical simulations with the lattice-Boltzmann method have been performed recently to study the aeroacoustic behaviour of the power car of the TGV POS

(*Paris-Ostfrankreich-Süddeutschland*, Paris, Eastern France, Southern Germany) high-speed train at full scale but no experimental validation was given in [27]. Figure 2.4 displays the iso-surfaces of the instantaneous λ_2 coefficient to visualize the vortices developed around the whole powercar, which confirms that the first bogie region is one of the most unsteady turbulent zones around the high-speed train. The calculations confirmed the main sources of aerodynamic noise, and the influence of several geometrical optimizations on both drag and aerodynamic noise were evaluated.

Also using the lattice-Boltzmann method along with a turbulence wall-function approach, the flow-induced noise from the main sources of a full-scale simplified high-speed train was studied to assess the far-field noise levels and to develop noise reduction methods in the train design phase [28]. Figure 2.5(a) shows that coherent vortices are developed from the leading edge of the first bogie, which are convected and impinge on the components inside the bogie cavity. Figure 2.5(b) displays the time derivative of the surface pressure field around the leading bogie, indicating that the unsteady flow developed in the front and rear parts of the bogie cavity might be strong aeroacoustic sources. Near-field noise levels at the locations within the simulation domain based on the acoustic analogy solver were compared to the results obtained directly from the simulation and good agreements were reported. The far-field noise predictions need to be verified by experimental measurements to improve confidence.

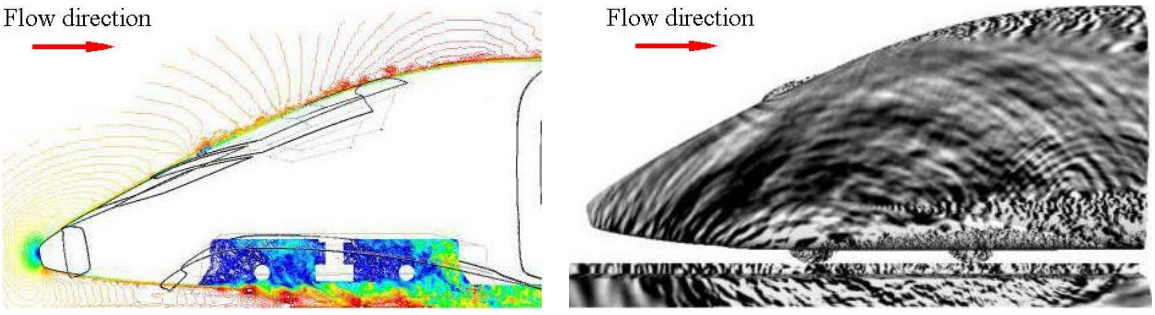

(a) Velocity field contours (b) Time derivative of pressure field

Figure 2.5: Instantaneous velocity and pressure fields around leading bogie [28]

Aeroacoustic sources in the bogie area of a real case are extremely hard to identify due to the complex configurations inside the bogie cavity, leading to the

difficulties to find effective solutions for noise reduction in this region. It has been found that by modifying the flow in the bogie areas and adding shaped fairings around the leading bogie, aerodynamic noise reductions are obtained, however, practical difficulties often prevent their implementations [9].

2.1.2 Pantograph

The pantograph is the current collector mounted on the train roof and exposed to the unsteady air flows. The mechanism of aerodynamic noise from the pantograph is characterized by periodic vortex shedding around the various structural components of which it consists. Although some broad-band noise is generated by several components, the noise produced by the pantograph is generally Aeolian tones identified evidently by their frequency peaks [11]. During the vortex shedding process, the vortices breaking away from the surface of a slender body will impact on the surrounding fluid and generate a fluctuating force which creates the typical dipole sound. Accordingly, the physical phenomena and generating mechanism are now well understood and some practical techniques are developed to control and reduce such aerodynamic noise.

Pantograph noise has become a major issue and it is necessary to make considerable efforts to reduce it as the noise barriers along the track do not shield such aerodynamic sources, i.e. ones that are located at the top of the train. This is particularly true where much of the new high-speed lines run on elevated structures fitted with noise barriers along some track areas.

In Japan, there are sound barriers 2m in height along most of the Shinkansen track, which will shield noise generated from lower parts of the train [29]. Therefore, noise from pantographs is a large contributor to the overall noise. A low-noise pantograph [30] designed by RTRI (Railway Technical Research Institute) is shown in Figure 2.6. It consists mainly of a panhead, an articulated frame and a base frame and has a relatively simple configuration to reduce aerodynamic noise. The panhead is mounted on the top of the articulated frame by a panhead support. It is found that with a smoothed-shape panhead, the shape modification on the panhead support is very important to pantograph

aerodynamic noise reduction. Furthermore, some techniques, such as shape modification on the panhead support and surface covering with porous material on the fairings, have been utilized and about 4 dB aerodynamic noise reduction was obtained [30]. In another single arm pantograph with components arranged to one side as displayed in Figure 2.7, the aerodynamic noise can be reduced further [29].

Figure 2.6: A low-noise pantograph [30]

Figure 2.7: Single arm pantograph [29]

A standard pantograph fitted to German ICE1 and ICE2 trains was modified to optimize cylinder shapes, as well as to test the principle of using ribs to break up coherent vortex shedding [10]. In wind-tunnel tests, the total noise reduction for this pantograph was nearly 5 dB in A-weighted sound level.

2.1.3 Pantograph recess

For high-speed trains such as the TGV, the pantograph protrudes from a cavity instead of being located on the roof of the coach, making it less exposed to the flow when retracted [11]. However, the pantograph recess itself may generate aerodynamic noise induced by the cavity.

The flow passing over a simple cavity was simulated to study the characteristics of the aerodynamic noise generated from a pantograph cavity through the acoustic analogy method [31]. Using the linearized Euler's equations for acoustic propagation based on the source term obtained from large-eddy simulation, the aeroacoustic calculations were performed on a forward-backward facing step pair

to simulate the pantograph cavity on the roof of a high-speed train [10]. It is found that the recess of the pantograph can be generally described as a closed cavity, in which the shear layer separates at the leading edge, reattaches on the cavity floor, impinges upon the cavity rear wall and separates again at the trailing edge. Correspondingly, aerodynamic noise can be produced due to these cavity flow separations and flow-structure interactions.

Wind-tunnel experiments on a 1:7 scale cavity representing a pantograph recess with and without pantographs have been performed in [32], which confirmed that the rear wall region of the pantograph recess was the main noise source area due to the strong turbulent flow interactions generated there. Moreover, it was demonstrated that no aerodynamic or acoustic self-sustained oscillations were observed within the flow developed around the pantograph recess due to the characteristics of the closed type of the shallow cavity. An effective way to reduce the noise from the recess of the pantograph was shown to be to prevent the flow from going into the recess by modifying the cavity geometry or by the use of spoilers.

2.1.4 Inter-coach spacing

The pantograph recess concerns only some types of trains while the case of inter-coach spacing concerns every train. Compared with the closed cavity from the recess of the pantograph, the inter-coach spacing has a smaller streamwise length-to-depth ratio and can be described as an open cavity. Experiments have shown that at low Mach numbers, deep rectangular cavities may lead to oscillations with discrete frequency peaks [33]. In most open cavity flows, the turbulent boundary layer separation is followed by a roll-up leading to coherent structures in the cavity shear layer, and the strength of these shear layer vortical structures depends on the turbulent boundary layer thickness and the cavity length. Acoustic disturbances can be generated when the coherent structures of the shear layer impinge on the leading corner along the downstream edge of the cavity. Thus, when the turbulent flows come over the discontinuities from inter-coach gaps of the train, an intense aeroacoustic coupling is generated between the cavity shear layer oscillations and the acoustic modes of the installation.

A good way to identify the unsteady flow phenomena, which occur in the inter-coach region and generate sound radiation, is on-board experiments. The characterization of the influence of these cavities can be obtained by comparing the spectra and coherence from the various probes. The use of anti-turbulence probes and the identification of acoustic waves from the experimental data can determine whether the phenomena radiate sound [21]. It was found that the inter-coach spacing showed particular radiating phenomena at well-defined frequencies; the noise radiation was concentrated in the low-frequency range below 500 Hz and dominated by various pure tones.

Some solutions have been proposed to reduce the aerodynamic noise from the inter-coach region, e.g., adding baffles to the ends of vehicles to eliminate the aerodynamic noise generated from the inter-coach regions [9]. In Series 300 and 700 Shinkansen [34], it was shown to be important to ensure that any misalignments of adjacent vehicles do not lead to the edges of baffles mounted on vehicle ends protruding into the flow. Additionally, at the lower part of the inter-coach area, a cover was mounted to prevent the sound from being transmitted upwards. Wind-tunnel tests on a scale model showed that rounding the corners of the vehicle ends could be more effective in reducing noise from the inter-coach gap than adding baffles to the coach ends [35].

2.1.5 Nose of power car

The power-car nose design is mainly concerned with improving aerodynamic performance, reducing pressure waves generated in tunnels and aeroacoustic optimization. At the nose of the leading car of the train where flow separation occurs, the turbulent boundary layer generated by the unsteady air flow can produce dipole sources rather than quadrupole noise which is comparatively less effective, particularly around the surface shape variation regions.

Many developments on the nose shape have been made to improve aerodynamic and aeroacoustic performance of high-speed trains. For Series 700 Shinkansen trains in Japan, a long streamlined nose has been used to reduce the severity of

'micro-pressure waves' [34]. These are shock waves generated in long tunnels with ballastless track which can result in a loud impulsive sound at the opposite end of the tunnel. Therefore, aerodynamic optimization of the power-car nose is also important in reducing pressure waves generated in tunnels and the corresponding aerodynamic noise. The design of the nose car in the ICE3 is another good example for the noise reduction where flow separation has been eliminated on the leading car by streamlining the noses [11]. Other improvements are also important for noise reduction from nose car. The body-shells are smooth with flush-mounted windows. The front skirt and an underfloor cover are introduced under the nose. The gap between the front skirt and the leading bogie are reduced and the leading bogie is shielded by fairings. The roughness of the surfaces should also be reduced particularly for the side doors where improved sealing and retractable covers for the handrails were implemented in Series 700 Shinkansen [34].

2.1.6 Rear power car

The flow features that can exist in the wakes are the shear layer separations, longitudinal helical flows, vortex streets, recirculation regions and others [36]. The helical vortices behind the train would extend a considerable distance into the vehicle wake and close to the ground. Such helical vortices generate some sort of regular oscillation in the train wake. Generally, the near wake is characterized by large scale recirculation and longitudinal vortex structures with unsteady fluctuations primarily caused by the separated shear layer and wake pumping [20]. As a large scale unsteady flow structure, the train wake generates increased instability from the flow and produces an additional source of aerodynamic noise of low frequency. Similar to the front power car nose, the rear power car should be streamlined to optimize the aerodynamic behaviour of the wake flow to further reduce the aerodynamic noise.

2.1.7 Coach wall surfaces

Aerodynamic noise is caused by the flow of air over the train as it travels at high speed. This flow is complex and includes a turbulent boundary layer around the train. Near the leading edge, this boundary layer is laminar while it rapidly forms into a turbulent boundary layer because of the influence of friction between the coach wall surface and the flow over the train due to the viscosity. The turbulent flow induced noise has a quadrupole-like radiation pattern. They are much less efficient radiators than monopoles or dipoles. Therefore, the sound produced by a turbulent flow is only a very small fraction of the flow energy, and this free turbulence is not the main source of aerodynamic noise for exterior railway noise. Compared with other sources for a high-speed train running at 300 km/h, this source is not predominant, but it can be significant for much higher speeds [11].

The turbulent boundary layer is distributed on the train surface with a low source level but a large area. It is also a correlated source over a noticeably large length at low frequency. Therefore, it is difficult to measure this low level source reliably using a microphone array due to contamination by side lobes from other sources or by background noise. Based on numerical simulations and measurements carried out on a scale model in a wind tunnel, it has been confirmed that the boundary layer does not grow markedly in width along the length of the train [9]. Nevertheless, a turbulent boundary layer over curved or rough surfaces can introduce oscillation in wall pressure and shear stress which are dipole sources, particularly where flow separation occurs, for example at the front and rear of the train.

An effective way for reducing the aerodynamic noise from the turbulent boundary layer is to keep the coach wall surface smooth to reduce dipole-type source generation which is an appreciably more efficient radiator in comparison with the quadrupole noise.

2.1.8 Ventilators, louvres and cooling fans

Noise sources due to ventilators could appear around power cars. Such sources are not always easily suppressed. However, they can be characterized by some specific frequencies and solutions can be obtained directly by optimizing the

ventilators themselves. Louvres can be considered as a series of cavities and can be studied by experiments in anechoic wind tunnels. Cooling fans tend to dominate the noise emissions from a power car under stationary and low-speed conditions, especially during hot-running conditions. As the power cars have a nearly continuous need for cooling, the fans tend to run at a steady speed, with a low speed setting for cool conditions and a high speed setting for hot conditions. Detailed studies of cooling fans could result in significant benefits for power car noise emission. It has been concluded that the acoustic emission of an axial fan could be reduced by 10 dB while improving the airflow performance used on an SNCF railcar [37].

2.1.9 Concluding remarks

For high-speed trains, there are several sources which contribute to the overall aerodynamic noise, each of which may have different physical characteristics and generation mechanisms. Significant progress has been made in the understanding of the physical mechanisms of some sources, such as those from the inter-coach spacing, the coach wall surfaces, the nose and rear of the power car, *etc*. Various solutions have been found to reduce the aerodynamic noise from these regions.

As the noise generating mechanism from pantographs is progressively understood, much development has been completed in reducing aerodynamic noise around such areas. By comparison, the aeroacoustic sources which can occur in the bogie area are complex and up to now, most aerodynamic noise behaviour from the bogie region has been characterized experimentally. The modelling of aerodynamic noise from the bogie area is still in its infancy. It can be expected that both numerical approaches and experimental methods could offer the opportunity to make parametric studies, characterize approximately the phenomenon and obtain potential solutions for noise reduction regarding the bogie region.

2.2 Theory on Aerodynamic Noise Prediction using Acoustic Analogy

The fundamental principles of aerodynamic noise prediction in an unbounded flow using acoustic analogy were initially derived by Lighthill [38]. Curle [39] extended it to consider the presence of solid boundaries in the flow region. Then, for predicting aerodynamic noise from moving bodies, Ffowcs Williams and Hawkings [40] developed a method to include the effect of a moving surface in the fluid on the generation of sound.

2.2.1 General sound sources

Aerodynamic noise generally includes the unsteady flow noise caused by the turbulent fluid motions and the flow interaction noise associated with the aerodynamic forces interacting with the body surfaces. Thus, based on their mathematical manipulations, the sound source distributions can be categorized to monopole, dipole and quadruple sources, respectively [40]. A monopole source corresponds to the noise produced by the unsteady fluid mass passing through the control surface. The sound field generated from the monopole source radiates omni-directionally. The dipole source is obtained by placing a neighbouring pair of point monopoles with equal strength out of phase, and thus its directivity pattern shows a maximum magnitude on the dipole axis since some cancellations occur in the acoustic field. The oscillating pressure forces acting on the wall surfaces can generate dipole noises. The quadruple source consists of two identical dipoles with opposite phase placed close together. There are two combinations of quadrupoles. One is termed a lateral quadruple with two dipole not lying on the same line and the other one is termed a longitudinal quadruple having two dipole axles lying along the same line. The lateral quadruple shows a directivity pattern with four lobes (directions) and the longitudinal quadruple has a directivity pattern similar to dipoles. The fluctuating stress exerted on the flow can produce quadruple noise.

2.2.2 Lighthill's theory: acoustic analogy

The origins of the theory of aerodynamically generated sound can be traced to Lighthill's influential work in 1952 [38]. Starting from the Navier-Stokes (N-S) equations for a compressible viscous fluid, the equations of fluid motion were

reformulated to have a wave operator on the left-hand side and all other terms were put on the right-hand side as equivalent source functions driving the sound field. Thus, the convection effects and turbulence are incorporated within the source function and the radiated sound is calculated as if it were in a uniform medium with zero mean flow. Lighthill's theory shows that there is an exact mathematical analogy between the sound radiated by a turbulent flow and that radiated by equivalent quadrupole sources in a non-moving medium for unbounded flow. For such analysis, a noise generation area governing the fluctuations in the fluid is decoupled from the wave propagation region of a uniform acoustic medium at rest. It is postulated that sound is a small component of the fluid motion and the flow behaviour in the source region can be determined without considering the effects of sound generation and propagation on the fluid. The unsteady flow generates sound and modifies its propagation while the sound waves do not affect the flow in any significant way. Thus, the acoustic source functions can be extracted from the flow field computed by time-accurate turbulence simulation tools.

Consider an unbounded region of space in which there is an unsteady fluid flow. Based on the conservation of mass and momentum, the exact equations of motion in an arbitrary continuous medium at rest are given by

$$\frac{\partial \rho}{\partial t} + \frac{\partial}{\partial x_i}(\rho u_i) = 0\,, \tag{2.1}$$

$$\frac{\partial}{\partial t}(\rho u_i) + \frac{\partial}{\partial x_j}\left(\rho u_i u_j + p\delta_{ij} - \tau_{ij}\right) = 0\,, \tag{2.2}$$

where the summation convention is used for repeated index; x_i and x_j represent the Cartesian coordinates ($i = 1,2,3$), ρ is the density, p the pressure, u_i the flow velocity. τ_{ij} is the viscous stress tensor and for Newtonian fluid it is given by

$$\tau_{ij} = \mu\left[\frac{\partial u_i}{\partial x_j} + \frac{\partial u_j}{\partial x_i} - \frac{2}{3}\left(\frac{\partial u_k}{\partial x_k}\right)\delta_{ij}\right], \tag{2.3}$$

in which μ is the dynamic viscosity and δ_{ij} is the Kronecker delta, $\delta_{ij} = 1$ for $i = j$ and 0 for $i \neq j$.

Now the wave equation can be deduced by taking the time derivative $\partial/\partial t$ of Equation (2.1) and the divergence $\partial/\partial x_i$ of Equation (2.2). This yields

$$\frac{\partial^2 \rho}{\partial t^2} + \frac{\partial^2 (\rho u_i)}{\partial x_i \partial t} = 0\,, \tag{2.4}$$

and

$$\frac{\partial^2 (\rho u_i)}{\partial x_i \partial t} + \frac{\partial^2 \left(\rho u_i u_j + p\delta_{ij} - \tau_{ij}\right)}{\partial x_i \partial x_j} = 0\,. \tag{2.5}$$

Subtracting Equation (2.5) from (2.4) gives

$$\frac{\partial^2 \rho'}{\partial t^2} = \frac{\partial^2 \left(\rho u_i u_j + p\delta_{ij} - \tau_{ij}\right)}{\partial x_i \partial x_j}\,, \tag{2.6}$$

where $\rho' = \rho - \rho_0$; ρ_0 is the non-perturbed density in the uniform medium. Introducing a term $c_0^2 \nabla^2 \rho'$ and subtracting it from both sides yields

$$\frac{\partial^2 \rho'}{\partial t^2} - c_0^2 \nabla^2 \rho' = \frac{\partial^2 T_{ij}}{\partial x_i \partial x_j}\,. \tag{2.7}$$

in which c_0 is the sound speed in the undisturbed free-stream medium; ∇ is the gradient operator and $\nabla^2 = \frac{\partial^2}{\partial x_j \partial x_j}$. This is Lighthill's acoustic analogy, with the Lighthill stress tensor T_{ij} defined as

$$T_{ij} = \rho u_i u_j - \tau_{ij} + (p - c_0^2 \rho')\delta_{ij}\,, \tag{2.8}$$

which represents a distribution of quadrupole sources where $\rho u_i u_j$ is the momentum flux tensor and corresponds to the fluctuating Reynolds stresses; $(p - c_0^2 \rho')$ is associated with non-isentropic effects and τ_{ij} is the viscous stress tensor and describes the effects of viscosity.

Representing sound propagation with a standard wave equation, Lighthill's analogy moves everything else to the right-hand side and treats them as equivalent sources. This is an acoustic analogy so these quadrupole sources are equivalent sources that generate exactly the same sound field as if the full Navier-Stokes equations had been solved. In aerodynamic sound predictions, the main problem now is to identify the components within the Lighthill stress tensor T_{ij}. The solution to Lighthill's equation for the radiated sound pressure can be readily obtained using the free space Green's function as the problem of predicting sound in a moving medium has been reduced to that of the equivalent classical acoustical problem in a uniform fluid at rest. The Green's function for three-dimensional wave equation satisfies

$$\left(\frac{\partial^2}{\partial t^2} - c_0^2\nabla^2\right) G(\mathbf{x}, t; \mathbf{y}, \tau) = -\delta(\mathbf{x}-\mathbf{y})\delta(t-\tau)\,. \tag{2.9}$$

Then, in free space the Green's function can be shown to be

$$G(\mathbf{x}, t; \mathbf{y}, \tau) = \frac{1}{4\pi|\mathbf{x}-\mathbf{y}|}\,\delta\left(t - \tau - \frac{|\mathbf{x}-\mathbf{y}|}{c_0}\right), \tag{2.10}$$

which is the causal solution of the wave equation generated by the impulsive point source $\delta(\mathbf{x}-\mathbf{y})\delta(t-\tau)$, located at the point $\mathbf{x}=\mathbf{y}$ at time $t=\tau$.

Therefore, if a quadrupole element of strength T_{ij} at source position $\mathbf{y}$ generates sound, the acoustic density perturbation at far-field observer position $\mathbf{x}$ can be written as

$$\rho'(\mathbf{x}, t) = \frac{1}{4\pi c_0^2}\iiint_V \frac{\partial^2}{\partial y_i y_j}\left[T_{ij}\left(\mathbf{y}, t - \frac{|\mathbf{x}-\mathbf{y}|}{c_0}\right)\right]\frac{d\mathbf{y}}{|\mathbf{x}-\mathbf{y}|}\,. \tag{2.11}$$

Note that

$$\frac{\partial}{\partial y_i}\left[\frac{\delta\left(t-\tau-\frac{|\mathbf{x}-\mathbf{y}|}{c_0}\right)}{|\mathbf{x}-\mathbf{y}|}\right] = -\frac{\partial}{\partial x_i}\left[\frac{\delta\left(t-\tau-\frac{|\mathbf{x}-\mathbf{y}|}{c_0}\right)}{|\mathbf{x}-\mathbf{y}|}\right]. \tag{2.12}$$

Then, Equation (2.11) can be expressed as

$$\rho'(\mathbf{x}, t) = \frac{1}{4\pi c_0^2}\frac{\partial^2}{\partial x_i x_j}\iiint_V T_{ij}\left(\mathbf{y}, t - \frac{|\mathbf{x}-\mathbf{y}|}{c_0}\right)\frac{d\mathbf{y}}{|\mathbf{x}-\mathbf{y}|}\,, \tag{2.13}$$

in which the integration is performed over the turbulent domain V where the sound sources are evaluated. Sound takes a certain amount of time to travel through space, i.e. sound emitted at source position $\mathbf{y}$ is heard by the observer at receiver position $\mathbf{x}$ at a time $(|\mathbf{x}-\mathbf{y}|/c_0)$ after emission. Since the sound travels at speed c_0 over a distance $(|\mathbf{x}-\mathbf{y}|)$ from source to observer, sound arriving at $\mathbf{x}$ at time t must have been launched from the source at a previous time, $t - |\mathbf{x}-\mathbf{y}|/c_0$, the retarded time (in other words, turning the clock back to when the sound was emitted).

When differentiating the integrand in Equation (2.13) in association with the points far enough from the flow to be in the radiation field of each quadrupole which is treated as a compact source, the spatial differentiation with respect to x_i can be replaced by a temporal differentiation represented as

$$\frac{\partial}{\partial x_i} \leftrightarrow -\frac{1}{c_0}\frac{x_i}{|\mathbf{x}|}\frac{\partial}{\partial t}. \tag{2.14}$$

In most flows, compared with momentum flux tensor $\rho u_i u_j$, the viscous shear stress τ_{ij} is generally very small. And for low Mach number flows, the heat conduction constitutes a second-order effect and can be neglected as well. Hence, it is the fluctuating Reynolds stresses, $\rho u_i u_j$, which are dominant source terms. Then, for low Mach number flows, the Lighthill stress tensor can be approximated to

$$T_{ij} = \rho u_i u_j . \tag{2.15}$$

Considering a typical velocity scale U and a typical length scale l, the characteristic frequencies of the flow are proportional to U/l. Thus, the fluctuations in $\partial^2 T_{ij}/\partial t^2$ are proportional to $\rho U^2 (U/l)^2$ and an estimate for the squared density variations corresponding to the sound intensity is given as [38]

$$(\rho')^2 \propto \left(\frac{1}{c_0^2}\right)^2 \left(\frac{1}{c_0^2}\right)^2 \left(\frac{U}{l}\right)^4 (\rho_0 U^2)^2 \left(\frac{l^3}{|\mathbf{x}|}\right)^2 = {\rho_0}^2 \left(\frac{U}{c_0}\right)^8 \left(\frac{l}{|\mathbf{x}|}\right)^2 , \tag{2.16}$$

which shows that the quadrupole sound intensity of low Mach number flow scales with the eighth power of the flow velocity.

2.2.3 Curle's theory: effect of solid boundaries

Since solid boundaries have a significant effect on the aerodynamic noise generation, the interaction of solid bodies with turbulent flows will produce increased sound compared with free space turbulence.

Taking into account the presence of solid boundaries, Curle extended Lighthill's theory. This modification is referred to as the Lighthill-Curle theory [39]. The quadrupole sound will be reflected and diffracted throughout the regions external to the solid boundaries. Due to the fluctuating forces on the solid body resulting from the unsteady flow, a dipole source distribution corresponding to the externally applied forces leads to

$$\rho' = \frac{1}{4\pi c_0^2}\frac{\partial^2}{\partial x_i x_j}\iiint_V T_{ij}\left(\mathbf{y}, t - \frac{|\mathbf{x}-\mathbf{y}|}{c_0}\right)\frac{d\mathbf{y}}{|\mathbf{x}-\mathbf{y}|}$$

$$+\frac{1}{4\pi c_0^2}\frac{\partial}{\partial x_i}\iint_S l_j P_{ij}\left(\mathbf{y}, t-\frac{|\mathbf{x}-\mathbf{y}|}{c_0}\right)\frac{dS(\mathbf{y})}{|\mathbf{x}-\mathbf{y}|}, \tag{2.17}$$

where S represents the surface of the solid boundary, l_j is the unit outward normal (towards the fluid) on surface S and P_{ij} is the compressive stress tensor given by

$$P_{ij} = p\delta_{ij} - \tau_{ij}\,. \tag{2.18}$$

Similar to the estimation of the quadrupole source in (2.13) by Lighthill through simplifying the volume integral at large distances from the flow, a dimensional analysis [39] of the density fluctuations due to the dipole term in (2.14) yields

$$(\rho')^2 \propto {\rho_0}^2\left(\frac{U}{c_0}\right)^6\left(\frac{l}{|\mathbf{x}|}\right)^2, \tag{2.19}$$

which indicates that for flows with low Mach number, compared with the results from Equation (2.16), the dipoles are more efficient sound radiators than the quadrupoles.

2.2.4 Ffowcs Williams-Hawkings method: effect of source motion

Most problems in aerodynamic noise generation are related to moving sources which influence the sound radiation pattern. Considering the effects of source motion, Ffowcs Williams and Hawkings [40] extended the Lighthill-Curle theory. To take into account the effects of surfaces in arbitrary motion, a Heaviside function $H(f)$ is introduced as

$$H(f) = \begin{cases} 1 & for\ f > 0 \\ 0 & for\ f < 0 \end{cases}, \tag{2.20}$$

where $f = 0$ denotes a mathematical surface used to embed the exterior flow problem, $f > 0$ in an unbounded space. Then $H(f)$ is equal to unity in the region exterior to the control surface and vanishes within the surface. By multiplying the equations of mass conservation (Equation 2.1) and momentum conservation (Equation 2.2) by $H(f)$, a wave equation for a moving source problem can be rearranged as

$$\frac{\partial^2[H(f)\rho']}{\partial t^2} - c_0^2\nabla^2[H(f)\rho'] = \frac{\partial}{\partial t}[Q\delta(f)] - \frac{\partial}{\partial x_i}[F_i\delta(f)] + \frac{\partial^2}{\partial x_i x_j}\left[T_{ij}H(f)\right], \tag{2.21}$$

where $\delta(f)$ is the Dirac delta function; Q and F_i are monopole and dipole source terms related to surface-flow interaction noise, i.e. $Q = \rho_0 v_n$ where v_n is surface normal velocity and $F_i = pn_i$ in which p is the surface gauge pressure and n_i is the component of unit normal vector pointing outward to the surface; T_{ij} is Lighthill's quadrupole source. This resulting equation is the Ffowcs Williams-Hawkings (FW-H) equation to cope with the motion of a surface. It is necessary to state two original ideas in the FW-H acoustic analogy [40,41]. First, the available simple Green's function is imposed on a larger domain into which the original problem is embedded. Another one is that conservation laws in differential form can be utilized to dispose of the jump conditions across flow discontinuities when all the fluid quantities are regarded as generalized functions.

The classical Ffowcs Williams–Hawkings equation is the most general form of the Lighthill acoustic analogy method and is appropriate for computing the acoustic field when provided with input of unsteady-flow conditions. A generic discontinuity surface S is introduced and the fluid extends inside the control surface with the conditions of the undisturbed medium at rest. Then, after embedding the original problem into an unbounded space, the wave equation is valid in the entire three-dimensional space and the simple Green's function can be utilized. Hence, the flow parameters have discontinuities across the data surface. Assuming the fluid parameters are generalized functions and utilizing conservation laws with generalized derivatives, the formal solution of the FW-H equation may be written as

$$p'(\mathbf{x},t) = \frac{\partial}{\partial t}\int_{f=0}\left[\frac{Q_i n_i}{4\pi|\mathbf{x}-\mathbf{y}|}\right]_{\tau_e} dS - \frac{\partial}{\partial x_i}\int_{f=0}\left[\frac{L_{ij} n_j}{4\pi|\mathbf{x}-\mathbf{y}|}\right]_{\tau_e} dS + \frac{\partial^2}{\partial x_i x_j}\int_{f>0}\left[\frac{T_{ij}}{4\pi|\mathbf{x}-\mathbf{y}|}\right]_{\tau_e} dV, \quad (2.22)$$

where the control surface is typically described by $f(\mathbf{x},t) = 0$ such that the unit outward normal vector $\hat{\boldsymbol{n}} = \nabla f$. $[\quad]_{\tau_e}$ denotes the evaluation at the emission time. $p'(\mathbf{x},t)$ on the left-hand side of the equation represents the acoustic pressure fluctuation perceived by the observer located at position $\mathbf{x}$ and at observer time t. Note that the acoustic pressure can be interpreted as $p' = c_0^2\rho' = c_0^2(\rho - \rho_0)$

when $\rho'/\rho_0 \ll 1$. The source terms under the integral sign on the right-hand side of the equation are defined as

$$Q_i = \rho(u_i - v_i) + \rho_0 v_i \,, \tag{2.23}$$

$$L_{ij} = (p - p_0)\delta_{ij} + \rho u_i\big(u_j - v_j\big) \,, \tag{2.24}$$

$$T_{ij} = \rho u_i u_j - \tau_{ij} + [(p - p_0) - c_0^2\rho']\delta_{ij} \,, \tag{2.25}$$

where Q_i and L_{ij} are terms corresponding to thickness and loading noise [41,42] ; T_{ij} is the Lighthill stress tensor. u_i and v_i are the flow and surface velocity components in the ith direction. τ_{ij} is the viscous stress tensor. The thickness and loading sources are surface sources and act only on the integration surface $f(\mathbf{x}, t) = 0$ as indicated by the presence of the Dirac delta function $\delta(f)$ in Equation (2.21). On the other hand, the quadrupole source is a volume distribution source as indicated by the Heaviside function $H(f)$ in Equation (2.21). The quadrupole source term accounts for all the flow non-linearity in the domain exterior to the control surface and acts throughout the volume beyond the data surface. It should be noted that when the source data surface is in motion, the thickness and loading sources behave differently from stationary monopole and dipole sources since the radiation patterns calculated from the above equations are changed for sources on a moving surface.

It is shown from Equation (2.22) that the pressure fluctuation at a far-field observer position is obtained through the superposition of contributions from spatially distributed source terms. The thickness source term models the noise generated by the displacement of fluid as the body passes. The dipole source term represents the noise resulting from the unsteady motion of the force distribution on the body surface. The thickness and loading source terms have been used extensively in aerodynamic noise prediction because they account for the predominant acoustic signals in many cases and they do not require knowledge of the flow field away from the data surface. In a low Mach number flow, the quadrupole source term contribution is negligible when compared with the contributions from the other sources.

For the cases of the high-speed train studied here, the strong flow interaction around the moving geometries will produce the surface pressure fluctuations

which generate the noise at a much higher efficiency, and therefore the surface dipole noise can be potentially the dominant aerodynamic noise source [9, 11, 28].

2.2.5 Theory of vortex sound

In an unbounded flow the velocity $\mathbf{u}$ can be decomposed into an irrotational part, with its potential given by φ and a rotational part $\mathbf{v}$ and expressed as

$$\mathbf{u} = \nabla\varphi + \mathbf{v}\,. \tag{2.26}$$

The irrotational velocity field corresponds to the dilatation and compression of the fluid elements. Then the vorticity vector is given by

$$\boldsymbol{\omega} = \nabla \times \mathbf{u} = \nabla \times \mathbf{v}\,, \tag{2.27}$$

and based on Equation (2.15), the source term in Lighthill's equation can be reformulated as [43]

$$\frac{\partial^2 T_{ij}}{\partial x_i \partial x_j} = \frac{\partial^2 (\rho u_i u_j)}{\partial x_i \partial x_j} = \rho\nabla\cdot(\boldsymbol{\omega}\times\mathbf{v}) + \nabla^2\left(\frac{1}{2}\rho\mathbf{v}^2\right). \tag{2.28}$$

It is concluded that at low Mach numbers, the component $\nabla^2\left(\frac{1}{2}\rho\mathbf{v}^2\right)$ may be neglected. Representing a dipole distribution, the term $\rho\nabla\cdot(\boldsymbol{\omega}\times\mathbf{v})$ is the principal volume sound source from Lighthill's quadrupole contributions $\partial^2(\rho u_i u_j)/\partial x_i \partial x_j$.

Thus, the acoustic pressure in the far-field is represented as [43,44]

$$p(\mathbf{x},t) \approx \frac{-\rho_0 \mathbf{x}}{4\pi c_0 |\mathbf{x}|^2}\frac{\partial}{\partial t}\iiint_V (\boldsymbol{\omega}\times\mathbf{v})\left(\mathbf{y}, t - \frac{|\mathbf{x}|}{c_0} + \frac{\mathbf{x}\cdot\mathbf{y}}{c_0|\mathbf{x}|}\right)d\mathbf{y}\,. \tag{2.29}$$

This result indicates that when the Lamb vector $(\boldsymbol{\omega}\times\mathbf{v})$ changes, the corresponding parts of the fluid will radiate sound.

2.3 Numerical Methods for Aeroacoustics

Flow unsteadiness is crucial to the flow-generated sound and the discipline of acoustics is intimately related to fluid dynamics. Therefore, the phenomena associated with sound generated by and propagated in fluid can be understood

and analysed in the general framework of fluid dynamics. However, the main challenge in numerically predicting sound waves stems from the fact that sound waves have much lower energy than fluid flow, typically by several orders of magnitude. This poses a great challenge to resolve sound waves numerically, especially in predicting sound propagation to the far-field which is required to perform the computation over long distances. The other difficulty comes from calculating the turbulence flow in the near field that are responsible for the sound generation, where fine resolutions are needed to solve the unsteady viscous flow.

Since the late 1990s, computational aeroacoustics has been developed as a separate area of study for numerical methods predicting the noise radiation from an aeroacoustic source or the propagation of sound waves in an inhomogeneous flow field [45-47]. This section provides an overview of approaches to compute aerodynamic noise. Considering the challenges and the discipline breadth encountered in aerodynamic noise generation, it is not surprising that various computational approaches with different degrees of sophistication and applicability have been developed. All these techniques require careful validation to ensure that the simulation results are in good agreement with full-scale and experimental data.

2.3.1 Direct computation methods

The nature of aeroacoustics problems is substantially different from those of traditional fluid dynamics and aerodynamics problems [48]. Aeroacoustics problems are time dependent, typically involving a frequency range over a wide bandwidth, with greatly different length scales in different parts of the computational domain. The classic CFD techniques designed for fluid mechanics problems are generally not adequate to simulate aeroacoustic problems accurately. To obtain a better understanding of the physics of the problem, the direct methods have been developed for determining the noise generation mechanisms and sound propagation processes.

In the direct method, both generation and propagation of sound waves are directly computed by solving the compressible Navier-Stokes equation which describes

both the flow field and the aerodynamically generated sound field. This requires considerably high numerical resolution due to the noticeable differences in the length scale present between the acoustic variables and the flow variables. Thus, It is computationally difficult and costly since very fine computational meshes are needed all the way to receivers to capture the finest scales of motion. Such computational cost becomes prohibitive for sound prediction in the far-field. Therefore, the direct methods become feasible only when receivers are in the near field where the flow unsteadiness is predominantly due to local hydrodynamic pressure which can be predicted with a reasonable cost and accuracy. Furthermore, since the acoustic radiation efficiency is markedly low, numerical errors can lead to serious overestimates of sound generation. One solution is the use of high-order and optimized finite difference schemes. However, even with high-order methods, direct numerical simulation (DNS) and large-eddy simulation (LES) require large numbers of computational nodes. Also, it is difficult to maintain high accuracy and computational efficiency for complex flows. Thus, the computational cost of the direct calculations is appreciable and only relatively simple flow configurations at low to moderate Reynolds numbers have been studied using this method [45]. In [49], sound radiation from a plane turbulent boundary layer was investigated using databases from direct numerical simulation, and therefore, the spectrum of turbulent boundary layer noise was predicted by the DNS data.

2.3.2 Integral methods based on acoustic analogy

Compared to the direct method for noise calculation, the integral techniques are computationally more efficient since only the near-field sources are calculated and fed to predict the far-field acoustic signals. As stated in Section 2.2.3, the FW-H formulation adopts Lighthill's acoustic analogy and can predict radiated sound by equivalent acoustic sources such as monopoles, dipoles and quadrupoles based on the time-accurate flow solution data obtained from CFD simulations. The time histories of sound pressure or acoustic signals at prescribed receiver locations are directly computed by evaluating surface integrals. Solid data surfaces are applied to concentrate predominantly the dipole

and monopole sources while permeable integration surfaces may be utilized to also account for the contributions from the quadrupoles enclosed by the source surfaces. To solve the near-field unsteady flow, the CFD methods of DNS, LES, RANS, DES (detached-eddy simulation) and LBM are applied in existing works and introduced as follows. DES is reviewed in more detail since it is utilized in this study.

Without any turbulence models, DNS solves the time-dependent Navier-Stokes equations and resolves all the relevant scales of turbulence. Since very fine meshes are needed to capture the finest scales of motion, DNS is computationally costly and becomes prohibitive for the complex flow, especially with three-dimensional configurations.

In LES, large energy-containing eddies are captured and resolved directly, while small eddies are modelled using a subgrid scale model [8]. Therefore, transporting mostly the momentum, mass, energy, and other passive scalars, the large eddies are dictated by the geometries and boundary conditions, while the small eddies are less dependent on the geometry, tend to be more isotropic and universal. LES should be run for a sufficiently long time to obtain stable statistics of the flow being modelled. However, with a high computational cost due to the resolution required, LES is still remarkably expensive for most geometries if turbulent flow eddies are developed within the boundary layer regions [50].

In RANS simulation of turbulence, the equations governing the transport of the time-averaged flow quantities are solved. Since the Reynolds-averaged approach substantially reduces the required computational efforts and resources, it is widely adopted for practical engineering applications. Time-varying solutions can be obtained from unsteady Reynolds-averaged Navier-Stokes (URANS) equations which model the turbulence and resolve only unsteady mean-flow structures [51].

As a hybrid technique, DES combines LES with RANS method to make use of the most favourable aspects of the two techniques [52]. In DES, a single

turbulence model used in RANS regions (e.g., attached boundary layers) is also employed as a sub-grid-scale model in LES regions (e.g., separated flows). DES models have been specifically designed to resolve massively separated wall-bounded flows at high Reynolds numbers, where the entire boundary layer is treated by URANS models and the LES treatment is applied to the separated regions.

The simulations around a sphere using different models from RANS, DES and LES were performed and compared with experiments at very high Reynolds numbers in [53,54]. It was found that both DES and LES resolve eddies down to the grid scales in the wake and DES is better able to capture unsteady phenomena than URANS. The numerical simulation of a simplified landing gear by DES and URANS was compared in [8,55] using structured grids. Compared with RANS, DES captured better the flow features. It was concluded that resolving a wide range of unsteady scales of motion successfully, DES is promising for sound prediction. Also, the accuracy of DES with unstructured grids has been evaluated [56]. Similar wake structures and close pressure distributions were obtained through simulations by structured and unstructured meshes. In close agreement with data from the experiments, the turbulent kinetic energy (TKE) in the vortex core was predicted accurately by the fine unstructured grid, which showed that unstructured meshes are capable of meeting the requirements for DES.

Unlike the traditional CFD methods solving the Navier-Stokes equations which describe fluid flow in macroscopic scales, the lattice-Boltzmann method (LBM) uses a distribution function to act as a representative for a collection of particles in the mesoscopic fluid flows between microscopic and macroscopic scales. The dynamics on tracking the streaming (advection) and collision (momentum transfer) of the fluid particles are described with a simple, advection-like, linear partial differential equation which requires less computational resources than solving the nonlinear Navier-Stokes equations for unsteady flows; thereby LBM is suitable to handle complex arbitrary geometries [57,58].

For numerical simulations, computations on a full-scale simplified train using the lattice-Boltzmann method along with the turbulence wall function approach can provide global information on the aerodynamic and aeroacoustic behaviour, while calculations on some simplified scaled geometries can reveal more details of the flow behaviour and the corresponding aeroacoustic mechanisms for some main noise-generating components of high-speed trains such as the bogie areas. Moreover, these numerical simulations can be performed with affordable computer resources and verified by experimental measurements in an anechoic wind tunnel [3,5].

2.3.3 Empirical methods

Empirical methods for airframe noise analysis started from similar geometrical configurations. Consisting of the wheels and main struts, the early aerodynamic noise prediction model didn't take into account the small details responsible for high frequency noise and thereby led to an under-prediction of the overall sound level of about 8 dB [59].

Applying various empirical constants to fit standard source characteristics to landing gear components such as struts, wheels and small features, a prediction model was developed to determine the overall level of the landing gear noise during fly-over [60]. Using the basic scaling law based on Curle's equation, this prediction method was found to agree well with experimental measurements from wind-tunnel tests with different landing gear configurations [61].

An empirical model has been developed by decomposing the landing gear noise spectrum into three components corresponding to low (wheels), mid (main struts) and high frequency components (small features) [62]. The sound pressure level for each frequency component is defined and the overall sound pressure level and frequency distribution are represented in terms of distance, length scale, flow velocity, complexity factor and the number of struts and wheels. Related to the measurable parameters in the aircraft design, a complexity factor is used to make the noise prediction in high frequencies feasible.

Based on the empirical model for landing gear noise prediction [62], a component-based model has been built and developed to predict the aerodynamic noise from high-speed trains [63,64]. Compared with measurements of the overall noise spectra levels at different speeds, such a method appears promising to determine the relative importance of various sources of aerodynamic noise from high-speed trains considering that the results can be obtained in a relatively short computation time. However, it relies on source terms that can be provided either empirically or from computation on simplified geometries.

2.4 Experimental Techniques for Aerodynamics and Aeroacoustics

Although numerical simulation becomes increasingly important to investigate the flow behaviour and acoustic properties, experimental methods still play an essential role to obtain global flow and noise quantities, particularly for turbulent flows over complex geometries such as the leading bogie area of a train. The wind-tunnel and on-board measurements are the main methods to test experimentally the aerodynamic noise from high-speed trains; moreover, the experimental measurements can be used to validate the numerical results. The general techniques are briefly summarized below, while such experimental measurements used particularly on trains were introduced mainly in Section 2.1.

2.4.1 Wind-tunnel measurements

Generally, a scale model of a high-speed train is tested in a wind tunnel whose dimensions restrict the model size. This often results in the scale models being simplified by removing the geometrical details and consequently their contributions to the noise generated at high frequencies are ignored. A number of wind-tunnel experiments carried out on different scale models from high-speed trains have been presented in [25,30,33,35,65].

2.4.1.1 Aerodynamic testing

Aerodynamic measurements can help to understand the flow features responsible for noise generation, for instance, vortex shedding has a close relation with the aeroacoustic tonal noise generation and the root-mean-square (RMS) values of the fluctuating forces produced around the geometries correspond to the noise source strength.

Hot-wire anemometry can be used to detect the flow unsteadiness for investigating flow properties such as velocity and turbulence levels. The principle of hot-wire anemometers is that the convective heat transferred from a heated element in a flow depends on the flow velocity. With extremely high frequency-response and fine spatial resolution, they are employed for the detailed study of turbulent flows, or any flow in which rapid velocity fluctuations are of interest. Note that hot-wire is not suitable for the flow measurements of the high turbulence intensity, such as cylinder wake with large vortex shedding, due to the wire vibration and filament motions. The pitot-static system of instruments uses the principle of air pressure gradient and works by measuring pressures or pressure differences to assess the speed and altitude.

Particle image velocimetry (PIV) is a non-intrusive measurement technique used to determine simultaneously the velocities at many points in a fluid flow. The technique involves seeding the upstream airflow with seeding material composed of water-based smoke particles, illuminating the region under investigation by laser and capturing two images of that region in rapid succession. Expanded through a cylindrical lens, two powerful laser pulses generate the laser sheets to capture the particles in each image pair. A series of sets of images allows an averaged velocity vector map to be created, reducing experimental uncertainty. Unsteady flow features can be determined by PIV. As an example, it was used to capture the mean velocity and vorticity fields in the vertical mid-plane surrounding the inline wheels of a landing-gear to determine the noise sources [66]. It was found that the vortex scrubbed turbulent eddies against the wheel surface and shifted locations between the wheels. Thus, it was concluded that the

aerodynamic noise is generated from the fluctuating flow and its interaction with surface components.

2.4.1.2 Aeroacoustic testing

In the early aeroacoustical measurements using stationary open facilities, the tests were carried out in open wind-tunnel sections, with microphones placed around the model and outside the core flow [67]. It was found that a tonal noise independent of flow velocity was associated with the cavity resonance of the wind tunnel and can be defined as background noise. To reduce the effect of sound reflection, anechoic test sections with a low background noise have been developed to measure and localize the sound sources [68].

An elliptical acoustic mirror microphone system consisting of a parabolic reflector and microphones located at its focus was used to measure the noise sources of a transport aircraft [69]. The elliptical mirror focuses the sound from a particular direction onto the microphone in front of it and amplifies the source signal. An image of the noise sources can be surveyed and obtained by traversing the mirror microphone unit over the object being tested. It is particularly useful in a wind tunnel but has also been used in field tests. Results showed that the strong aerodynamic noise sources located at the bogies, especially the leading bogie, and the snowplough region produce considerable noise at higher frequencies, as do the pantographs [69]. Nevertheless, the drawbacks of traversing the mirror and the large size needed for capturing lower frequency signals make such an instrument less popular.

An alternative to the acoustic mirror is the phased microphone array, consisting of a number of microphones at different planar (spiral, cross or star-shaped) locations [9]. By combining the outputs from the microphones with a suitable time delay, the sound from a particular direction can be obtained either during the measurement or by post-processing. Such a process is called beam-forming [70]. An image of the relative importance of noise sources in a plane can be obtained through adjusting the propagation delay and steering the microphone array to

different positions. Meanwhile, various different shaped microphone arrays with improved phased-array signal processing methods designed for sparse arrays have been developed to achieve accurate acoustic source localization through using many fewer microphones to scan an area [71].

Another method developed recently is the application of phased microphone arrays in hard-walled wind tunnels. Covered by a porous surface material, the microphone array is recessed in a sidewall of the wind tunnel. Isolating the microphones from direct contact with the turbulent boundary layer, the porous surface allows acoustic signals to pass through it and reduces the background noise noticeably [72]. Employing a phased microphone array in a hard-walled tunnel makes it possible for pressurized wind tunnels to be used to increase the Reynolds number of the flow with no changes in velocity and model size [73]. However, due to the space limitation, the measurements conducted in hard-walled wind tunnels are often taken in the near field where background noise levels are relatively high, leading to an overestimation of the acoustical signals. Furthermore, the interaction between direct and reflected acoustic waves from the walls of the test section may result in the corruption of the sound field and is responsible for some discrepancies in the aeroacoustic tests. Therefore, the facilities in hard-walled wind tunnels should be acoustically treated before being used for noise measurements [74]. The objective of such experiments carried out in a wind tunnel is to locate the main noise sources and to characterize the unsteady flow around them. One of the main advantages of a wind-tunnel experiment is the ability to carry out parametric studies and to identify the contribution of each part to the global noise level. Nevertheless, due to limitations of the measurement technique and complexity of different parts, the results from wind-tunnel experiments cannot be extrapolated to a full-scale case directly. For instance, the background noise of the wind tunnel, the boundary layer on microphone array, the different Reynolds numbers and the general differences of details from the original train and the scale model, etc., have an influence on the measurements.

To absorb the sound in the walls and avoid its reflection, an anechoic chamber can be used for aeroacoustic tests. The chamber walls are covered with sound absorbing materials, such as glass-fiber cored wedges, which extend from the walls. The empty chamber can provide free field conditions over certain frequencies. When the nozzle of an open-jet wind tunnel is located in the chamber, some sources of background noise corresponding to the open-jet facilities will be generated and mainly are concentrated at low frequencies. The aeroacoustic measurements of the model tests on the scaled train and its components have been performed in an anechoic open-jet wind tunnel to obtain the far-field noise signals and study the aerodynamic noise generation and radiation mechanism from these geometries [25,32,64].

2.4.2 Field and on-board measurements

Microphone array techniques can be used in the field to identify the main source locations and measure the sound pressure level when a vehicle is passing. With appropriate treatments, such measurements can be used to investigate a better characterization of the physical phenomena of aerodynamic sources and derive source models [24]. However, the acoustic signals obtained have a short duration; this makes it difficult to identify correctly the different sources, to describe them statistically, and further to determine their spectrum or directivity.

Another approach is to attach a number of microphones near the sources making use of anti-turbulence sensors which are intended to filter turbulence and to record acoustic waves located downstream of the source region [21]. The long-time stationary signals can be recorded and thus the statistical averages can be obtained. It should be noted that the measured series are not purely acoustic as they involve the aerodynamic components due to the fluctuating part from the turbulence and moreover, the acoustic components might come from different noise sources. With this approach, the acoustic field was measured on a TGV to characterize aerodynamic sources in the bogie and inter-coach spacing areas [21]. The efficiency and the reliability of the methods were demonstrated by the experimental measurements.

2.5 Summary

It is shown that the flow around the train bogie is extremely dynamic and the aeroacoustic sources which can occur in this region are complex. Due to this complexity, it seems necessary to carry out various studies through numerical approaches and experimental methods to characterize the aerodynamic and aeroacoustic behaviour in the bogie area. Considering the effects of source motion, the Ffowcs Williams-Hawkings method can be applied to predict the propagation of acoustic signals from near-field sources to far-field observers with solid and permeable integration surfaces being utilized. Based on the theory of vortex sound, the main acoustic volume source contributions can be visualized by the spatial distribution of the divergence of the Lamb vector. Different experimental methods of wind-tunnel tests, field and on-board measurements can be used to investigate the flow behaviour, locate the main sound sources and identify the noise contribution from each part of a high-speed train.

Chapter 3

Research Description

In general, the procedure for aerodynamic noise calculation using a hybrid method consists of two stages. Firstly, a time-accurate flow simulation is performed to obtain the time-histories of the relevant variables (e.g., pressure, velocity, density, *etc*.) on the selected source surfaces. Then, the sound pressure signals at the user-specified receiver locations are computed using the source data collected, for example, by integrating the FW-H equation.

The research methodology to be used in the current study is presented in this chapter. An overview of the research outline is given firstly and followed by numerical simulation procedures: the grids around the models are generated primarily to discretize the domain; then, the computational mesh is imported into some CFD solvers to obtain flow solution which is fed to far-field noise prediction; subsequently, all the simulation data will be exported for post-processing. Thereafter, the arrangements for wind-tunnel experiments are briefly introduced.

3.1 Research Outline

Existing research has shown that, for high-speed trains, the bogie area, particularly the leading bogie, is one of the main aerodynamic sound generation sources, and the aeroacoustic behaviour around the bogie region still needs further study, especially numerical investigations which can reveal more information on the flow physics. For a complex structure like high-speed train bogie, it is necessary to focus on some isolated components as an initial step before analyzing the flow and noise behaviour around the whole structure.

First of all, as a benchmark case, the flow behaviour and far-field noise radiation from a circular cylinder, representative of the axle, is presented. A detailed mesh resolution study is performed and the numerical simulations are verified by experimental measurements from the literature.

Thereafter, the aerodynamic and aeroacoustic behaviour of an isolated wheelset, two tandem wheelsets, a simplified bogie and the bogie inside the bogie cavity with and without the fairing as well as considering the ground effect for the case without the fairing are investigated. The solid surfaces of these geometries are applied as integration surfaces for noise prediction using the FW–H method. The numerical simulations on the isolated wheelset, tandem-wheelset and simplified bogie cases are verified by comparison with experimental measurements from an anechoic open-jet wind tunnel.

Finally, an aerodynamic noise prediction code is implemented based on the convective FW–H formulation. The validity of the code is demonstrated by the test cases of a point monopole as well as point dipole radiating sound in a moving medium and the idealized wheel case. Thereafter, for the bogie-inside-cavity cases, the noise contributions from the permeable integration surfaces close to the bogie and parallel to the carbody side wall are calculated and compared to determine the noise shielding effect from the fairing mounted around the bogie cavity regions and the noise radiation effect from the ground.

3.2 Numerical Approach

The CFD code used here is OpenFOAM®. As a free, open source software, OpenFOAM contains the broad physical modelling capabilities to model flow and turbulence based on the finite volume method and can resolve the flow-field features with more complex geometries [75]. The wall pressure is saved in each timestep and then imported to the aeroacoustics module in ANSYS Fluent® to compute aerodynamically generated sound using the solid data surfaces of the geometries based on Farassat's Formulation 1A [41]. Furthermore, an in-house code has been made to predict the aerodynamic noise generated from the

permeable data surface based on the convective FW-H equation, which will be described later in Chapter 8.

3.2.1 Computational mesh generation

With an equal number of adjacent elements, a structured mesh has regular interconnection patterns between elements and can be recognized by all interior nodes. Quadrilateral or hexahedral meshing are the most common forms of structured mesh generation. Compared with unstructured meshing, the structured grid strategy is flexible in grid refinement and has the advantages of numerical efficiency and accuracy [76]. However, structured grids generating is a time-consuming task. Generating structured meshes on complicated geometries is extremely difficult, making such an approach more challenging and somewhat impractical.

Unstructured mesh generation allows any number of elements to meet at a single node. Triangle or tetrahedral meshes are most commonly employed in unstructured meshing. With the convenience of grid generation, unstructured grid methodology has been gaining popularity in recent years for solving unsteady flow over complex configurations [77]. However, compared with structured grid counterparts, unstructured mesh solvers require significantly higher computational resources and their solution accuracy needs further improvement.

In this research, multi-block fully structured meshes with hexahedral cells are created for all geometries to keep higher orders of accuracy. The software Gridgen V15.15 [78] is used for mesh generation. The main configuration studied, the bogie geometry, is symmetrical along the axle mid-span where the flow influence of the wheel and frame is small. Neglecting unsteady flow features across the mid-span would be a reasonable simplification to reduce computational cost. Therefore it is reasonable to include only half of the geometry and make use of the symmetry to reduce the simulation size and time. Nevertheless, the extensive structured grid generation with a good cell quality throughout the domain is arduous and much care should be taken to prevent highly skewed and high aspect ratio cells.

It is suggested that a meaningful grid refinements should be conducted to establish a suitable grid quality for CFD simulation [79]. However, a rigorous grid convergence study for a complex geometry case is difficult to achieve because of the large calculations required for the unsteady flow. As a main part of the wheelset, the axle is a typical circular cylinder, from which numerical and experimental data are available for comparison. Therefore, a mesh refinement study has been performed on a circular cylinder case and is used to provide guidelines for the mesh generations on the other geometries here.

Depending on the resolution of the mesh and the Reynolds number ($\mathrm{Re} = U_0 L/\nu$, where L is characteristic length and ν kinetic viscosity) of the flow, the value of normalized wall-normal distance y^+ is based on the viscosity and wall shear stress of a flow and is defined as

$$y^+ = \frac{y u_\tau}{\nu}, \tag{3.1}$$

in which y is the distance from the wall, u_τ is the friction velocity and ν is kinetic viscosity. For RANS simulation or DES, the y^+ in the first near-wall cell should be very small (on the order of y^+=1) for all current cases which ensures that the boundary layer is resolved properly and the turbulence model employed can account for the low-Reynolds number effects inside the viscous sublayer.

3.2.2 CFD solution process

The fundamental principles and main settings for the flow field simulations are described in this section, which include the incompressible Navier-Stokes equations, the one-equation Spalart-Allmaras turbulence model, the delayed detached-eddy simulation model and the numerical schemes utilized in the present CFD code.

3.2.2.1 Governing equations

Aerodynamically, high-speed trains are operating within the low Mach number ($M \leq 0.3$) flow regime, for example at 300 km/h the Mach number is about 0.25. The incoming flow simulated here is also at low Mach numbers (0.09 and 0.2

corresponding to 30 and 70 m/s) and thereby the compressibility effects may be neglected compared with the hydrodynamic flow field, i.e. the density fluctuations are negligible and the flow field obtained is approximately the same from the compressible and incompressible flow solvers. Moreover, at low Mach number the dominant noise sources are the dipole sources from wall pressure fluctuations, which can be predicted essentially through incompressible flow modelling. Therefore, the unsteady, incompressible Navier-Stokes equations are solved for the flow field and the corresponding continuity and momentum equations in tensor notation are represented as follows

$$\frac{\partial u_i}{\partial x_i} = 0\,, \tag{3.2}$$

$$\frac{\partial u_i}{\partial t} + u_j \frac{\partial u_i}{\partial x_j} = f_i - \frac{1}{\rho}\frac{\partial p}{\partial x_i} + \nu \frac{\partial^2 u_i}{\partial x_j \partial x_j}\,, \tag{3.3}$$

where x_i and x_j denote the Cartesian coordinates ($i = 1,2,3$), p is the pressure, ρ is the density, ν the kinematic viscosity, f_i are the body forces and u_i the flow velocity components in the x_i direction. Here ρ and ν are constants for incompressible flow. There are various turbulence models developed to solve these nonlinear equations.

3.2.2.2 Turbulence models

As mentioned in Section 2.3.2, DES is a hybrid RANS/LES with URANS modelling in the near-wall region to resolve the boundary layer and LES in the outer regions to capture the large eddy structures. In the DES model [8,80], the one-equation Spalart-Allmaras (S-A) turbulence model with a modified length scale is proposed for the URANS in the near-wall region. Accordingly, the Spalart-Allmaras turbulence model is applied in this research.

It is very difficult to resolve all turbulence scales which require a very fine grid and a fine resolution in time. Therefore, the instantaneous variables are decomposed into a mean and a fluctuating part,

$$u_i = U_i + u_i', \;\; p = P + p'\,, \tag{3.4}$$

in which U_i and u_i' are the mean and the fluctuating velocity components, P and p' are the mean and the fluctuating pressure components.

Taking the ensemble average of Equations (3.2) and (3.3), and thus the RANS equations can be derived from the N-S equations as

$$\frac{\partial U_i}{\partial x_i} = 0\,, \tag{3.5}$$

$$\frac{\partial U_i}{\partial t} + U_j \frac{\partial U_i}{\partial x_j} = F_i - \frac{1}{\rho}\frac{\partial P}{\partial x_i} + \frac{\partial}{\partial x_j}\left(\nu \frac{\partial U_i}{\partial x_j} - \overline{u_i' u_j'}\right), \tag{3.6}$$

in which F_i are the body forces. The RANS equations are similar to original N-S equations, except for the additional term, the Reynolds stresses $-\overline{u_i' u_j'}$, which couple the mean flow to the turbulence and lead to the so-called closure problem, i.e. the nonlinear Reynolds stress terms should be modelled to close the RANS equations for solving.

As an eddy-viscosity based RANS model, the S-A model uses the Boussinesq hypothesis to relate the Reynolds stresses to the mean velocity gradients:

$$-\overline{u_i' u_j'} = \nu_t S_{ij} - \frac{2}{3} k \delta_{ij}, \tag{3.7}$$

$$S_{ij} = \frac{1}{2}\left(\frac{\partial U_j}{\partial x_i} + \frac{\partial U_i}{\partial x_j}\right), \tag{3.8}$$

in which S_{ij} represents the mean strain rate tensor, ν_t is the turbulent kinematic viscosity and $k\left(=\frac{1}{2}\overline{u_i' u_i'}\right)$ is the turbulent kinetic energy.

The S-A model is a one-equation model which solves a convection-diffusion equation for the modified turbulent kinematic viscosity, $\tilde{\nu}$. The transport equation is given as [81]

$$\frac{\partial \tilde{\nu}}{\partial t} + U_j \frac{\partial \tilde{\nu}}{\partial x_j} = G_\nu + \frac{1}{\sigma_{\tilde{\nu}}}\left[\frac{\partial}{\partial x_j}\left((\nu + \tilde{\nu})\frac{\partial \tilde{\nu}}{\partial x_j}\right) + C_{b2}\frac{\partial^2 \tilde{\nu}}{\partial x_i^2}\right] - Y_\nu\,, \tag{3.9}$$

where G_ν is the production term of turbulent viscosity and defined as

$$G_\nu = C_{b1}\tilde{S}\tilde{\nu}\,, \tag{3.10}$$

in which

$$\tilde{S} = S + \frac{\tilde{\nu}}{\kappa^2 d^2}\left(1 - \frac{\chi}{1 + \chi f_{v1}}\right), \tag{3.11}$$

where κ is the Kármán constant and d is the distance from the wall, f_{v1} is a viscous damping function and given by

$$f_{v1} = \frac{\chi^3}{\chi^3 + C_{v1}^3}, \tag{3.12}$$

in which C_{v1} is a constant and

$$\chi = \frac{\tilde{\nu}}{\nu}. \tag{3.13}$$

The turbulent kinematic viscosity ν_t is obtained from

$$\nu_t = \tilde{\nu} f_{v1}, \tag{3.14}$$

where f_{v1} acts as a damping coefficient in the near-wall region and $\tilde{\nu}$ is equal to ν_t elsewhere.

In Equation (3.11) S is a scalar measure of the deformation tensor, and based on the magnitude of the vorticity, it is represented by

$$S = \sqrt{2\Omega_{ij}\Omega_{ij}}, \tag{3.15}$$

where Ω_{ij} is the mean rate-of-rotation tensor and defined by

$$\Omega_{ij} = \frac{1}{2}\left(\frac{\partial U_i}{\partial x_j} - \frac{\partial U_j}{\partial x_i}\right). \tag{3.16}$$

In the transport equation (3.9), Y_ν is the destruction term of turbulent viscosity in the near-wall region and modelled as

$$Y_\nu = C_{w1} f_w \cdot \left(\frac{\tilde{\nu}}{d}\right)^2, \tag{3.17}$$

where

$$f_w = g\left[\frac{C_{w3}^6 + 1}{C_{w3}^6 + g^6}\right]^{1/6}, \tag{3.18}$$

$$C_{w1} = \frac{C_{b1}}{\kappa^2} + \frac{1 + C_{b2}}{\sigma_{\tilde{\nu}}}, \tag{3.19}$$

$$g = r + C_{w2}(r^6 - r), \tag{3.20}$$

$$r = \frac{\tilde{\nu}}{\tilde{S}\kappa^2 d^2}. \tag{3.21}$$

In Equations (3.17)~(3.21), C_{b1}, C_{b2}, C_{w2}, C_{w3}, $\sigma_{\tilde{\nu}}$ are constants.

The model constants have the following default values [81]:
$C_{b1} = 0.1355$, $C_{b2} = 0.622$, $\sigma_{\tilde{\nu}} = 0.5$, $C_{v1} = 7.1$, $C_{w2} = 0.3$, $C_{w3} = 2$ and $\kappa = 0.4187$.

Taking into account the effect of the mean strain on the turbulence production, a vorticity-strain relationship [82] has been proposed for justification of the default expression for S and the modified production term is given by

$$S \equiv |\Omega_{ij}| + C_{prod}\, min\left(0, |S_{ij}| - |\Omega_{ij}|\right), \tag{3.22}$$

where $|\Omega_{ij}| (\equiv \sqrt{2\Omega_{ij}\Omega_{ij}})$ is the magnitude of vorticity, $|S_{ij}| (\equiv \sqrt{2S_{ij}S_{ij}})$ is the magnitude of the strain tensor and $C_{prod} = 2$.

As referred to previously, the standard S-A model uses the distance to the closest wall as the length scale d to determine the level of production and destruction of turbulent viscosity. The DES model [8,80] replaces d everywhere with a new length scale $\tilde{d}$ defined as

$$\tilde{d} \equiv min\,(d, C_{\text{des}}\,\Delta), \tag{3.23}$$

where the grid spacing, $\Delta = max(\Delta x, \Delta y, \Delta z)$, is based on the largest grid spacing in the x, y, or z direction forming the computational cell and the empirical constant $C_{\text{des}} = 0.65$ is calibrated for homogeneous turbulence.

Therefore, the turbulence model will use URANS mode to compute the ensemble-averaged flow field when $d < C_{\text{des}}\,\Delta$ and the LES mode to resolve the filtered flow field when $d > C_{\text{des}}\,\Delta$. It should be noted that in such a method the grid must be generated following guidelines in the transition region where the model switches from URANS to LES to ensure the whole boundary layer is being solved with the URANS mode.

For RANS meshes with high aspect ratios in the boundary layer, a new formulation of DES has been developed to avoid grid-induced separation caused by modelled stress depletion and preserve the RANS mode throughout the boundary layer. This is known as delayed detached-eddy simulation (DDES) [83]. In this, the DES length scale $\tilde{d}$ is redefined as

$$\tilde{d} \equiv d - f_d max\,(0, d - C_{\text{des}}\,\Delta)\,, \tag{3.24}$$

where d is the distance from the field point to the nearest wall and the delay function f_d is given by

$$f_d \equiv 1 - tanh((8r_d)^3)\,, \tag{3.25}$$

in which the parameter r_d applied to any eddy-viscosity model becomes slightly more robust in the irrotational regions and is represented as

$$r_d \equiv \frac{\nu_t + \nu}{\sqrt{U_{i,j}U_{i,j}}\kappa^2 d^2} \ , \tag{3.26}$$

where $U_{i,j} = \partial U_i / \partial x_j$ are the velocity gradients and the molecular kinematic viscosity ν is employed to rectify the very-near-wall behaviour through keeping r_d away from zero. The function f_d is designed to be 1 in the LES region and 0 elsewhere, and then, the length scale $\tilde{d}$ is equal to d through setting f_d to 0 and yields RANS mode.

Compared with Equation (3.23), there is a qualitative change in Equation (3.24): the length scale $\tilde{d}$ depends on both the geometrical parameters (such as the cell wall distance and grid spacing) and the time-dependent eddy-viscosity field. If a point is indicated to be inside a boundary layer by the value of r_d and the function f_d, the RANS treatment is kept active in the turbulence model. However, when massive flow separation occurs, f_d increases quickly and the LES mode is applied.

The applications of DES in the fully turbulent mode have been confirmed by the Benchmark problem for Airframe Noise Computations (BANC-I) workshop results with different codes [3]. The CFD simulation results using DDES with layered grid show good agreement quantitatively with the experimental data, and further computational results of far-field noise prediction using the acoustic analogy will be presented in the BANC-II workshop [84]. Therefore, the DDES model is employed for aerodynamic simulation in the current research.

3.2.2.3 Solution procedure

As mentioned in Section 3.2, the open source software OpenFOAM-2.2.1 is employed to solve the governing equations for CFD simulations. A second-order accurate scheme is utilized for the convection and diffusion terms of the spatial derivatives and the temporal discretization follows a second-order fully implicit scheme. The pressure-velocity algorithm PIMPLE, combining PISO (pressure

implicit with splitting of operator) and SIMPLE (semi-implicit method for pressure-linked equations) algorithms [75], is applied to solve iteratively the resulting discretized linear-algebra equation system. Compared with the other solvers, the PIMPLE algorithm is more robust and efficient to solve the transient incompressible flow with a large timestep.

The solution needs to converge at each timestep through sub-iterations and the Courant-Friedrichs-Lewy (CFL) condition is a necessary condition for convergence to produce correct simulation results. Therefore, the timestep must be less than a certain value for the solution to be stable. The physical timestep size in the aerodynamic noise calculation is small as it is based on the local advective and acoustic time scales of the flow. As the implicit time-marching schemes used for numerical solutions, a CFL number of less than 1 within most part of the computational domain and the maximum value of 2 within the whole computational domain will be used for all current cases to ensure an adequate temporal resolution for flow simulation in solving certain partial differential equations.

Noise calculation using the hybrid method combines computational fluid dynamics and acoustic analogy. Before extracting the flow source data for an unsteady acoustic analysis, it is necessary to establish a quasi-stationary flow state. This means that the unsteady flow field has become fully developed and runs to a point where its statistics do not change with time. Monitoring the major flow variables at selected points in the domain is helpful for determining whether such a quasi-stationary state has been established.

The simulations are performed on the Iridis3 and Iridis4 clusters at the University of Southampton. The solutions are computed in parallel on different compute nodes (processors). Taking the isolated wheelset case as an example with a physical timestep size of 1×10^{-5} s run on the Iridis3 cluster, the calculations are parallelized over 96 processors and approximately 3.8×10^{4} timesteps are required to reach a fully developed flow field. Thereafter, the collection of acoustic

data needs to be run further for around 5.5×10^4 timesteps to obtain a reasonable frequency resolution in data processing.

3.2.3 Far-field noise prediction

For the current study, owing to a low Mach number flow around the geometries, the surface dipole is the dominant source while noise radiation of the quadrupole sources resulting from the fluctuating stresses of the fluid outside the integration surface is typically small, and thereby may be neglected. As solutions to the FW-H equation (Equation 2.23) with surface sources moving at subsonic speed and eliminating the quadrupole contribution, the equations known as Formulation 1 and Formulation 1A derived by Farassat have been successfully used for helicopter rotor, propeller and other noise predictions for many years [41,42]. With an observer time derivative taken numerically, Formulation 1 increases computational time and reduces the accuracy of the calculation. Formulation 1A is somewhat more complex than Formulation 1; however, any numerical differentiation of an integral of quantities depending on the retarded time is not required. Therefore, the speed and accuracy of the noise calculation is improved in Formulation 1A by eliminating the time derivative of the integral in Formulation 1. This has the great advantage and is especially important for cases of a moving observer. These formulations may be employed to predict the noise generated from an acoustic source moving in a fluid at rest and have been among the commonly used acoustic analogies for a wide range of fly-over and moving-observer problems because of their robustness and relatively low computational cost. With an integral solver based on the retarded time approach, Farassat's Formulation 1A may be written as

$$p'(\mathbf{x},t) = p'_T(\mathbf{x},t) + p'_L(\mathbf{x},t)\,, \tag{3.27}$$

in which p'_T and p'_L represent the thickness and loading noise contributions to the far-field sound pressures and are obtained receptively from [42]

$$4\pi p'_T(\mathbf{x},t) = \int_{f=0} \left[\frac{(\dot{Q}_n + Q_{\dot{n}})}{r|1-M_r|^2}\right]_{ret} dS$$
$$+ \int_{f=0} \left[\frac{Q_n(r\dot{M}_r + c_0 M_r - c_0 M^2)}{r^2|1-M_r|^3}\right]_{ret} dS\,, \tag{3.28}$$

$$4\pi p'_L(\mathbf{x},t) = \frac{1}{c_0}\int_{f=0}\left[\frac{\dot{L}_r}{r|1-M_r|^2}\right]_{ret} dS + \int_{f=0}\left[\frac{L_r - L_{\mathrm{M}}}{r|1-M_r|^2}\right]_{ret} dS$$
$$+\frac{1}{c_0}\int_{f=0}\left[\frac{L_r(r\dot{M}_r + c_0 M_r - c_0 M^2)}{r^2|1-M_r|^3}\right]_{ret} dS\,. \qquad (3.29)$$

In Equations (3.28) and (3.29), the items among brackets '$[\quad]_{ret}$' are determined at retarded time $\tau = t - |\mathbf{x}-\mathbf{y}|/c_0$; the variables $Q_n(= Q_i n_i = [\rho(u_i - v_i) + \rho_0 v_i\,]n_i)$ and $L_i\big(= L_{ij}n_j = [(p-p_0)\delta_{ij} + \rho u_i\big(u_j - v_j\big)]n_j\big)$ are introduced; the dot over each variable indicates the derivative of that variable with respect to the source time, and $\mathbf{n}$, $\mathbf{r}$ and $\mathbf{M}$ correspond to the unit vectors in the surface normal direction, in the sound radiation direction and in the surface velocity direction, respectively; $\mathbf{M}$ is also called a local Mach number vector with the components M_i and correspondingly, $M_r = M_i r_i$ and $L_M = L_i M_i$; the definitions of the other quantities can be found in Chapter 2. The terms with $1/r$ dependence contribute predominantly to the far-field and those with $1/r^2$ dependence dominate the near-field.

Based on Farassat's Formulation 1A, the far-field noise calculations using the solid surface contributions in the FW-H method will be carried out for all the present cases in this study. For the wind-tunnel cases considered here, both the source and the observer are stationary in a uniform flow. This equates to the case in which source and observer moving with speed $-\mathbf{U}_0$ (inflow velocity $\mathbf{U}_0$) in a quiescent medium to utilize Formulation 1A for noise predictions. When the applied integration surface coincides with the solid surfaces in the wind-tunnel cases, the thickness source does not contribute to the noise generation and only the pressure fluctuations on the geometry wall surfaces are calculated.

3.2.4 Post-processing of simulation results

In order to understand the flow behaviour and the corresponding aerodynamic noise mechanism of all current cases, the techniques for the post-processing of the simulation results are briefly introduced here.

The main post-processing methods of aerodynamic results are listed as follows:

1. The instantaneous velocity and vorticity fields on several main cut surfaces of the geometries are presented.
2. The instantaneous vortical structures are visualized using iso-surfaces of the second invariant of the velocity gradient (see Chapter 4), coloured by the velocity magnitude.
3. Monitors are set in specific locations within the computational domain to investigate local flow features inside the wake region behind the geometries.
4. The actual lift and drag coefficients are extracted at every timestep for the whole assembly as well as its various components. The power spectral densities (PSDs) of the lift and drag force histories are computed and displayed.

The power spectral density (PSD) of the signal is determined based on Welch's method [85]. The signal processing approach used by [86] is followed, in which the signal is separated into several segments, each with 50% overlap. A Hanning window is applied to each segment and the PSD of all sections is averaged and compensated. Compared with analyzing the total signal wholly, the advantage of this method is reducing the variance of spectral estimate of the short records in time.

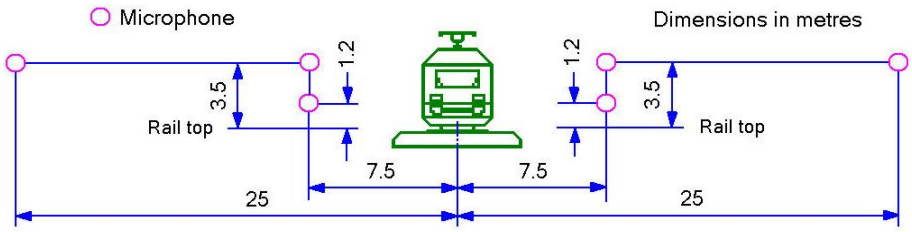

Figure 3.1: Lateral microphone positions for measurements on vehicles with constant speed [87]

The main post-processing steps of aeroacoustic results are presented below:

1. According to the lateral microphone positions arranged for measurements on vehicles illustrated in Figure 3.1 from the international standard (ISO 3095) [87], the receiver positions to obtain acoustic pressure signals are defined and adjusted according to the scale model used.

2. Using Welch's method with a Hanning window, a spectral analysis of the receiver signals is performed based on the fast Fourier transform (FFT).
3. An overall sound pressure level (OASPL) is calculated from the PSD over a certain frequency range for various receiver locations; and based on the OASPL, the directivity of noise radiation to the far-field is depicted.

The overall sound pressure level can be obtained by integrating over all resolved frequencies and given by

$$OASPL = 10\log\left(\sum 10^{SPL_i/10}\right), \tag{3.30}$$

where the SPL (sound pressure level) is defined as

$$SPL = 20\log(p_e/p_{ref}), \tag{3.31}$$

in which p_e is the effective sound pressure and p_{ref} $(= 20\mu Pa)$ is the reference acoustic pressure.

As mentioned in Section 3.2.1, a symmetry plane is used to reduce the simulation cost and only the flow data of half the geometry are available and applied for the far-field noise calculation using the acoustic analogy method. Thus, the sound pressure level from the whole geometry consisting of two symmetrical components is represented as

$$L_p = 10\log(10^{L_{p_1}/10} + 10^{L_{p_2}/10}), \tag{3.32}$$

where L_{p_1} and L_{p_2} are the sound pressure levels of two receivers located symmetrically along the symmetry plane with the same sound source generated from the half geometry and are assumed uncorrelated.

3.3 Experimental Arrangement

Particle image velocimetry experiments for an isolated wheelset case have been carried out to capture an image of the mean velocity field in the wheel mid-span plane of the isolated wheelset to compare with the results from the CFD calculations. The measurements have been arranged in the 7'×5' wind tunnel at the University of Southampton. The working section of the 7'×5' wind tunnel is 2.1m wide, 1.5m high and 4.4m long.

Additionally, the aerodynamic noise measurements for the isolated wheelset, tandem wheelsets and simplified bogie have been arranged in the open-jet anechoic wind tunnel at the Institute of Sound and Vibration Research (ISVR) of the University of Southampton. The dimensions of the nozzle are 350mm wide and 500mm high. The microphones are located in the far field to receive the sound signals and the acoustic measurements will be utilized to verify against the numerical simulations.

3.4 Summary

The brief research outline has been presented. The fully structured meshes with hexahedral cells are created for all geometries to keep higher orders of accuracy. Developed to preserve the RANS mode throughout the boundary layer and apply the LES mode for the massive flow separation, the DDES model is employed for the current flow calculations. Obtained from the CFD simulations, the near-field unsteady flow results are used as the input data to predict the sound field away from the acoustic source region. The PIV experiments are arranged in the 7'×5' wind tunnel to investigate the mean velocity field and the aerodynamic noise measurements are carried out in the open-jet anechoic wind tunnel to receive far-field sound signals. The numerical calculations and wind-tunnel measurements can be verified against each other.

Chapter 4

Circular Cylinder

Many components within the bogie region are of cylindrical shape with various sizes, such as the axles, shock absorbers, suspension springs, anti-roll torsion bar, different types of damper, hydraulic lines and various cables. The interaction of unsteady wakes with these elements creates additional sources of aerodynamic noise. Being of fundamental interest as well as of crucial importance in many engineering applications, the large-scale vortex shedding from cylindrical bluff bodies has been widely studied both numerically and experimentally to investigate the fluid-mechanical behaviour and predict the resulting aerodynamic noise [88-93]. Recently, various configurations of cylinders have been put forward for flow investigation and noise computation, and the numerical results are compared with the experimental measurements [94]. However, even now there are still more challenges to model and simulate with sufficient accuracy the complex flow behavior of flow transition and separation developed from flow passing over a circular cylinder at high Reynolds numbers, which will affect the aerodynamic noise prediction. This chapter investigates this benchmark problem using a CFD approach based on the DDES model and the FW-H acoustic analogy method for calculating the radiated noise. The influence of mesh refinement is presented in detail and the numerical simulations are verified by comparison with the experimental results from the literature.

4.1 Experimental Study in Literature

An experimental study of sound generated by flows around cylinders of different cross-section has been performed in an anechoic wind tunnel [93]. As illustrated in Figure 4.1, the test section of the open-jet was surrounded by an anechoic

chamber. The exit nozzle had a rectangular cross-section and the turbulence level in the jet core was below 0.5%. Positioned along the centreline of the nozzle, the cylinder was fully immersed within the core flow and its lower parts were wrapped with rough emery cloth to suppress the aerodynamic noise generated by vortex shedding from such a portion. Also, the table and mounting fixture were draped with a thick sheet of sponge rubber to prevent either reflections or flow interactions with the shear layer generating unwanted noise.

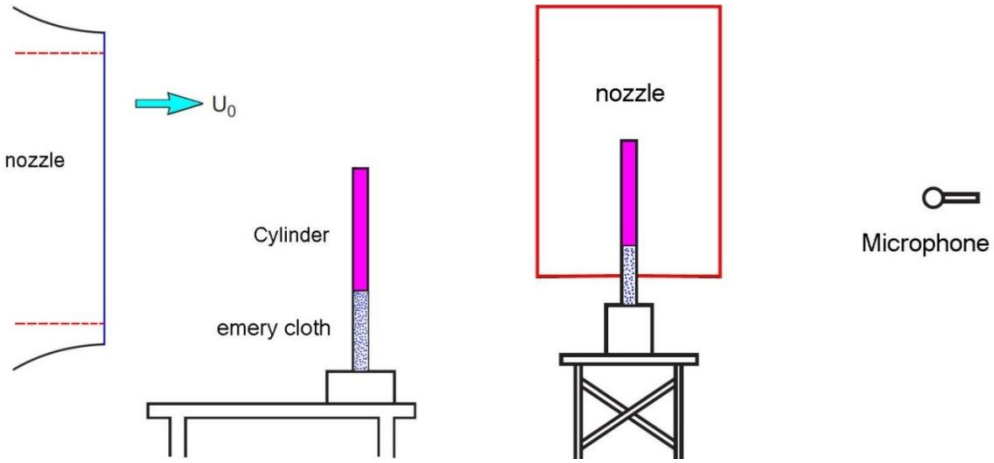

(a) Side view (b) Upstream view

Figure 4.1: Arrangement of cylinder in test section of wind tunnel [93]

The sound was measured by a microphone located at a distance of 1.4 m away from the cylinder centreline and at the height of the mid-point of the cylinder, as sketched in Figure 4.1(b). It was found that for circular cylinders with one free end, the acoustical parameters such as the Strouhal number of the peak frequency and sound pressure level are no longer influenced by the aspect ratio (the length of the cylinder divided by its diameter) if it is greater than about 25. Therefore, a shorter span cylinder with periodic boundary conditions in the spanwise direction can be applied in the numerical simulation to consider most of the turbulence correlation length over a range of frequencies, and thus improve greatly the calculation efficiency. However, it should be noted that if the aspect ratio of a cylinder with one free end is not high enough or the microphone is placed at a positon near the vicinity of the free end, the end effects may play an important role in the aerodynamic noise generation.

4.2 Numerical Setup

The numerical calculation is presented for a cylinder diameter (D) of 20 mm and freestream velocity (U_∞) of 64 m/s (at a Mach number of 0.19), corresponding to experimental data in [93]. This results in a Reynolds number of 87,600, which is typical of the subcritical Reynolds number regime. In the subcritical flow regime ($\mathrm{Re} \leq 1 \times 10^5$), the boundary layer separates on the front of the cylinder and vortex shedding occurs with a Strouhal number of about 0.2 [95]. As the Reynolds number increases, the transition in the boundary layer moves forward over the separation point and separates at the rear of the cylinder. Flow around the cylinder could reach the critical flow state where a typical separation bubble appears; subsequently, in the supercritical Reynolds number range, a separation bubble followed by turbulent separation occurs and in the transcritical range the separation is purely turbulent [95].

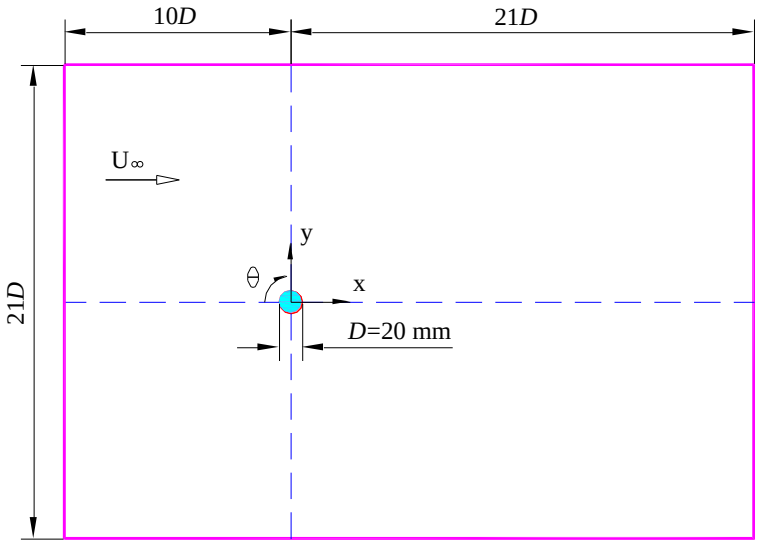

Figure 4.2: Two-dimensional sketch of computational domain with the cylinder

The computational domain is described in Figures 4.2 in which the top and bottom boundaries are located at 10.5D from the cylinder axis and the velocity inlet and pressure outlet are placed, respectively, at 10D and 21D from the cylinder axis (as recommended by [92,96]). According to the turbulence condition inside the jet core applied in the experiment [93], a steady uniform flow with low turbulence level (corresponding to a turbulence intensity of 0.5%) is imposed at the upstream

inlet boundary of the domain. The downstream exit boundary is defined as pressure outlet with a gauge pressure of zero and the same low turbulent viscosity ratio of the inlet is used for the backflow. The outlet boundary condition has negligible influence on the near-wake flow region as it is kept sufficiently far from the cylinder. Far away from the cylinder, the top and bottom boundaries are given the conditions of zero-shear slip wall.

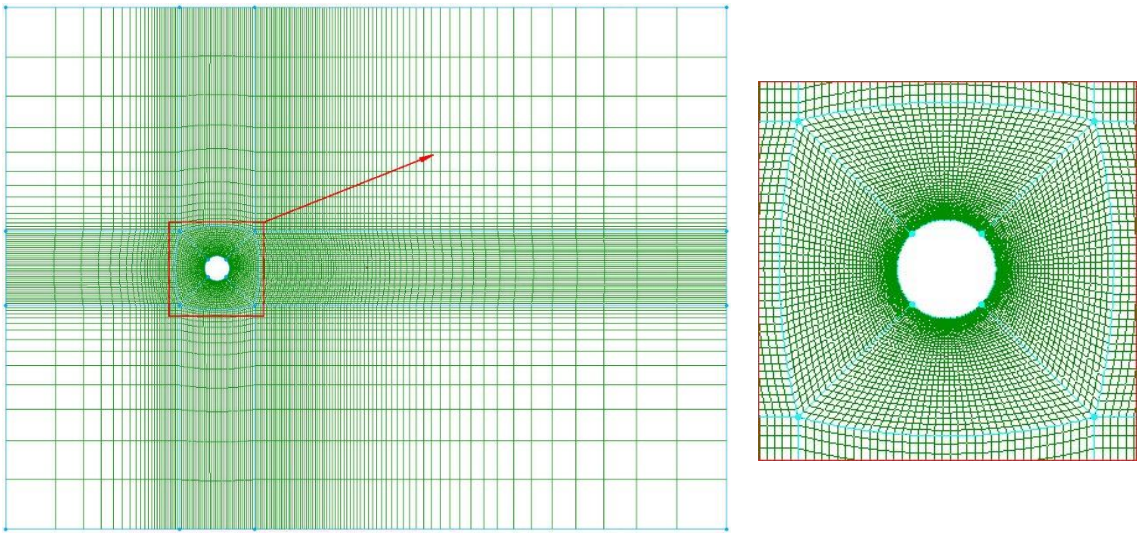

Figure 4.3: Structured mesh generated around the cylinder

In previous studies, based on the experimental fluctuating lift forces, a spanwise correlation length of $3.16D$ was used on the computation domain for a cylinder flow with a Reynolds number of 90,000 [97] and a LES simulation using a spanwise length of $2D$ and $2.5D$ obtained the quite good results verified by the experiments [92]. Although a spanwise length of $2D$ was also applied in DES simulations and the corresponding results agreed fairly well with experimental measurements [92,98], the spanwise length of the domain is set here at $3D$ with periodic conditions employed on the two lateral boundaries. For the cylinder surface, a standard no-slip boundary condition is applied.

For the two-dimensional (*x-y* plane) grids (displayed in Figure 4.3) in the 'Baseline' model which is mainly adopted in this simulation, 150 grid points are equidistantly located on the cylinder surface around the perimeter (i.e. the finest cell size is 0.42 mm). The first cell spacing normal to the wall inside the boundary layer is

set to $1.25 \times 10^{-4}D$ (or 2.5×10^{-6} m), which ensures a sufficient spatial resolution of $y^+ < 1$ (around 0.55). The definition of this non-dimensional distance in the wall boundary layer is based on the viscosity and wall shear stress of a flow as discussed in Section 3.2.1. Figure 4.4(a) displays the y^+ distributions around the cylinder surface where θ is measured in the clockwise direction with zero at the front stagnation point. The mid-span radial profile of y^+ presented in Figure 4.4(b) shows that the maximum y^+ appears in the regime before flow separation where the wall friction velocity or the wall shear stress on the cylinder surface is the largest. Inside the recirculation region of the cylinder wake, the wall friction velocity decreases, leading to a smaller y^+ value. Moreover, y^+ is fluctuating, owing to the oscillating wake after the flow separation.

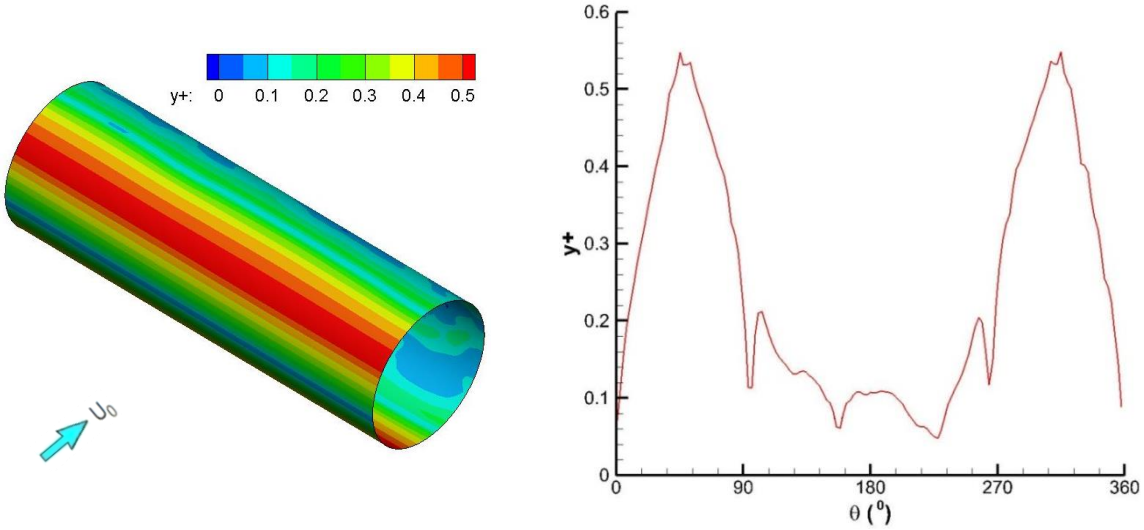

(a) Cylinder surface distributions (b) Mid-span distributions

Figure 4.4: Instantaneous y^+ distributions around the cylinder surface

In the direction normal to the cylinder surface, the stretching ratio of the neighbouring cells is in the range of 1.1 to 1.2. Then, considering the thickness of the boundary layer on the cylinder surface, the spanwise grid spacing $\Delta z = 0.05D$ (or 1 mm) is applied so there are 60 grid points equidistantly located in the spanwise direction. As mentioned before, for the DES model the grid spacing (Δ) is based on the largest grid space in three spatial directions (x, y, z). Here, Δz (1 mm) is the largest grid spacing around the cylinder and this affects the switching between the URANS and LES modes in that region. The total number of grid points reaches 1.2 million. The dimensionless timestep ($\Delta t U_\infty / D$) is set at

0.0128 (the physical timestep size of 4×10^{-6} s), resulting in a sufficiently small CFL number of less than 2 within the computational domain to ensure an adequate temporal resolution for the CFD simulation to be converged at each timestep.

4.3 Grid Sensitivity Study

The influence of spatial resolution has been quantified by using different grid points in the *x*-*y* plane (cases named 'Coarse', 'Baseline' and 'Fine') and the spanwise (*z*) direction; the effect of time resolution has also been examined through reducing the timestep size to one-fifth of that used in the 'Baseline' model. Relative to the 'Baseline' grids, the 'Coarse' grids are reduced by a factor of $\sqrt{2}$ in the number of grid points in each (*x* and *y*) direction and the 'Fine' grids are generated by increasing the refinement in each (*x* and *y*) direction by a factor of 2. Note that the 'Fine' grids need to run with a smaller timestep, one-fourth of that used in the 'Baseline' model. The influence of spatial resolution in the spanwise direction (*z*) is determined by comparing three different grid sizes of 40, 60 and 120 cells with the same *x*-*y* plane grids from the 'Baseline' case.

Grid	Grid points (*x*,*y*)	Grid points (*z*)	Mesh size	$\Delta t U_\infty / D$
Different resolutions in (*x*,*y*)				
Coarse	8500	60	0.51 M	0.0128
Baseline	19125	60	1.15 M	0.0128
Fine	76500	60	4.6 M	0.0032
Different resolutions in (*z*)				
Z1	19125	40	0.77M	0.0128
Z2 (Baseline)	19125	60	1.15 M	0.0128
Z3	19125	120	1.72 M	0.0128
Different resolutions in time				
T1 (Baseline)	19125	60	1.15 M	0.0128
T2	19125	60	1.15 M	0.00256

Table 4.1: Overview of the mesh size and timestep size for grid independence study

Grid	y^+	St	C_L'	C_D'	$\bar{C}_D$	θ_{sep}	L_r/D
Different resolutions in (*x*,*y*)							
Coarse	0.47	0.198	0.775	0.089	1.218	89.8	1.05
Baseline	0.55	0.196	0.486	0.083	1.061	86.8	1.29
Fine	0.50	0.195	0.442	0.081	1.108	85.9	1.41
Different resolutions in (*z*)							
Z1	0.51	0.198	0.637	0.091	1.112	88.5	1.18
Z2 (Baseline)	0.55	0.196	0.486	0.083	1.061	86.8	1.29
Z3	0.55	0.194	0.460	0.086	0.966	87.9	1.15
Different resolutions in time							
T1 (Baseline)	0.55	0.196	0.486	0.083	1.061	86.8	1.29
T2	0.49	0.195	0.493	0.087	1.124	87.8	1.10
Different resolutions in y^+							
Y1 (Baseline)	0.55	0.196	0.486	0.083	1.061	86.8	1.29
Y2	1	0.191	0.475	0.086	0.986	84.6	1.18
Y3	2	0.186	0.499	0.095	0.906	79.3	1.11

Table 4.2: Summary of computations with different mesh and time resolutions

The mesh and timestep size for this grid independence study are described in Table 4.1 where $\Delta t U_\infty/D$ represents the non-dimensional timestep. In addition, the influences of mesh and time resolution are summarized in Table 4.2, the parameters of which are: y^+ is the dimensionless first-cell wall-normal spacing, St is the Strouhal number corresponding to the primary vortex shedding around the cylinder, C_L' and C_D' represent root-mean-square fluctuating lift and drag coefficients, $\bar{C}_D$ is mean drag coefficient, θ_{sep} the separation angle and L_r/D the dimensionless recirculation length. It is noted that the lift and drag coefficients exhibit larger modulations for the coarse grid which indicates its inadequate mesh resolution. The fine mesh case has a slightly smaller separation angle, indicating early flow separation and hence resulting in a longer recirculation region behind the cylinder. Furthermore, increasing the grid or time resolution reduces the dominant shedding frequency slightly (seen in terms of St). The results of different resolutions in y^+ show that the difference in each term is smaller between $y^+ = 0.55$ and $y^+ = 1$ than the corresponding difference between $y^+ = 0.55$ and $y^+ = 2$. In general, all the predicted results have been found to exhibit

a certain degree of grid convergence. The differences between cases 'Baseline' and 'Fine' are smaller than those between cases 'Coarse' and 'Baseline'. The variation of each parameter is less than 10% between the 'Baseline' and 'Fine' case. There is a difference of less than 11% in the results between the 'Baseline' case and the case with fine resolution in the *z* direction. Using a fine timestep also gave little difference in the results. Therefore, the 'Baseline' case is demonstrated to have adequate resolution and is used to guide the generation of grids in the simulations of all remaining cases here.

4.4 Aerodynamic Results

The near-field unsteady flow results are used as the input data to predict the far-field acoustic signals using the FW-H method. Thus, the radiated noise calculation depends on the accuracy of the aerodynamic simulation. According to the grid convergence study achieved above, the flow calculations using the 'Baseline' model are performed. In order to understand the flow behaviour around the cylinder, the simulation results based on the velocity and vorticity fields, the iso-surfaces of Q criterion, the fluctuating lift and drag coefficients, the gauge pressure at a position in the wake, the cylinder surface pressure spectra and the divergence of Lamb vector field are presented and analyzed as follows.

4.4.1 Properties of the DDES model

In order to illustrate the functioning of the DDES scheme to check the RANS/LES switching of the model, Figure 4.5 shows the radial profiles of the mean velocity, the model length scale ratio (r_d), DDES function $(1 - f_d)$ and the ratio of modified length scale to wall distance ($\tilde{d}/d$) at two locations of $\theta = 60^0$ and $\theta = 75^0$ where θ is the angle measured clockwise from the cylinder front stagnation point. The definition of each quantity is described in Chapter 3. In terms of r/D (the dimensionless distance to the wall surface) in the abscissa, the boundary layer extends to (i.e. based on U/U_∞) about 0.008 and RANS/LES switching occurs (the location where $\tilde{d}/d$ becomes less than 1) at around 0.03. It is noted that for both locations, the whole boundary layer is being solved using the RANS method

and the interface from RANS to LES regions remains well outside the boundary layer. When the massive flow separation occurs, the function $(1 - f_d)$ and r_d drop quickly to zero within the boundary layer, enabling the growth of instabilities in the LES region. Therefore, it is demonstrated that the switch from RANS treatment to the LES method occurs abruptly and the grey area corresponding to the interface between the RANS and LES regions becomes narrow within the DDES model used in the numerical simulation.

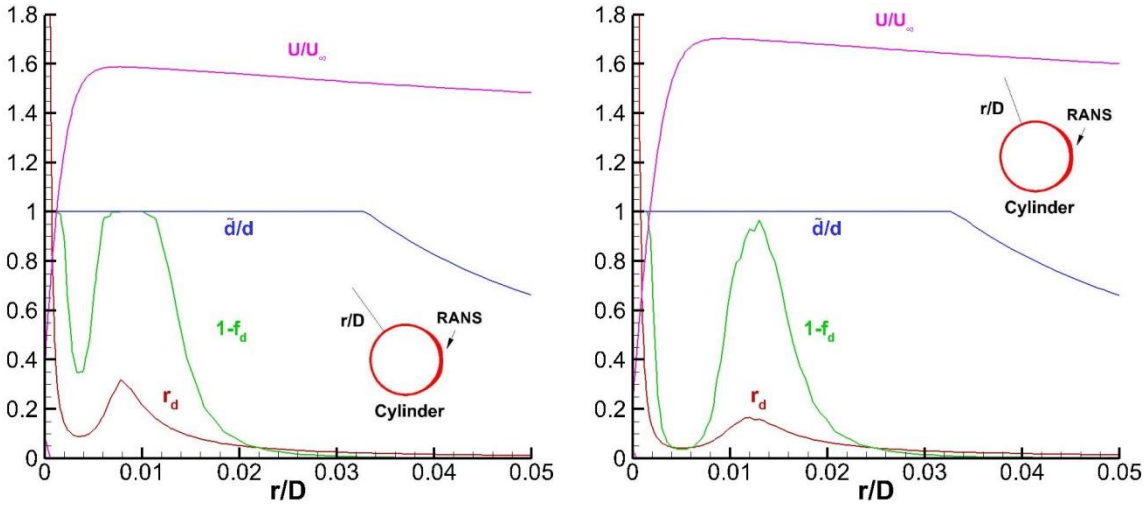

(a) $\theta = 60^0$ (b) $\theta = 75^0$

Figure 4.5: Delayed detached-eddy simulation model properties

4.4.2 Instantaneous flow field and time-dependent forces

Figure 4.6 displays the instantaneous non-dimensional streamwise velocity fields along the cylinder mid-span. It shows that with laminar inflow, the flow separates just ahead of the cylinder maximum thickness region and breaks up into a turbulent wake which is dominated by large-scale shedding vortices.

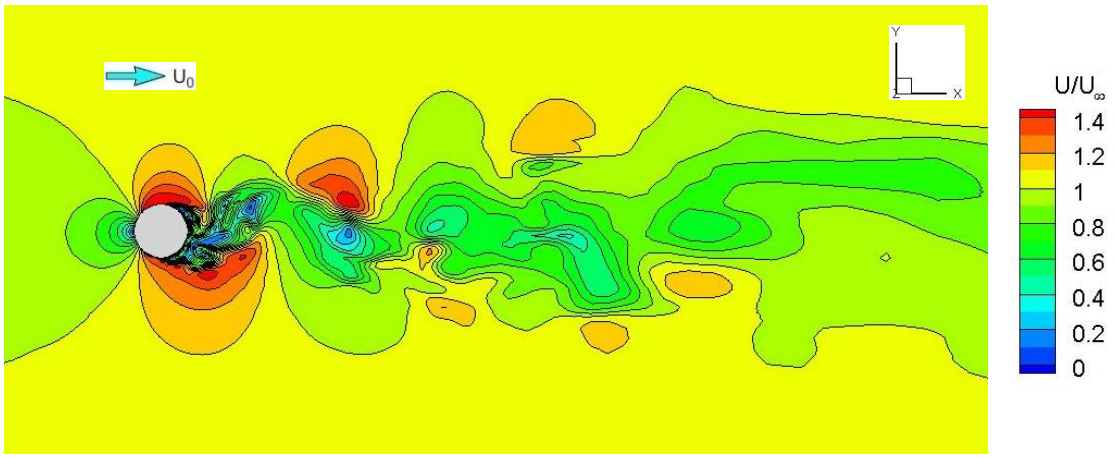

Figure 4.6: Contours of instantaneous streamwise velocity fields

Figure 4.7 depicts the instantaneous non-dimensional spanwise vorticity fields ($\omega_z = (\partial V/\partial x - \partial U/\partial y)D/U_\infty$, where D is the cylinder diameter) in the wake behind the cylinder at the mid-span. It can be seen that a vortex is formed in the region behind the separation point on the cylinder top side, and at the meantime, a corresponding vortex on the bottom side breaks away from the cylinder. The vortices are transported downstream and dissipated gradually in the wake. Afterwards, the vortex on the cylinder top side breaks away and a new vortex begins to develop on the bottom side alternately. Thus, a regular vortex street persists in the cylinder wake and the vortices within the turbulent cores are shed periodically.

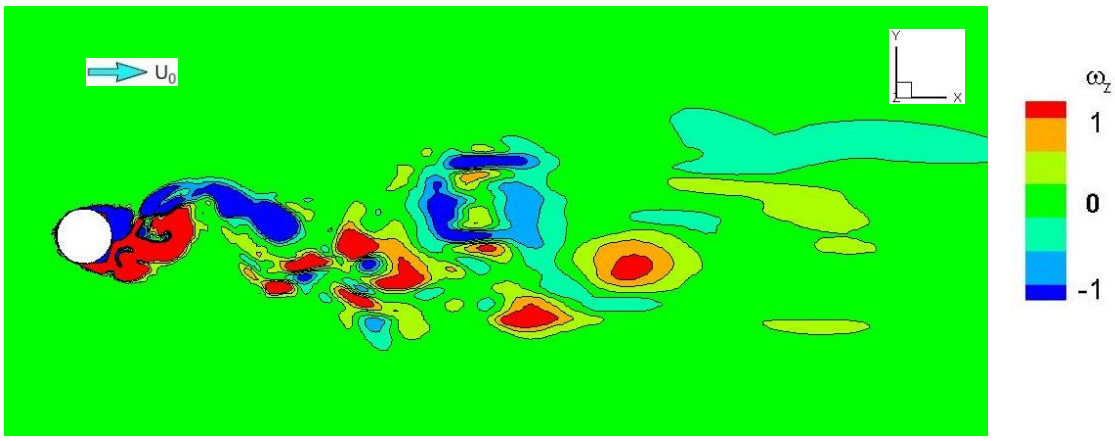

Figure 4.7: Contours of instantaneous spanwise vorticity fields

In order to understand the instantaneous three-dimensional flow field developed in the cylinder wake, the Q criterion named after the second invariant of the

velocity gradient tensor ($\nabla \boldsymbol{u}$) is applied [99,100]. For computation, the second invariant Q is given by $\left(Q = \frac{1}{2}\left(\Omega_{ij}\Omega_{ij} - S_{ij}S_{ij}\right)\right)$ in which $S_{ij} = \left(u_{i,j} + u_{j,i}\right)/2$ and $\Omega_{ij} = \left(u_{i,j} - u_{j,i}\right)/2$ defined as before are respectively the symmetric and the antisymmetric components of $\nabla \boldsymbol{u}$. Therefore, Q represents the local balance between the strain rate $S^2 = S_{ij}S_{ij}$ and the rotation rate $\Omega^2 = \Omega_{ij}\Omega_{ij}$; a rotating structure can be viewed as an iso-surface of positive constant Q. The iso-surfaces with positive Q isolate the regions where the rotation strength overcomes the strain strength, making those surfaces eligible as vortex envelopes. Herein Q is normalized as $\alpha = Q/[(U_0/D)^2]$ (where D is the cylinder diameter) where α is a non-dimensional constant set to a certain value to obtain a good view of the flow structures. Figure 4.8 visualizes the instantaneous cylinder wake structures described by the iso-surfaces of normalized Q criterion value of 0.5 (coloured by non-dimensional velocity magnitude). It is noted that a large-scale vortex shedding is predicted in the cylinder wake. The formation of the vortex sheet and the vortex strength are the dominant wake characteristics that control the aerodynamic tonal noise generation, as will be discussed subsequently.

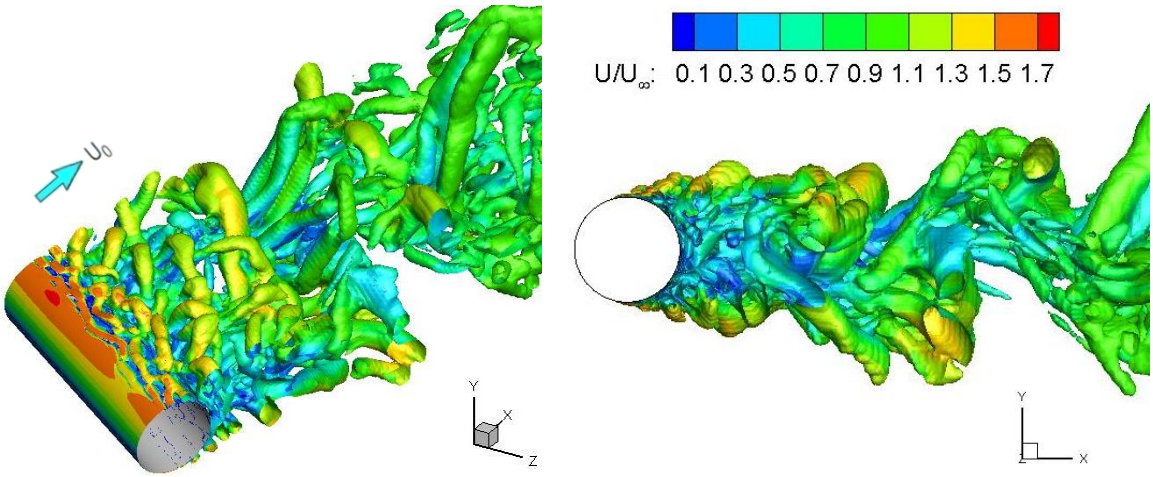

(a) Isometric view (b) Side view

Figure 4.8: Iso-surfaces of the instantaneous normalized Q criterion

As the wake vortices are formed in the flow field around cylinder, time-dependent forces are generated on the cylinder to balance the rate of change of fluid momentum corresponding to the circulation of each vortex. The time histories of

the lift and drag coefficients of the cylinder are shown in Figure 4.9. The forces are non-dimensionalized by $\left(\frac{1}{2}\rho_0 U_\infty^2 A\right)$ in which A is the projected frontal cross-sectional area of the cylinder and equates to the cylinder length multiplied by its diameter. In comparison with the drag force fluctuating randomly with a much lower variation level, the lift force shows regular modulations of higher amplitude, as a result of the occurrence of unsteady vortex break-up along the spanwise cylinder producing the regular large-scale vortex shedding. Table 4.3 summarizes the RMS and mean results from the three 50% overlapping time windows. It is shown that the variations of the RMS values between different segments are small (less than 4%) and the discrepancies in mean drag coefficient are less than 5%. The mean lift coefficient for each segment is close to zero (not shown in the table). Therefore, it indicates that temporal convergence is achieved and the transient flow field has become statistically steady.

		Segment1 (0.1-0.2s)	Segment2 (0.15-0.25s)	Segment3 (0.2-0.3s)	Total length (0.1-0.3s)
RMS value	Fluctuating lift	0.5472	0.5401	0.5603	0.5553
	Fluctuating drag	0.1028	0.1011	0.105	0.1039
Mean value	Drag coefficient	1.0255	1.0262	1.0675	1.0461

Table 4.3: Root-mean-square and mean values of lift and drag coefficients

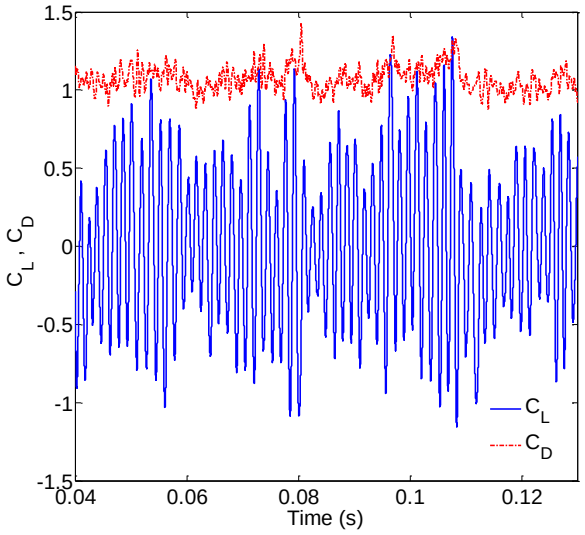

Figure 4.9: Time-history of lift and drag coefficients (part)

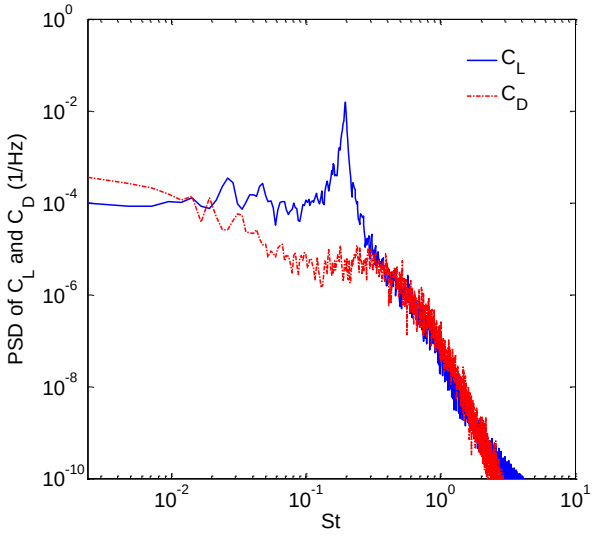

Figure 4.10: Power spectral density of lift and drag coefficients

After removing the initial transient variations, the PSDs of the fluctuating lift and drag coefficients are computed based on Welch's method using a Hanning window with a 50% overlap. To obtain the reliable statistics, a total length of 0.4 s (from the time of 0.3 s to 0.7 s) using 7 segments is employed for PSD calculation and presented in Figure 4.10. The spectrum of lift coefficient shows that a clear peak appears at the Strouhal Number ($St = fD/U_\infty$) of about 0.196 associated with the primary shedding frequency of 626 Hz. This result is in good agreement with the well-known St value between 0.19 and 0.20 for a circular cylinder with an essentially infinite aspect ratio at subcritical Reynolds numbers, as stated in Section 4.2. Moreover, compared to the lift coefficient of the cylinder, the spectrum of drag coefficient is broadband and its level is much lower in most of the frequency range.

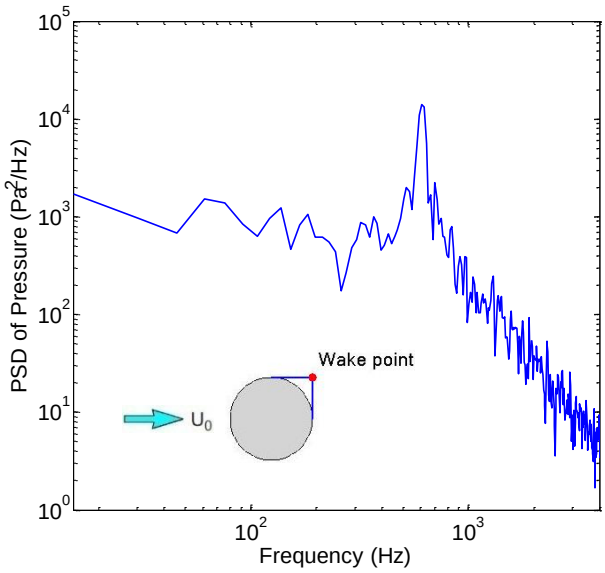

Figure 4.11: Power spectral density of pressure at the wake position of cylinder

The vortex shedding frequency can also be obtained from the gauge pressure at cylinder wake positions by calculating the frequency of the pressure disturbances which are associated with the individual vortices. As the vortices of alternating sign pass by this wake point, the direction of the velocity disturbance will alternate. Thus, if the vortices move with a velocity U_c and the vortices with the same circulation direction have a streamwise separation distance l, an undulating velocity of frequency ($f_s = U_c/l$) can be measured. The wake monitor point is set on the top side of the cylinder in the mid-span plane, with a distance of one

cylinder radius from the cylinder surface as illustrated in Figure 4.11. Based on the time-history of the gauge pressure on this wake point, the dominant vortex shedding frequency of 626 Hz can also be obtained as shown in Figure 4.11.

4.4.3 Mean flow characteristics

Figures 4.12 and 4.13 show the time-averaged streamlines and streamwise mean velocity contours in the flow field around the cylinder based on the CFD simulation and PIV experiment from the literature [101] respectively. It can be seen from Figure 4.12(a) that a pair of narrow recirculation bubbles generate a strong and wide backflow towards the cylinder, and the wake is split into two entirely independent elongated recirculation areas separated by a large backflow region along the symmetry axis. This agrees well with the result from the PIV measurements on a circular cylinder (displayed in Figure 4.13 as an example) performed in the same subcritical Reynolds number range [101,102]. The reason for the formation of the two symmetric eddies obtained in the cylinder wake is that the averaging of the passage of the alternating vortices results in a symmetric pattern for the streamwise mean velocity. Furthermore, the averaged wall shear stress (τ_w) illustrated in Figure 4.14 indicates that the separation points (at the value of $\tau_w = 0$) on the upper side of the cylinder are at the angle of $\theta_{sep} = 86.8^0$ (or on the lower side at the angle of $\theta_{sep} = -86.8^0$). The transition to turbulence in the flow field occurs immediately following the flow separation from the cylinder. The recirculation length (L_r, the size of the flow separation bubble) is defined as the distance from the flow separation point to the end point of the recirculation region (saddle point). The dimensionless recirculation length (L_r/D) of 1.29 is measured in the mean velocity iso-contours presented in Figure 4.12. It is mentioned in [101] that the dimensionless recirculation length is measured to be 1.28$\pm$0.03 for a mean flow at Re=140,000 described in Figure 4.13 and values between 1.1 and 1.4 are found by the other researchers for the same Reynolds number range. Therefore, both the shape and the length of the cylinder wake are comparatively well predicted by the simulations for the mean flow structures.

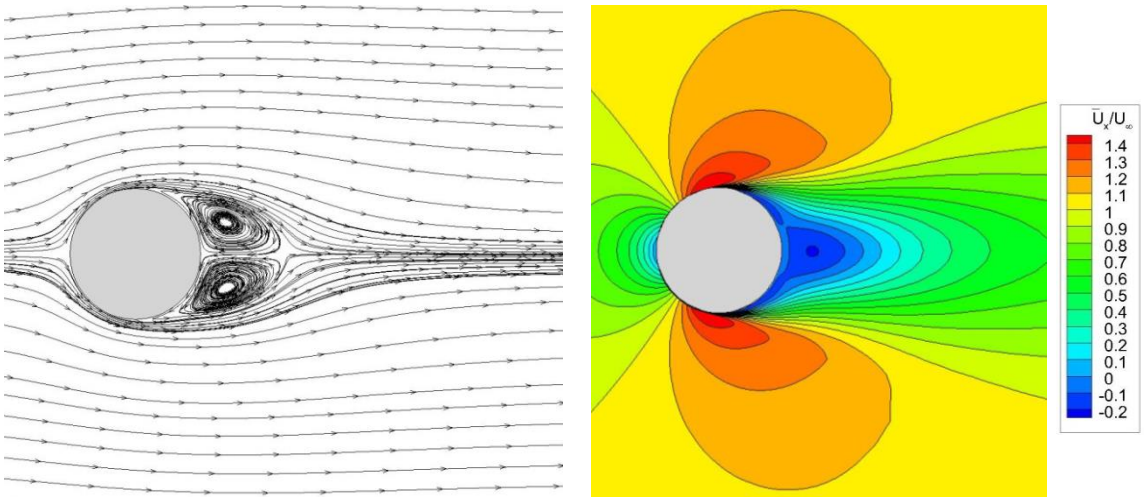

(a) Mean streamline (b) Non-dimensional mean velocity

Figure 4.12: Streamwise mean velocity field (CFD simulation)

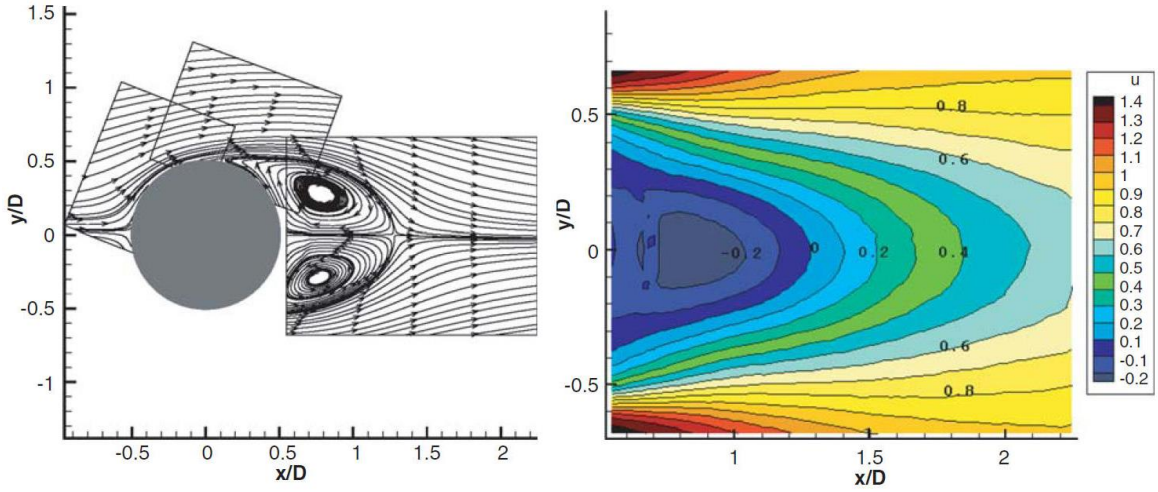

(a) Mean streamline (b) Non-dimensional mean velocity

Figure 4.13: Streamwise mean velocity field (PIV experiment) [101]

The distribution of the mean pressure coefficient $C_p = (\bar{P} - P_0)/\left(\frac{1}{2}\rho_0 U_\infty^2\right)$ on the cylinder surface around the circumferential direction is depicted in Figure 4.15, as a function of the circumferential angle θ measured clockwise from the cylinder front stagnation point. The various distributions of C_p at the different cut-surfaces located along the cylinder span with equal intervals are averaged to extract the span-averaged data. Its shape is in overall agreement with the experimental measurements within the same subcritical Reynolds number range [97,103]. The location of the minimum pressure coefficient, the cylinder aft region of pressure recovery and subsequently the extent of cylinder rear region where the pressure coefficient is practically constant are well predicted.

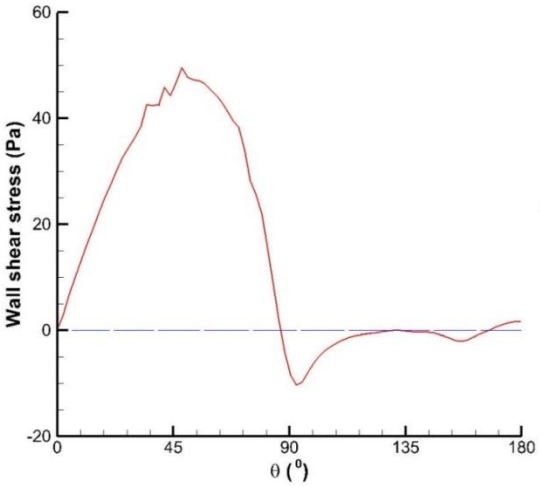

Figure 4.14: Mean wall shear stress around the cylinder

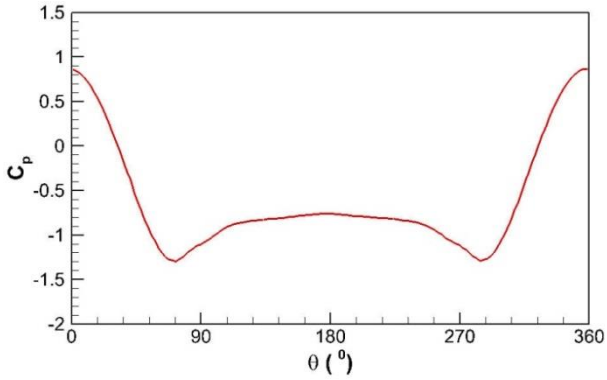

Figure 4.15: Mean pressure coefficient on the cylinder surface

4.4.4 Surface pressure spectra

To obtain some insight into the noise contribution from the near-field source, the sound pressure level of the surface pressure on the top of the cylinder is presented in Figure 4.16. A high tonal peak appears at $f = 626$ Hz which is related to the primary frequency of the vortices shed from the cylinder top surface. The overall sound pressure level of the surface pressure signals attains 153 dB considering the frequency range below 5 kHz. Due to grid resolutions, some numerical artefacts appear above 5 kHz and are neglected as they are not within the main energy-containing frequency range. It should be noted that in such an analysis, the surface regions of high pressure fluctuations are identified, not the acoustic perturbations only, since the near-field pressure fluctuations are very large and contain a substantial amount of hydrodynamic oscillations. In essence, not all pressure fluctuations around the cylinder translate into radiated noise. The fluctuations in the far-field are only associated with the acoustic waves since only the acoustic disturbances can propagate far away from the source region. Although the hydrodynamic fluctuations dominate and have comparatively larger magnitudes than those typical acoustic signals, all pressure perturbations including both hydrodynamic and acoustic disturbances in the near-field should be recovered by applying the FW-H method. Therefore, the accurate simulation results for the near-field surface pressure are critical for the far-field noise prediction.

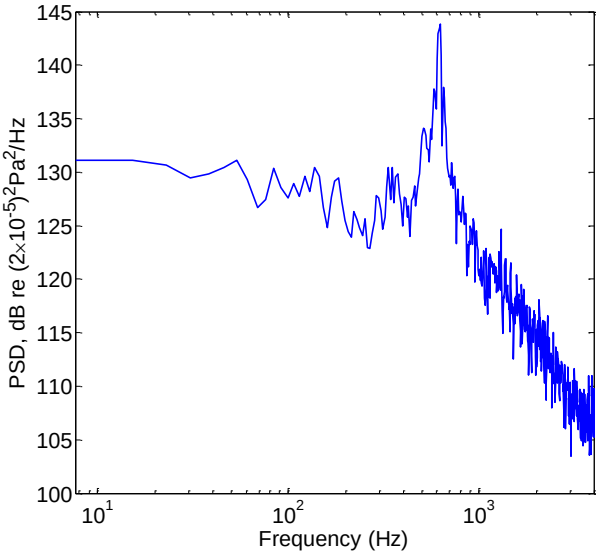

Figure 4.16: Spectrum of pressure on the cylinder top surface

4.4.5 Divergence of Lamb vector

In the numerical implementations described above, the noise contribution from the quadrupole source term can be neglected for flows with low Mach number. In order to display the spatial distributions of the aeroacoustic volume sources and to see the wake behavior influence the wall surface pressure fluctuations (Lighthill's quadrupole source term for incompressible flows), the divergence of the Lamb vector (i.e. $\nabla \cdot (\boldsymbol{\omega} \times \boldsymbol{v})$ in which $\boldsymbol{\omega}$ is the vorticity vector and $\boldsymbol{v}$ the fluid velocity vector) based on the theory of vortex sound [43,44] is presented in Figure 4.17. This shows that the cylinder wake containing both periodic and broadband vortical fluctuations corresponds to the main volume source contributions, especially the vortex shedding in the near wake region close to the cylinder body which plays the dominant role of volume noise generation. It also indicates that the turbulent wake activities have an influence on the cylinder wall surface pressure fluctuations.

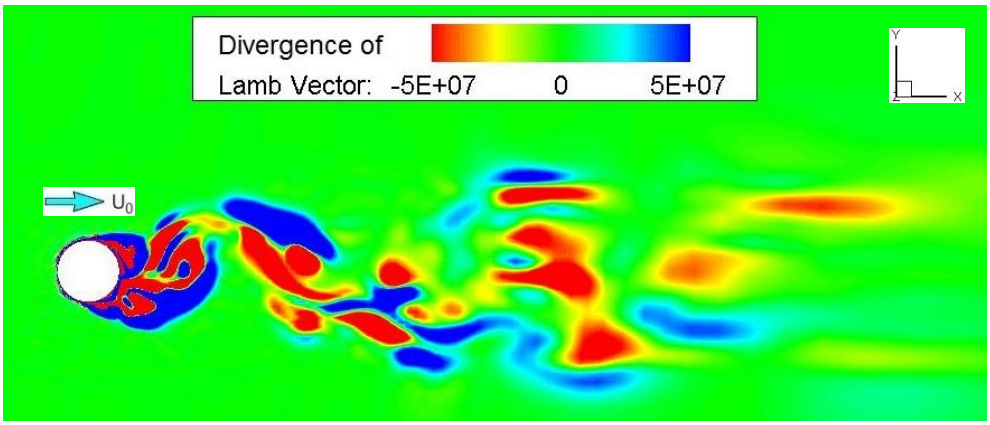

Figure 4.17: Visualization of the divergence of the Lamb vector

4.5 Aeroacoustic Results

It can be judged whether the transient flow field has become statistically steady by monitoring the lift and drag forces. As discussed in Section 4.4.2, in the 'Baseline' model, the transient flow field becomes statistically steady after the simulation has been run for 0.3 s and the near-field flow data can be collected to predict the far-field noise using the FW-H method.

4.5.1 Acoustic spectra computation and verification

For the 'Baseline' mesh case, the length of the time signal used as input for the noise calculation is related to the last 0.4 s of the simulation, as discussed in Section 4.4.2. The physical timestep size (Δt) for simulation is 4×10^{-6} s, leading to a maximum frequency of 125 kHz which is much higher than the audible range of interest. The same sampling rate of the maximum frequency is applied for the noise calculation. The 8,732 panels (surface elements) around the cylinder accounting for the acoustic sources are utilized as the solid data surface for the FW-H method. The PSD is computed based on Welch's method with a Hanning window. There are 5 segments with segment length of 0.13 s, giving a frequency resolution of 7.7 Hz bandwidth.

In the 'Fine' mesh model, the physical timestep for simulation is 1×10^{-6} s and 17,464 panels on the cylinder surface correspond to the acoustic sources in the

FW-H method. There are 3 segments with segment length of 0.065 s used in Welch's method, giving a frequency resolution of 15.3 Hz bandwidth.

Figure 4.18 depicts the spectral comparisons of the radiated noise at the observer between the noise predictions from the 'Baseline' mesh case and the experiment measurement [93] as well as the 'Fine' mesh case. It shows that the frequency of the tonal peaks generated by the periodic vortex shedding is accurately predicted. The receiver point (0, 1.4m, 0) in the simulations coincides with the microphone position from the experiment. A limited range of frequencies from 100 Hz to 1 kHz is available in the experiment. It is found from Figure 4.18 (a) that good agreement is obtained between the far-field noise predictions and the experimental measurements, for both the shape of the spectra and the overall levels. Compared with the experimental values, the tonal peak level from the numerical simulation is about 1.5 dB higher. This trend is possibly connected to the periodic boundary conditions (corresponding to increased coherent shedding and enhanced spanwise uniformity) applied in the numerical calculation and the finite length as well as the free end used in the experiments result in the slight difference of radiated noise between them. Additionally, Figure 4.18 (b) shows that as the grid resolution increased and the timestep decreased, the noise spectrum becomes a little higher in most of the frequency range above 200 Hz and the dominant shedding frequency shifts slightly lower. This is because compared to the lower resolution case, more vortex amalgamations and interactions are developed within the wake region close to the cylinder surface in the 'Fine' mesh case. However, on the whole, the noise predictions based on the 'Baseline' and 'Fine' grids match very well despite the fact that in the 'Fine' mesh model, the time signal used for noise calculation starts at $t = 0.14$ s when the initial transient variation might not be removed fully and the frequency resolution utilized is twice that applied in the 'Baseline' mesh case.

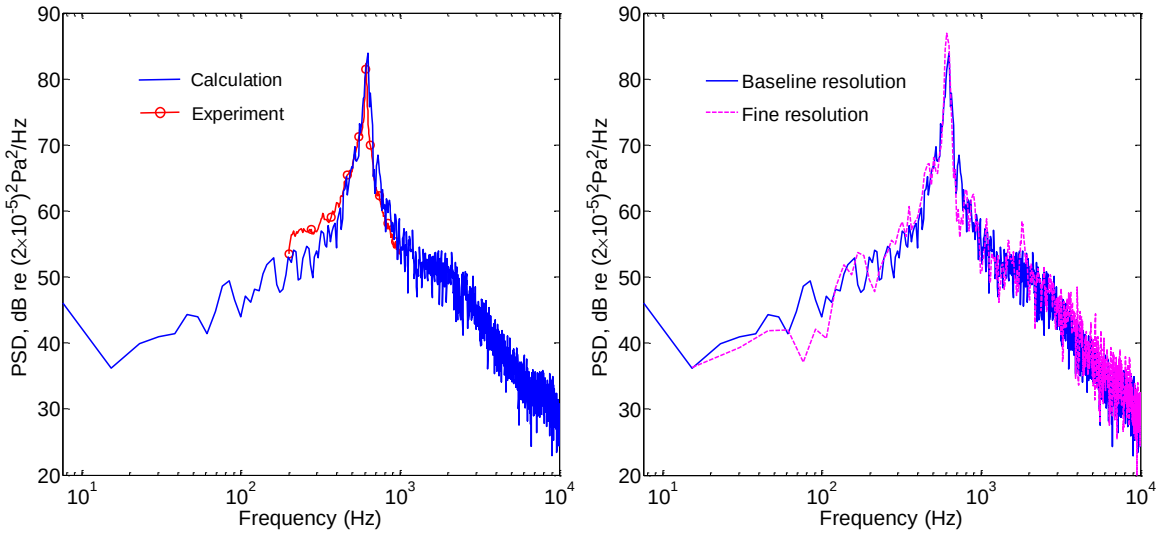

(a) Simulation and experiment [93] (b) 'Baseline' and 'Fine' grids

Figure 4.18: Spectra comparisons of the radiated noises

4.5.2 Acoustic directivity

The OASPL is calculated for the frequency range (from 100 Hz to 1 kHz) as a function of the angle α which is 0^0 in the downstream direction and positive in the counter-clockwise direction. Using the receivers located along a circular frame vertical to the cylinder through its mid-point, the noise directivity in the mid-span section at a constant distance 1.4 m from cylinder centreline is presented in Figure 4.19 which shows the typical dipole pattern of directivity for the sound radiation from a circular cylinder using 'Baseline' mesh. It is due to the fact that aerodynamic noise generated from the vortex shedding is a dipole source. Note that the OASPL values are not equal to zero on the dipole axis with respect to $\alpha = 0^0 - 180^0$ because the sound generation in this direction comes from those represented by the oscillating drag forces exerted on the fluid around the cylinder.

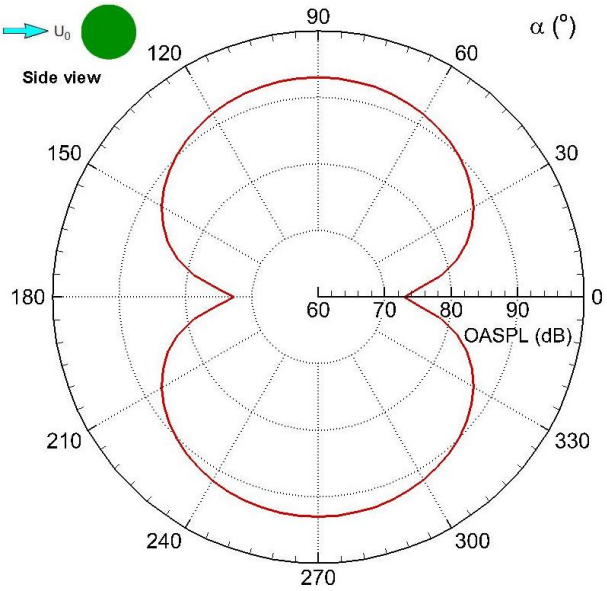

Figure 4.19: Noise directivity for the cylinder (calculation)

4.6 Summary

The aerodynamic and aeroacoustic behaviour of the flow past a circular cylinder has been investigated using the DDES model and the FW-H acoustic analogy method. The mesh resolution study has shown that a certain degree of grid convergence is achieved and the 'Baseline' grids may be applied for the CFD simulation. It is found that a large-scale vortex shedding is formed behind the cylinder, leading to the dominant behaviour of a fully periodic wake. The far-field aerodynamic noise generated by the flow around the cylinder is primarily associated with the vortex shedding, which can be seen clearly from the dominant frequencies in the SPL spectrum of the radiated noise. The typical dipole pattern of OASPL directivity is predicted due to the dipole characteristics of the noise source generation from the vortex shedding around the cylinder. Additionally, the numerical simulations based on the 'Baseline' grids compare fairly well with the experimental data for the typical flow characteristics and the radiated noise in general. Moreover, there is a good agreement between the noise predictions based on the 'Baseline' and 'Fine' mesh cases. Therefore, the 'Baseline' grids are fine enough and may be utilized for noise predictions.

Chapter 5

Isolated Wheelset

The aerodynamic and aeroacoustic behaviour of an isolated wheelset is investigated numerically and experimentally in this chapter. The flow behaviour of the isolated axle and wheel and the noise radiation from the isolated wheel are calculated for comparison. Experiments consist of flow velocity measurements in a wind tunnel and aeroacoustic measurements in an open-jet anechoic wind tunnel. The isolated wheelset is the assembly of two wheels attached to a central axle. Since the camera used in the PIV system is fixed on the base with a certain height to capture the images, the test objects cannot be too small if they are put close to the ground. On the other hand, considering the blockage allowed in the open-jet anechoic wind tunnel, the configuration geometry of the measured objects is limited corresponding to the nozzle dimensions. Taking into account the dimensions of the anechoic wind tunnel (for aerodynamic noise tests) and 7'×5' wind tunnel (for PIV tests) at the University of Southampton, a 1:10 scale wheelset is for the aeroacoutic experiments while a 1:5 scale wheelset is used for the PIV tests. Numerical simulations are performed based on these two scaled wheelsets placed inside the corresponding wind tunnels and the results are compared with the experimental measurements. Moreover, the flow structure and noise directivity from an idealized wheel and detailed wheel are discussed to see the influence from the simplification of the generic wheel.

5.1 Wheelset Geometry

Generally, axle-mounted disc brake systems are used on high-speed trains. However, since there is no sufficient space to accommodate these axle-mounted braking discs, wheel-mounted braking systems are often implemented on the

power bogies [104,105]. Figures 5.1(a) and 5.1(b) show that the braking discs are attached to the wheel on two sides with bolts. To keep the heat convection for cooling the discs which are heated during braking, a gap is left between the wheel tyre rim and disc edge. As an initial step for numerical simulation, a wheelset with a simplified geometry illustrated in Figure 5.1(c) is considered in which the details like the flange on the inner edge of the running surface, the bolts and the gap between the wheel and braking discs are removed. Fully structured meshes with hexahedral cells are created to improve accuracy in simulation.

(a) Wheel-mounted disc (b) Disc-mounted wheelset (c) Wheelset model

Figure 5.1: Simplifying of wheelset model

5.2 Numerical Setup

The configuration of the 1:10 scale isolated wheelset is displayed in Figure 5.2. The coordinate system (shown in Figure 5.2a) adopted is that *x* is the flow direction, *y* the vertical direction and *z* the spanwise direction. In this 1:10 scale model, the axle has a diameter (d) of 17.5 mm and the wheels have a diameter (D) of 92 mm. The axle is a typical cylinder and the wheel may be called a 'coin-like' or 'disc-shaped' cylinder on account of its small aspect ratio (L/D, where L is the spanwise length of the wheel and D is the wheel diameter) [106].

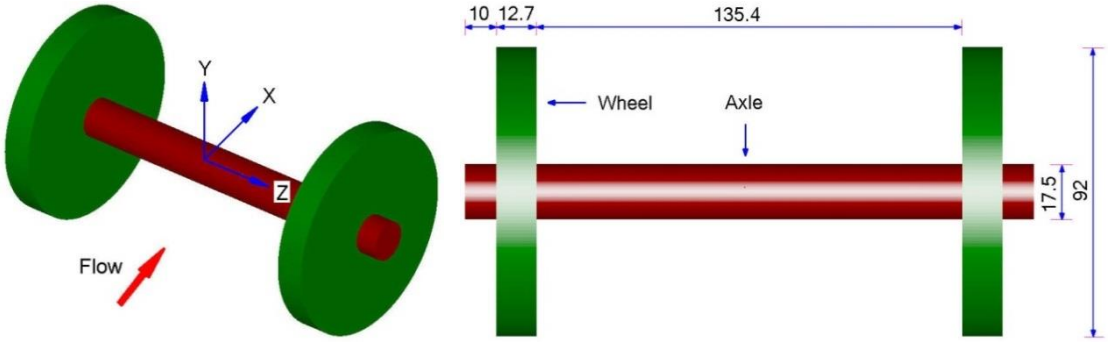

(a) Isometric view (b) Front view

Figure 5.2: Isolated wheelset model (1:10 scale, dimensions in millimetre)

The wheelset geometry is symmetrical along the axle mid-span where the flow influence from the wheel is small. Therefore, it is reasonable to make use of symmetry to limit the computational domain to half the axle and a single wheel. Figure 5.3 illustrates the computational domain which has dimensions of $15D \times 10D \times 6D$ (length, height and width, where D is the wheel diameter). Thus, the blockage ratio (defined as the ratio of the projected wheelset area to the domain cross-sectional area) is 0.5%, which is well within the prescribed range for cylinder flow (less than 3%) [106]; and the outlet boundary is far enough downstream to have negligible influence on the near-wake flow around the wheelset. The following boundary conditions are applied: the upstream inlet flow is represented as a steady uniform flow (U_∞) with a low turbulence intensity corresponding to the experimental measurements from an anechoic open-jet wind tunnel (the potential core of the free jet has a typical turbulence intensity of about 0.1% [107]). Thus, in the S-A turbulence model used here, the production term of the transport equation is activated and the eddy viscosity comes into equilibrium with the velocity field rapidly as soon as the fluid enters the boundary layer. Additionally, the top, bottom, symmetrical plane along the axle mid-span and side boundaries are specified as symmetry boundaries which are equivalent to zero-shear slip walls and assume no flux of any quantity across them; a pressure outlet with zero gauge pressure is imposed at the downstream exit boundary and all wheelset surfaces are defined as either stationary or moving (for rotating case) no-slip walls. The wheel rotation effect is implemented by imposing the corresponding rotation velocity on the solid surface. Numerical calculations are performed mostly at freestream velocity of 30 m/s with some

additional results presented for 70 m/s. The resulting Reynolds numbers (based on the axle diameter and the freestream properties) are 36,000 and 83,900, which are within the subcritical Reynolds number regime. As is well known, and as shown in Chapter 4 for a uniform stream passing over the axle of cylindrical shape, the boundary layer separation is laminar and vortex shedding occurs in the wake area with a Strouhal number (St) of about 0.2 in the subcritical flow regime below Reynolds numbers of 1×10^5.

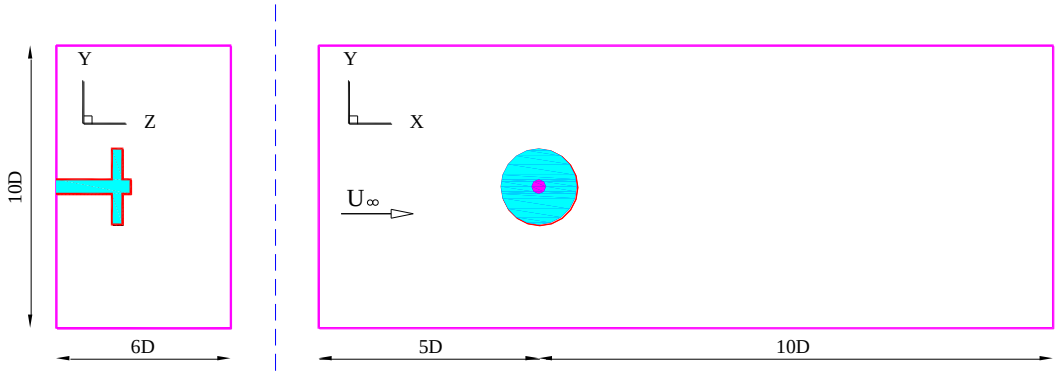

(a) Front view (b) Side view

Figure 5.3: Sketch of the computational domain with the isolated wheelset (not to scale)

Based on the results of the grid convergence study on the isolated circular cylinder case presented in Chapter 4, a fully block-structured mesh (displayed in Figure 5.4) is generated around the wheelset. The cell sizes on the wheel and axle surfaces are implemented corresponding to the cylinder 'Baseline' case around the circumference and in the spanwise direction. The mesh in the corner area between the wheel and axle is refined with double grid points in the wheel radial direction and the axial direction of the axle. Therefore, the cell size of the axle area is implemented as 0.42 mm around the perimeter and 0.88 mm in the spanwise direction (corresponding to a grid spacing of $\Delta z = 0.05d$, where d is the axle diameter); and the maximum cell size on the wheel surface is 0.98 mm. The average value of $\Delta x^+ (= \Delta x \cdot u_\tau/\nu)$ and Δz^+ $(= \Delta z \cdot u_\tau/\nu)$ of the meshes around the wheelset is about 42 and 40. For the case with inlet velocity of 30 m/s, the distance from the wheelset to the nearest grid point is set as 10^{-5} m and stretched with a growth ratio of 1.1 in the wall-normal direction inside the boundary layer. This yields a maximum value of y^+ less than 1. For RANS simulations or DES, the y^+ in the first near-wall cell should be very small (on the

order of $y^+ = 1$) to ensure the turbulence models employed inside the viscous sublayer account for the low-Reynolds number effects. The total number of grid points in the entire domain is 5.5 million. The physical timestep size is 5×10^{-6} s followed by 10^{-5} s which gives an adequate temporal resolution for the simulation with respect to the CFL number of less than 2 within the computational domain considering the implicit time marching scheme used here.

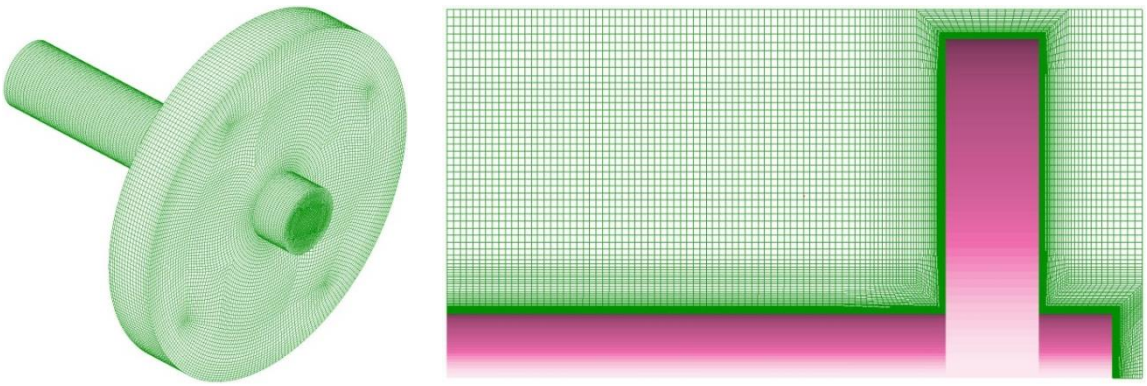

(a) Surface mesh (b) Mesh topology

Figure 5.4: Structured mesh generated around the wheelset

5.3 Aerodynamic Results from Simulation

Based on the aerodynamic simulation, the unsteady surface pressure on the solid surface is used as input for the far-field noise prediction. Compared to the isolated cylinder case as discussed in Chapter 4, much emphasis will be put on the flow interactions developed around the wheel and the axle for the isolated wheelset case. In order to understand the flow behaviour around the isolated wheelset, the calculation results of the velocity as well as vorticity fields, the iso-surfaces of Q criterion and the divergence of Lamb vector field are presented. The fluctuating lift and drag coefficients from the isolated wheelset and the gauge pressure at wake positions are displayed and compared.

5.3.1 Properties of the DDES model

Similar to the cylinder case for checking the RANS/LES switching of the DDES scheme, Figure 5.5 shows the radial profiles of the mean velocity, the model length scale ratio (r_d), DDES function $(1 - f_d)$ and the ratio of the modified length

scale to wall distance ($\tilde{d}/d$) at $\theta = 60^0$ (measured clockwise from the front stagnation point) in the mid-span locations of wheel and axle. For the half wheelset configuration used for numerical simulation here, the wheel mid-span represents the cut surface from the mid-point along the axial direction, whereas the axle mid-span is defined as midway between the wheel and the axle centreline. In terms of r/D, the boundary layer (i.e. based on U/U_∞) extends to 0.003 and RANS/LES switching occurs (the location where $\tilde{d}/d$ becomes less than 1) around 0.008 at the wheel mid-plane. At the axle mid-plane the boundary layer extends to 0.007 and RANS/LES switching occurs at 0.033. It is shown that the RANS-LES interface remains well outside the boundary layer and the DDES delay function f_d reaches 1 within the LES region. Therefore, it is confirmed that the RANS method is imposed over the entire boundary layer and the LES treatment is applied elsewhere when using the DDES model in the simulation.

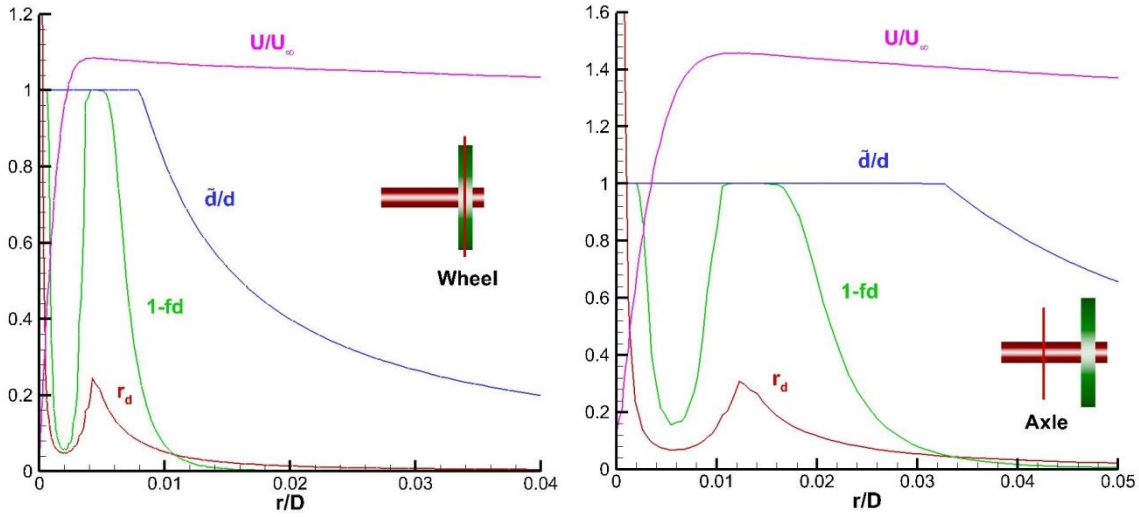

(a) Wheel mid-span (b) Axle mid-span

Figure 5.5: Delayed detached-eddy simulation model properties ($\theta = 60^0$)

5.3.2 Instantaneous flow field and time-dependent forces

Figure 5.6 displays the instantaneous non-dimensional velocity field of the wheelset at the horizontal *x-z* mid-plane. The massive separations from the front sharp edges at the wheel side surfaces are displayed and flow separation near the axle free end can be seen clearly. In the wake around the wheelset, eddies of different sizes develop rapidly following the boundary layer detachment,

leading to a complicated flow structure as a consequence of the interaction from the various vortices.

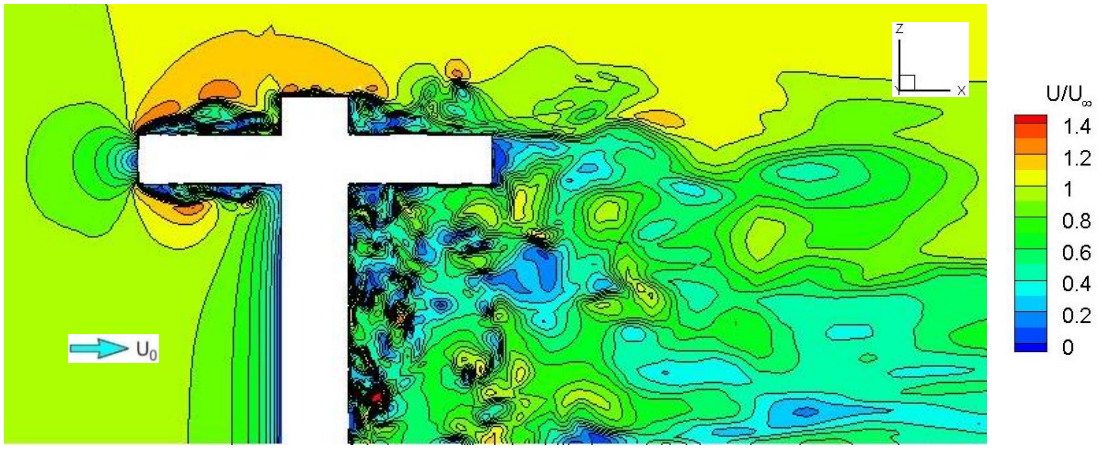

Figure 5.6: Contours of instantaneous velocity magnitude in horizontal plane through centre of wheelset (bottom view)

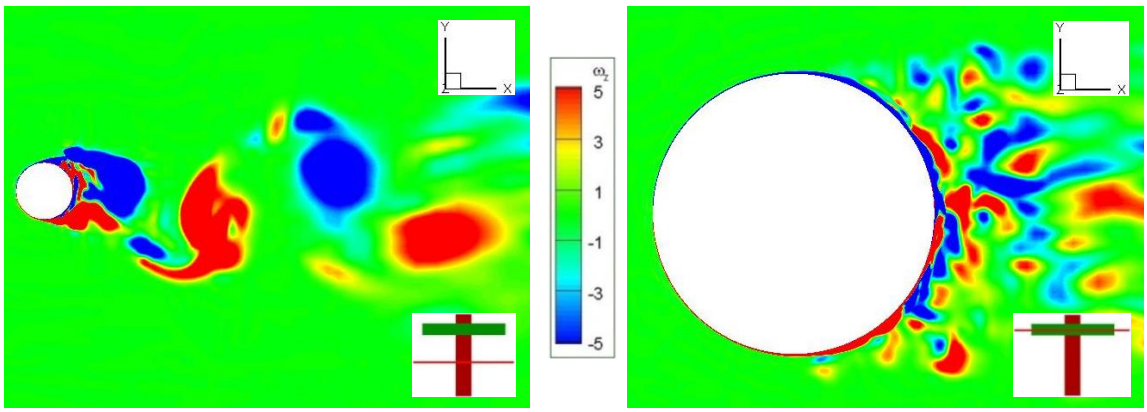

(a) Axle mid-span (b) Wheel mid-span

Figure 5.7: Contours of instantaneous spanwise vorticity fields in vertical planes through centre of wheel and axle (side views)

The instantaneous non-dimensional spanwise vorticity fields ($\omega_z = (\partial V/\partial x - \partial U/\partial y)D/U_\infty$, where D is the wheel diameter) in the wake area behind the axle and wheel are displayed in Figure 5.7. This reveals that the flow behaviour around the axle is different from that around the wheel: the organized vortex structures in the axle wake are clearly formed and dominated by a large alternating shedding while the wheel wake is highly turbulent with eddies of various scales. This is understandable as the axle is two-dimensional and provides the appropriate spanwise correlation length to generate vortex shedding whereas the wheel is three-dimensional with small aspect ratio, as mentioned in Section 5.2. The flow

separation from the side surface influences the vortices shed behind the wheel, causing the flow structure behind the wheel to be fully three-dimensional and less organized, with different scales.

Figure 5.8 shows the instantaneous non-dimensional spanwise vorticity fields (ω_z) in the axle wake at different distances to the wheel inner surface. It can be seen from Figure 5.8(a) that in the axle wake at 5mm away from the wheel inner surface, the vortices shed from the axle interact with the vortices generated from the wheel circumferential edge; they deform largely and are merged into the eddies formed behind the wheelset, leading to the synchronized behaviour of the wheelset wake. Close to the wheel (shown in Figure 5.8b), the interaction of the vortices generated from the axle and wheel becomes weaker and the wake is dominated by flow separations occurring on the wheel top and bottom rim edges.

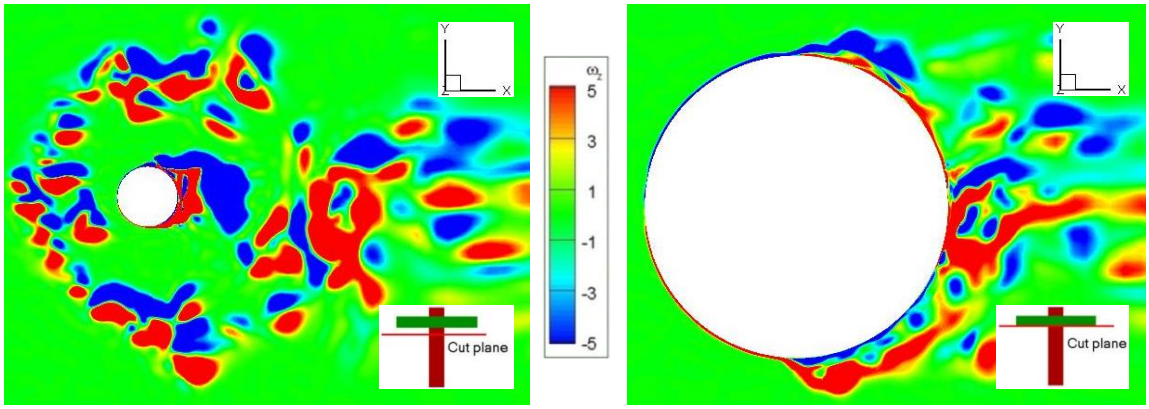

(a) 5mm from wheel (b) Close to wheel

Figure 5.8: Contours of instantaneous spanwise vorticity fields in vertical planes through corner of wheel and axle (side views)

Figure 5.9 depicts the time-averaged streamlines on an *x*-*z* horizontal plane cut at $y = 0.25D$ through the wheel (Figure 5.9a) and close to the wheel outer side surface with a distance of 0.1 mm (Figure 5.9b). It can be noted that around the wheel, the flow is dominated by a primary separation from the front rim edges along the circumference on both sides. The flow disturbance may grow more rapidly and, consequently, the separated boundary layer undergoes transition to turbulence with rapid thickening which causes the lower edge of this separated turbulent shear layer to come back to reattach as a turbulent boundary layer onto the wheel side surfaces. Thereby, a primary separation bubble is formed within the separated

shear layer between the flow separation point and reattachment point in the upstream region of the wheel side surfaces. Underneath the primary separation bubble, a stagnant fluid pocket with a small separation bubble generated inside forms between the primary and secondary separation points and behind this, a circulatory motion develops, as illustrated in Figure 5.9(a). Compared to the flow developed on the inner wheel side surface, the flow separation is stronger on the wheel outer side surface as a consequence of the reduced flow interaction with the shorter axle there. Thus, a relatively larger separation bubble is generated on the wheel outer surface. Figure 5.9b shows that the arc-shaped secondary separation line and the crescent-shaped secondary reattachment line appear on the cut surface very close to the wheel outer side wall and their positions are located around the estimated positions of $x/D = 0.15$ and 0.05 respectively at the wheel equatorial axis.

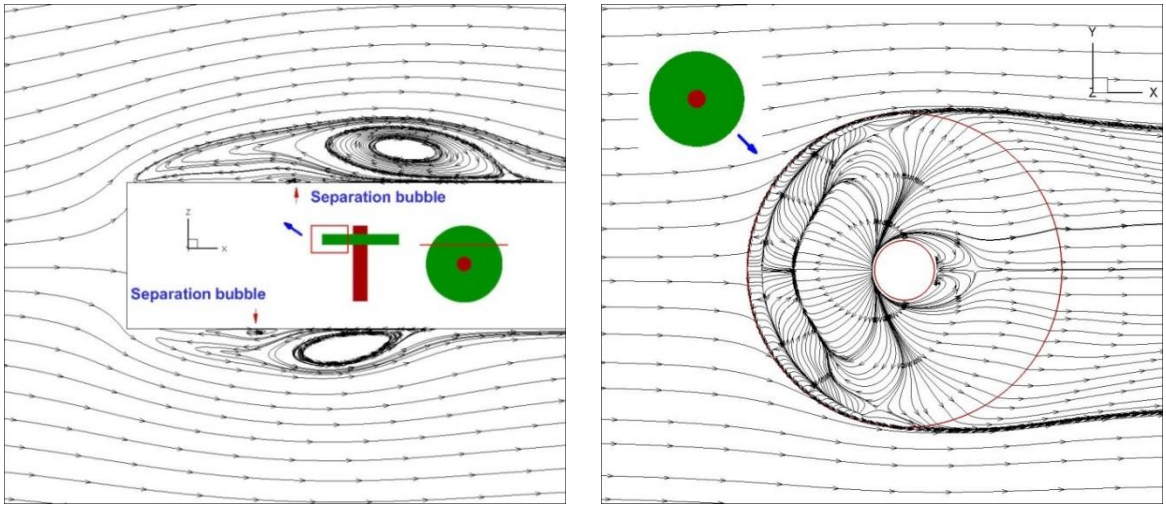

(a) On the wheel horizontal cut-surface (b) Near the wheel outer side surface

Figure 5.9: Mean streamlines around the wheel of the wheelset

Figure 5.10 visualizes the wheelset's wake structures represented by the iso-surfaces of the normalized Q criterion at the value of 50 (based on $Q/[(U_0/D)^2]$, where D is the wheel diameter). They are coloured by the velocity magnitude. The flow past the isolated wheelset shows a complicated wake structure which is characterized by considerable coherent alternating vortex shedding with different sizes and orientations, originating from the top, bottom, end and corner regions of the wheel and axle. It can be seen that flow separates at the wheel front edges, and reattaches within a very short distance on the wheel flat side surface, forming

a crescent-shaped separation bubble; the subsequent horseshoe-shaped eddies are generated and carried downstream. In the axle wake, two-dimensional spanwise vortices are formed first straight behind the axle, followed by streamwise 'rib' vortices developed further downstream, suggesting a three-dimensional character of the flow in the wheelset wake area. Additionally, due to the adverse pressure gradient, flow separations are formed on the wheel tread, coinciding with the detachment of the horseshoe-shaped eddies in the wake area. Likewise, the similar flow behaviour occurs at the free end of the axle: the scaled horseshoe-shaped eddies are visualized in Figure 5.10(a).

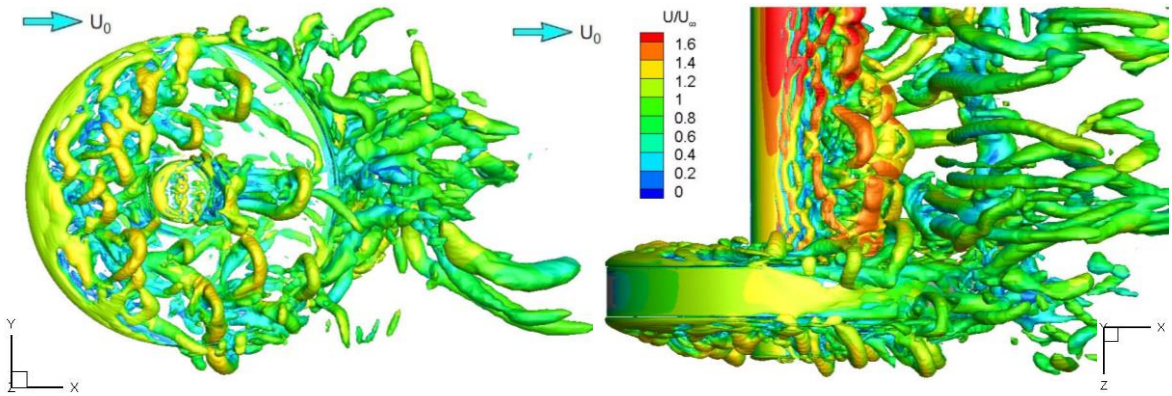

(a) Side view (b) Top view

Figure 5.10: Iso-surfaces of the instantaneous normalized Q criterion

Figure 5.11 shows the power spectral density of the gauge pressure at different positions in the wheelset wake: behind the axle, wheel and at the inside wheel-axle corner. A tonal peak at 311 Hz is clearly seen in Figure 5.11(a) showing the PSD at a point with a distance of one axle radius from the top side of the axle at mid-span. This frequency is associated with the vortex shedding from the axle, and the corresponding Strouhal number (non-dimensionalized by the freestream velocity and the axle diameter) is 0.182. Figure 5.11(b) illustrates that the PSD of the pressure at a point with a distance of one wheel radius away from the top of the wheel at mid-span is broadband and its amplitude is much lower than that in the axle wake. This indicates that flow behind the wheel is fully three-dimensional and the wake contains turbulent structures with various scales. Figure 5.11(c) shows the results for points located at 3 mm and 13 mm away from the wheel inner rim in line with the top of the axle. Two peaks appear at the frequencies of 311 Hz and 622 Hz, and these correspond respectively to the axle vortex

shedding and the interaction between the vortex shedding from the axle and the unsteady flow around the wheel in the drag direction. It is noted that closer to the wheel, the tonal peak amplitude of the pressure signal becomes lower; particularly, the second peak at 622 Hz drops by more than the first one at 311 Hz. This is because the vortex shedding from the axle is less strong there and much weaker impact is generated by the axle shedding vortices on the unsteady flow around wheel, resulting in the less drag fluctuation produced in the wheel-axle corner region.

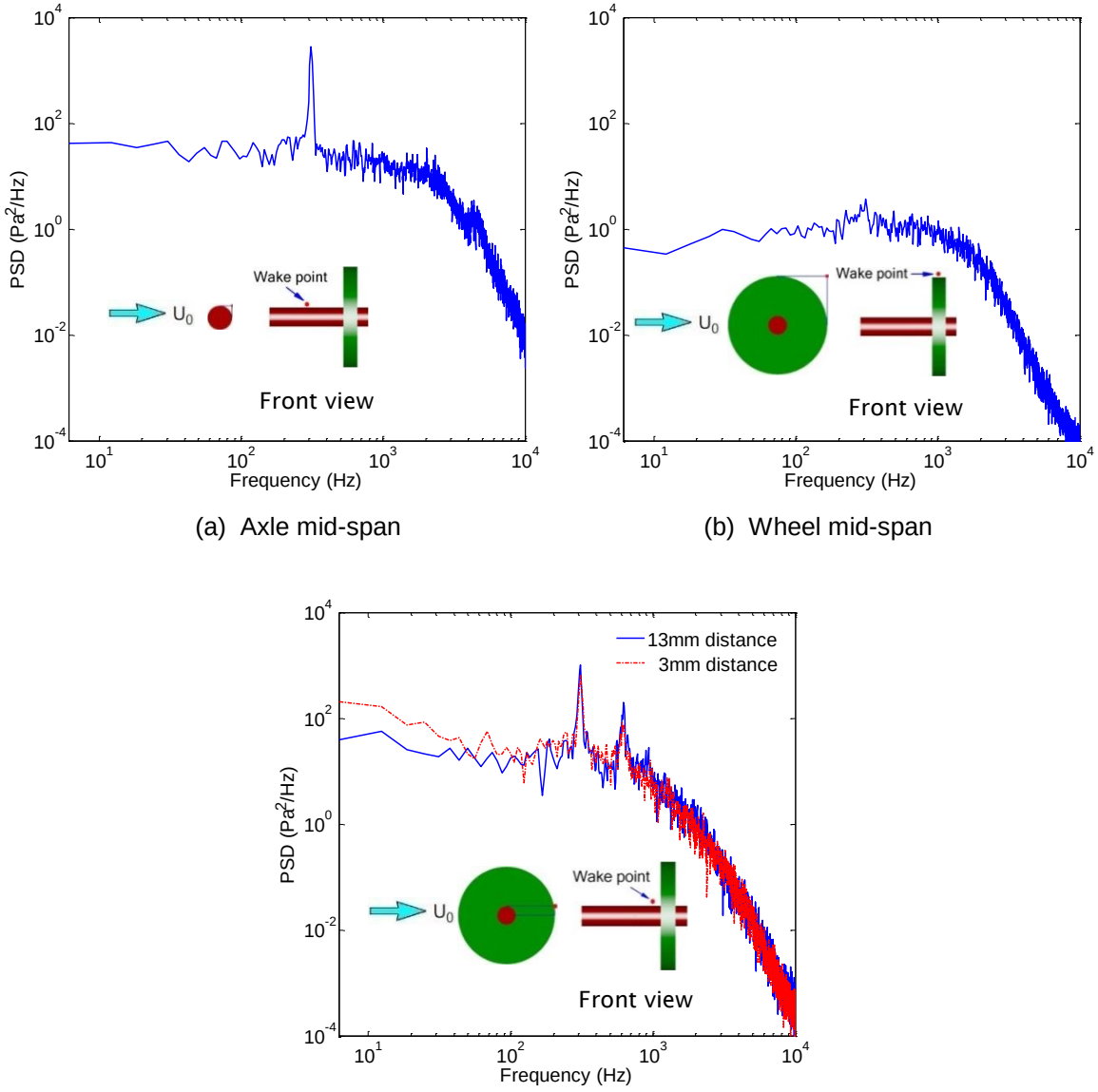

(a) Axle mid-span

(b) Wheel mid-span

(c) Inner wheel-axle corner

Figure 5.11: Power spectral density of pressure at wheelset wake positions

5.3.3 Lift and drag coefficients

Time histories of the lift and drag coefficients are represented in Figure 5.12. The lift and drag forces show periodic modulations as a consequence of the regular large-scale vortex shedding produced along the wheelset after the flow initial transient stage. Table 5.1 summarizes the results for the RMS fluctuating lift and drag coefficients and the mean drag coefficient calculated from three overlapping time windows. It is shown that the variations in the RMS values between different segments are less than 4% and the discrepancies in mean drag are less than 0.5% and in side force coefficient less than 5%. The mean lift coefficient is very close to zero (less than 0.004, not shown in the table) for each segment. Therefore, it is suggested that the transient flow field has reached a statistically steady state and the source data can be collected for far-field noise prediction.

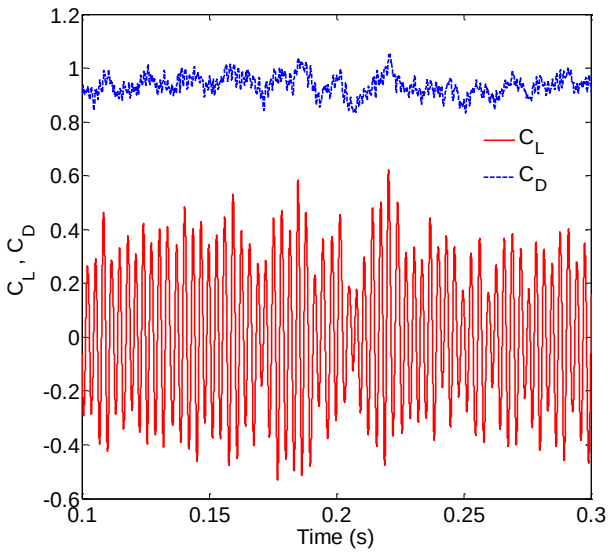

Figure 5.12: Time-history of lift and drag coefficients (part)

		Segment1 (0.05-0.2s)	Segment2 (0.125-0.275s)	Segment3 (0.2-0.35s)	Total length (0.05-0.35s)
RMS value	Fluctuating lift	0.261	0.266	0.263	0.262
	Fluctuating drag	0.0376	0.0391	0.0381	0.0379
	Fluctuating side force	0.0411	0.0415	0.0415	0.0413
Mean value	Drag coefficient	0.935	0.936	0.933	0.934
	Side force coefficient	0.0573	0.0567	0.0548	0.0551

Table 5.1: Root-mean-square and mean values of aerodynamic force coefficients (isolated wheelset)

The PSDs of the lift and drag coefficients of the wheelset are presented in Figure 5.13. In addition, in order to provide insight, results are shown for the separate components for the wheel and axle when they form part of the wheelset. A clear peak appears in all lift coefficient PSDs at 311 Hz, corresponding to a Strouhal number (non-dimensionalized by the freestream velocity and the axle diameter) of 0.182. This peak is associated with the axle primary shedding frequency. By comparison, another lower peak is observed in the drag coefficient curves at twice the shedding frequency. As is well known, the aerodynamic lift force acting in the transverse direction normal to the flow fluctuates with a larger amplitude at half the frequency of the drag force which acts in the streamwise direction parallel to the flow [92]. It can be seen that the flow around the wheelset and that around its components have the same shedding frequencies. This is because the periodic, alternating vortex shedding produced from the axle dominates the wake unsteadiness and interacts with the wall boundary layer and unsteady flow separated from the wheel (consistent with Figures 5.8 and 5.11c), thereby the resulting wake induces the regular fluctuating forces on the whole wheelset. Compared to the axle where the massive vortex shedding occurs, the wheel has the same dominant frequencies in the lift and drag forces, but with much lower amplitude. Figure 5.14 shows the PSDs of the lift and drag coefficients of the axle and wheel in isolation from each other. It is noted that the main peak of the lift or drag force cannot be identified for the isolated axle case while the flow around the isolated wheel is fully irregular, resulting in the broadband force coefficient distributions.

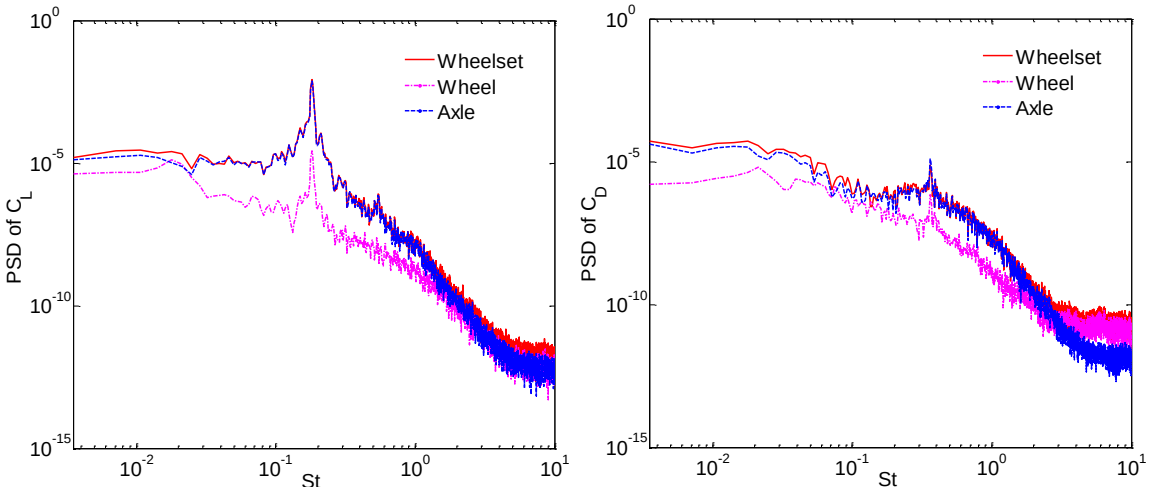

(a) Lift coefficient (b) Drag coefficient

Figure 5.13: Power spectral density of lift and drag coefficients (isolated wheelset)

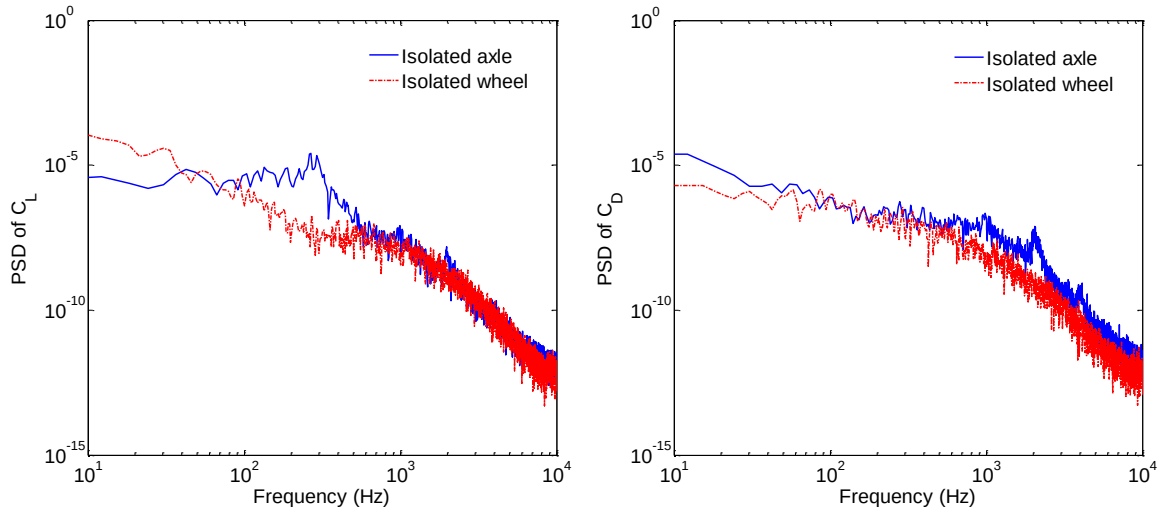

Figure 5.14: Power spectral density of lift and drag coefficients (isolated axle and isolated wheel)

5.3.4 Divergence of Lamb vector

Figure 5.15 visualizes the divergence of the Lamb vector as stated in Section 2.2.4 to depict the spatial distributions of the aeroacoustic volume sources. This indicates that the flow separations generated from the wheel front sharp edges and the various shedding vortices developed in the near wake area around the wheelset are associated with the main volume source contributions and play a dominant role in the corresponding volume noise generation.

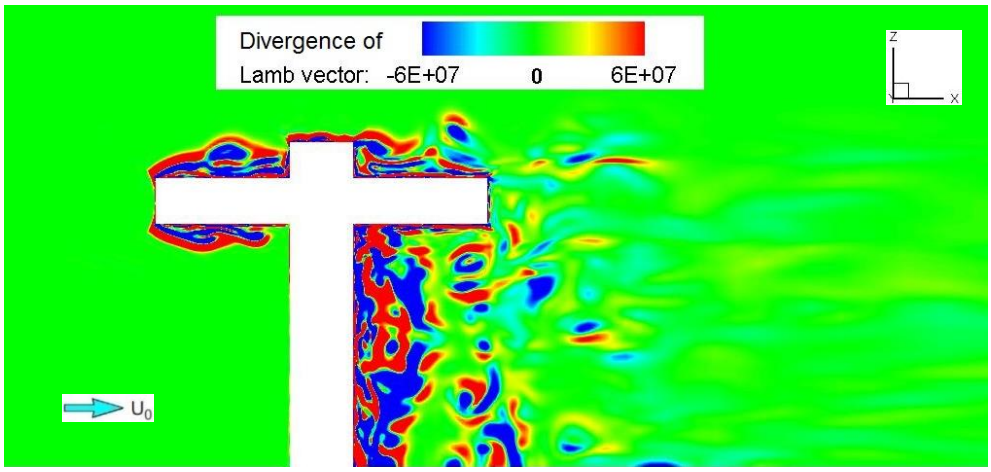

Figure 5.15: Visualization of the divergence of the Lamb vector in horizontal plane through centre of wheelset (bottom view)

5.4 PIV Experiment versus Numerical Simulation

A PIV experiment for the isolated wheelset has been performed in the 7'×5' wind tunnel at the University of Southampton. A 1:5 scale wheelset model made of aluminum was attached on the mounting struts fixed on the wind-tunnel roof and a gap of 40 mm between the wheelset and the ground was considered to represent the distance of the wheels above the ground when running on the rails. Afterward, the PIV measurement was compared with the numerical simulations.

5.4.1 PIV experiment

Figure 5.16 gives a schematic diagram of the 7'×5' wind tunnel layout and the PIV experimental setup in the test section of this wind tunnel. This system consists of a Gemini PIV 15 laser with two Tempest Ng:YAG lasers of 125 mJ/pulse at a wavelength of 532 nm, and a TSI PowerView CCD camera (2048×2048 pixels resolution) to capture the images. The seeding material is composed of water-based smoke particles of approximately 1 micron in diameter and is produced from a smoke generator which is located downstream of the test section to avoid the flow disturbation generated in the inflow by the smoke generator itself. Therefore, the seeding material can be circulated and produced within the inlet flow in this closed circuit wind tunnel (shown in Figure 5.16a). The displacement of seeding particles over a short duration is measured to obtain the

velocity field; thus, the time delay between the successive laser pulses should be determined properly for the camera to capture a better illumination. Some strict procedures have been followed when setting up the PIV experiments to obtain accurate results. For instance, the laser sheet should be aligned properly in the desired plane with an accuracy of ±0.5 mm and $\pm 0.1^0$; the camera should be positioned perpendicularly to the investigated plane within $\pm 0.1^0$ at a distance to the PIV measurement domain determined by the available focal length and the desired image size. For the freestream velocity of 30 m/s used in this test, the 1mm thickness of the laser sheet is chosen with a time interval of 15 μs. The size of the captured image is kept below 200mm×200mm to keep a good resolution quality of the camera. During the data acquisition, the smoke needs to be added continuously and it is determined, by adjusting the correlation of particles between two images, to be mostly successful.

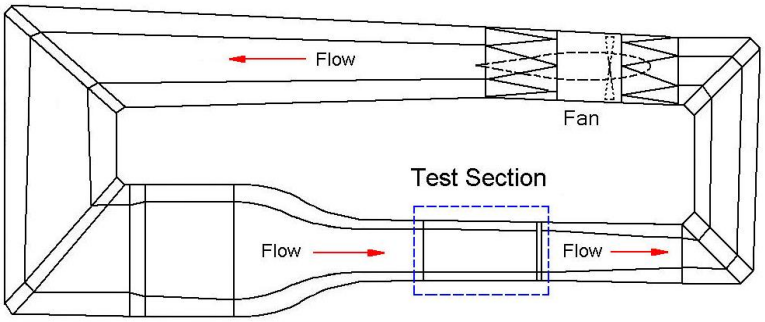

(a) 7'×5' wind tunnel layout

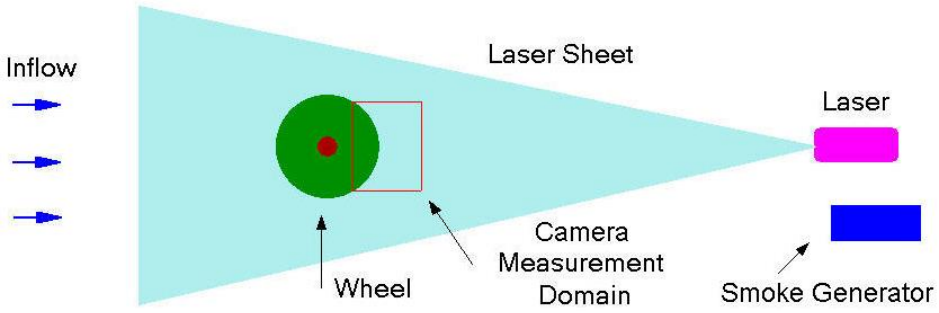

(b) PIV experimental setup in the test section

Figure 5.16: Schematic diagram of the 7'×5' wind tunnel layout and the PIV experimental setup

Figure 5.17 shows the front view of the experimental setup of the isolated wheelset case in the 7'×5' wind tunnel with the PIV system installed. The mid-span of one wheel along the streamwise direction from the PIV experiment is

investigated and Figure 5.18 displays the streamwise mean velocity field in the wake region of the wheel. Asymmetric flow conditions are readily apparent around the wheel wake region in Figure 5.18(b) since an angle of 9.7^0 between the central mean streamline and the wheel equatorial axis is observed downward to the ground. This is believed to result from the ground effect: when the ground is fixed, the boundary layer develops on the ground surface and interferes with the separated shear layer from the bottom side of the wheelset. Such influence of the ground effect is also confirmed by the CFD simulation presented below. It may be pointed out that the reflection from the wheel surface makes the images captured for the axle wake area in the PIV experiment hard to be identified and they cannot be used for analysis.

Figure 5.17: Front view of the PIV experimental setup of isolated wheelset case

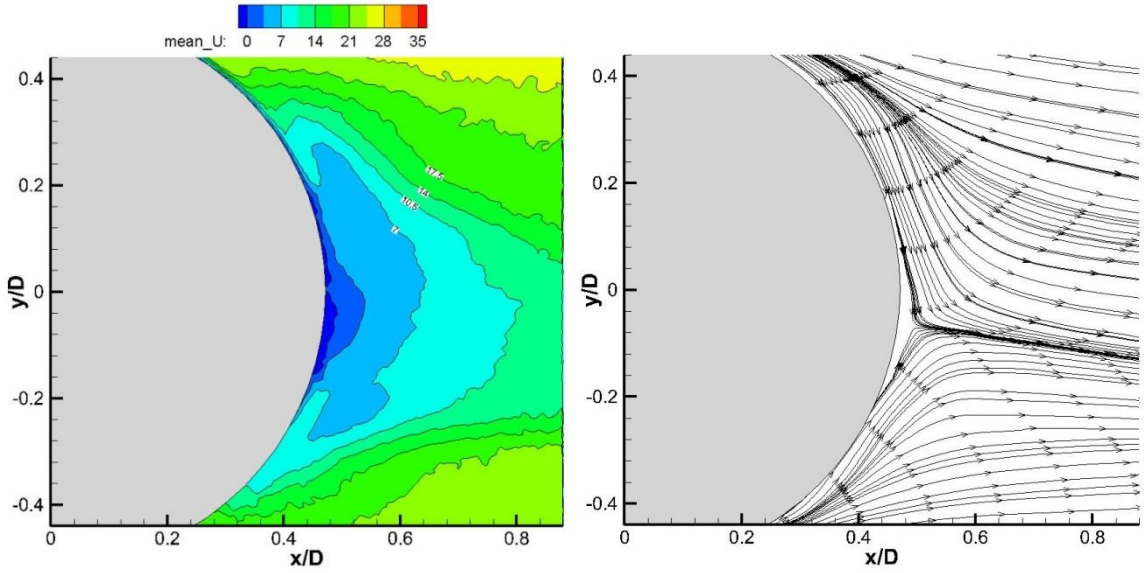

(a) Mean velocity (b) Mean streamline

Figure 5.18: Streamwise mean velocity field (PIV experiment)

5.4.2 Numerical simulation corresponding to PIV experiment

Computations are carried out based on the dimensions and experimental conditions from the 7'×5' wind tunnel. The computational domain is illustrated in Figure 5.19 in which 'D' (=184 mm) is the diameter of the 1:5 scale wheel and 'h' (=40 mm) is the gap between the bottom of the wheel and the ground to simplify all components between them. The corners in the tunnel are simplified to be rectangular. In the simulation, the wheelset and the ground are both defined as stationary no-slip walls. The symmetry plane along the axle mid-span is set to a symmetry boundary condition which assumes no flux of all qualities across it. Equivalent to a zero-shear slip wall, the tunnel ceiling and the side wall of the domain are also defined as symmetry boundary conditions to avoid a high grid density required to resolve the wind-tunnel boundary layer. The upstream boundary is set to a velocity inlet with a normal velocity of 30 m/s. As the wind tunnel is of low turbulence intensity ($\approx 0.3\%$), a low turbulent viscosity ratio of unity is applied for the inlet flow. The downstream boundary is defined as a pressure outlet with a gauge pressure of zero. The physical timestep size is 5×10^{-6} s followed by 10^{-5} s which gives the temporal resolution for the simulation with respect to the CFL number of less than 2 within the computational domain.

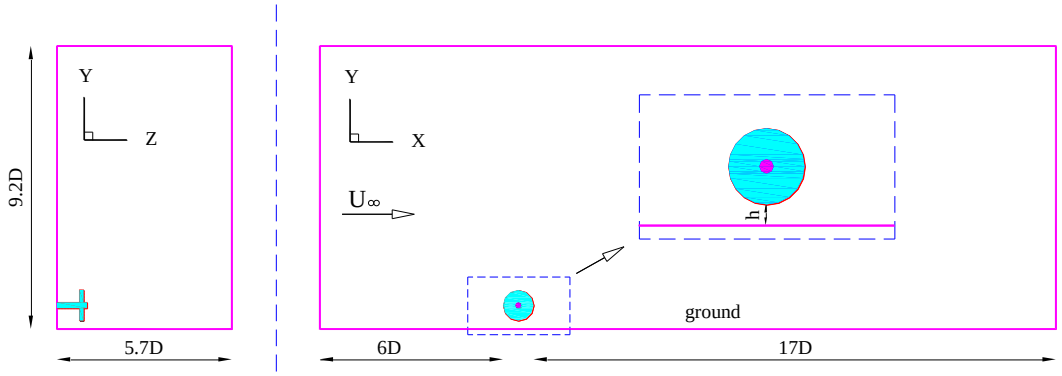

(a) Front view (b) Side view

Figure 5.19: Sketch of the computational domain with the wheelset (not to scale)

The grid topology of the CFD model of the 1:5 scale wheelset (a Reynolds number of 72,000 based on the axle diameter and the freestream properties) basically

follows that used for the 1:10 scale wheelset model as referred to previously. The total number of grid points in the entire domain is 19.4 million.

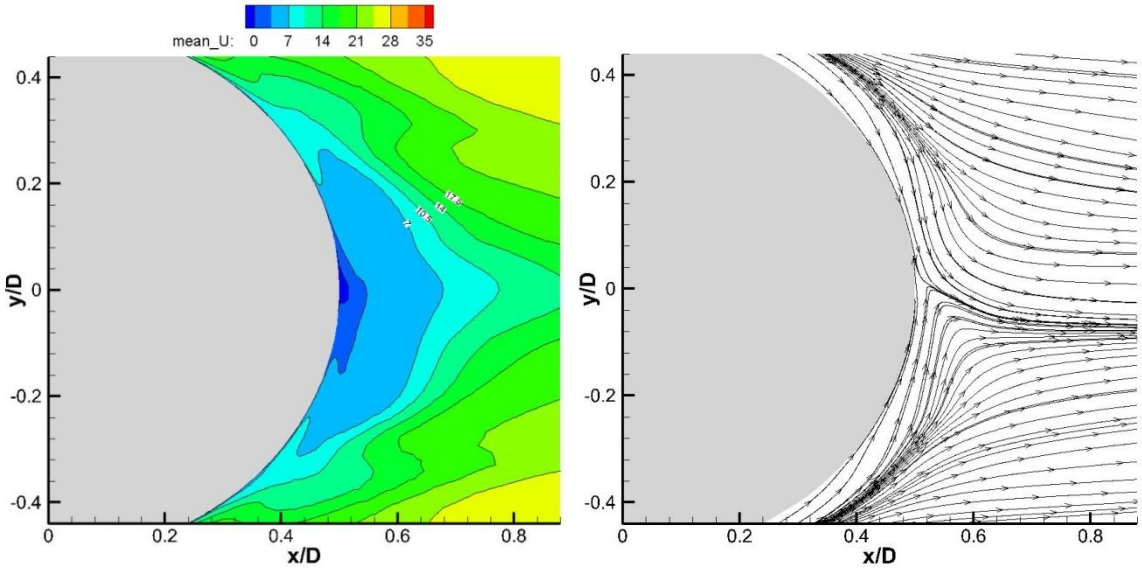

(a) Mean velocity (b) Mean streamline

Figure 5.20: Streamwise mean velocity field (CFD simulation)

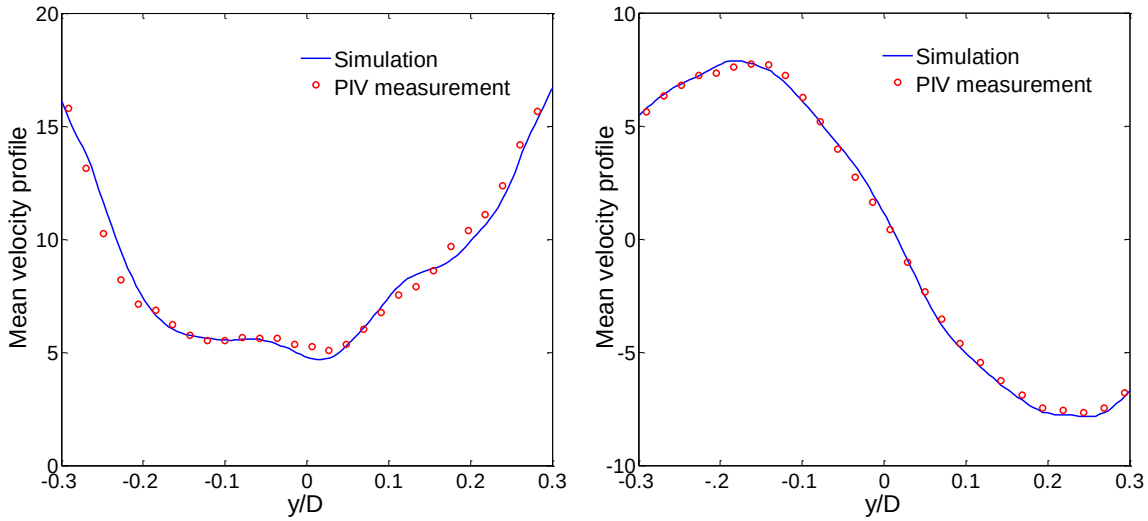

(a) Streamwise (b) Vertical

Figure 5.21: Comparisons of streamwise and vertical mean velocity profiles at x/D=0.6

Corresponding to the PIV experiment, the equivalent data from the CFD analysis are displayed in Figure 5.20. The computed flow patterns shown in this figure are qualitatively similar to those from the PIV measurements (Figure 5.18). Likewise, asymmetric flow conditions with an averaged angle of 9.9^0 between the central mean streamline and the wheel equatorial axis downward to the ground is

observed in Figure 5.19(b). Figure 5.21 compares the mean velocity profiles behind the wheel of the isolated wheelset at x/D =0.6 in the wheel mid-span between the calculation and experiment results. It can be seen that the CFD simulation successfully captured the streamwise and vertical mean wake profiles of the wheelset. Therefore, the above results give a reasonable indication that the wheel wake pattern is properly identified by the numerical simulation by its good agreement with the experimental measurements.

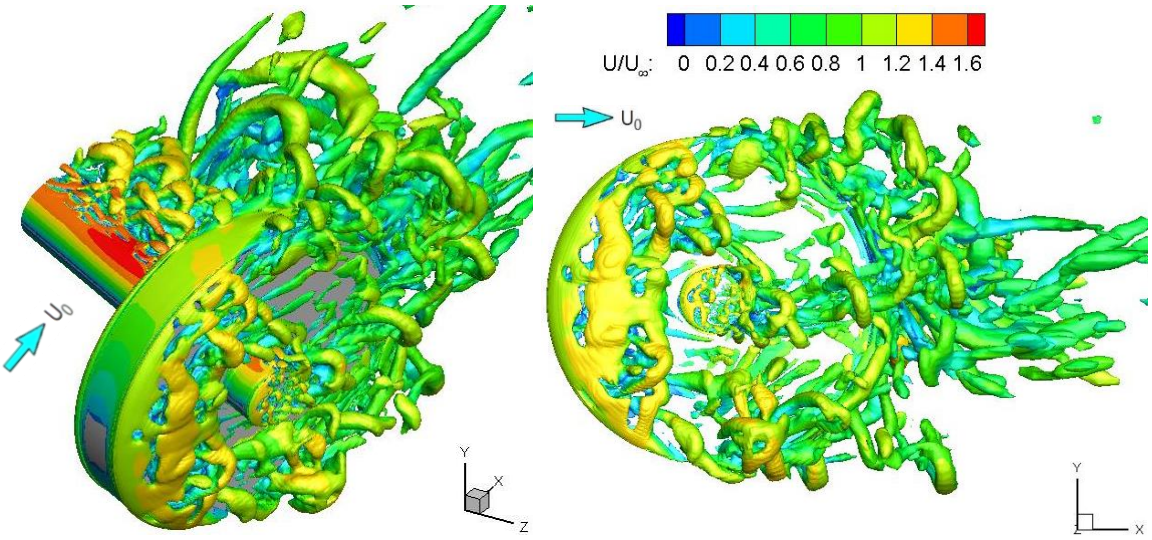

(a) Isometric view (b) Side view

Figure 5.22: Iso-surfaces of the instantaneous normalized Q criterion

Figure 5.22 visualizes the instantaneous wake structures of the wheelset represented by the iso-surfaces of normalized Q criterion value of 25 (based on $Q/[(U_0/D)^2]$, where D is the wheel diameter). They are coloured by the velocity magnitude. Similarly, it can be seen that the crescent-shaped separation bubble and subsequent horseshoe-shaped eddies are generated along the front sharp edges of the wheel as discussed in Section 5.3.2. As a consequence of the interference with the boundary layer developed on the ground surface, a pressure gradient is produced in the wheel wake region and the shear flow separated from the upper part of the wheel declines in the downward direction due to this low pressure. These differences are revealed to lead to the forming of an asymmetric flow pattern in the wheelset wake structure as seen in Figures 5.18 and 5.20. With no influence from the ground boundary layer, the turbulent vortices in the

upper part of the wheel are developed more fully and have the potential to penetrate further into the wake region downwards toward the ground direction.

5.5 Aeroacoustic Results

Based on the near-field unsteady flow data obtained from the CFD calculations, the FW-H method can predict far-field noise signals by equivalent acoustic sources as stated in Section 2.3.2. There are 22,016 panels (surface elements) around the wheel and 15,232 panels on the axle which account for the acoustic sources on the solid integration surfaces. The receivers are distributed uniformly along a circumference with 2.5 m radius at an interval of 5º as sketched in Figure 5.23 to measure the noise directivity from the wheelset centreline in the vertical *z-y* plane. Additionally, equivalent circular-shaped receiver positions are defined in the horizontal *x-z* plane (the coordinates referred to Figure 5.2a). This distance corresponds at full scale to 25 m as recommended for field measurements of railway noise, e.g., in ISO 3095 [87]. For the three-dimensional directivity calculation, the far-field observers are distributed on a spherical surface also with a radius of 2.5 m, composed of 1,946 receivers with a resolution of 5º for the azimuthal and polar angles. The directivity characteristics of the source are obtained to represent the overall acoustic field through calculating the overall sound pressure level from the time history of the acoustic pressure at each specified receiver over the resolved frequency range.

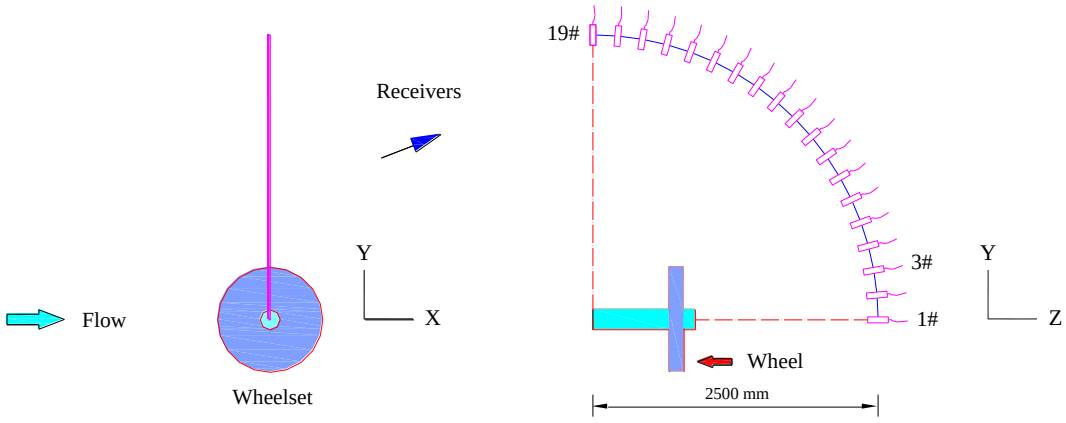

Figure 5.23: Sketch of receiver locations

5.5.1 Acoustic spectra computation

The CFD simulations were run for 0.93 s corresponding to 20 times the flow-through time (L_x/U_∞, where L_x is the computational domain length). The acoustic sources are collected over the last 0.55 s of the computation. Predicted far-field acoustic pressure is used to calculated the PSD by segmental average (50% overlap) using a Hanning window applied to 5 segments, giving a frequency resolution of 6 Hz.

Based on the numerical simulations on the symmetrical half wheelset and whole isolated wheel (i.e. without the axle), Figure 5.24 shows the spectra of the noise radiated from the non-rotating wheelset and the isolated wheel at three receivers in the *z-y* plane as described in Figure 5.23. In addition, components of the noise radiated by the wheelset (separate components of the wheel and axle) are shown at one receiver. From the wheelset case in Figure 5.24(a), it is noted that the tonal peaks appear at the frequencies of 311 Hz and 622 Hz at receiver 3 which is located 0.434 m above the axle axis. The primary peak corresponds to the oscillating lift forces exerted back on the fluid around the wheelset and the peak at the second harmonic is associated with the oscillating drag forces. As referred to in Section 5.3.3, the frequency of the fluctuating drag is twice that of the fluctuating lift. The overall sound pressure level obtained from the acoustic signals corresponding to the frequency range below 5 kHz is 60.2 dB. Of this, the primary peak between 300 to 330 Hz corresponds to 56.6 dB and the second harmonic in the range of 600 to 630 Hz contributes 50.8 dB; thus, the contribution from the remaining broadband noise is about 56.7 dB. The largest drag dipole component is found at receiver 1 while receiver 19 shows the highest lift dipole component. At receiver 3 both the lift and drag dipole components are found.

Figure 5.24(b) compares the spectra of the noise radiated from the sources on the axle and the wheel separately (as part of the wheelset) at receiver 3. Again, two tonal noises are found with dominant frequencies corresponding to the lift and drag forces respectively. Therefore, in the vertical *z-y* plane normal to the flow direction the sound radiation produced from the separated wheel in the presence of the axle is mainly associated with the drag forces, whereas the noise

generated by the separated axle in the presence of the wheel mainly corresponds to lift forces. Compared with the wheelset case, the noise radiated from the isolated wheel in Figure 5.24(a,c,d) is more broadband with a lower spectral level, resulting from the irregular flow with no periodic shedding generated around it as indicated from Figure 5.14.

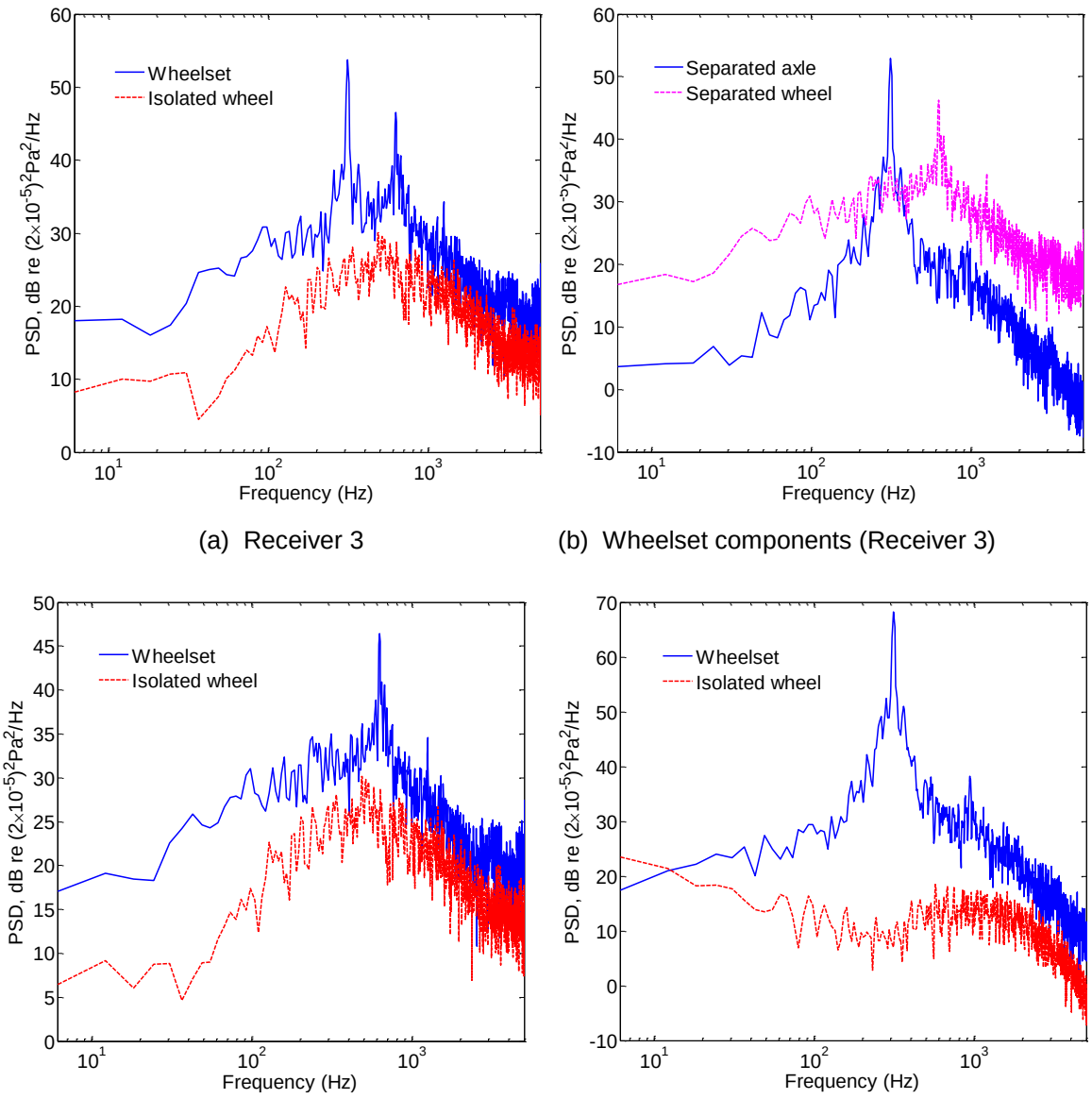

(a) Receiver 3 (b) Wheelset components (Receiver 3)

(c) Receiver 1 (d) Receiver 19

Figure 5.24: Spectra of acoustic pressure at far-field receivers (U_∞=30 m/s)

Furthermore, to improve the completeness of current analyses, the spectra of the noise generated from a rotating wheelset (U_∞=30 m/s) and a non-rotating wheelset (U_∞=70 m/s) at receiver 3 are compared with the non-rotating wheelset case (U_∞=30 m/s) and shown in Figure 5.25. The speed of U_∞=70 m/s is closer

to the high-speed train case. It is found from Figure 5.25(a) that the frequencies of the two dominant peaks in the rotating wheelset case are both about 6 Hz higher but with similar amplitude compared to those from the non-rotating wheelset. Thus, the rotation of the wheelset is expected to have a small influence on the noise generation for the current isolated cases. Figure 5.25(b) shows that as the inflow velocity increases to 70 m/s, the OASPL increases noticeably by about 20 dB and the frequencies of the two spectral peaks (726 Hz and 1447 Hz) increase in proportion to the flow speed, corresponding to an invariant Strouhal number characterized by regular vortex shedding. Note that for the real case, the inflow passing over the wheelset is turbulent, the fluctuating lift amplitudes will be reduced, and thus the tonal noise levels will be decreased while the broadband noise levels increased.

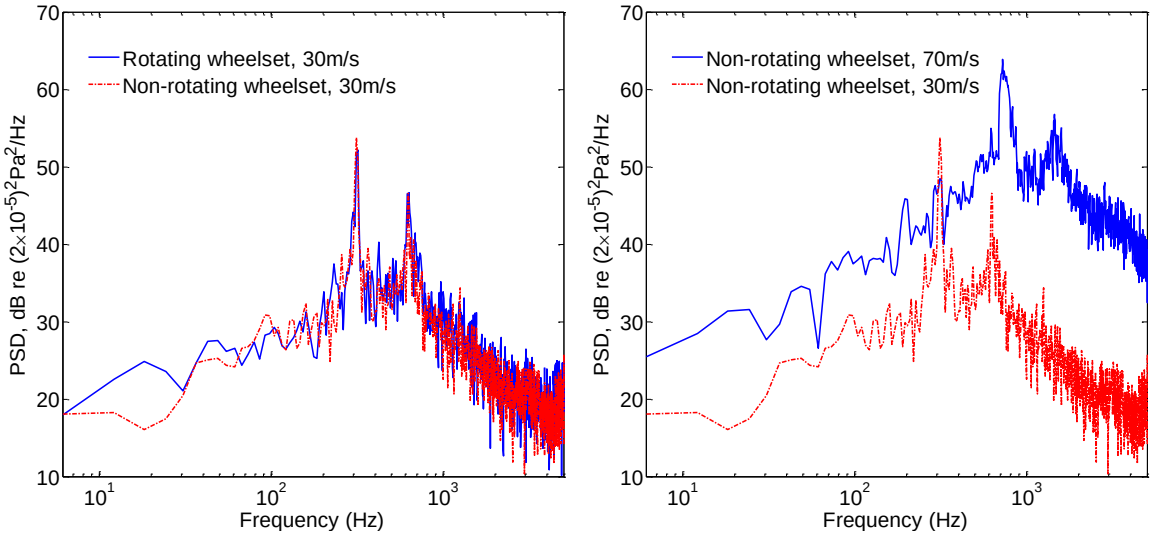

(a) Rotating and non-rotating wheelset (30 m/s) (b) Non-rotating wheelset (30 and 70 m/s)

Figure 5.25: Spectra of acoustic pressure at receiver 3

5.5.2 Experimental verification

An experimental measurement of sound generated by flow past a non-rotating wheelset was made in an open-jet anechoic wind tunnel. Figure 5.26 displays the experimental setup in which the test model is mounted in the working section on a rigid baffle (2.9m wide and 1.2m high), which is constructed by an aluminum sheet and covered by acoustic foam on the flow-facing side. A 1:10 scale half-wheelset is immersed within the core flow and the remaining parts are wrapped

with sound-absorbing sponge to suppress the aerodynamic noise generated by vortex shedding from such a portion. The wheelset model is made of aluminum and has same geometry as calculations. The flow speed is 30 m/s with the turbulence level in the jet core below 0.3%. In accordance with the numerical predictions, two receivers identified as ‘top microphone’ and ‘side microphone’ are located at (-18, 1375, 31.3) and (0, 185, 2211.3), of which the dimensions in millimetre and the coordinates (see Figure 5.26b) have their origin at the centre of the axle outer end surface. The measurement was made with a sampling rate of 48 kHz and contained a time signal of length 10 s. Corresponding to the frequency resolution used in the simulation, the PSD of test data is computed by Welch’s method with 6 Hz bandwidth.

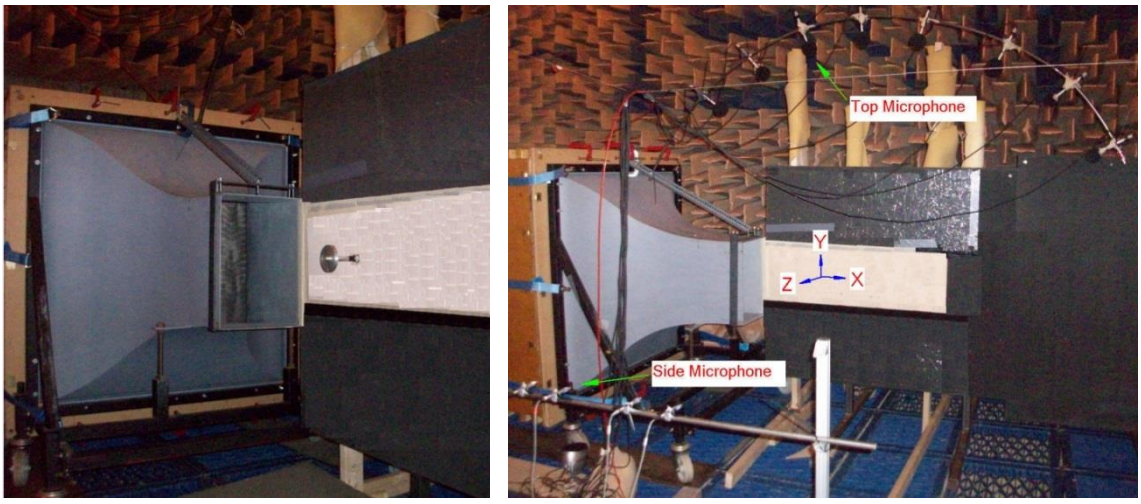

(a) Test model of half-wheelset (b) Receivers and coordinates

Figure 5.26: Experimental setup in the anechoic chamber

Figure 5.27 displays the spectra of background noise in the anechoic chamber for a mean stream flow speed of 30 m/s. It shows that for frequencies below 100 Hz a high background noise is caused by the fans, the duct and the nozzle flow in the anechoic wind-tunnel [64]. These frequencies are therefore not considered.

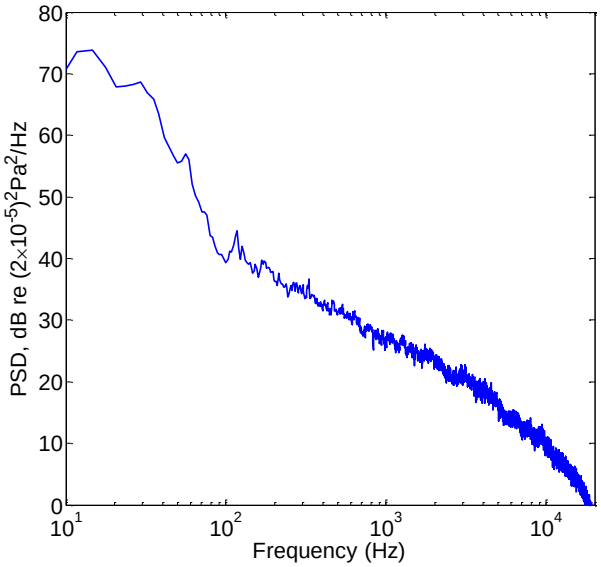

Figure 5.27: Background noise for a mean stream flow speed of 30 m/s (top receiver)

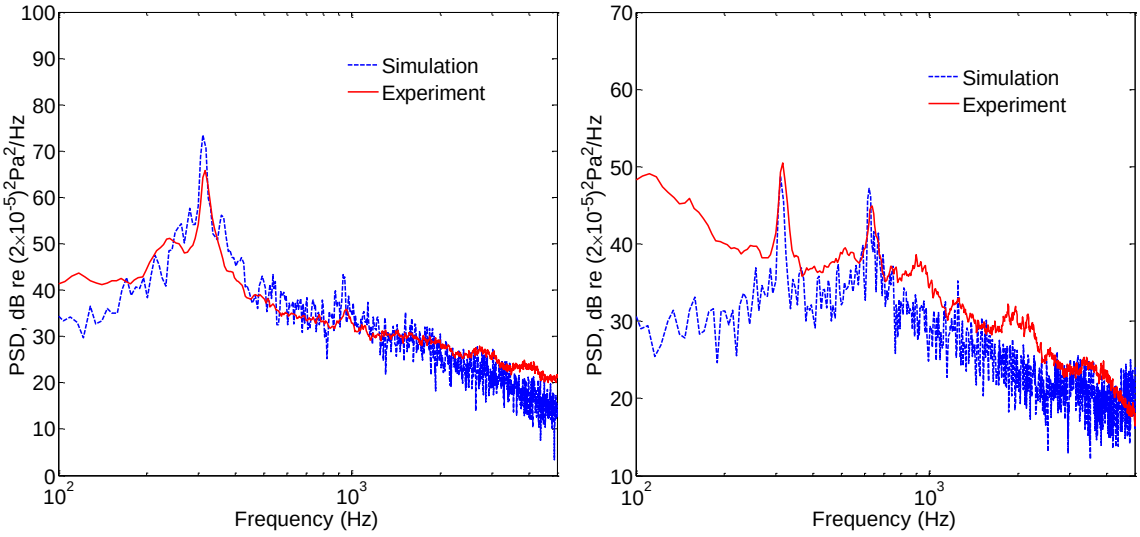

(a) Top receiver (b) Side receiver

Figure 5.28: Comparisons of spectra of far-field sound from simulations and experiments

Figure 5.28 depicts the spectra of the radiated noise at the two receivers. Figure 5.28(a) compares the predicted and measured PSD levels for the top microphone. Good agreement can be found for the dominant frequency of tonal noise and the shape of the spectrum; even a small peak around 960 Hz (third harmonic) is accurately predicted in the computation. In the experiment a low amplitude peak appears around 234 Hz, which is not observed in the simulation. This peak may be associated with the noise contribution from the interaction between the axle wake and the baffle plate, i.e. the vortex shedding in the axle wake region close to the baffle is decreased by the unsteady flow developed on the rigid plate and

thereby the corresponding shedding frequency is reduced. This is demonstrated by the same phenomenon occurring in the experiments of the flow-induced noise from wall-mounted cylinders [108]. Compared with the experimental data, the main tonal peak is higher in the calculated spectrum. Again, this is likely to be due to the solid wall (rigid baffle) used in the experiment which weakens the coherent vortex shedding from the axle compared to the symmetric boundary conditions with stronger spanwise uniformity applied in the simulation.

Figure 5.28(b) shows the spectra of the radiated noise from prediction and experiment at the side microphone. Note that the experimental noise levels are systematically higher than the predictions at the side microphone due to the additional noise contributions caused by reflections from the baffle plate. The two tonal peaks in the measurements correspond fairly well with the noise predictions: both the dominant frequency values and the harmonic behaviour. This indicates that the sound reflection from the baffle plate has little effect on the frequencies of the main peak and harmonics caused by the vortex shedding from the wheelset.

5.5.3 Acoustic directivity

The directivity of radiated noise predicted in the far-field is obtained based on the overall calculated SPL which is determined from the PSDs over the frequency range below 5 kHz. Figure 5.29 shows the noise directivity radiated from a rotating wheelset (30 m/s) and non-rotating wheelset (30 m/s and 70 m/s) in the vertical *z-y* plane normal to the flow direction and in the horizontal *x-z* plane along the streamwise direction. This reveals a vertical dipole pattern of directivity for the sound radiation of the wheelset, which is due to the strong periodic vortex shedding generated at the top and bottom surface of the axle. Note that in an incompressible flow solver, the acoustic shielding and scattering of sound waves by solid surfaces cannot be properly calculated. For the isolated wheelset case, the noise generated from the axle would expected to be shielded by the wheel, especially for the side receivers close to the axle central axis. Nevertheless, the noise directivity pattern from the axle which can be treated as a cylinder is a dipole, i.e. less acoustic waves are radiated to the side receivers. Moreover, the vortex shedding from the axle close to the wheel is weakened (as discussed in

Section 5.3.2) and accordingly the less noise will be generated around the inner wheel-axle junction areas. Therefore, the influence of the noise shielding by the wheel for the isolated wheelset case would be expected to be relatively small. This can be seen from Figure 5.28(b). When the inflow speed increases from 30 m/s to 70 m/s, the noise levels are increased by 18.5 dB with a similar directivity pattern. This corresponds to an increase in the radiated sound power in proportion to about the sixth power of the flow speed as expected for an aeroacoustic dipole source.

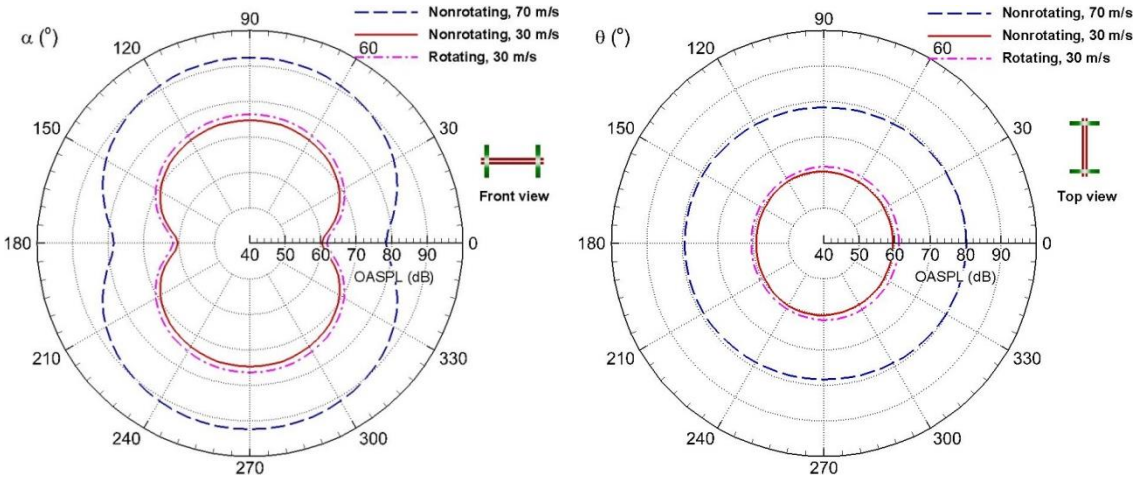

(a) Vertical *z*-*y* plane (b) Horizontal *x*-*z* plane

Figure 5.29: Noise directivity from rotating and nonrotating wheelsets

Figure 5.30(a) shows the directivities in the *x*-*y* plane. Based on the noise directivities shown in Figure 5.29 and Figure 5.30(a), it can be concluded that the dipole patterns of the noise generated from the rotating and non-rotating wheelset are very close, with noise levels that are about 2 dB higher for the rotating case. Figure 5.30(b) shows the noise directivity from the separate components from the wheel and axle of the rotating and non-rotating wheelset. It can be seen that the vertical dipole pattern of the non-rotating wheel is inclined upwards towards the inflow direction for the rotating wheel and the difference in the noise levels between them is small. Compared to the separated wheel, the noise generated from the axle part is much larger. This leads to the vertical dipole pattern of noise radiation from the rotating wheelset presented in Figure 5.31, which clearly shows that the lift dipole dominates the directivity shape. The non-rotating wheelset case has the similar vertical dipole directivity pattern as seen from Figure 5.29.

Additionally, compared with the non-rotating case, the noise generated from the rotating axle is slightly greater as a consequence of the stronger flow-axle interaction caused by the rotation effect, making the noise of the rotating wheelset slightly higher as mentioned above.

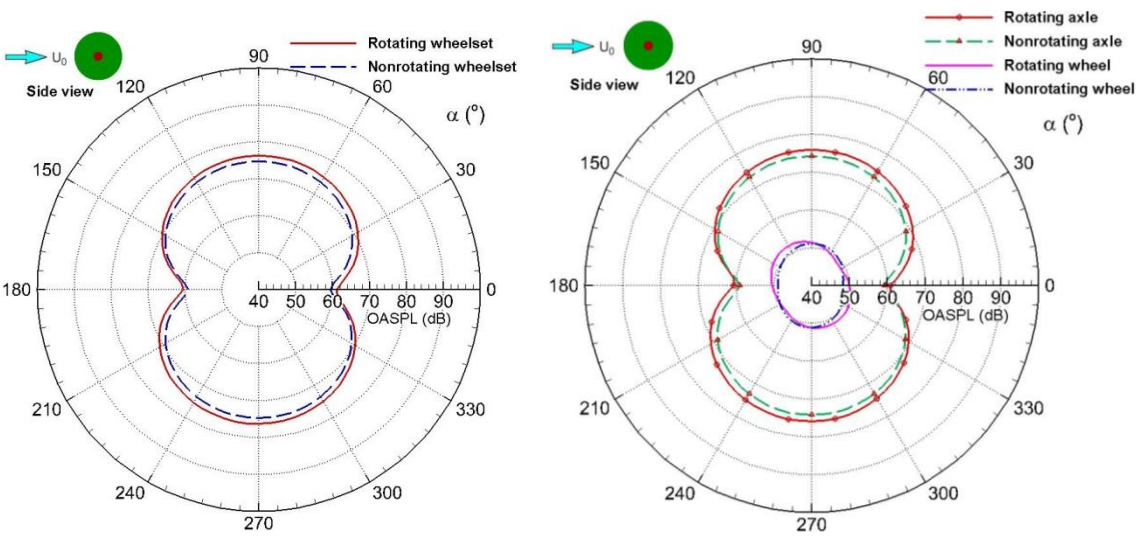

(a) Whole wheelset (b) Separated wheel and axle

Figure 5.30: Noise directivity for rotating and non-rotating wheelsets (streamwise *x*-*y* plane)

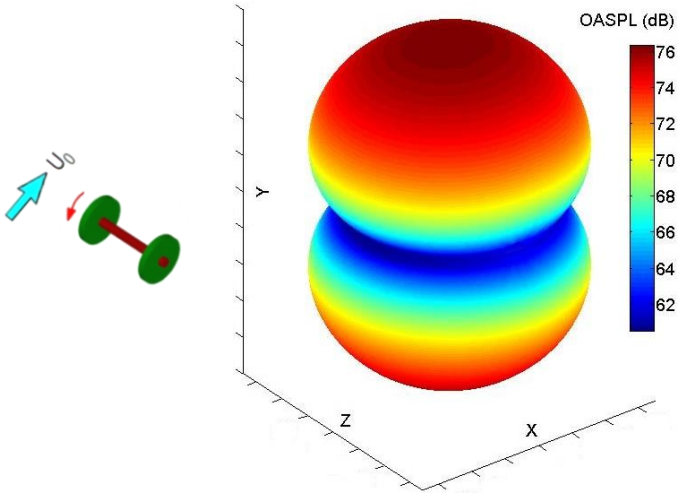

Figure 5.31: Three-dimensional noise directivity for a rotating wheelset (centre of directivity pattern corresponds to 40 dB)

5.6 Likely Effect of Simplified Wheels

The details of the real case with complex geometry had to be neglected for structured mesh generation considering the computer ability and computation

efficiency. In order to know the possible influence from the simplification of the geometries, the instantaneous wake structures and noise directivities are compared for the idealized wheel and a more detailed wheel. The geometries of these two isolated wheels are illustrated in Figure 5.32 which shows that their configurations are different around the wheel web region. Both idealized and detailed wheels are symmetrical along wheel mid-span and are assumed stationary here. The structured mesh topology used for them is similar to the isolated wheelset case.

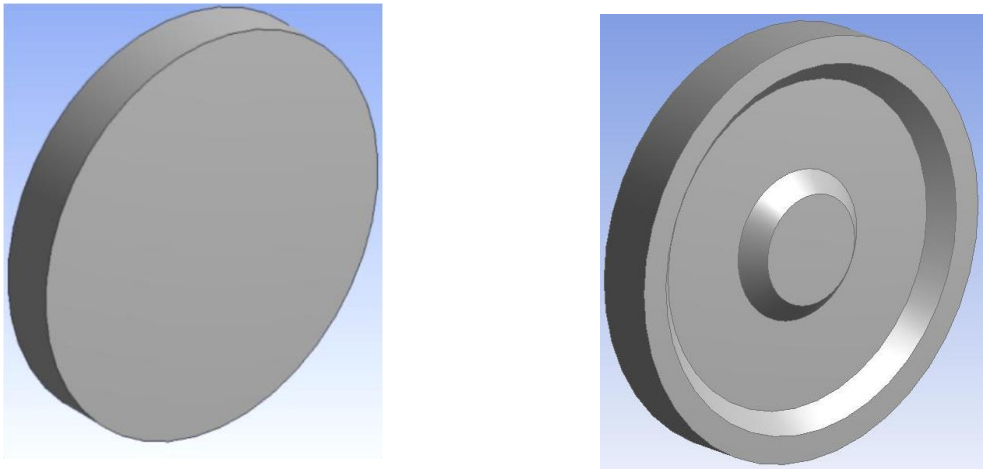

(a) Idealized wheel (b) Detailed wheel

Figure 5.32: Idealized wheel and detailed wheel models (1:10 scale)

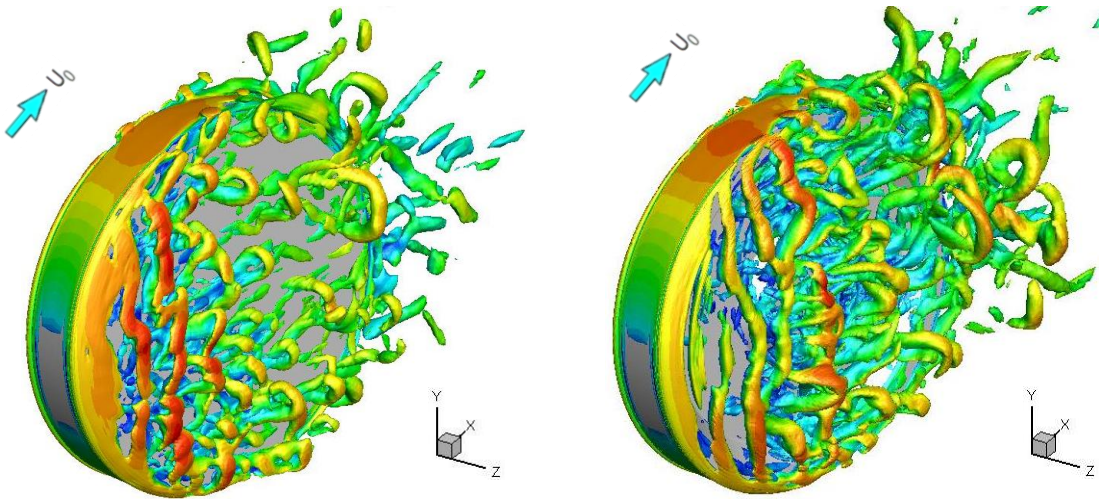

(a) Idealized wheel (b) Detailed wheel

Figure 5.33: Iso-surfaces of the instantaneous normalized Q criterion (isometric view)

Figure 5.33 presents the instantaneous wake structures of these two isolated wheels represented by the iso-surfaces of the normalized Q criterion at the value

of 50 (based on $Q/[(U_0/D)^2]$, where D is the wheel diameter). They are coloured by the velocity magnitude. It can be seen that for the idealized wheel case (shown in Figure 5.33a), a separation bubble is formed along the wheel front sharp edges and the horseshoe-shaped eddies are developed on the flat wheel side surfaces, convected downstream, detached and dissipated into the wake region. Compared to the flow passing the idealized wheel, the horseshoe-shaped eddies generated around the detailed wheel side surfaces develop more irregularly and a higher level of flow-field unsteadiness occurs in the flow there as shown in Figure 5.33(b). The shear layer separates from the wheel tyre leading edge and impinges on the wheel hub and the wheel tyre trailing edge, leading to a noticeably turbulent flow generated near the wheel lateral side surfaces and a comparatively unsteady wake developed behind the wheel.

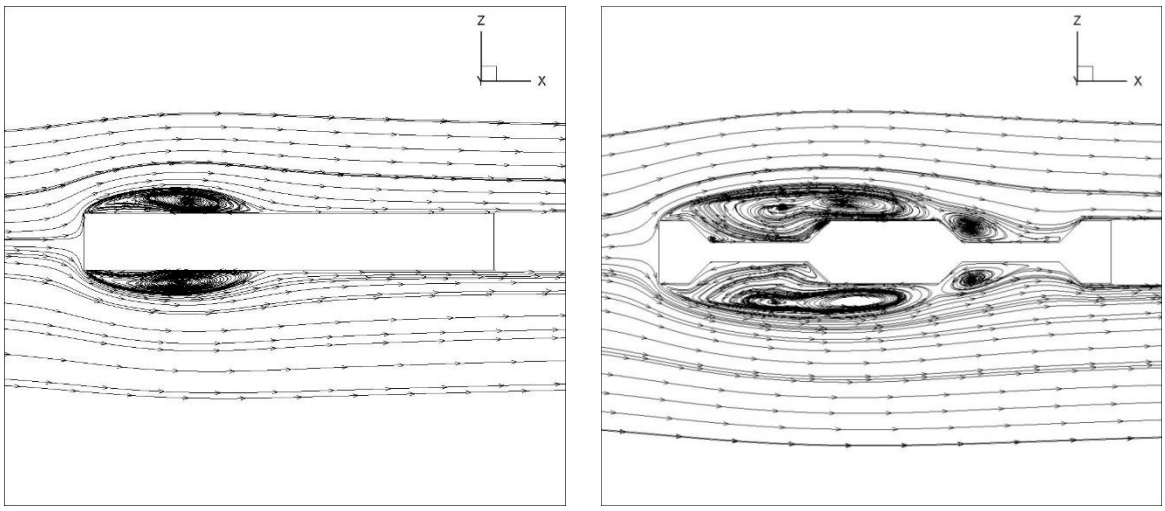

(a) Idealized wheel (b) Detailed wheel

Figure 5.34: Mean streamlines around the isolated wheel

Figure 5.34 displays the time-averaged streamlines on the *x*-*z* horizontal central plane through the two isolated wheels. Figure 5.34(a) shows that for the idealized wheel case, a separation bubble is generated in the upstream region of the wheel side surfaces and subsequently, the flow attaches on the most rear areas of the wheel flat surfaces. Moreover, it can be found from Figure 5.34(b) that for the detailed wheel case, the flow separation also occurs at the wheel front rim edges, but then reattaches onto the wheel web region and separates again at the wheel hub. Thus, a large fluid bubble is formed along the upstream half wheel surface. Thereafter, the separated shear layer reattaches on the rear part of the wheel web

and a recirculation region at the upstream corner of the web is generated. By comparison, the flow developed around the detailed wheel is more irregular than that around the idealized wheel.

The PSDs of the fluctuating lift and drag coefficients of the idealized wheel and detailed wheel are presented in Figure 5.35. It is noted that the spectra of the fluctuating force coefficients from the two isolated wheels are broadband as there is no massive coherent vortex shedding generated around them. Compared with the idealized wheel case, the spectrum level of the detailed wheel is relatively larger in most of the frequency range, resulting from the more turbulent flow developed around it.

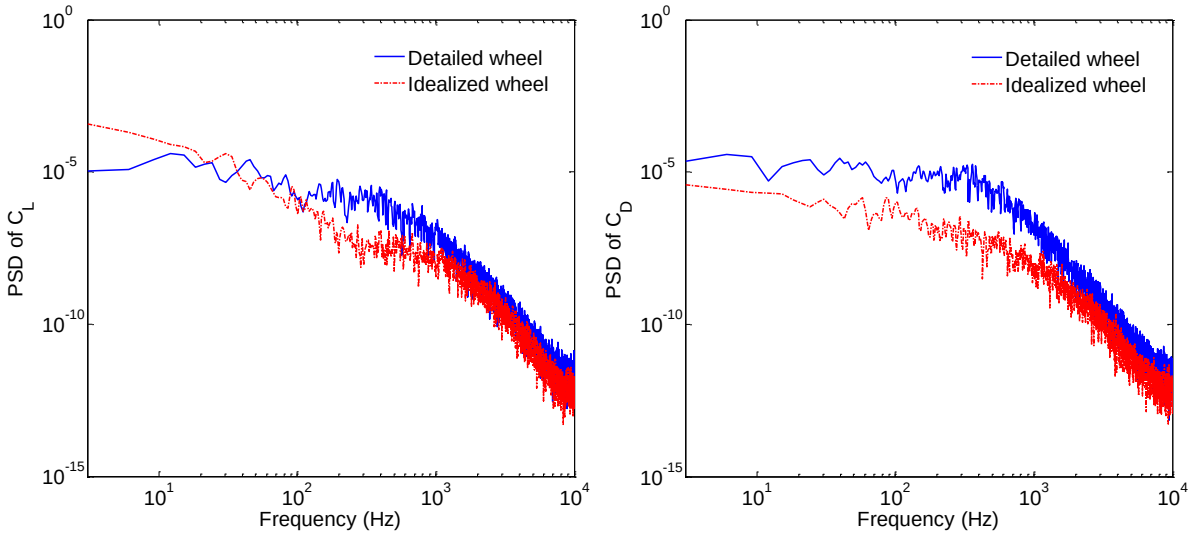

(a) Lift coefficient (b) Drag coefficient

Figure 5.35: Power spectral density of lift and drag coefficients

Figure 5.36 depicts the noise directivity radiated from the non-rotating isolated wheels and wheelset in the vertical *z*-*y* and horizontal *x*-*z* planes along the wheelset centreline. For the noise directivity calculation here, two parallel idealized wheels are in the same configuration as the isolated wheelset case but with the axle removed. They are replaced by two detailed wheels thereafter for the detailed wheels case. This shows that the noise level is generally around 5 dB larger from the detailed wheels than from the idealized wheels except in the horizontal plane along the geometry centreline parallel to the flow direction (i.e. θ=0º and 180º shown in Figure 5.36b) where the difference of the noise level

between them reaches about 10 dB. This is because a more irregular and unsteady flow is developed around the detailed wheel which makes the noise radiation much stronger and more multi-directional, resulting in the noise directivity pattern being less disparate in magnitude with a higher level. However, the mechanisms of the flow separation and interaction and the corresponding noise generation are very similar between these two isolated wheel cases. Moreover, the sound radiation from the idealized wheel or detailed wheel is much lower than the wheelset case in which the significant tonal noise is generated from the vortex shedding around the axle.

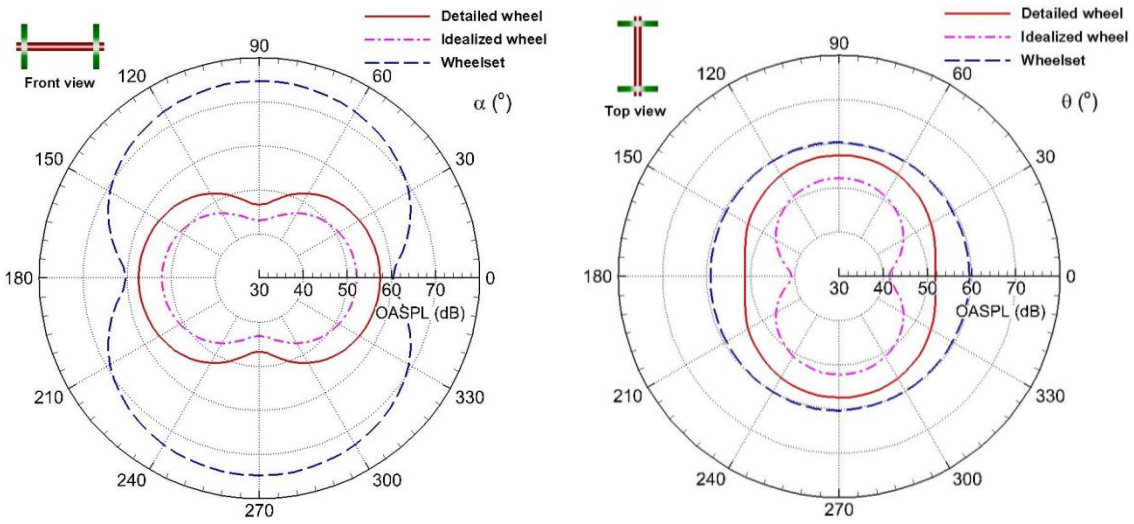

(a) Vertical *z*-*y* plane (b) Horizontal *x*-*z* plane

Figure 5.36: Noise directivity from non-rotating isolated wheels and wheelset

5.7 Summary

The aerodynamic and aeroacoustic behaviour of the flow past an isolated wheelset (1:10 scale) where the ground effect is neglected has been studied using the DDES model and the FW-H acoustic analogy method. It is found that the turbulent flow around the wheelset has a complicated three-dimensional wake structure: both streamwise and spanwise vortices are generated due to the vortex shedding and flow separation around it. In aeroacoustic prediction, the noise calculation agrees fairly well with experimental measurements. Tonal noise is generated with dominant frequencies corresponding to the lift and drag forces; and a vertical dipole pattern of noise directivity is predicted. Including wheel

rotation it is found that a slightly higher noise level is generated but the basic mechanisms are unaffected. As the inflow velocity increases, the frequencies of tonal peaks increase corresponding to an invariant Strouhal number of about 0.18 (based on the axle diameter) characterized by regular vortex shedding and the noise levels increase significantly.

The flow behaviour of an isolated non-rotating wheelset with a ground underneath has been investigated numerically and experimentally at 1:5 scale to see the ground effect. It is revealed that when the wheelset is close to the ground, an asymmetric flow pattern in the wheelset wake structure is formed. This is due to the shear flow separated from the lower part of the wheel interferes with the boundary layer developed from the ground surface, and thus the upper separated flow is carried downwards since a pressure gradient is produced in the wheel wake region. The wheel wake shape predicted by the CFD simulation is verified by the PIV measurements.

Furthermore, comparisons of the flow behaviour and noise directivity between the idealized wheel (separated from the wheelset) and a more detailed wheel show that the noise radiated from the detailed wheel is larger and more broadband due to a more highly turbulent flow developed around it; nevertheless, the noise generation mechanism of the two isolated wheel cases is very similar. Compared with the isolated wheelset case, the isolated wheel (idealized wheel or detailed wheel) has a lateral dipole pattern of noise directivity and its sound radiation is generally much weaker.

Chapter 6

Tandem Wheelsets and Simplified Bogie

The flow field developed around the bogie area in the real case is complex and remains challenging to simulate numerically. This chapter extends the wheelset case to investigate the flow behaviour and far-field sound radiation characteristics for two wheelsets arranged in tandem and a simplified bogie consisting of the tandem wheelsets and a frame formed of a square cylinder. The numerical predictions on noise radiation from the geometries (1:10 scale) will be compared with experimental measurements in the anechoic wind tunnel at the University of Southampton. For both cases, special attention is paid to the characteristic of the vortices shed from the upstream wheelset, the impingement onto the downstream wheelset and the interaction with the various vortical structures in the flow field. The turbulent flow around the bogie without a carbody is different from that for bogies running in reality. However, the aerodynamic characteristics of the isolated bogie and the comparison with the tandem-wheelset case can help to understand the flow behaviour produced by the bogie structure itself.

6.1 Flow Structure of Tandem Circular Cylinders

Normally, a certain level of simplification was applied to the real geometry to focus on the dominant flow physics and the main noise mechanisms. Being representative of a simplified geometry for many practical applications, two cylinders in tandem formation have been widely used to investigate the flow interaction and noise generation mechanisms of bluff bodies. Flow patterns around tandem circular cylinders with different separation lengths (i.e. centre-to-centre lengths) can be classified into three regimes [109,110]: (i) when the ratio of the separation length, L, to the cylinder diameter, D, is small, $L/D < 2$, the two

cylinders are sufficiently close to act as a single structure and the free shear layers shed from the upstream cylinder pass over the downstream cylinder; (ii) at intermediate separation length when $2 < L/D < 5$, the shear layers are separated from the upstream cylinder and reattached on the downstream cylinder; (iii) at large separation length when $L/D > 5$, vortex shedding occurs from each cylinder and the vortices generated from the upstream cylinder impinge on the downstream one, referred as co-shedding flow pattern. Recently, as a Benchmark problem for Airframe Noise Computations (BANC-I [111] & BANC-II [112]), flow behaviour and noise radiation from tandem cylinders have been measured and the databases are used to assess the accuracy of different numerical methods for aeroacoustic applications [113].

6.2 Numerical Setup

Figure 6.1 shows the simplified bogie model at 1:10 scale used in this study. The tandem wheelsets have the same configurations as the simplified bogie but with the frames removed. In the scale model, the axle has a diameter (d) of 17.5 mm and the wheels have a diameter (D) of 92 mm. The wheelbase (centre-to-centre length of two axles) is 252 mm which is about 14 times the axle diameter. This compares to the large separation length ($L/D > 5$) discussed above.

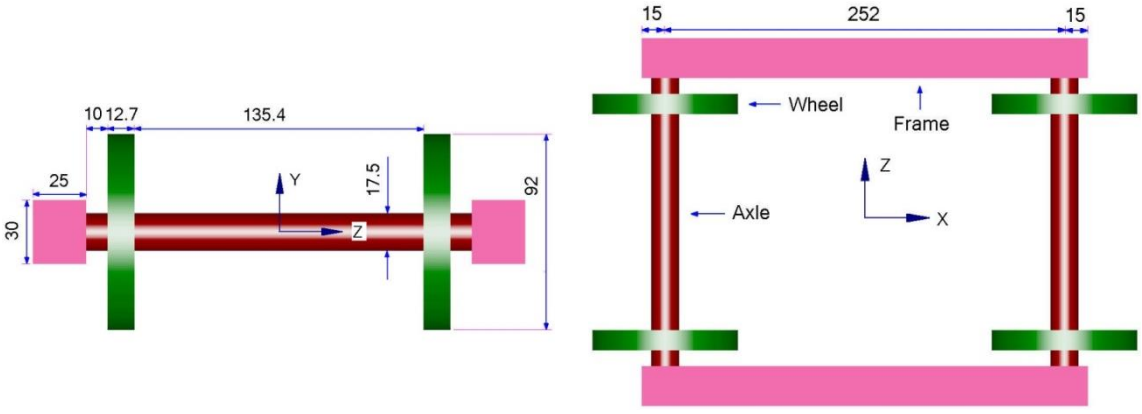

(a) Front view (b) Top view

Figure 6.1: Simplified bogie model (1:10 scale, dimensions in millimetre)

The bogie geometry is symmetrical along the axle mid-span where the flow influence of the wheel and frame is small; thereby as in the previous chapter it is

reasonable to include only half of the bogie and make use of the symmetry of the geometry to reduce the computation cost, as shown in Figure 6.2. The computational domain for the bogie case has dimensions of $17.7D$, $10D$ and $6.3D$ (where D is the wheel diameter) along the streamwise (x), vertical (y) and spanwise (z) direction, respectively, yielding a blockage ratio (defined as the ratio of the projected bogie area to the domain cross-section area) of 0.6%, which is well within the prescribed range for cylinder flow (less than 3%) [106]. The outlet boundary is far enough downstream to have negligible influence on the near-wake flow around the bogie.

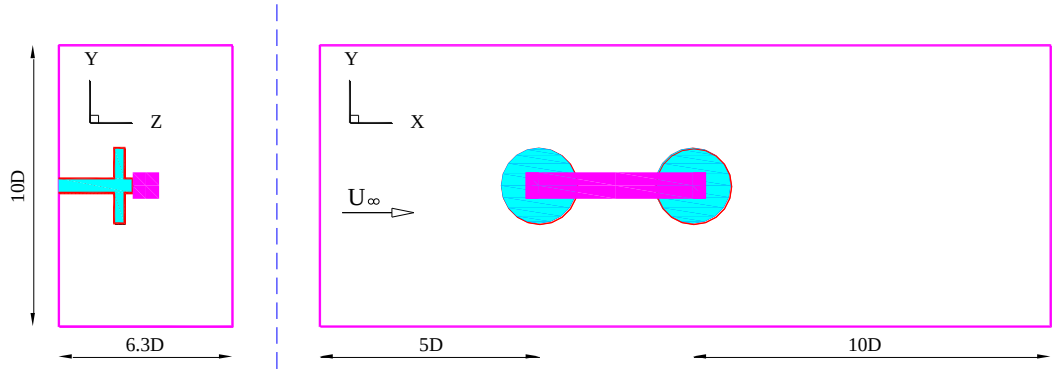

(a) Front view (b) Side view

Figure 6.2: Sketch of the computational domain (not to scale)

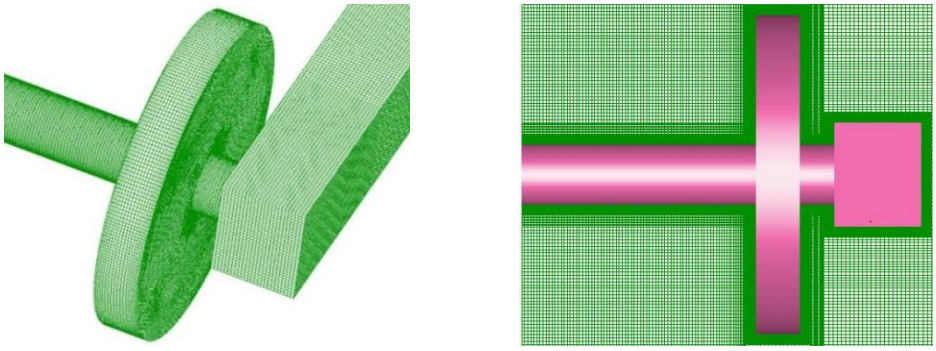

(a) Bogie surface (b) Wheelset mid-plane

Figure 6.3: Structured mesh topology around the bogie

Based on the results of the grid convergence study for the cylinder case as discussed in Section 4.3, a fully block-structured mesh is generated around the tandem wheelsets and bogie with resolution similar to the cylinder 'Baseline' grids. For both cases, the mesh topology used for the upstream and downstream wheelsets is identical to the isolated wheelset case and the grids between two

wheelsets (cell size of 0.92 mm in the streamwise direction) are kept fine enough to allow the wake full development. Figure 6.3 illustrates the mesh topology applied around the bogie geometry. Much effort has been taken to generate the structured grids with low skewness and good quality between the circular-shaped wheelset and the square-shaped frame. The cell size of the frame is implemented as 0.92 mm in the streamwise direction and 0.9 mm along the spanwise direction. The distance from the geometry wall surface to the nearest grid point is set as 10^{-5} m and stretched with a growth ratio of 1.1 in the wall-normal direction inside the boundary layer. The upstream inlet flow is set to 30 m/s with a low turbulence intensity. Thus, the average values of Δx^+, Δz^+ and y^+ of the tandem wheelsets and bogie cases are similar to the isolated wheelset case stated in Chapter 5. The total number of grid points in the entire domain is 14.6 million for the bogie case and 11.8 million for the tandem-wheelset case.

The boundary conditions applied are identical to the isolated wheelset case. A physical timestep size of 5×10^{-6} s followed by 1×10^{-5} s is utilized for the numerical simulations. The Reynolds number (based on the freestream properties and the axle diameter) of the tandem wheelsets or bogie case is the same at around 36,000, which is within the subcritical Reynolds number regime.

6.3 Aerodynamic Results

In order to understand the flow behaviour around the tandem wheelsets and bogie, the simulation results based on the instantaneous iso-surfaces of Q criterion around the geometries and the velocity as well as vorticity fields on several main cut surfaces are presented. The gauge pressure at different positions in the wake area, the fluctuating force coefficients and the wall pressure fluctuations from the geometries, and the divergence of Lamb vector field are presented and analyzed.

6.3.1 Instantaneous flow field

Figure 6.4 shows the instantaneous non-dimensional velocity field of the tandem wheelsets and bogie on the horizontal plane through centre of wheelset. It can be observed that for both cases, the main flow separations occur from the wheel front sharp edges of the upstream wheelset. Thereafter, vortices are formed in the gap between the two wheelsets and convected downstream, leading to turbulence separation and greater irregularity of flow around the rear wheelset. Additionally, for the bogie case displayed in Figure 6.4(b), a pronounced flow separation is generated at the front edge of the frame outer side surface, resulting in the unsteady flow developed further downstream on the frame and separated again at the frame end.

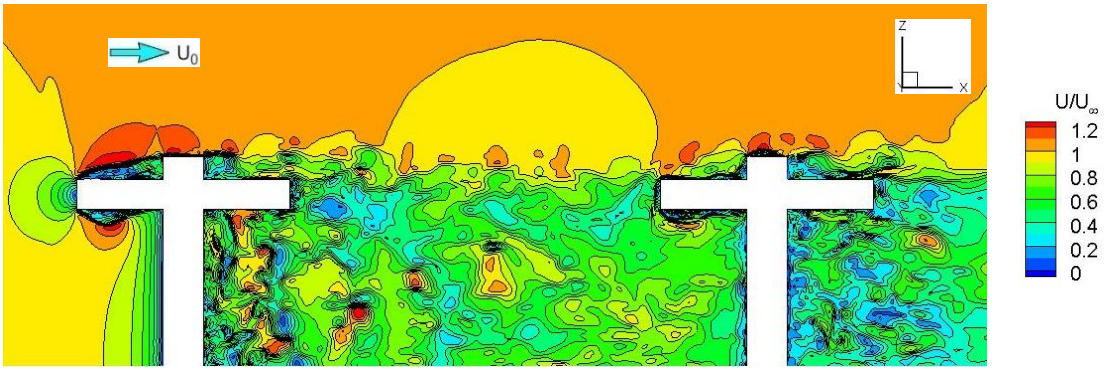

(a) Tandem wheelsets

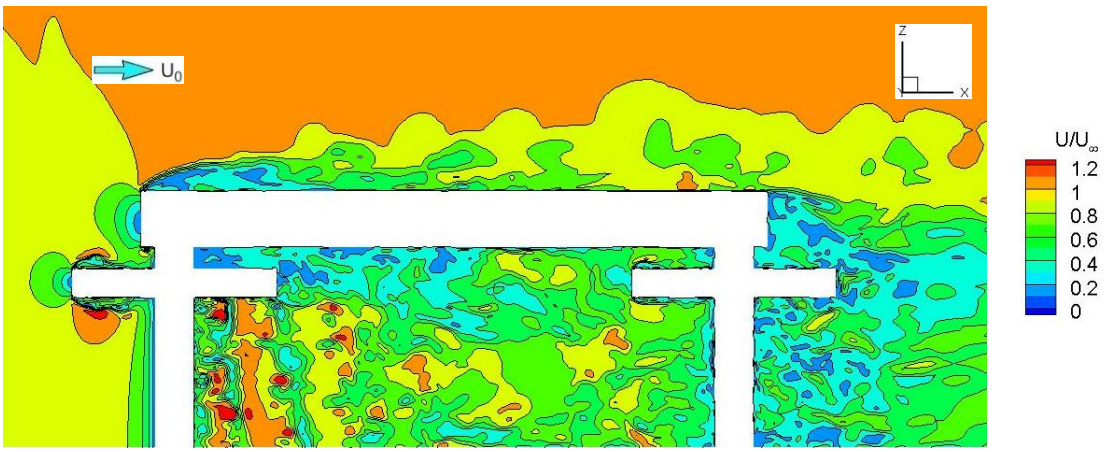

(b) Simplified bogie

Figure 6.4: Contours of instantaneous velocity magnitude in horizontal plane through centre of wheelset (bottom views)

Figure 6.5 shows the corresponding velocity field at the axle vertical mid-plane. For both tandem wheelsets and bogie cases, it is noted that the large scale

shedding is generated in the upstream axle wake whereas the flow structure behind the downstream axle is less organized and becomes highly turbulent.

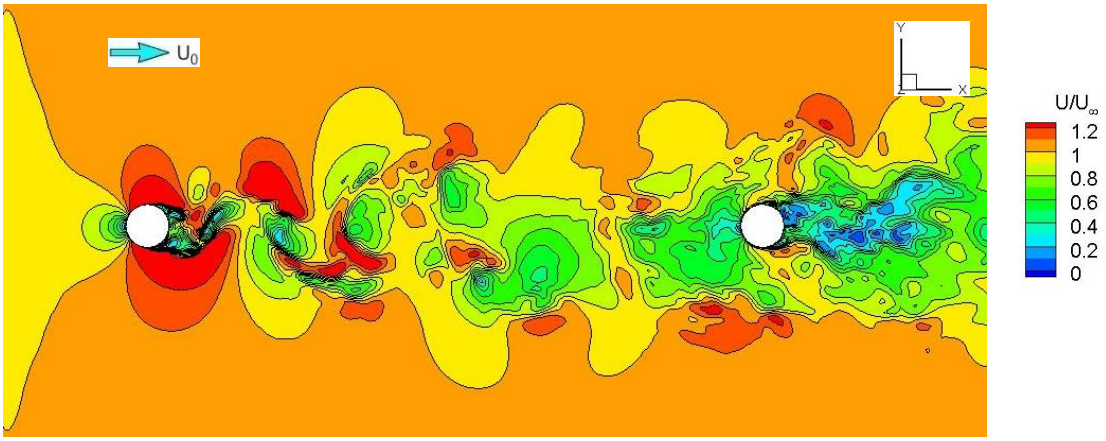

(a) Tandem wheelsets

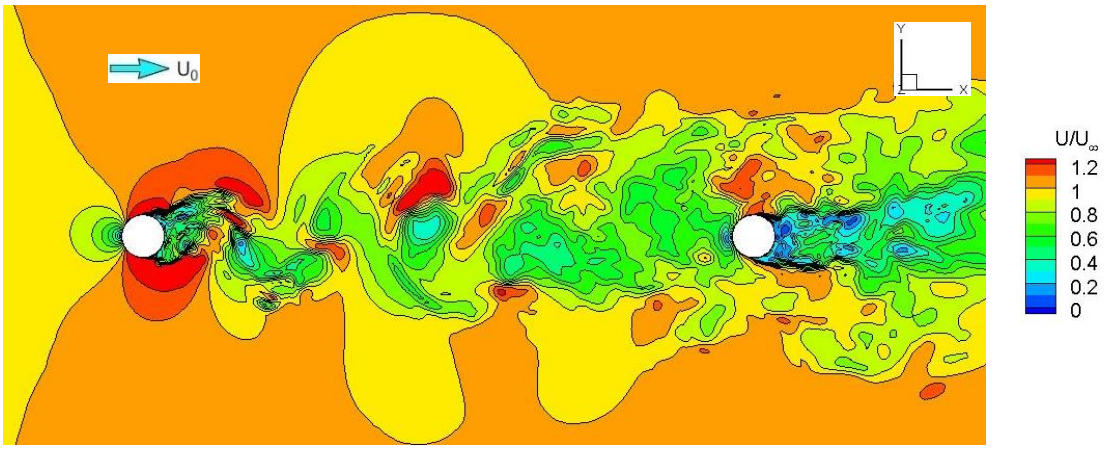

(b) Simplified bogie

Figure 6.5: Contours of instantaneous velocity magnitude in vertical plane through axle mid-span (side views)

Figure 6.6 visualizes the wake structure of the tandem wheelsets represented by the iso-surfaces of the normalized Q criterion at the value of 50 (based on $Q/[(U_0/D)^2]$, where D is the wheel diameter). They are coloured by the velocity magnitude. This shows that the vortices are shed from the upstream wheelset, impinge on the downstream wheelset, deform largely and are merged into the eddies formed behind the rear wheelset, making the wake of the downstream wheelset highly turbulent. Moreover, on the flat side surface of the front wheel, the crescent-shaped separation bubble and the subsequent horseshoe-shaped eddies as described previously for the isolated wheelset case can be seen in

Figure 6.6(b). However, the eddy structures on the rear wheel surface are not well organized: the crescent-shaped separation bubble regions from the primary separation along the wheel front rim edge are distorted severely by the incident vortices, and the horseshoe-shaped eddies are dissipated rapidly downstream.

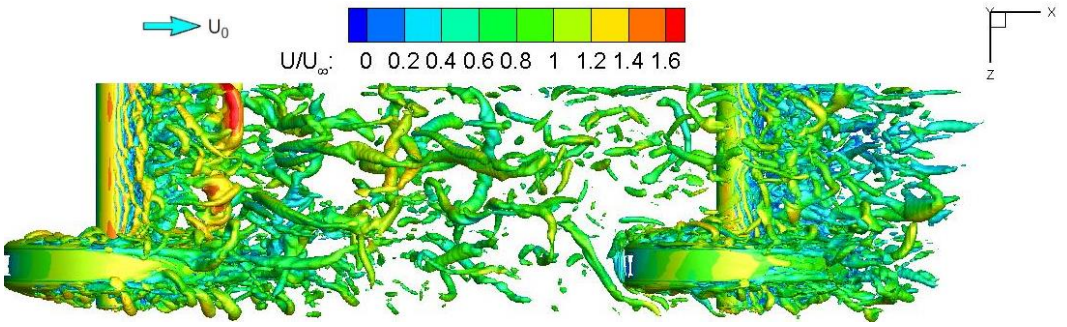

(a) Top view

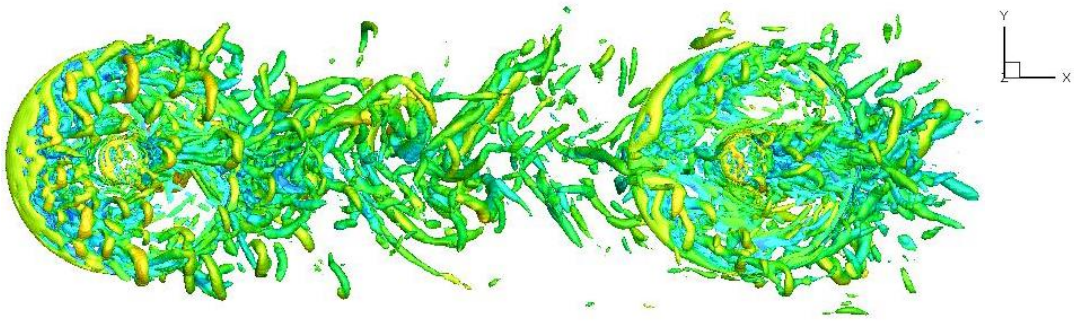

(b) Side view

Figure 6.6: Iso-surfaces of the instantaneous normalized Q criterion (tandem wheelsets)

Figure 6.7 displays the bogie wake structure represented by the iso-surfaces of the normalized Q criterion at the value of 50 (based on $Q/[(U_0/D)^2]$, where D is the wheel diameter). They are coloured by the velocity magnitude. Figure 6.7(a) shows that the various scales of vortices are formed near the wheel-frame junction regions as the geometry components are relatively more concentrated there. Another characteristic worthwhile noting is that the streamwise 'rib' vortices developed behind the upstream axle inside the wheels are evidently seen and distributed obliquely along the streamwise direction since the turbulent flow develops more rapidly close to the mid-span axle region due to much less blockage far away from the wheel-frame junction area within the bogie.

Based on Figure 6.7(b), it can be noticed that along the front sharp edges of the upstream wheel, a crescent-like separation bubble is formed and has a much narrower distribution compared with the tandem-wheelset case (shown in Figure 6.6b). The horseshoe-shaped eddies are located semi-circularly along the axle on the upstream wheel front surface, dissipating and mixing with the eddies generated from the wheel tread surface. The reason for the different vortex distribution along the wheel surface of the bogie compared with the isolated and tandem-wheelset cases is that the presence of the frame changes the flow behaviour around the wheelset. Moreover, after the flow is separated at the front edge of the frame, the vortices interfere with the upstream wheelset wake mainly along the front half part of the frame and then dissipate rapidly downstream.

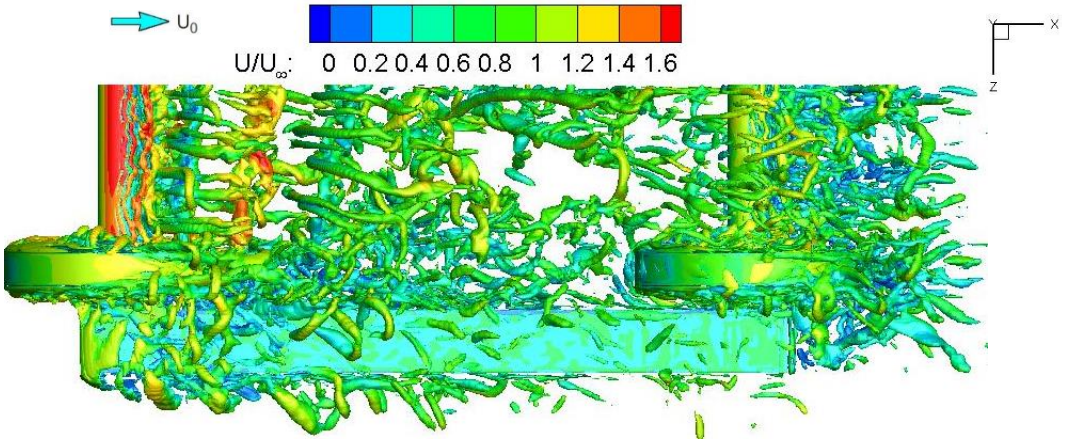

(a) Top view

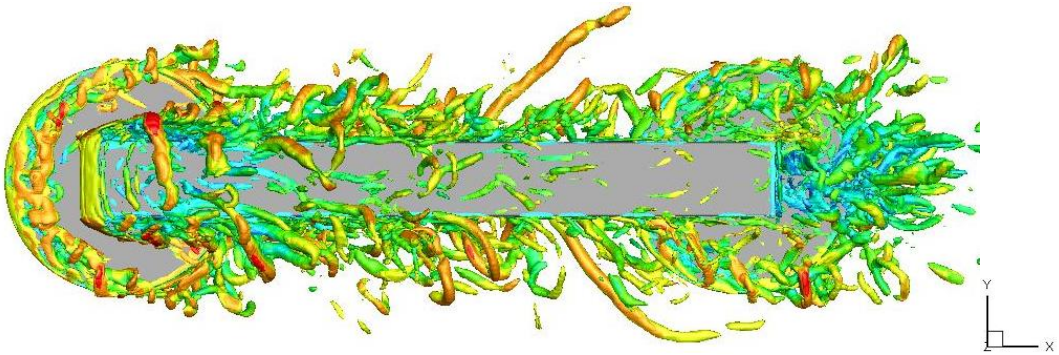

(b) Side view

Figure 6.7: Iso-surfaces of the instantaneous normalized Q criterion (simplified bogie)

For the current case, the front and rear axles are separated by the distance of 14 times the axle diameter. Within this large separation length, the downstream axle is well outside the recirculation region of the upstream axle wake and the

turbulent flow convected from the upstream axle changes the shedding characteristics of vortices generated from the downstream axle. This is shown in Figure 6.8(a) where the wake structures behind the two axles are illustrated by the contours of the instantaneous non-dimensional spanwise vorticity fields ($\omega_z = (\partial V/\partial x - \partial U/\partial y)D/U_\infty$, where D is the wheel diameter) in axle mid-span. As the downstream axle is sufficiently far away from the upstream one, the vortex shedding may be generated from both axles as a co-shedding flow pattern as stated in Section 6.1. It is shown that the downstream axle experiences the periodic impingement of vortices shed from the upstream axle; consequently, the flow around the downstream axle becomes highly unsteady. The incident vortices are greatly deformed as they are swept over the downstream axle; thereby, all vortices are mixed up behind the rear axle, leading to the synchronized behaviour of the downstream axle wake. Additionally, in this axle mid-span, the flow separation around the rear axle ($\theta = 88.2^0$) occurs later than for the front axle ($\theta = 82.1^0$) as the boundary layer developed around the downstream axle becomes turbulent due to the incoming flow interactions. The separation angle θ is defined here in the clockwise direction with zero at the axle front stagnation point.

In comparison with the flow developed behind the axles, the flow around the wheels shows different characteristics, as displayed in Figure 6.8(b) in terms of contours of the instantaneous spanwise vorticity fields (ω_z) in the wheel mid-span. This shows that the wakes behind both the upstream and downstream wheels are highly unsteady with lower turbulence levels since no large-scale coherent vortex shedding occurs there. Compared to the axle, the wheel has a very small aspect ratio (the ratio of geometry spanwise length to its diameter) with sharp rim edges. Thus, the wake behind the upstream wheel is different from that near the upstream axle. The flow separates from the upstream wheel front edges and interferes with the flow separations generated on the wheel tread. Therefore, the coherent vortex shedding cannot be formed behind the front wheel and the wake developed there becomes fully three-dimensional. The separation length between the front and rear wheels is about three times the wheel diameter, leading to the downstream wheel being under strong influence from the wake of

the upstream wheel. The incident vortices convected from the upstream geometries impinge on and interfere with the vortices separated from the downstream wheel, making the flow structure around the downstream wheel less organized but highly unsteady.

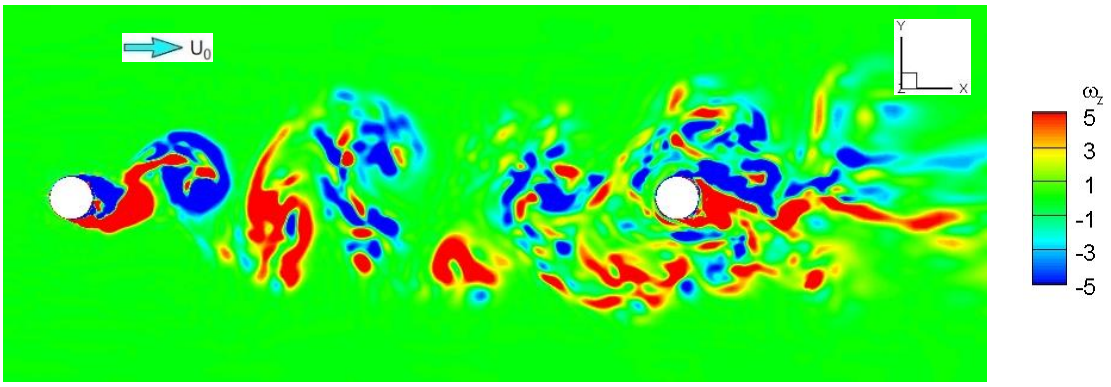

(a) Axle mid-span

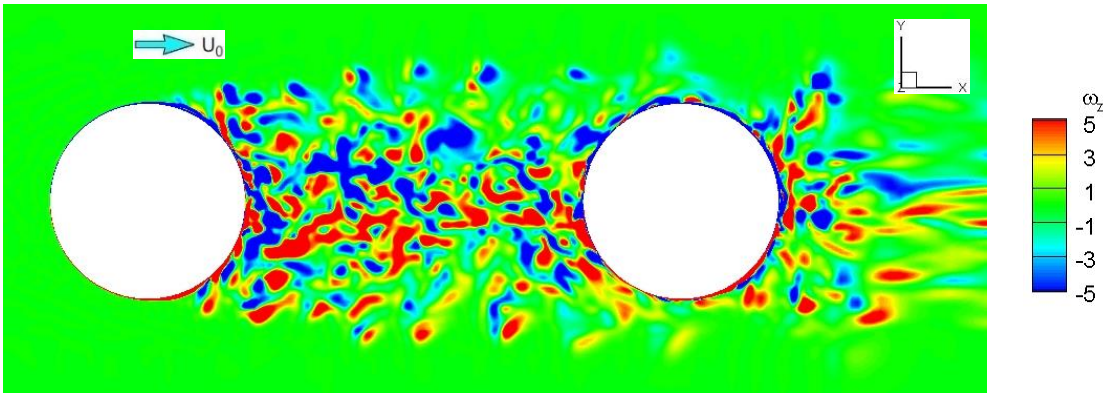

(b) Wheel mid-span

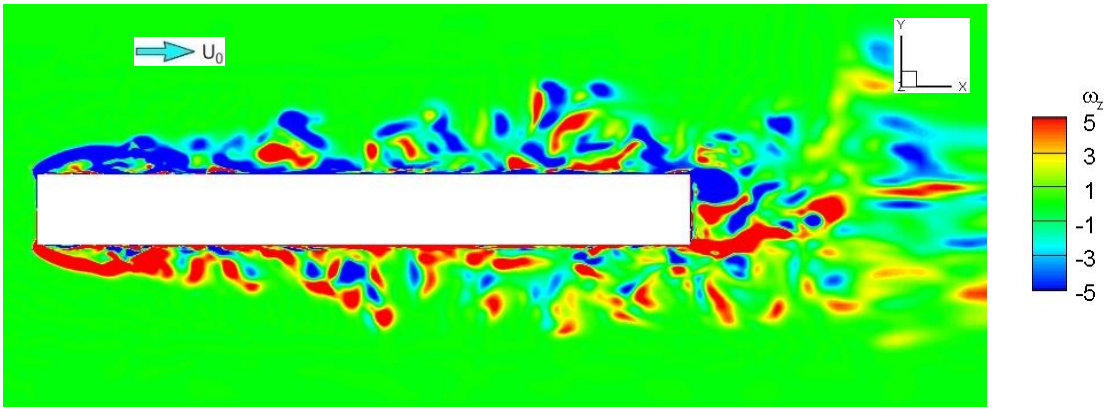

(c) Frame mid-span

Figure 6.8: Contours of the instantaneous spanwise vorticity fields in a vertical plane (side views)

The contour of the instantaneous spanwise vorticity fields (ω_z) along the frame mid-span is displayed in Figure 6.8(c). This shows that flow separation occurs at the front edge of the frame, interfering with the boundary layer developed on the frame top and bottom surfaces. The vortices generated and convected downstream along the frame are separated again at the frame trailing edge, resulting in a wake area with irregular shear flow.

The distinct characteristics of the wakes behind the axle and wheel can also be revealed by the flow unsteadiness. Figure 6.9 shows the power spectral densities of the gauge pressure at different positions in the wakes of the front and rear wheelsets: behind the axle and the wheel and at the inner wheel-axle corner. Considering a point with a distance of one axle radius from the top side of the front axle at the mid-span between the wheel inner side surface and bogie symmetry plane, a tonal peak appears in the spectrum at 324 Hz as seen in Figure 6.9(a). This frequency is associated with the vortex shedding from the front axle, and the corresponding Strouhal number (non-dimensionalized by the freestream velocity and the axle diameter) is 0.19, typical of vortex shedding from a cylinder. By contrast, the pressure signal at a similar position behind the rear axle is more broadband with no tonal peak and lower amplitudes. Figure 6.9(b) illustrates the spectra of the pressure at the point with a distance of one wheel radius away from the top of the front and rear wheels at wheel mid-span. The PSDs are broadband with no evident peak and their amplitudes are similar to each other, indicating that the flow behind the front and rear wheels is fully turbulent and the wake contains similar turbulence structures with various scales. Figure 6.9(c) shows the results of points located at 13 mm ($0.75d$) away from the wheel inner rim in line with the top of the axles. From the front wheelset inner wheel-axle corner, two peaks appear at the frequencies of 324 Hz and 641 Hz: the tonal peak (first harmonic) is related to the axle vortex shedding as mentioned in Section 5.3.2; and the second harmonic with twice the shedding frequency corresponds to the interaction between the periodic vortex shedding from the axle and the wheel inner surface, resulting in the surface fluctuations developed on the wheel surface downstream of the axle. The flow interactions mainly change the fluctuating drag from the wheelset and introduce a tonal peak at double the

shedding frequency. It is also noted that due to the influence of the turbulent wake interaction effects, the spectrum of the pressure signal at the point in the inner wheel-axle corner of the rear wheelset is more broadband and with much lower amplitude than that from the front wheelset.

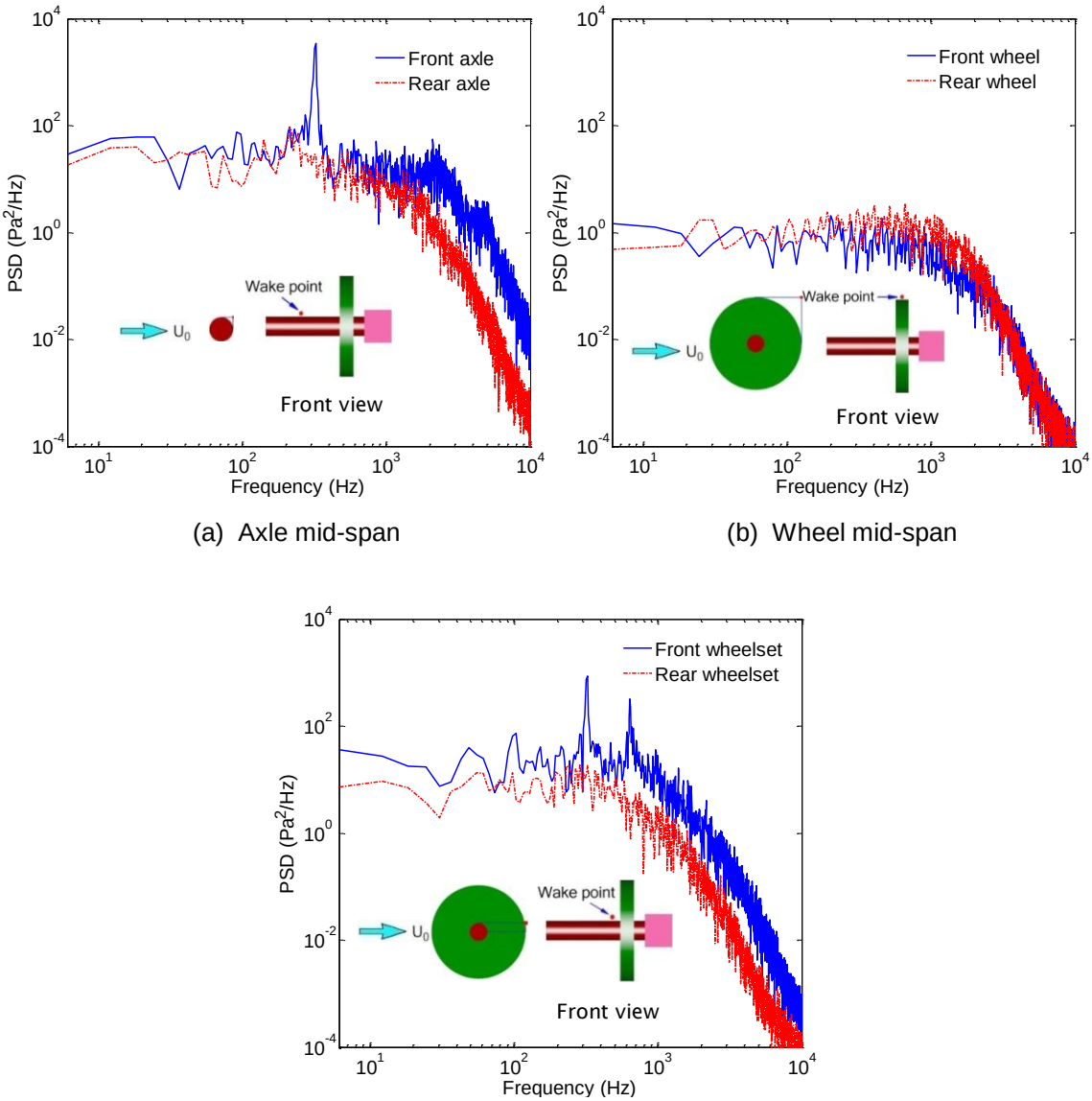

(a) Axle mid-span

(b) Wheel mid-span

(c) Inner wheel-axle corner

Figure 6.9: Power spectral densities of pressure at bogie wake positions

6.3.2 Lift and drag coefficients

All simulations were run for 0.1 s to allow the flow field to stabilize before collecting the time histories. These are expressed as lift and drag coefficients in which the forces are non-dimensionalized by $(\frac{1}{2}\rho_0 U_\infty^2 A)$, where A is the projected

frontal cross-section area of the bogie. The data are divided into three 50% overlapping segments. Mean and root-mean-square fluctuating lift and drag coefficients are calculated for each segment, which can be used to check the development of the flow and the convergence of the statistics collected. Table 6.1 summarizes the RMS and mean results from the three overlapping time windows. It is shown that the variations of the RMS values between each segment are very small (less than 4%) and the discrepancies in mean drag coefficient are less than 0.1% and in side force coefficient less than 4%. The mean lift coefficient is always less than 0.005 for each segment (not shown in the table). Therefore, this indicates that the transient flow field has become statistically steady and the source data collected can be used for far-field noise prediction. Note that the RMS lift coefficient is about six times larger than the RMS drag coefficient, suggesting that the oscillation of unsteady force is much higher in the direction normal to the axis than that along the flow direction.

		Segment1 (0.1-0.35s)	Segment2 (0.225-0.475s)	Segment3 (0.35-0.6s)	Total length (0.1-0.6s)
RMS value	Fluctuating lift	0.2289	0.2280	0.2243	0.2267
	Fluctuating drag	0.0390	0.0398	0.0398	0.0394
	Fluctuating side force	0.0781	0.0811	0.0809	0.0791
Mean value	Drag coefficient	1.4991	1.4978	1.4986	1.4989
	Side force coefficient	-0.2681	-0.2588	-0.2597	-0.2639

Table 6.1: Root-mean-square and mean values of aerodynamic force coefficients (simplified bogie)

The PSDs of the fluctuating lift coefficients of the symmetrical half bogie simulated and its components (frame, front and rear wheelsets) are presented in Figure 6.10. A tonal peak (Figure 6.10a) appears in the lift coefficient of the bogie at 324 Hz, giving a Strouhal number (non-dimensionalized by the freestream velocity and the axle diameter) of 0.19. As mentioned in the previous section, this peak is related to the vortex shedding around the axle of the upstream wheelset, which appears in the spectrum of the front wheelset shown in Figure 6.10(b). A

broad hump between 160 Hz and 390 Hz can be observed in the lift coefficient of the rear wheelset (Figure 6.10b), which may correspond to the mixture of the incident vortices convected inside the bogie with the eddies generated by the flow passing the rear wheelset. Moreover, the contribution to the oscillating lift force from the frame is much smaller (Figure 6.10a) compared with other components of the bogie.

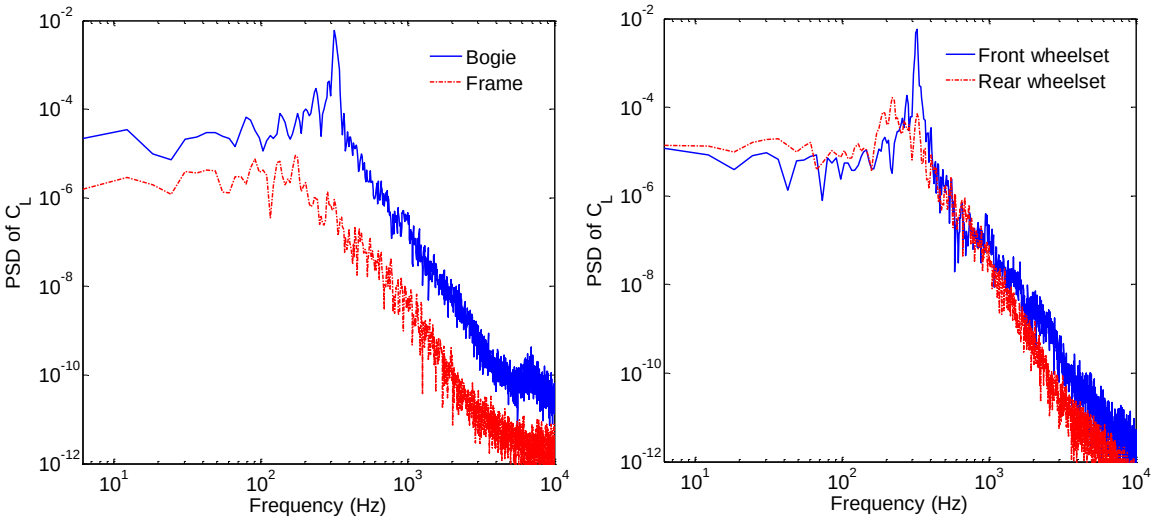

(a) Bogie and frame (b) Front and rear wheelsets

Figure 6.10: Power spectral densities of lift coefficients

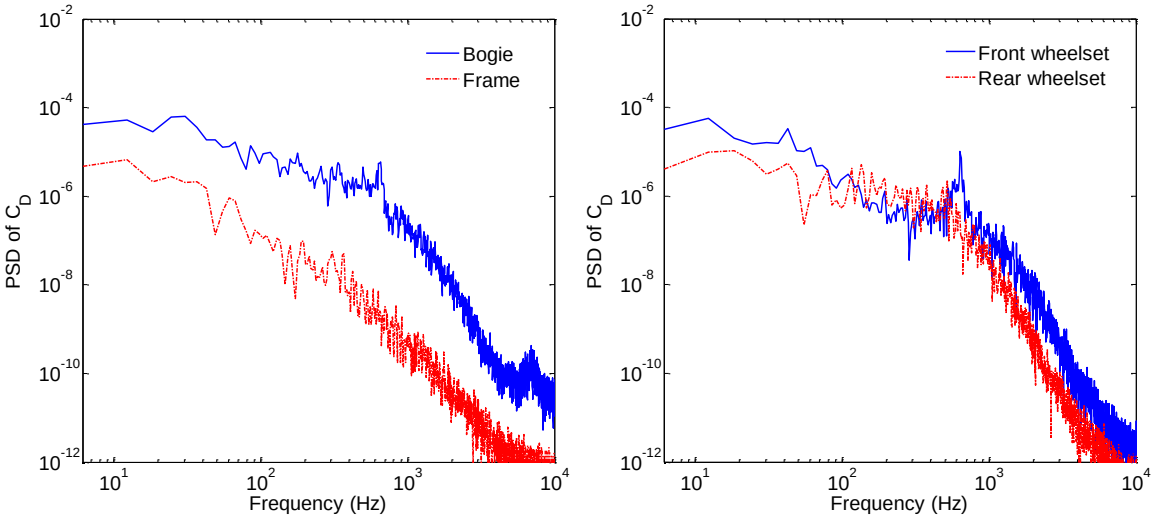

(a) Bogie and frame (b) Front and rear wheelsets

Figure 6.11: Power spectral densities of drag coefficients

Figure 6.11 shows the PSDs of the fluctuating drag coefficients of the symmetrical half bogie and its components. A peak appears in the drag coefficient of the bogie and the front wheelset at 641 Hz, which is twice the frequency of the tonal peak

in the lift coefficient while at a much lower amplitude. This peak corresponds to the fluctuating drag induced by the vortex shedding from the upstream axle. As for the isolated wheelset, the alternate periodic vortex shedding from the front axle interacts with the boundary layer developed on the wheel side surface and the unsteady flow separated from it; thus, the resulting wake induces a regular fluctuating drag around the front wheelset. It is noted that the spectra of the drag coefficient from the frame and the rear wheelset are broadband as there is no significant coherent vortex shedding developed around them. Compared with the front wheelset, the spectrum level of the rear wheelset is lower in most of the frequency range and the contribution to the fluctuating drag force from the bogie frame is comparatively small, about one order of magnitude smaller.

6.3.3 Wall pressure fluctuations

Figure 6.12 displays the wall fluctuating pressure level in decibels ($L_p = 10\log(\overline{p'^2}/p_{ref}^2)$, where $\overline{p'^2}$ is mean-square fluctuating pressure and p_{ref} is reference acoustic pressure $20\mu Pa$) on the bogie surface, which can be used to identify the potentially significant noise source regions. This shows that the surface pressure fluctuations are generally high in the rear half of the upstream axle due to vortex shedding and flow recirculation behind the front axle. As shown in Figure 6.12(a), high pressure fluctuations appear on the upstream wheel inner side surface behind the axle as the consequence of the flow interacting between the axle wake and the flat wheel side surface. Moreover, a crescent-shaped large pressure fluctuation region develops at the upstream half of the front wheel side surfaces owing to the flow separation generated from the wheel front sharp edges. All these high pressure fluctuations are the main contributors to the lift and drag dipoles developed from the front wheelset, as will be discussed in the next section. This also indicates that the massive vortex shedding generated from the front axle may potentially be a major contributor to the noise radiated from the bogie. Furthermore, the high pressure fluctuations can be seen around the downstream wheelset due to the flow impingement by the incoming vortex convected from the upstream geometry as well as the flow separation developed from the rear wheel front edges and the vortex shedding formed behind the rear axle. However, the distributions of the fluctuating pressure on the downstream wheelset are rather

irregular and mainly concentrated in the upstream area. Compared to the wheelsets, the pressure fluctuations on the frame surface are much sparser and also distributed mainly on the upstream half. Additionally, the wall pressure fluctuations on the outer surfaces (Figure 6.12b) of the wheel and frame have similar distribution properties to those on the inner surfaces of them as described above.

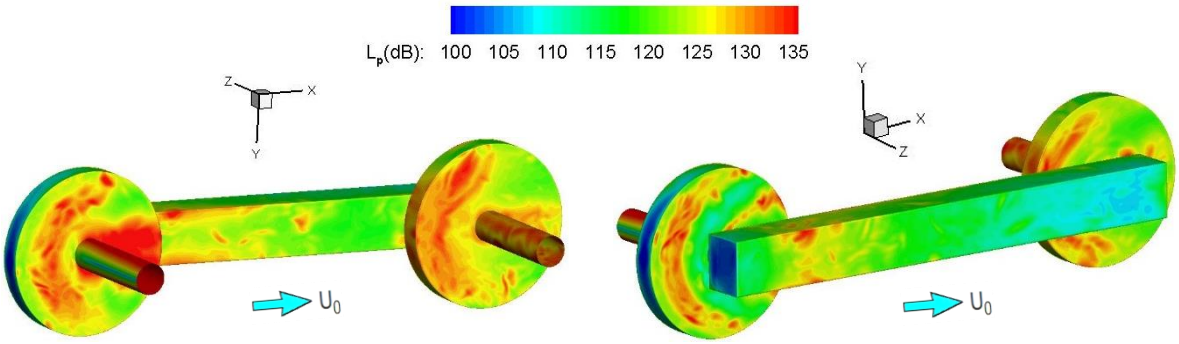

(a) Bogie inner surfaces (b) Bogie outer surfaces

Figure 6.12: Wall pressure fluctuation level of the simplified bogie

6.3.4 Divergence of Lamb vector

Figure 6.13 visualizes the divergence of the Lamb vector (defined in Section 2.2.4) to display the spatial distribution of the aeroacoustic volume sources produced from the tandem wheelsets and isolated bogie. It shows that for both cases, the predominant contributions of volume noise sources come from the massive flow separations generated from the front edges of the upstream wheels and the various shedding vortices developed within the front axle wake. Furthermore, the volume noise sources located along the downstream wheelset of the tandem wheelsets (shown in Figure 6.13a) develop more abundantly compared to those situated around the downstream wheelset of the bogie (shown in Figure 6.13b). This is due to the presence of the frame which makes the incoming flow to the downstream wheelset less energetic for the bogie case. It also indicates that the turbulent wake behavior has an effect on the wall surface pressure fluctuations. Some noise sources can be seen at the axle end surfaces of the tandem wheelsets and the frame front corners of the bogie owing to the flow separations occurring there. However, such flow separations are relatively weak in

comparison with the flow unsteadiness developed around the front and rear wheelets.

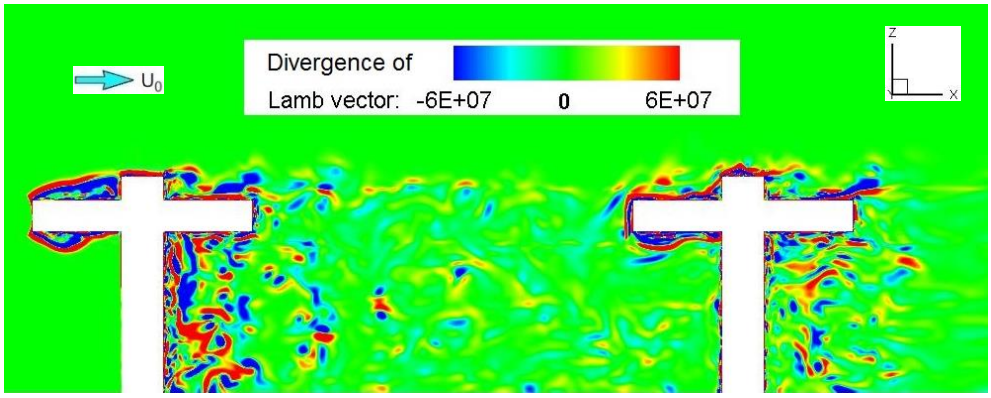

(a) Tandem wheelsets

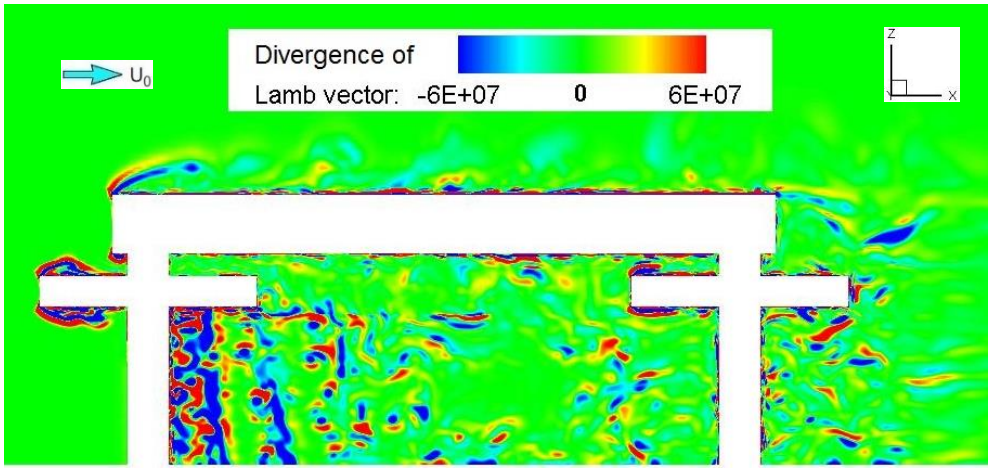

(b) Simplified bogie

Figure 6.13: Visualization of the divergence of the Lamb vector in horizontal plane through centre of wheelset (bottom views)

6.4 Aeroacoustic Results

The source data are collected for far-field noise prediction only when the transient flow field has become statistically steady, as discussed in Section 4.5. Based on the near-field unsteady flow data obtained from the CFD calculations, the far-field noise signals can be predicted by the FW-H method using equivalent acoustic sources. There are 104,928 panels (surface elements) around the bogie which account for the acoustic sources on the solid surfaces and 74,496 noise source panels for the tandem-wheelset case. As in Chapter 5, the receivers are distributed uniformly along a circumference with 2.5 m radius at an interval of 5º

as sketched in Figure 6.14 to measure the two-dimensional noise directivity through the upstream and downstream wheelset centreline respectively along the vertical *z-y* plane. A similar circular-shaped grid of receiver positions is defined along the horizontal *x-z* plane (see Figure 6.1). Note that the sound waves generated from the axles of the two cases here would be shielded by the wheel or frame for the side receivers close to the tandem-wheelset or bogie horizontal central plane, which cannot be accounted for by an incompressible flow solver. Nevertheless, similar to the isolated wheelset case discussed in Section 5.5.3, the influence of the noise shielding by the wheel or frame would be expected to be rather small, especially for the current cases with low Mach numbers.

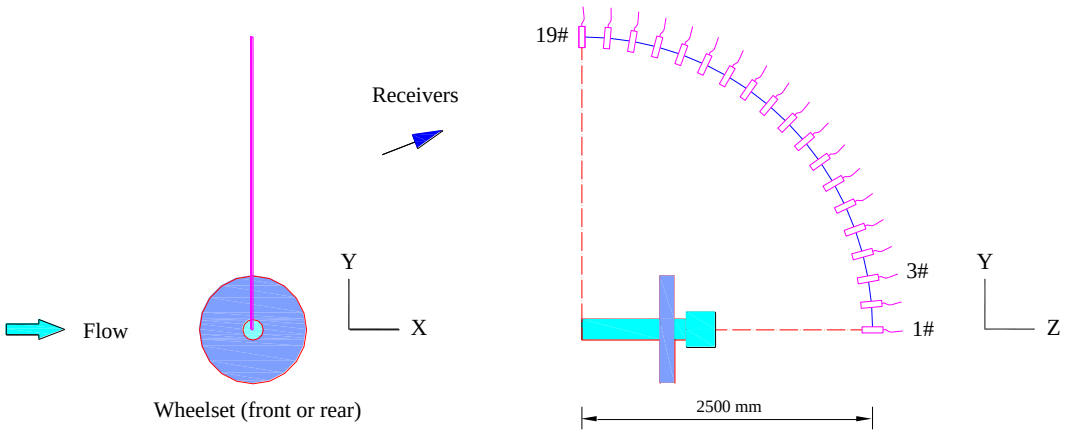

Figure 6.14: Sketch of receiver locations in the *z-y* plane

6.4.1 Acoustic spectra computation

The CFD simulations were run for 1.2 s corresponding to 21 times the flow-through time (L_x/U_∞, where L_x is the computational domain length). The length of the time signal used as input to the FW-H method for noise calculation is related to the last 0.56 s of the computation. As previously, the PSD is computed from the predicted far-field noise time-history by Welch's method and averaged over 50% overlapping segments using a Hanning window applied to 5 segments, giving a frequency resolution of 6 Hz.

Figure 6.15 shows the spectra of the noise radiated from the front and rear bogies (i.e. the front and rear half parts of the half bogie symmetrical along the axle mid-span) at three receivers in the *z-y* plane as described in Figure 6.14. The spectra

at receiver 3, which is located 0.434 m above the axle axis, are plotted in Figure 6.15 (a). It can be seen that two tonal peaks appear at the frequencies of 324 Hz and 652 Hz since both lift and drag dipole components influence the radiated sound at this receiver, especially from the front bogie. The primary peak corresponds to the dominant peak in the oscillating lift forces related to the vortex shedding from the axle as seen in Figure 6.10. The peak at the second harmonic is associated with the dominant peak in the oscillating drag forces (see Figure 6.11). As stated in Section 5.3.3, the frequency of the fluctuating drag is twice that of the fluctuating lift. Additionally, the highest peak corresponding to the oscillation lift dipole component appears at receiver 19 as it is located right above the bogie, as shown in Figure 6.15(b), while the largest drag dipole component occurs at receiver 1 (Figure 6.15c) which is in the lateral direction. Compared with the front part of the bogie, the noise radiated from the rear part of the bogie is more broadband, resulting from the irregular and unsteady flow passing over it. In a turbulent inflow condition, the tonal peak related to the periodic vortex shedding generated around the downstream axle still can be observed on receivers 3 and 19; however, its amplitude is much lower compared to that of the upstream axle since the turbulent flow convected from the front axle becomes dissipated as indicated from Figure 6.7 and the incoming flow speed around the rear axle is decreased to about 18 m/s of the mean velocity compared to the inflow velocity of 30 m/s.

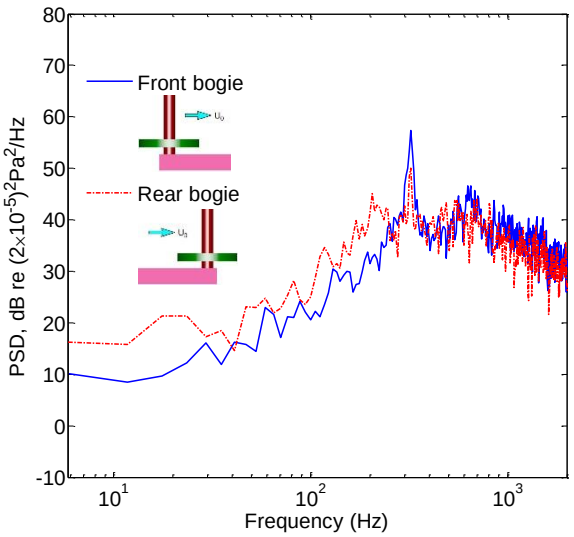

(a) Receiver 3

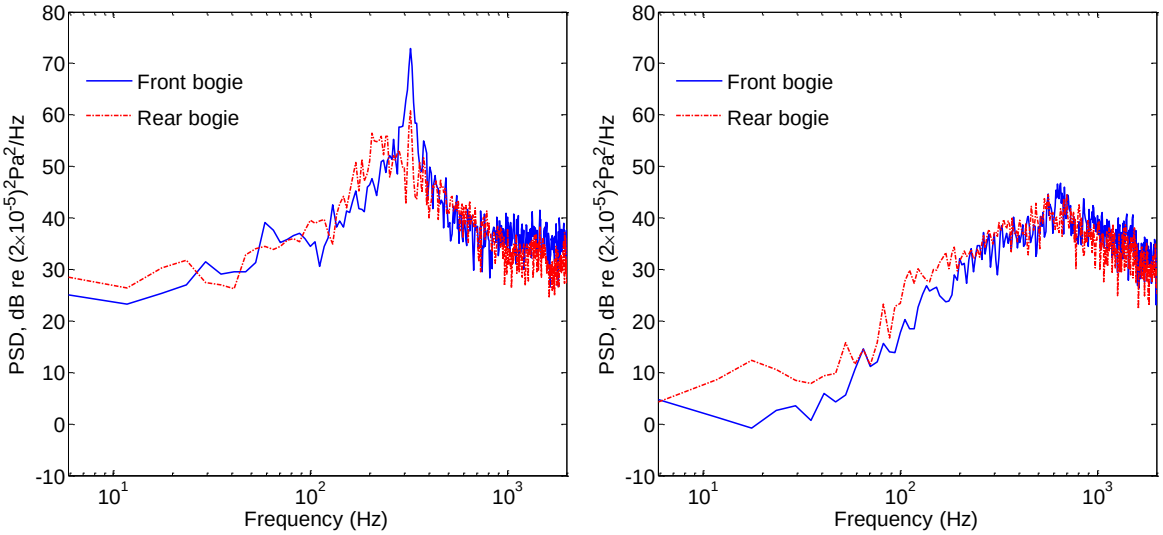

(b) Receiver 19 (c) Receiver 1

Figure 6.15: Spectra of acoustic pressure on far-field receivers (U_∞=30 m/s)

6.4.2 Experimental verification

Experimental measurements of sound generated by flow past the tandem wheelsets and simplified bogie were carried out in an open-jet anechoic wind tunnel. Measurements were taken for the same geometries as used in the numerical simulations. A model consisting of two half wheelsets connected by a bogie frame was attached to a baffle plate. The bogie was immersed within the core flow and the remaining parts in connection with the baffle plate were wrapped with foam to suppress the aerodynamic noise generated due to flow interaction with these regions. The experimental setup for the tandem-wheelset case is displayed in Figure 6.16(a) and for the bogie case in Figure 6.16(b), where the test model is mounted in the working section on the rigid baffle. The same instruments of signal analyser and microphone array were used for both cases. Identical to the isolated wheelset case (see Section 5.5.2), the flow speed was 30 m/s with the turbulence level in the jet core below 0.3%. The measurement was made with a sampling rate of 48 kHz and contained a time signal of length 10 s. Corresponding to the frequency resolution used in the simulation, the PSD of the experimental data was also computed by Welch's method with 6 Hz bandwidth. In accordance with the numerical predictions, the receiver identified as 'top microphone' in Figure 6.16(b) was located at (-18, 1375, 31.3) of which

the dimensions were in millimetres and the coordinates (see Figure 6.2) were defined with the origin at the centre of upstream axle outer end surface.

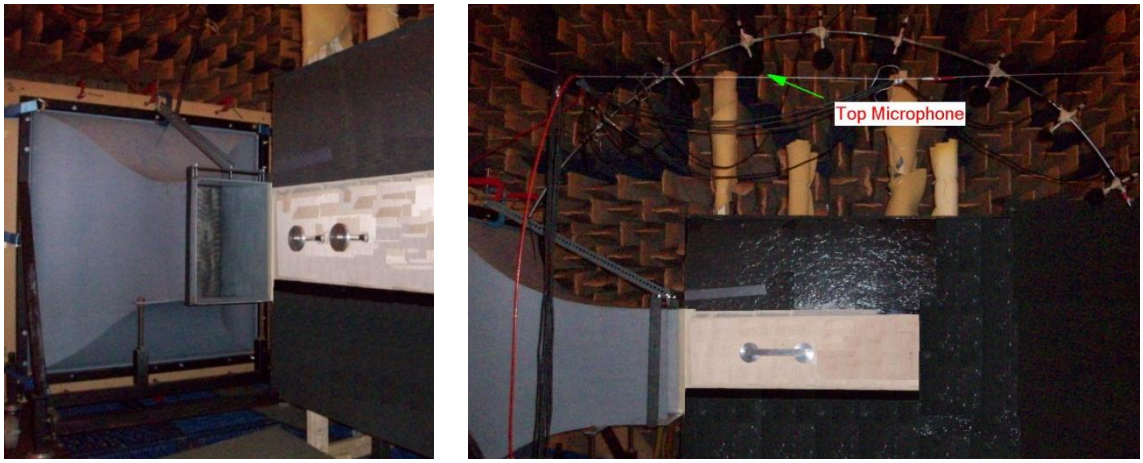

(a) Tandem wheelsets (b) Simplified bogie

Figure 6.16: Experimental setup in the anechoic chamber

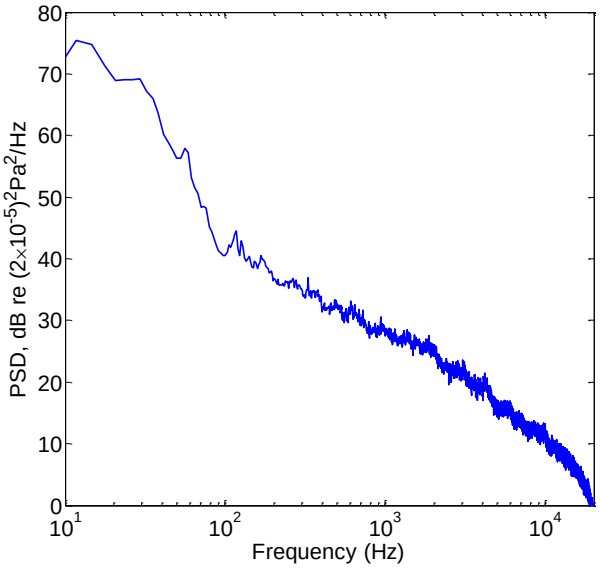

Figure 6.17: Background noise for a mean stream flow speed of 30 m/s (top receiver)

Figure 6.17 displays the spectra of background noise in the anechoic chamber for a mean stream flow speed of 30 m/s. Same as the wheelset case (see Section 5.5.2), the experimental results are only considered above 100 Hz due to the low-frequency background noise generated in the anechoic wind-tunnel.

Figure 6.18 displays the spectra of the radiated noise at the top microphone receiver (shown in Figure 6.16b) for the tandem wheelsets and bogie cases.

Figure 6.18(a) compares the PSD level of the tandem-wheelset case between the noise prediction and experimental measurement. Very good agreement is achieved for the dominant frequency of the tonal noise and the shape of spectra. Even a small peak around 940 Hz (third harmonic) is properly captured in the computation (as also seen for the isolated wheelset).

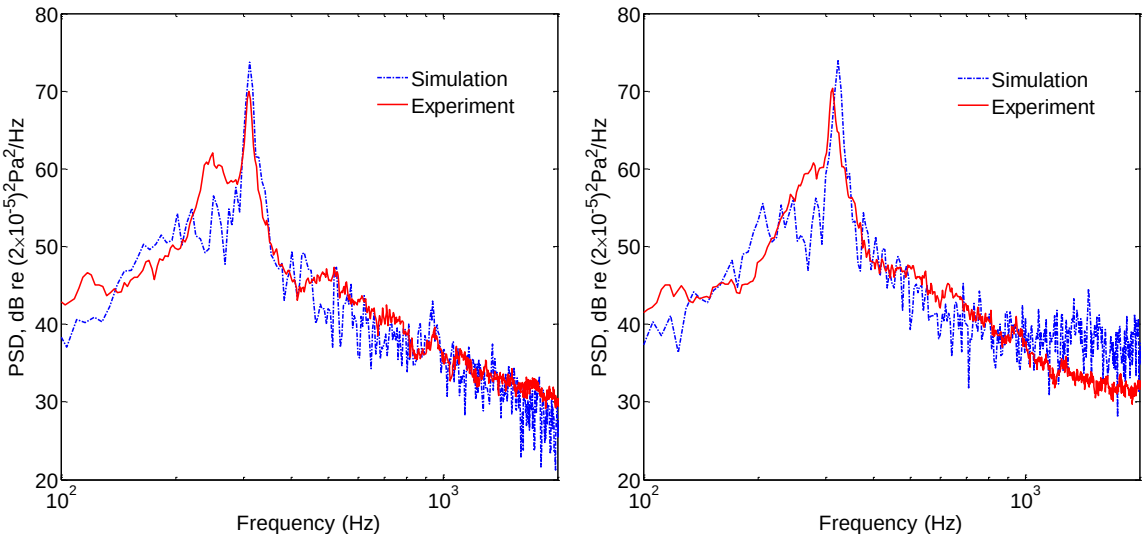

(a) Tandem wheelsets (b) Simplified bogie

Figure 6.18: Comparisons of far-field noise spectra between simulation and experiment

Figure 6.18(b) shows that the PSD of the far-field noise radiation generated from the bogie in the numerical simulation also compares well with the experimental measurements for this case. The dominant frequency of the tonal noise from the experiment (314 Hz) is slightly lower (around 3%) than the prediction (324 Hz). This is likely due to that the bogie has a relatively long configuration longitudinally and may not be situated completely inside the core region of the open-jet flow. Compared with the bogie case, the blockage effect of the open-jet wind tunnel is smaller for tandem wheelsets without frame. It is noted that a broadened hump appears around 250 Hz for the tandem-wheelset case and 280 Hz for the bogie case in the measurements; however, no such humps are observed in the simulations of both cases. As discussed in Section 5.5.2, these broad peaks may correspond to the noise contribution from the interaction between the (front or rear) axle wake and the baffle plate, i.e. the vortex shedding generated from the axle at the axle-baffle junction area is decayed by the unsteady flow developed on the rigid plate and thereby the corresponding shedding frequency is decreased.

This same phenomenon has been found in the experiments of flow-induced noise from wall-mounted cylinders [108]. Note that compared to the spectrum from the bogie, the low frequency broadened hump is larger from that of the tandem wheelsets, which is due to the stronger interaction between the vortex shedding and the baffle plate boundary layer produced around the axle-plate junction areas of the tandem wheelsets. As this broad peak amplitude is about 8 dB lower than the tonal peak level, accordingly, its contributions to the overall sound pressure level are not significant. Moreover, compared with the experimental data, the tonal peak has a higher amplitude from the calculations in both cases. This may be influenced by the solid wall (rigid baffle) used in the experiment which weakens the coherent vortex shedding from the axle while the symmetric boundary conditions with stronger spanwise uniformity are applied in the simulation. The OASPL in the frequency range between 100 Hz and 2 kHz is calculated for the experimental measurements and it is slightly higher (0.7 dB) in the bogie case than the tandem-wheelset case, indicating that the noise contribution from the frame of the bogie is small.

6.4.3 Acoustic directivity

The directivity of the noise radiated to far-field is calculated based on the OASPL determined from the PSD in the frequency range below 2 kHz. Some numerical artefacts of the far-field noise simulation appear above 2.5 kHz due to grid resolutions and are not included in calculating the OASPL as this is in excess of the main energy-containing frequency range. This can be confirmed from the experimental results (see Figure 6.18) in which the noise level is much lower and drops remarkably for frequencies above 2 kHz. Figure 6.19 displays the noise directivities from the front and rear wheelsets in the vertical *z-y* plane. It can be seen that the noise level from the front or rear wheelset of the tandem wheelsets and bogie are very similar except at the horizontal plane through the axle centreline (α=0º or 180º) where the presence of the frame leads to the differences between them (3 dB for front wheelset and 0.8 dB for rear wheelset). Compared with the front wheelset, the noise radiated from the rear wheelset is reduced by up to 9 dB except near α=0º or 180º. This is because the turbulent flow convected from the front wheelset is dissipated while the trailing wheelset is subject to a

smaller mean incident flow velocity of about 16 m/s. Moreover, the incident vortices impinge upon and interact with the vortices separated from the downstream wheelset, and thus the sound generated from periodic shedding at the rear wheelset may be lost and replaced by a broadened spectrum with a lower level. Nevertheless, at the axle centreline along the lateral side (α=0º or 180º), the flow separation is stronger from the downstream wheelset than from the upstream wheelset, leading to the noise level there being about 3 dB higher for tandem-wheelset case and slightly larger for bogie case.

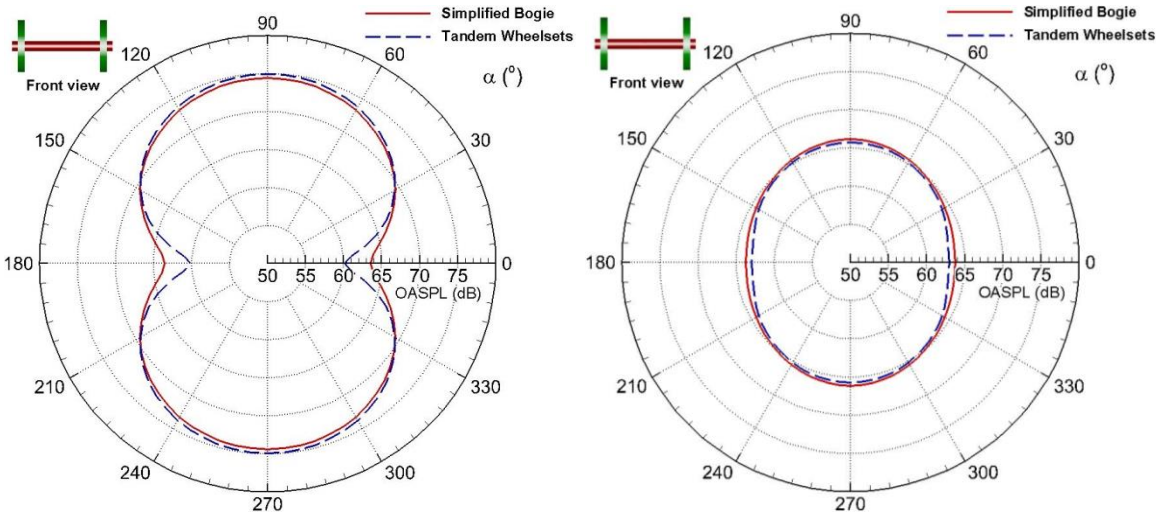

(a) Front wheelset (b) Rear wheelset

Figure 6.19: Noise directivity of front and rear wheelsets in vertical *z-y* plane

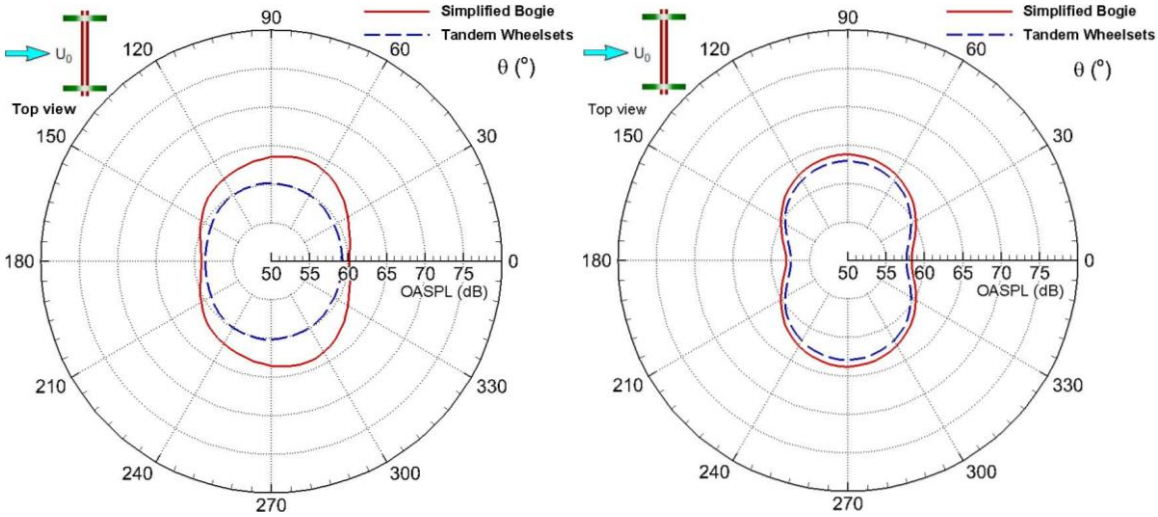

(a) Front wheelset (b) Rear wheelset

Figure 6.20: Noise directivity of front and rear wheelsets in horizontal *x-z* plane

The directivities of noise radiated from the front and rear wheelsets in the horizontal *x*-*z* plane along the flow direction are illustrated in Figure 6.20. Since the frame of the bogie changes the flow behaviour around the wheelset, the noise generated from the front wheelset of the bogie is up to 4 dB higher than that from the tandem wheelsets while for the rear wheelset the corresponding difference is about 1 dB.

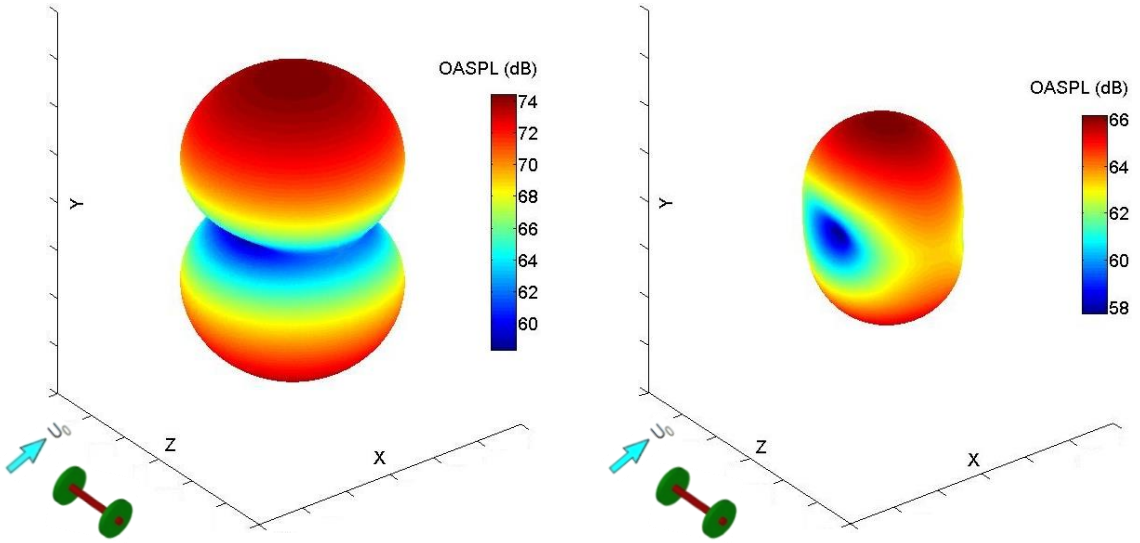

(a) Front wheelset (b) Rear wheelset

Figure 6.21: Three-dimensional noise directivity for front and rear wheelsets of simplified bogie (centre of directivity pattern corresponds to 50 dB)

The three-dimensional directivities of noise calculated from the surface source on the front and rear wheelsets of the whole bogie are shown in Figures 6.21(a) and 6.21(b) respectively. Again, it is noted that a distinct dipole pattern of directivity perpendicular to both the freestream direction and the wheelset axis is predicted for the sound radiation from the upstream wheelset (Figure 6.21a), indicating that the lift dipole is a dominant noise source (see also Figure 5.30 for the isolated wheelset). By comparison, the directivity pattern of the downstream wheelset (Figure 6.21b) is omni-directional with more uniform magnitude in each direction, resulting from the contributions from the lift and drag dipoles which are aligned perpendicular to each other. This is because the flow separated from the axle of the front wheelset is dominated by the periodic vortex shedding, whereas the rear wheelset is submerged in the upstream wheelset wake and situated in a turbulent condition as shown in Figure 6.7, and thus the irregular flow feature makes the

noise radiation more broadband and multi-directional. Additionally, it also shows that the amplitude of the noise radiated by the rear wheelset is much smaller compared to that from the front wheelset, as discussed above.

Figure 6.22 displays the same results, the noise directivities from the front and rear half parts (divided by the frame transverse mid-plane) of the whole bogie in the vertical *z-y* plane. In addition, their components are shown. It can be seen that the noise radiated from the rear half-bogie is smaller (up to 7.3 dB) than from the front half-bogie. This is because the upstream geometries are in the freestream conditions and the surrounding flow is characterized by large-scale regular vortex shedding; however, the approaching flow around the downstream geometries is highly turbulent but less energetic. Note that the noise is 0.7 dB higher from the downstream half-bogie at α=0º or 180º along the bogie lateral side, which is due to a slightly stronger flow separation generated from these regions. Moreover, the noise levels for the front half-bogie and front wheelset are very close and the difference in noise level between the rear half-bogie and rear wheelset is around 1 dB. In contrast the noise from the frame is much smaller. This again suggests that for the simplified bogie case, the main noise contributions come from the wheelsets. The noise radiated from the rear frame is 2.5-4.5 dB larger than from the front frame because of the stronger vortex shedding and flow separation occurring at the frame ends, but is still at least 5 dB lower than the noise from the corresponding wheelset.

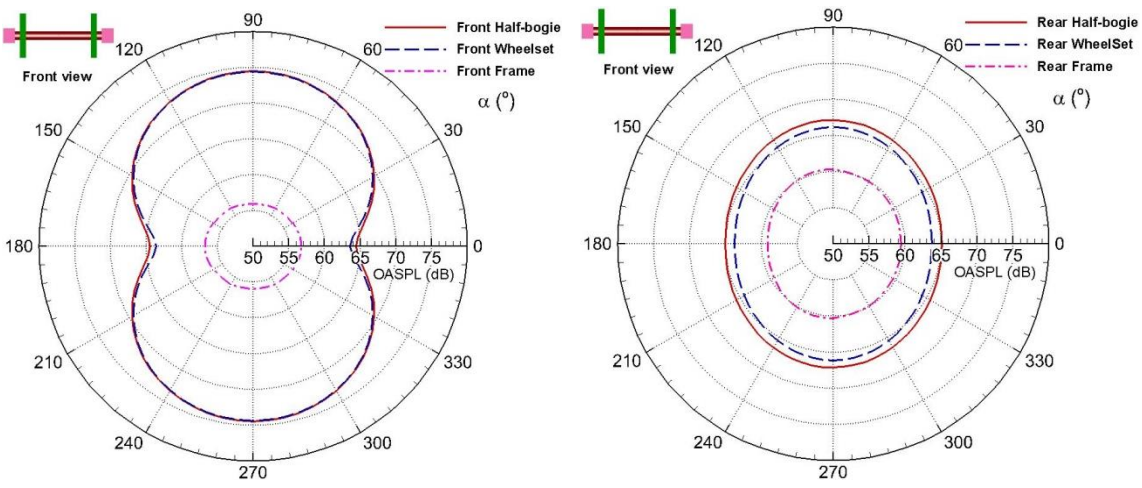

(a) Front half-bogie (b) Rear half-bogie

Figure 6.22: Noise directivity of front and rear half-bogies in vertical *z-y* plane

Figure 6.23 depicts the three-dimensional directivity pattern (starting at 50 dB) of noise radiated from the whole bogie. The noise directivity from the bogie in the vertical *x-y* plane is compared with that from the tandem wheelsets in Figure 6.24. It can be seen that for both cases, the directivity pattern exhibits a dipole with an evident radiation bias upwards to the inflow direction and almost symmetrical fore and aft along the horizontal *x-z* central plane. Note that the similar directivity pattern of sound radiation occurs from the two cases with the slight difference of noise levels between them, which also demonstrates that the wheelsets are the dominant noise sources of the bogie and the noise contribution from the bogie frame is relatively small.

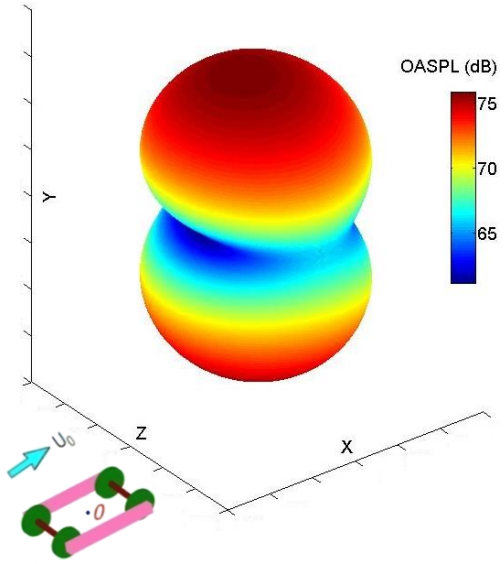

Figure 6.23: Three-dimensional noise directivity for bogie (starting at 50 dB)

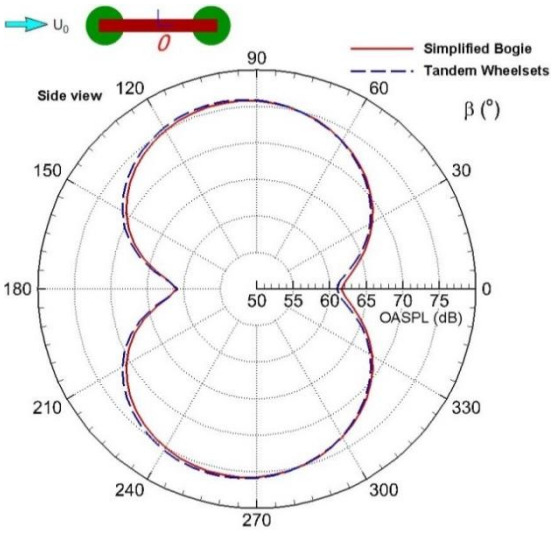

Figure 6.24: Noise directivity of whole geometry in vertical *x-y* plane

6.5 Summary

The flow behaviour and the aerodynamic noise characteristics developed from tandem wheelsets and a simplified bogie have been studied using the DDES model and the FW-H acoustic analogy method. It is found that both streamwise and spanwise vortices are generated due to flow separation and vortex shedding around the tandem wheelsets and the bogie. The primary behaviour of the flow past the two geometies is that the vortices shed from the upstream geometries

are convected downstream and impinge on the downstream ones, leading to a highly turbulent wake behind the downstream bodies. For both bogie and tandem-wheelset cases, good agreements are achieved between the numerical predictions and experimental measurements in terms of the tonal peak characteristics and spectra shapes. Tonal noise is generated with dominant frequencies corresponding to the lift dipole due to the vortex shedding around the axles. Furthermore, a vertical dipole pattern of noise radiation is predicted for the upstream wheelset, whereas the downstream wheelset has a multi-directional directivity pattern due to a combination of lift and drag dipoles and its sound generation is relatively weaker. Expressed relative to the geometry centre, the noise directivity has a biased dipole pattern towards the upstream direction as a consequence of large-scale regular vortex shedding produced from the upstream geometries whereas the downstream bodies are submerged in the decayed and less energetic turbulent incoming flow. Compared to the wheelsets, the frame of the bogie is a minor noise source. Note that for the real case, the bogie is situated inside the bogie cavity and the inflow passing over it is turbulent, and thus the fluctuating lift amplitudes and the corresponding tonal noise levels will be changed. This will be discussed in the next chapter.

Chapter 7

Simplified Bogie inside Bogie Cavity

The isolated bogie case studied in the previous chapter focuses on the behavior of flow and noise produced from the bogie structure alone. In reality, the bogie is situated in the bogie cavity. The flow underneath the vehicle carboby will interact with the flow developed around the bogie areas. This chapter investigates the flow behaviour and noise radiation characteristics for a simplified bogie situated inside the bogie cavity beneath the train and the differences from using a fairing for the bogie cavity are compared. For the bogie-inside-cavity case with the ground underneath, the influence of a moving ground plane and the rotation of the wheelsets is discussed. The emphasis will be put on the flow interactions between the bogie and the bogie cavity, and then the corresponding characteristics of the noise generated from the bogie structure alone and all the geometries when the bogie is located inside the bogie cavity. The differences of the flow and noise behavior between the isolated bogie case and bogie-inside-cavity case will be compared.

7.1 Geometry of Bogie Cavity without and with the Fairing

The bogie-inside-cavity case is again symmetrical in the axle mid-span where the flow influence of the wheel and frame is small; therefore it is reasonable to include only half of the geometry and make use of the symmetry to reduce the simulation size and time. Figure 7.1 shows the models of the simplified bogie inside the bogie cavity without and with the fairing at 1:10 scale used in this study. The dimensions of the half symmetrical cavity (see Figure 7.1a) are $4.5D \times 1.5D \times 0.8D$ (length, width and depth, where D is the wheel diameter) and thereby the bogie cavity has a length-to-depth ratio of about 6, which may be described as an open cavity. The

carbody under-floor surfaces are 4 mm higher than the bogie horizontal central plane. The fairing is shown in Figure 7.1(b). It has a thickness of 3.5 mm and an identical length and depth to the bogie cavity. The top half of the bogie is situated within the bogie cavity and covered by the fairing.

(a) Without fairing (b) With fairing

Figure 7.1: Models of simplified bogie inside the cavity

7.2 Numerical Setup

The computational domain for the case of the half bogie inside the cavity without the fairing is illustrated in Figure 7.2. It has dimensions of $20.7D$, $11D$ and $6.3D$ (where D is the wheel diameter) along the streamwise (x), vertical (y) and spanwise (z) directions, respectively. Thus, the outlet and side boundaries are far enough away to have negligible influence on the flow developed around the bogie and the cavity. For both cases of bogie inside the bogie cavity with and without the fairing, the mesh topology and boundary conditions applied are identical to the isolated bogie case as discussed in Chapter 6. Here the carbody and fairing surfaces are also defined as stationary no-slip walls where the distance from the geometry wall surface to the nearest grid point is set as 10^{-5} m and stretched with a growth ratio of 1.1 in the wall-normal direction inside the boundary layer to keep y^+ on the order of 1 to account for the low-Reynolds number effects. The upstream inlet flow is again set to 30 m/s with a low turbulence intensity and the downstream boundary is defined as a pressure outlet with a gauge pressure of zero. Note that a periodic boundary condition could be better for the multi-bogie case of high-speed train in reality but for the sake of comparison, the similar boundary conditions as the previous cases are applied. The total number of grid points in the entire domain is 36.5 million for the bogie-inside-cavity case without the fairing and 38.9 million for the case with the fairing. The same mesh models

will be utilized subsequently in Chapter 8 for the noise predictions using permeable data surfaces in the FW-H method.

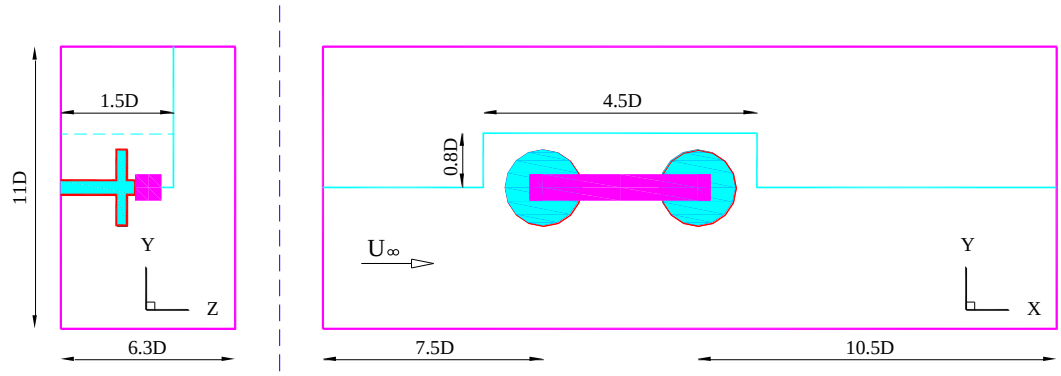

(a) Front view (b) Side view

Figure 7.2: Sketch of the computational domain of bogie cavity case without fairing (not to scale)

7.3 Aerodynamic Results

As in previous chapters, in order to investigate the flow-field characteristics developed around the geometries, the velocity and vorticity fields, the instantaneous iso-surfaces of Q criterion, the gauge pressure at wake positions, the fluctuating force coefficients and the wall pressure fluctuations from the geometries are presented and compared.

7.3.1 Instantaneous flow field

Figure 7.3 depicts the instantaneous non-dimensional velocity field of the bogie inside the cavity without and with the fairing at the wheelset horizontal mid-plane, displayed as a bottom view. It is shown that a massive flow separation occurs at the front edge of the frame outer corner, interfering with the boundary layer developed on the frame side surfaces. The vortices are convected downstream along the frame surface and separated again at the frame ends. Also, the noticeable flow separations are generated from the upstream wheel front edges at the side surfaces. The vortices formed in the front wheelset wake are convected downstream inside the bogie region and impinge on the rear wheelset, leading to the unsteady flow developed around the rear wheelset. Thereafter, the flow

impinges on the cavity rear wall and as a result, the flow interactions are decreased significantly and a weak wake is generated downstream along the vehicle underbody surface except at the cavity rear corner where the wake is relatively stronger due to more turbulent flow impingements and interactions occurring there. When the bogie cavity is mounted with the fairing, the flow separations occurring at the front edge of the frame outer side surface and cavity rear corner are reduced since the flow development around these areas is impeded considerably by the existence of the fairing; however, the flow field becomes more energetic around the outer surface of the downstream half frame as the flow interactions are strengthened inside the gap region between the frame and the fairing.

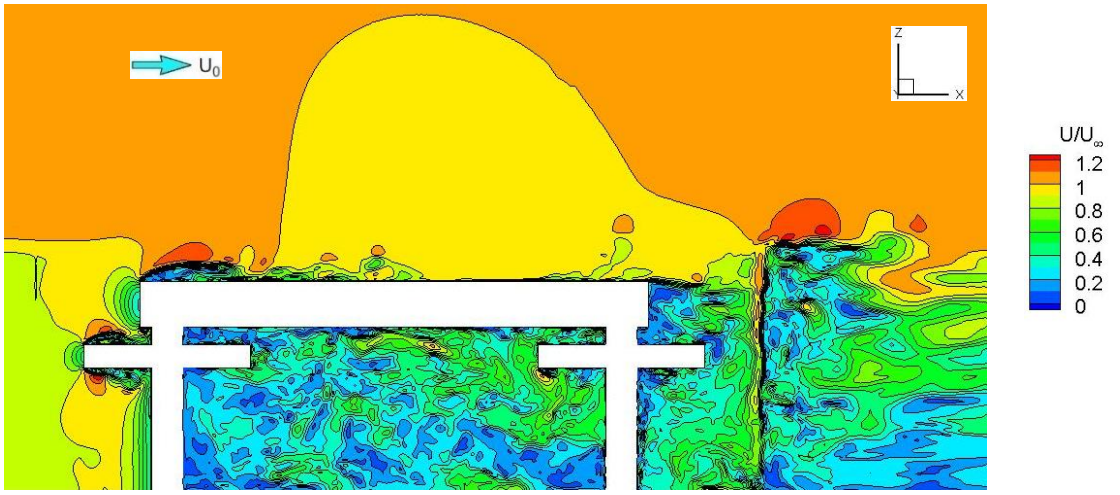

(a) Bogie inside bogie cavity without fairing

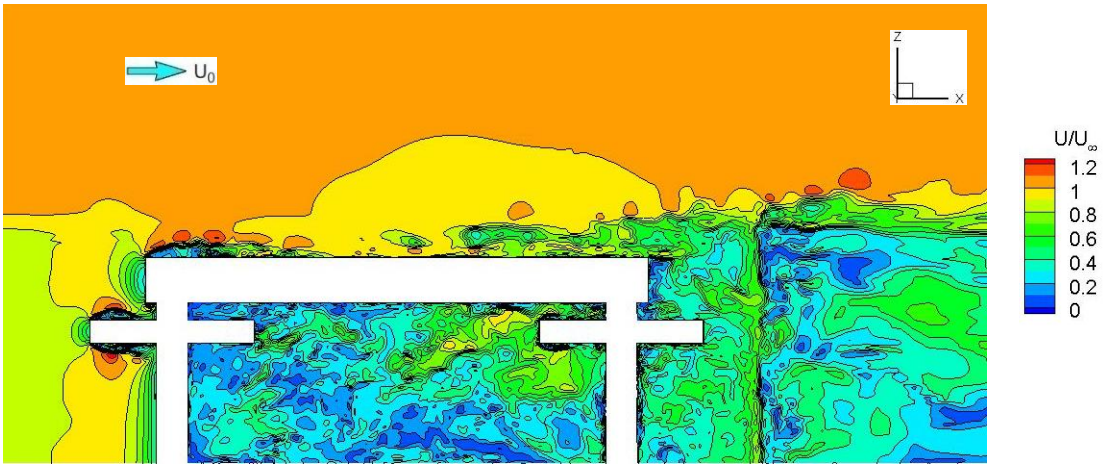

(b) Bogie inside bogie cavity with fairing

Figure 7.3: Contours of instantaneous velocity magnitude in horizontal plane through centre of wheelset (bottom views)

Figure 7.4 shows the corresponding velocity field at the half-axle vertical mid-plane. For both cases with and without the fairing, it is noted that the direction of the incoming flow to the upstream axle goes upwards toward the cavity upper wall. As a consequence, the boundary layer on the axle surface cannot be fully developed and separated earlier. Thus, no vortex is formed in the region behind the separation point and the subsequent vortex shedding is lost. This is different with the isolated bogie case (shown in Figure 6.5) where the organized vortex structures are formed and dominated by a large alternating vortex shedding in the upstream axle wake. Compared to the front axles, the rear axles are immersed in the turbulent flow and also no regular vortex shedding is developed around them.

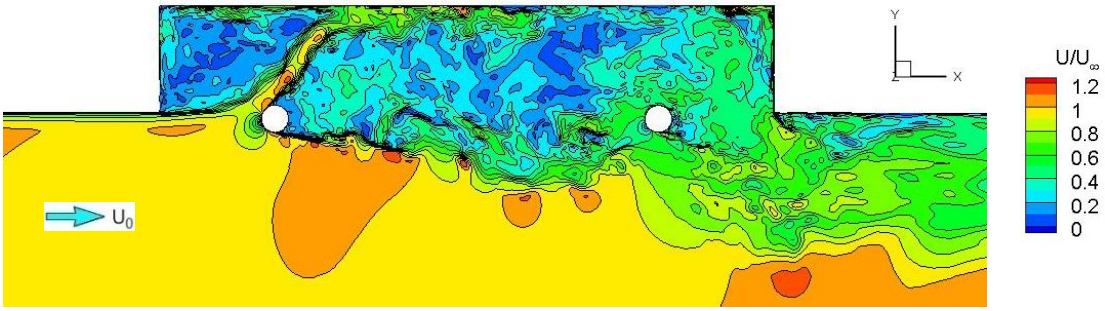

(a) Bogie inside bogie cavity without fairing

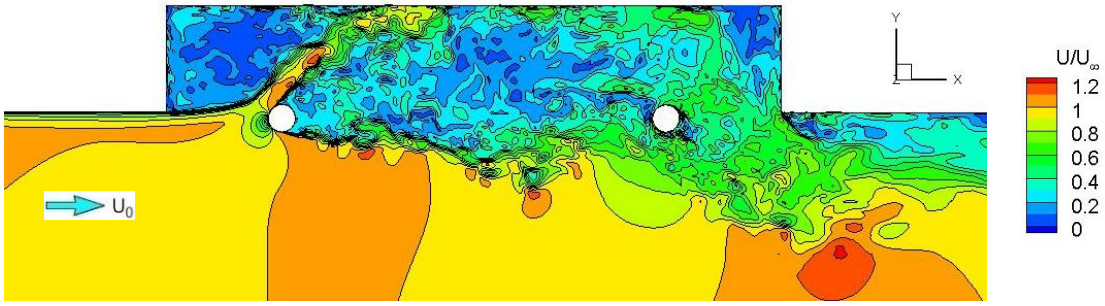

(b) Bogie inside bogie cavity with fairing

Figure 7.4: Contours of instantaneous velocity magnitude in vertical plane through axle mid-span (side views)

Figure 7.5 visualizes the flow structure represented by the iso-surfaces of the normalized Q criterion at the value of 50 (based on $Q/[(U_0/D)^2]$, where D is the wheel diameter) for the bogie located in the bogie cavity without the fairing. They are coloured by the velocity magnitude. Figure 7.5(a) shows that the vortices shed from the upstream geometries impinge on the downstream ones, generating a highly turbulent wake behind the bogie; and subsequently, all vortices impinge on

the cavity rear wall, deform largely and are merged into the eddies formed downstream behind the cavity. It can be observed from Figure 7.5(b) that different scales of vortices are generated between the upstream wheelset and cavity top wall as the various flow interactions and impingements occur there. Moreover, compared with the flow developed around the bogie, a higher level of flow-field unsteadiness is generated in the wake close to the cavity rear wall; nevertheless, it dissipates rapidly downstream as the flow development is impeded by the vehicle carbody wall surface.

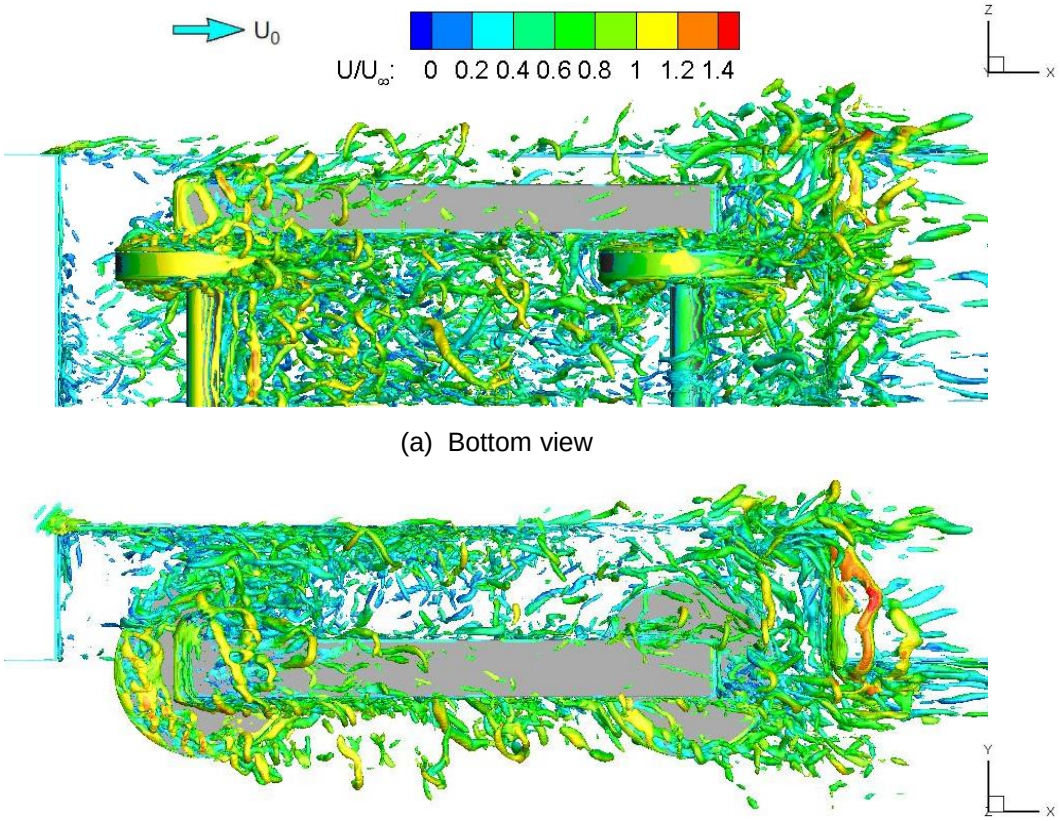

(a) Bottom view

(b) Side view

Figure 7.5: Iso-surfaces of the instantaneous normalized Q criterion (case without fairing)

Figure 7.6 displays the corresponding results for the bogie cavity case shielded by the fairing. It can be seen that the flow structures are very similar for the two bogie cavity cases without and with the fairing except around the regions of the downstream half of the cavity and the cavity rear wall where the unsteady turbulent flow is reduced markedly in the case with the fairing in comparison with the case without the fairing since the flow development in these areas is impeded by the fairing. Moreover, the velocity magnitude of the flow developed around the bogie

inside the cavity with the fairing is distributed evenly with the similar contour levels, indicating that an energetic turbulent flow with relatively uniformity is generated within the bogie cavity.

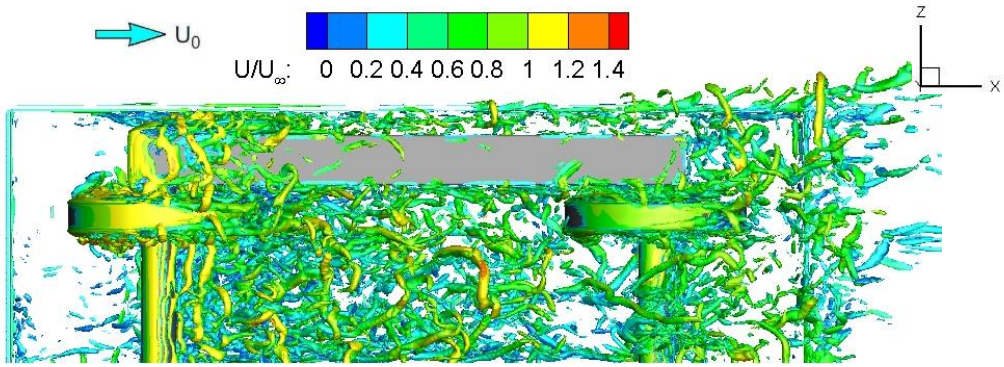

(a) Bottom view

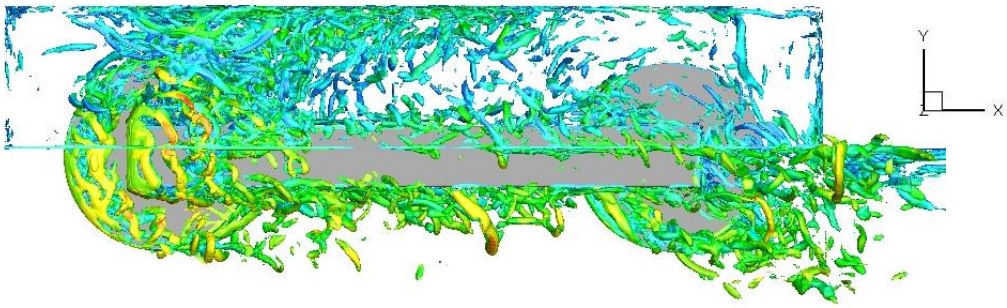

(b) Side view

Figure 7.6: Iso-surfaces of the instantaneous normalized Q criterion (case with fairing)

Figure 7.7(a) depicts the instantaneous non-dimensional spanwise vorticity field ($\omega_z = (\partial V/\partial x - \partial U/\partial y)D/U_\infty$, where D is the wheel diameter) in the axle mid-span for the bogie-inside-cavity case without the fairing. It shows that a shear layer is shed from the cavity leading edge and bent upwards quickly in the streamwise direction. This shear layer travels downstream and has a strong interaction with the flow separated from the upstream axle. Subsequently, all vortices are mixed up and impinge on the upper wall of the cavity, leading to the unsteady flow with complex structure formed there. Additionally, it can be observed that the wake behind both the upstream and downstream axles is highly turbulent. The downstream axle experiences the impingement of vortices shed from the upstream axle and the vortices developed behind the downstream axle are greatly deformed as they impinge on the cavity rear wall; thereby, all vortices are amalgamated

behind the rear axle, leading to the downstream axle wake and the flow near the cavity rear corners becoming highly irregular and unsteady.

In comparison with the flow developed behind the axles, the flow around the wheels shows different characteristics, as displayed in Figure 7.7(b) for the instantaneous spanwise vorticity fields (ω_z) contours in the wheel mid-span. The shear layer generated from the cavity leading edge is bent upwards and attached on the wheel tread as the gap between the wheel and cavity leading edge is relatively small. Subsequently, the vortices are separated from the wheel top surfaces as a consequence of the interaction between the attached shear layer and the boundary layer developed on the wheel tread. Note that the wake behind the upstream wheel is less organized and more irregular compared to that behind the upstream axle. The incident vortices convected from the upstream wheel impinge on and interact with the vortices separated from the downstream wheel, resulting in a highly turbulent flow generated around the area of the downstream wheel and cavity rear wall as well as the corner.

The contour of the instantaneous spanwise vorticity field (ω_z) along the frame mid-span is displayed in Figure 7.7(c). Once more, a shear layer developed from the cavity leading edge is bent upwards and interacts with the vortices separated from the frame top surfaces; thus, the vortical structure between the frame and the cavity top wall becomes highly turbulent due to flow impingement and recirculation occurring there. The vortices developed and convected along the frame surface are separated at the frame ends, generating an unsteady wake region between the frame and the cavity wall.

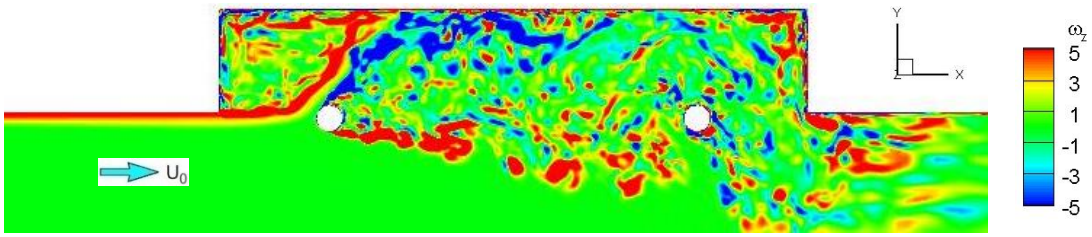

(a) Axle mid-span

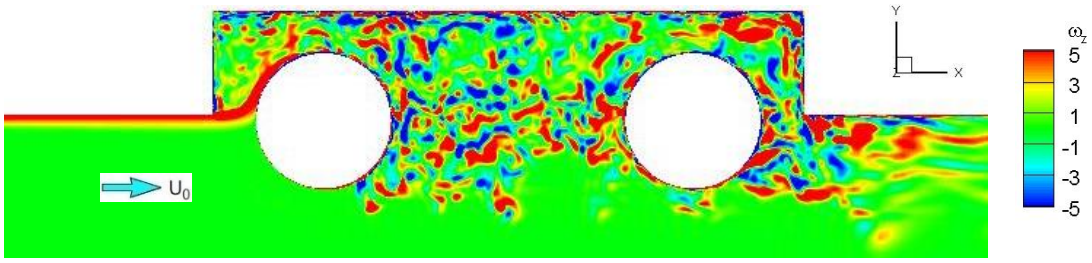

(b) Wheel mid-span

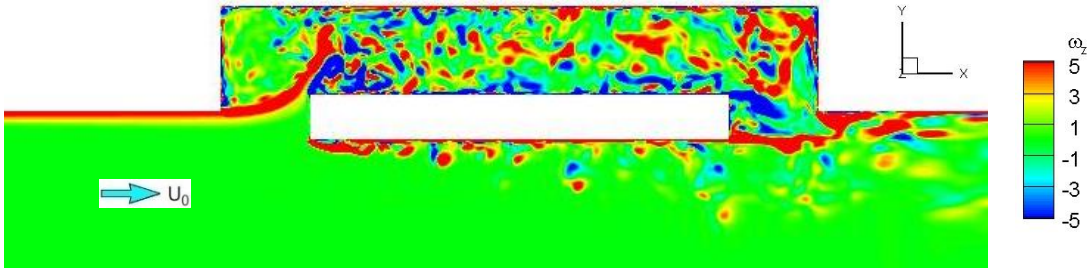

(c) Frame mid-span

Figure 7.7: Contours of the instantaneous spanwise vorticity fields in a vertical plane for bogie without fairing

Figure 7.8 shows the power spectral densities of the gauge pressure at different positions around the bogie wake for the case without the fairing: behind the axle and wheel respectively, at the inside wheel-axle corner and on the top of the frame. Compared with the corresponding results in Chapters 5 and 6 (Figures 5.11 and 6.8), it is striking that the tonal component has been suppressed. A broad hump from 200 Hz to 1 kHz appears in the spectrum in Figure 7.8(a) at a point with a distance of one axle radius from the top side of the front axle at mid-span, which may correspond to the mixture of the vortex shed from the front axle under the condition of turbulent inflow. By comparison, the pressure signal from the downstream axle at mid-span is more broadband with a higher amplitude. This is because the turbulent flow convected from the front wheelset interacts with the bogie cavity flow and therefore the trailing axle is subject to a more energetic incident flow, as indicated from Figure 7.5. The results in Figure 7.8(b) are shown for points located at 13 mm away from the wheel rim in line with the top of the front and rear axle. It is also noted that due to the influence of the turbulent wake interaction effects, the spectra of the wheel-axle corner pressure signal behind both the front and rear wheelsets are broadband. Moreover, due to more strongly unsteady flow generated around the upstream axle, the spectrum from the front wheelset has a higher level than that from the downstream wheelset in the

frequency range over 200 Hz. Figure 7.8(c) shows that the spectra of the pressure at the points with a distance of one wheel radius away from the top of the front and rear wheel at mid-span are also broadband and the amplitude from the front wheel is larger than that from the rear wheel within the frequency range above 100 Hz. The reason is that both the upstream and downstream wheels are close to the cavity top wall where the strong flow impingements and interactions are developed, whereas the front wheel experiences additionally the impingement of shear layer shed from the cavity leading edge, as mentioned earlier. Figure 7.8(d) illustrates that the spectra of the pressure at the points near the front and rear edge of the frame at mid-span are broadband with the amplitude from the rear frame slightly higher in most of the frequency range. Note that all the spectra of the gauge pressure at the described positions are broadband with no distinct peak, indicating that the flow developed around the bogie inside the cavity is fully irregular and highly turbulent.

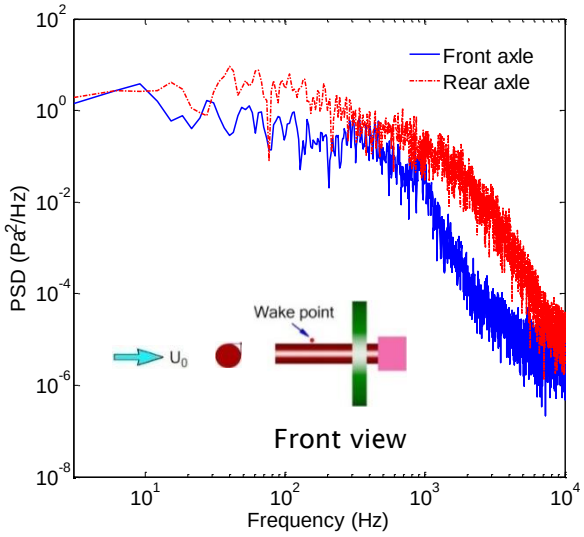

(a) Axle mid-span

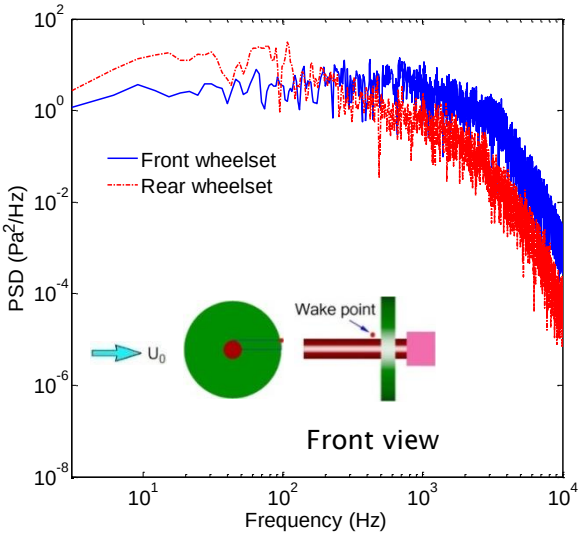

(b) Inner wheel-axle corner

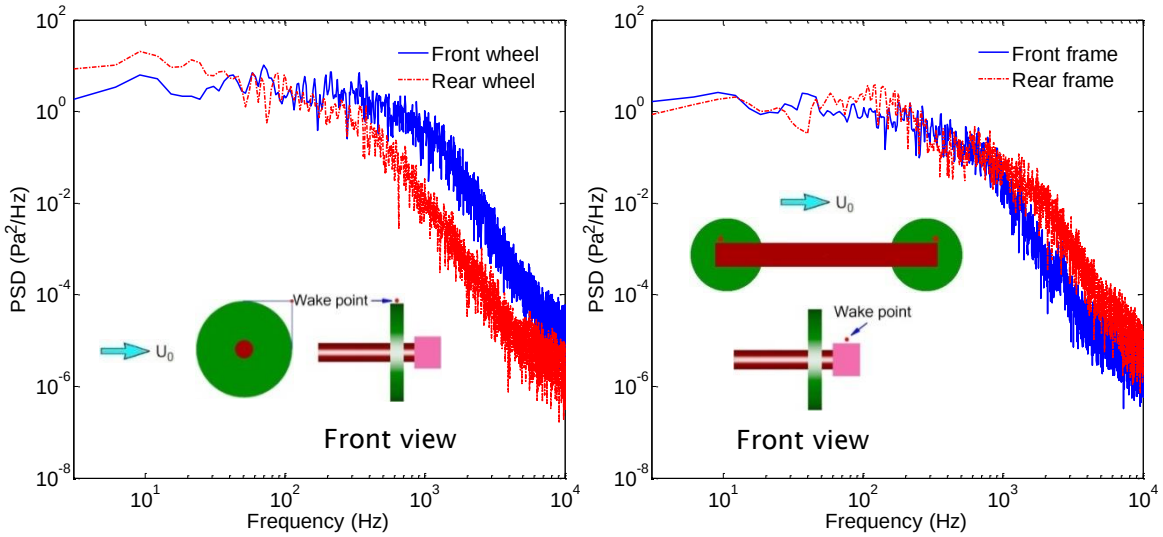

(c) Wheel mid-span (d) Frame mid-span

Figure 7.8: Power spectral densities of pressure at bogie wake positions for bogie cavity case without fairing

7.3.2 Fluctuating force coefficients

All simulations were run for 0.2 s before collecting the time histories of aerodynamic force coefficients in which the forces on the bogie surfaces are non-dimensionalized by $(\frac{1}{2}\rho_0 U_\infty^2 A)$, where A is the projected frontal cross-section area of the bogie. Table 7.1 summarizes the RMS and mean results from the three 50% overlapping time windows for the bogie-inside-cavity case without the fairing. It is shown that the variations of the RMS values between each segment are small (less than 5%) and the discrepancies in mean drag and side force coefficients are less than 3%. The mean lift coefficient for each segment is always around -0.056. Therefore, it indicates that the transient flow field has become statistically steady and the source data collected can be used for far-field noise prediction. Note that the RMS side force coefficient is twice the RMS lift coefficient which is only slightly larger than the RMS drag coefficient, suggesting that the oscillation of unsteady force is much higher in the lateral direction normal to the flow for the bogie cavity without the fairing. Compared with the former isolated bogie case presented in Table 6.1, here the mean drag is about half what it was for the isolated bogie and the fluctuating drag is similar to that for the bogie alone whereas the fluctuating lift is greatly reduced by the presence of the cavity.

		Segment1 (0.2-0.41s)	Segment2 (0.305-0.515s)	Segment3 (0.41-0.62s)	Total length (0.2-0.62s)
RMS value	Fluctuating lift	0.0512	0.0493	0.0488	0.0497
	Fluctuating drag	0.0398	0.0415	0.0396	0.0405
	Fluctuating side force	0.0996	0.1032	0.1036	0.1013
Mean value	Lift coefficient	-0.0565	-0.0564	-0.0564	-0.0565
	Drag coefficient	0.7292	0.7229	0.7082	0.7137
	Side force coefficient	0.2297	0.2328	0.2363	0.2314

Table 7.1: Root-mean-square and mean values of aerodynamic force coefficients (bogie-inside-cavity case without the fairing)

The PSDs of fluctuating lift, drag and side force coefficients of the bogie and its components (frame, front and rear wheelsets) for the bogie-inside-cavity case without the fairing are presented in Figures 7.9-7.11. Compared with the drag and side force coefficients, the contribution of the frame to the oscillating lift force is comparatively larger (shown in Figure 7.9a, Figure 7.10a and Figure 7.11a). This is in contrast to the isolated bogie case (Figure 6.9) where the oscillating lift force contributions from the frame are relatively small. The reason for such a striking difference between these two cases is that the shear layer shed from the cavity leading edge impinges on the frame leading edge (see Figure 7.7c), and hence, the interaction of the formed upstream vortex with the frame surface induces more effective fluctuating lift forces. Also different from the isolated bogie case, the spectrum levels of the rear wheelset are generally higher in most of the frequency range for all force coefficients than those of the front wheelset, as shown in Figure 7.9(b), Figure 7.10(b) and Figure 7.11(b). This is because the inflow changes the direction due to the influence from the cavity for the leading wheelset and subsequently no vortex shedding is formed in its wake area; additionally, more energetic turbulent incoming flow is generated around the downstream geometries due to the strong flow impingement and interaction occurring within the rear region inside the bogie cavity.

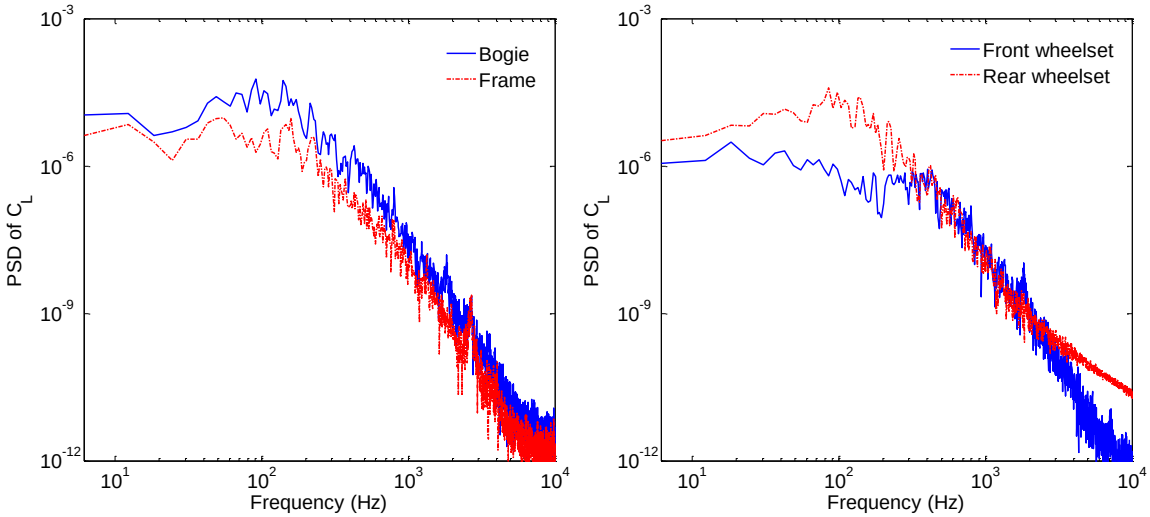

(a) Bogie and whole frame (b) Front and rear wheelsets

Figure 7.9: Power spectral densities of lift coefficients

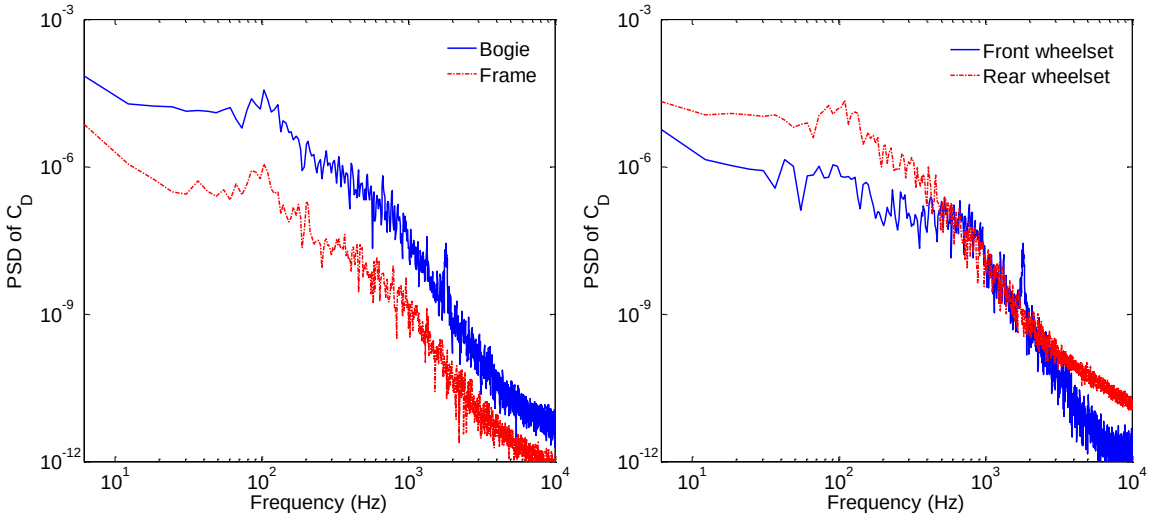

(a) Bogie and whole frame (b) Front and rear wheelsets

Figure 7.10: Power spectral densities of drag coefficients

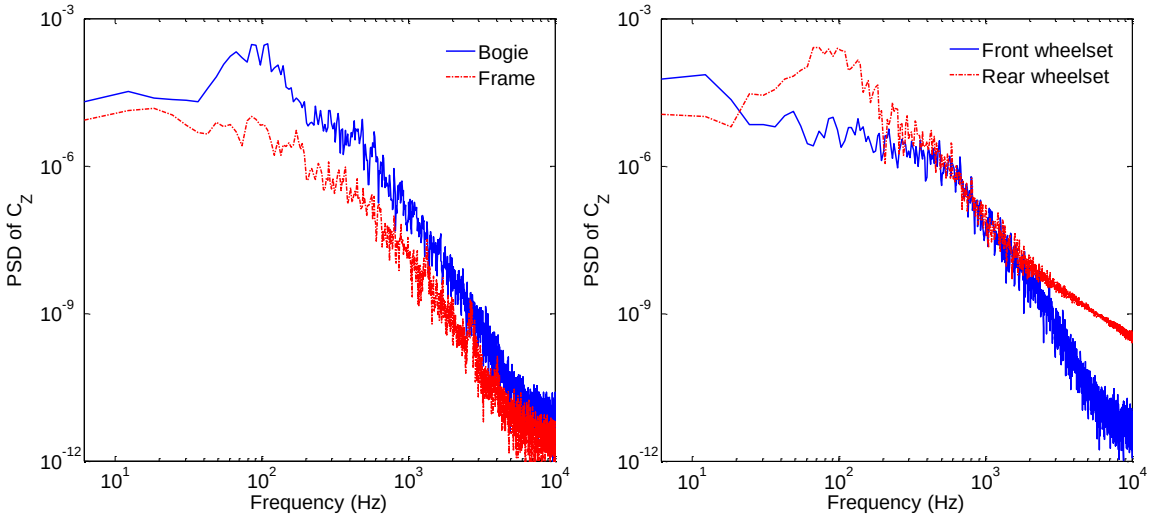

(a) Bogie and whole frame (b) Front and rear wheelsets

Figure 7.11: Power spectral densities of side force coefficients

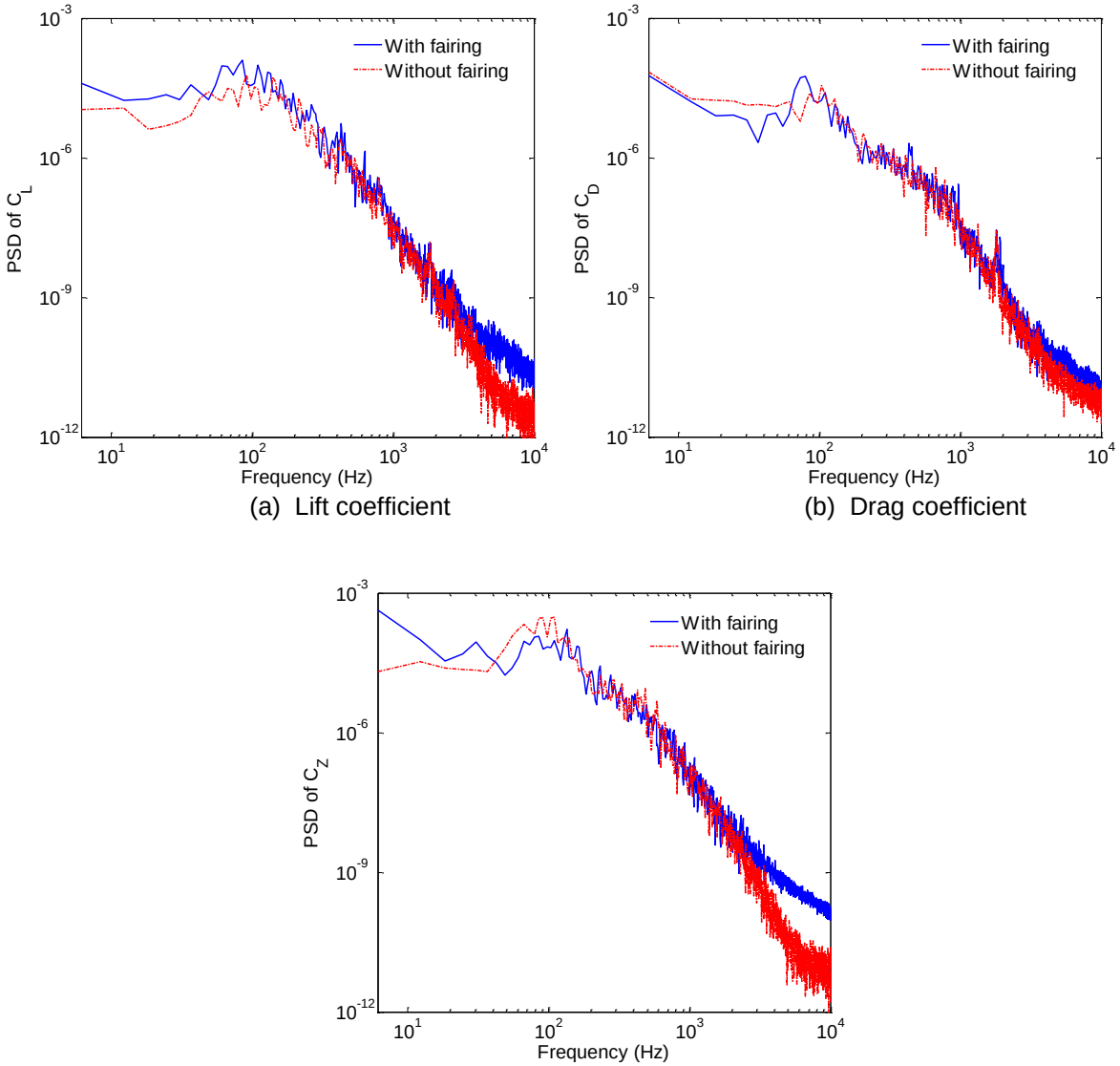

(a) Lift coefficient

(b) Drag coefficient

(c) Side force coefficient

Figure 7.12: Power spectral densities of force coefficients of the bogie-inside-cavity cases

Figure 7.12 depicts the PSDs of fluctuating lift, drag and side force coefficients of the bogies for the bogie cavity cases with and without the fairing. This shows that the lift and side force coefficients are close to each other within the frequency range of 200-2000 Hz and the drag coefficients are similar in most of the frequency range, indicating that the flow developed around the bogie in the two cavity cases contains the similar turbulence structure with various scales. In the frequency range below 200 Hz, the lift coefficient is higher for the case with the fairing (Figure 7.12a), suggesting that the vortex impingement on the bogie is increased by the presence of the fairing. Moreover, a broad hump between 40 Hz and 130 Hz with higher spectrum level can be seen in the side force coefficient of the bogie cavity case without the fairing (Figure 7.12c), which may correspond to the interaction between

the shear layer shed from the cavity side leading edge and the flow developed around the bogie. Note that at higher frequencies, above 2 kHz, the spectrum amplitude is larger for the case with the fairing in the lift and side force coefficients since more small-scale eddies are generated around the bogie in the cavity covered by the fairing.

7.3.3 Wall pressure fluctuations

Figure 7.13 displays the wall fluctuating pressure level as defined in Section 6.3.3 on the bogie surfaces for the bogie-inside-cavity cases without and with the fairing. This shows that for both cases, a high pressure fluctuation appears on the wheel and frame inner side surface and the axle surface near the axle-wheel junction region. The surface pressure fluctuations are considerably higher on these areas for the case with the fairing. This is due to the stronger flow impingement and interaction occurring around the bogie inside the cavity shielded by fairing, suggesting that more flow-induced noise may potentially be generated from the bogie structure itself. Moreover, similar distributions of the wall pressure fluctuations are developed on the outer surfaces of the wheel and frame for both bogie cavity cases, as shown in Figure 7.14.

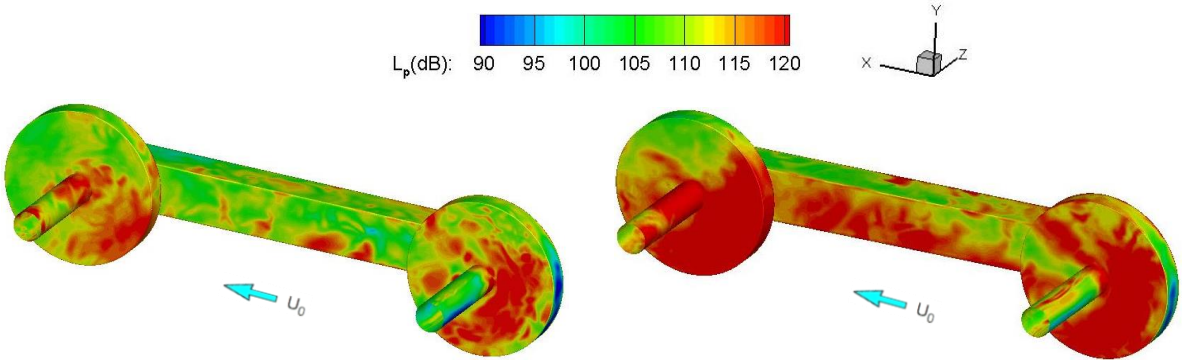

(a) Without fairing (b) With fairing

Figure 7.13: Wall pressure fluctuation level of inner bogie surfaces inside the cavity

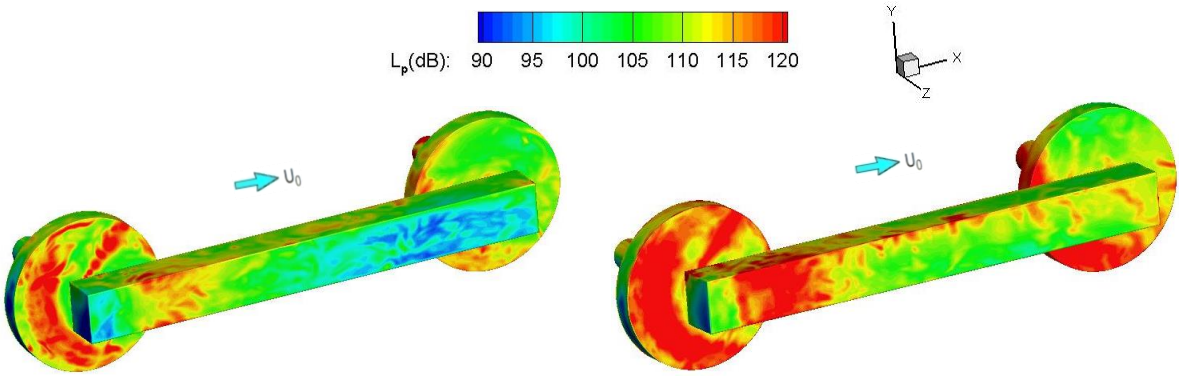

(a) Without fairing (b) With fairing

Figure 7.14: Wall pressure fluctuation level of outer bogie surfaces inside the cavity

7.4 Aeroacoustic Results

When the transient flow field has become statistically steady, the far-field noise can be predicted by the FW-H method using the near-field unsteady flow data. For both bogie-inside-cavity cases, noise assumed to be generated from the bogie solid surfaces alone and radiated to a free space is calculated and compared here. This will give an indication on the changes of the noise sources from the bogie solid surfaces. The panels (surface elements) distributed on the bogie surfaces which account for the acoustic sources and the far-field receiver positions defined are same as the isolated bogie case, see Section 6.4.

7.4.1 Acoustic spectra computation

The CFD simulations were run for 1.1 s corresponding to 17 times the flow-through time. The length of the time signal used as input to the FW-H method for noise calculation is related to the last 0.52 s of the computation. The PSD of the far-field noise signal is computed by Welch's method with a frequency resolution of 6 Hz.

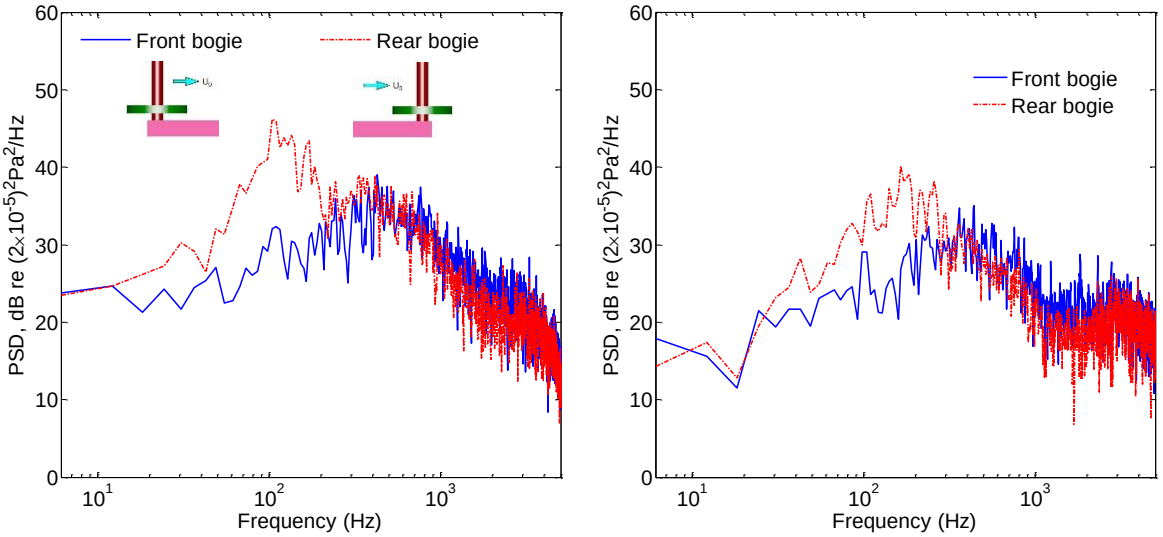

(a) Receiver 3 (b) Receiver 19

Figure 7.15: Spectra of acoustic pressure on far-field receivers (bogie inside bogie cavity without fairing)

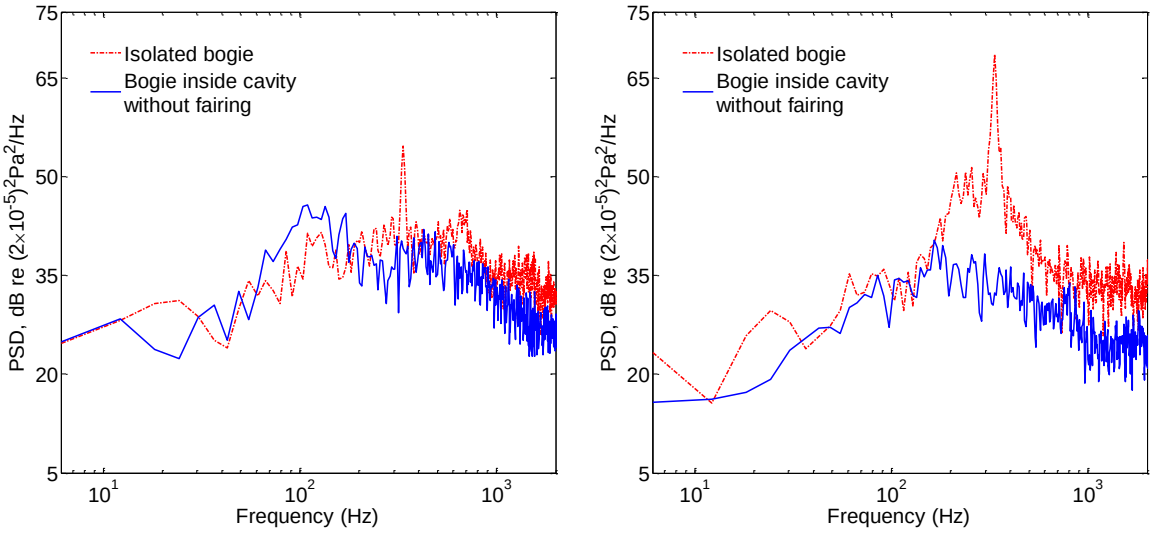

(a) Receiver 3 (b) Receiver 19

Figure 7.16: Comparisons of spectra of acoustic pressure on far-field receivers

Figure 7.15 shows the spectra of the noise radiated from the front and rear bogies alone (i.e. the front and rear half parts of the half bogie symmetrical along the axle mid-span) of the bogie-inside-cavity cases at receiver 3 and receiver 19 in the vertical *z-y* plane as described in Figure 6.13. It can be noted that the noise spectra from both the front and rear bogies are broadband with no vortex shedding peaks since the flow developed around the bogie inside the cavity is fully unsteady as discussed in Section 7.3.1. Compared with the front bogie, the spectral level of noise radiated from the rear bogie is much higher within the frequency range below

400 Hz. This is due to the stronger flow impingement and interaction developed around the downstream geometries inside the bogie cavity. Moreover, Figure 7.16 displays the spectra of the radiated noise from the half bogie symmetrical along the axle mid-span. It is found that compared to the isolated bogie case, the noise level from the bogie-inside-cavity case without the fairing is lower, particularly at top receiver 19 where the noise is significantly reduced (the OASPL below 2 kHz changes from 72.7 dB to 55.2 dB) as no massive vortex shedding is generated around the bogie inside the cavity.

7.4.2 Acoustic directivity

In order to compare with the isolated bogie case as discussed in Chapter 6, the noise directivities for whole bogie geometries of bogie cavity cases are obtained based on OASPL which is calculated from the PSD in the frequency range below 2 kHz. Assuming that the near-field wall pressure fluctuations on the bogie surfaces are radiated to the free space, Figure 7.17 displays the three-dimensional directivity pattern of the noise radiated from the whole bogie surfaces relative to the geometry centre of x=y=z=0 inside the bogie cavity without and with the fairing. The noise directivities in the vertical z-y and x-y planes are depicted and compared in Figure 7.18. This shows that the noise directivity of the bogie in the two cases exhibits a similar lateral dipole pattern with dominant radiation towards the trackside direction and by comparison, the noise levels between them are very similar except in the bogie symmetry plane along the axle mid-span where the noise level is about 1 dB higher for the case with the fairing as a consequence of the stronger flow interactions generated around the bogie central region. It should be noted that the sound shielding effect from the bogie fairing cannot be taken into account here because only the pressure fluctuations on the bogie wall surfaces are used when the integration surface coincides with a solid surface in the FW-H method.

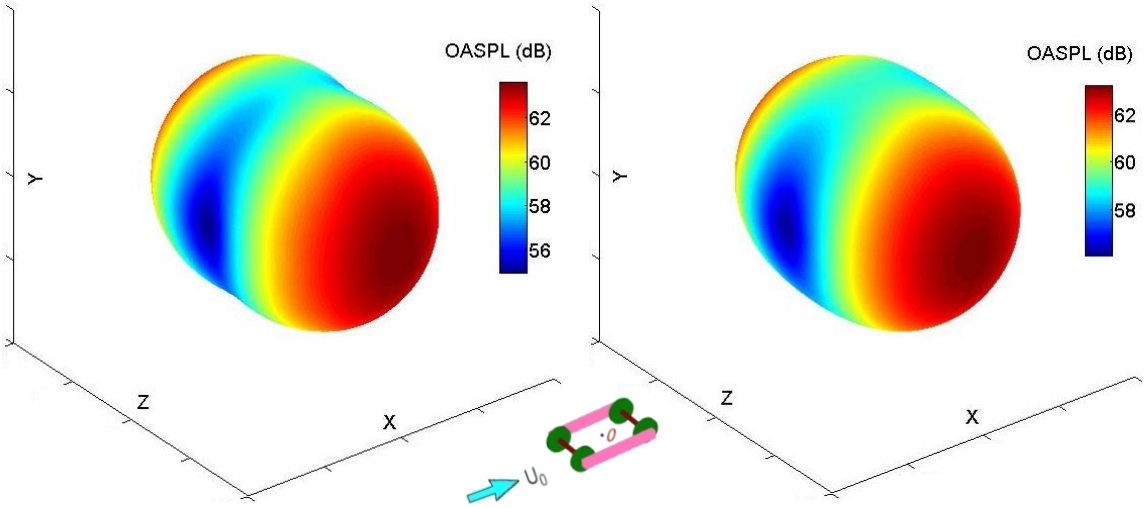

(a) Without fairing (b) With fairing

Figure 7.17: Three-dimensional noise directivity radiated from bogie surfaces inside the cavity (centre of directivity pattern corresponds to 40 dB)

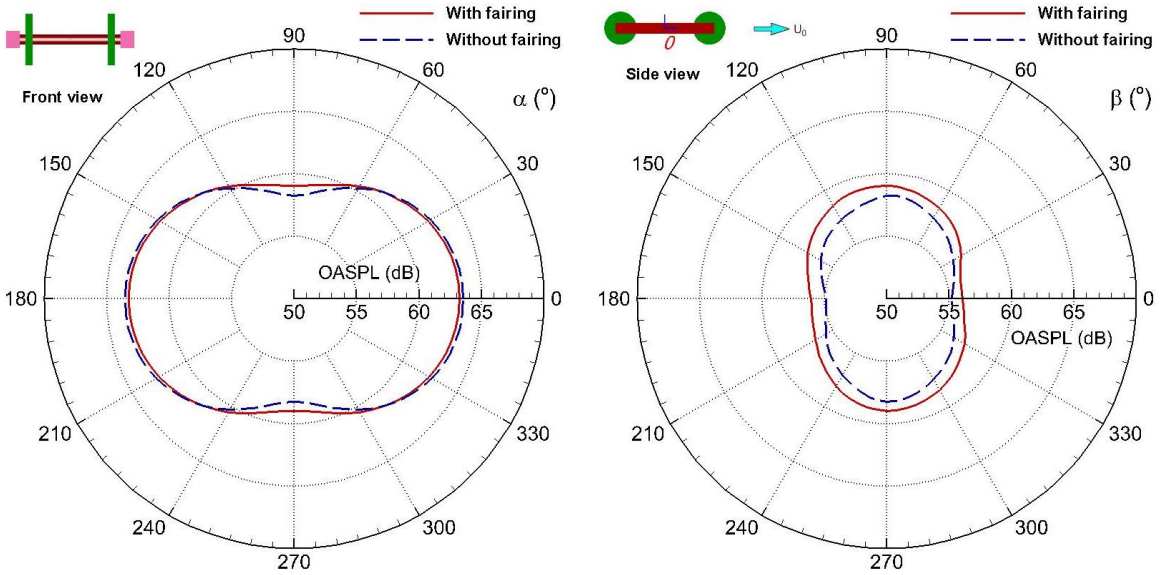

(a) Spanwise vertical *z*-*y* plane (b) Streamwise vertical *x*-*y* plane

Figure 7.18: Two-dimensional noise directivity radiated from bogie surfaces inside the cavity

7.5 Bogie inside Bogie Cavity with Ground underneath

For the case of the bogie located inside the cavity with the ground underneath, the influence of the moving ground and the rotation of the wheelsets is discussed here. Figure 7.19 shows the model of the bogie inside the bogie cavity with a ground plane underneath at 1:10 scale (case without the fairing). The dimensions of the bogie, bogie cavity and carbody are same as the bogie-inside-cavity case as

introduced in Section 7.1. The gap between the bottom of the wheel and the ground is 25 mm to represent the distance of the wheels above the ground when running on the rails. As shown in Figure 7.20, the computational domain with half symmetrical geometries has dimensions of $18.5D$, $5.8D$ and $6.3D$ (D=92 mm is the wheel diameter) along the streamwise, vertical and spanwise direction, respectively. All wheelset surfaces are defined as moving no-slip walls and the rotation effect is implemented by imposing the corresponding rotation velocity on the solid surface. The ground is set as no-slip walls moving with the inflow velocity. The other boundary conditions are same as the bogie-inside-cavity cases described in Section 7.2. The total number of grid points of the entire domain is 39.5 million for the bogie-inside-cavity case with the ground underneath (having no fairing). As the other cases, the DDES model is applied for flow simulation and the FW-H acoustic analogy method is used for far-field noise prediction.

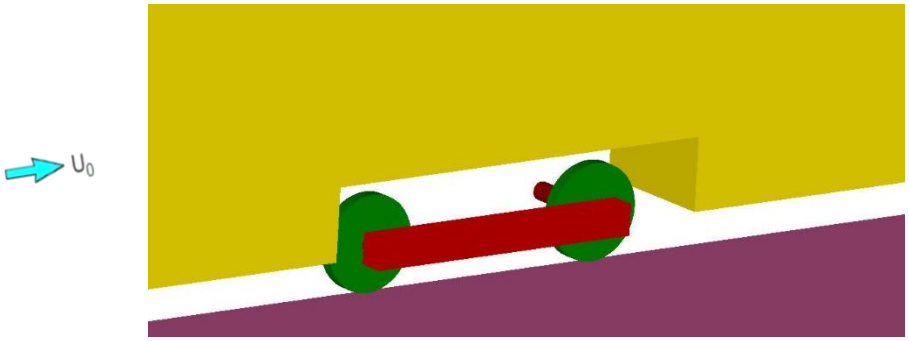

Figure 7.19: Model of simplified bogie inside the cavity with ground underneath

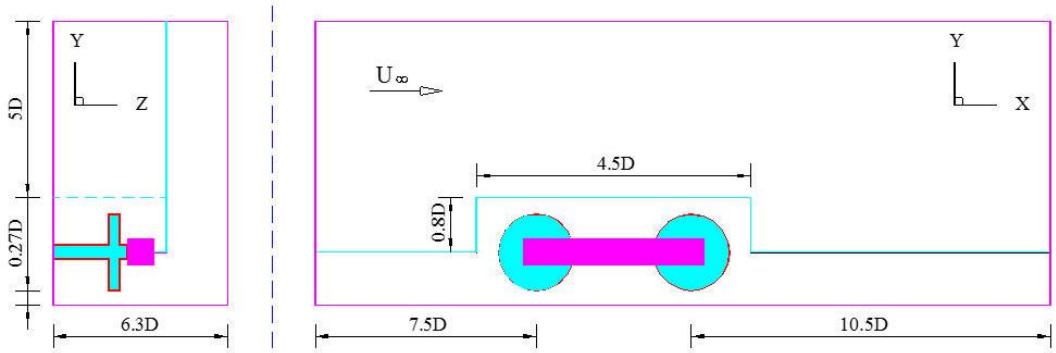

(a) Front view (b) Side view

Figure 7.20: Sketch of the computational domain of bogie inside the cavity with ground underneath (not to scale)

7.5.1 Instantaneous flow structure

In order to investigate the flow-field characteristics developed around the geometries for the case of bogie located in the bogie cavity with the ground underneath (without the fairing), Figure 7.21 visualizes the flow structure represented by the iso-surfaces of the normalized Q criterion at the value of 50 (based on $Q/[(U_0/D)^2]$ in which D is the wheel diameter and coloured by the velocity magnitude) and Figure 7.22 depicts the instantaneous non-dimensional spanwise vorticity field ($\omega_z = (\partial V/\partial x - \partial U/\partial y)D/U_\infty$, where D is the wheel diameter) in the axle mid-span. These show that compared with the flow field of bogie-inside-cavity case without the ground as displayed in Figures 7.5(a) and 7.7(a), more eddies with various scales are developed inside the bogie region (especially around the rear wheelset) since the rotating wheelsets and moving ground generate more flow interactions there.

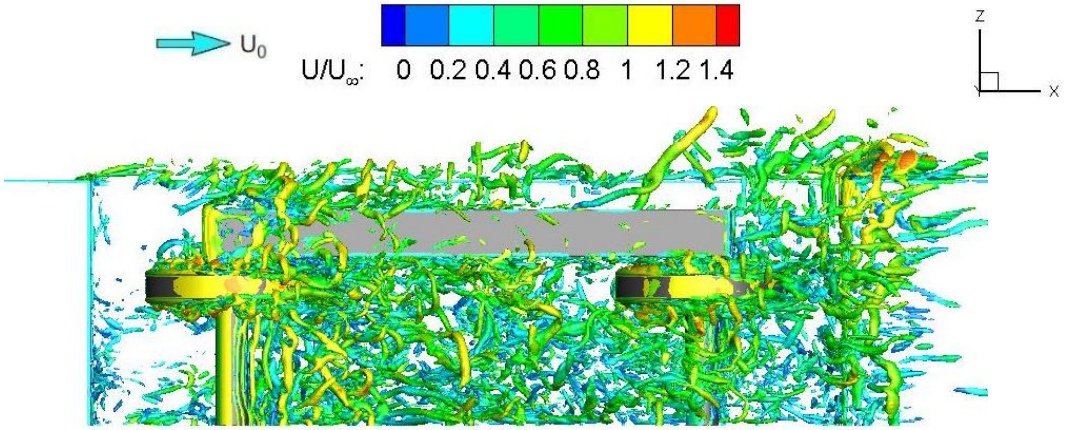

(a) Bottom view

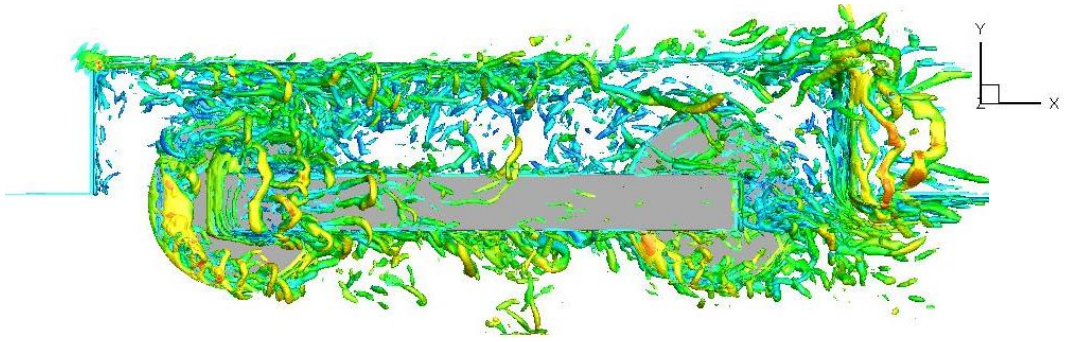

(b) Side view

Figure 7.21: Iso-surfaces of the instantaneous normalized Q criterion for the case with ground underneath

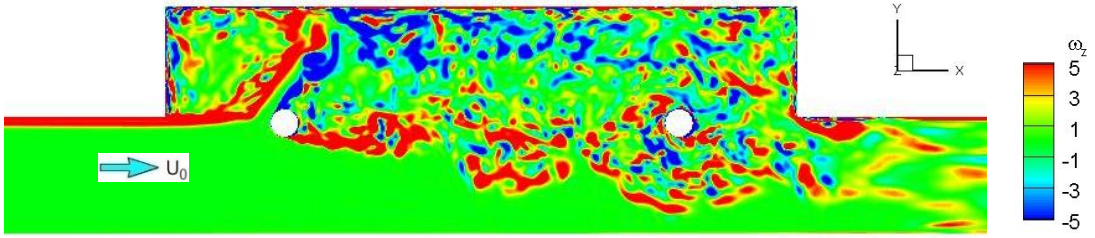

Figure 7.22: Contours of the instantaneous spanwise vorticity fields in a vertical plane for the case with ground underneath (axle mid-span, side view)

7.5.2 Acoustic spectra and directivity

As for the bogie-inside-cavity cases mentioned in Section 7.4, noise assumed to be generated from the bogie solid surfaces alone and radiated to a free space is calculated for the bogie-inside-cavity case with the ground underneath here to investigate the changes of the noise sources on the bogie solid surfaces from the various bogie-inside-cavity cases. The CFD simulations were run for 1 s corresponding to 16 times the flow-through time. The length of the time signal used as input to the FW-H method for noise calculation is related to the last 0.5 s of the computation. Again, the PSD of the far-field noise signal is computed by Welch's method with a frequency resolution of 6 Hz.

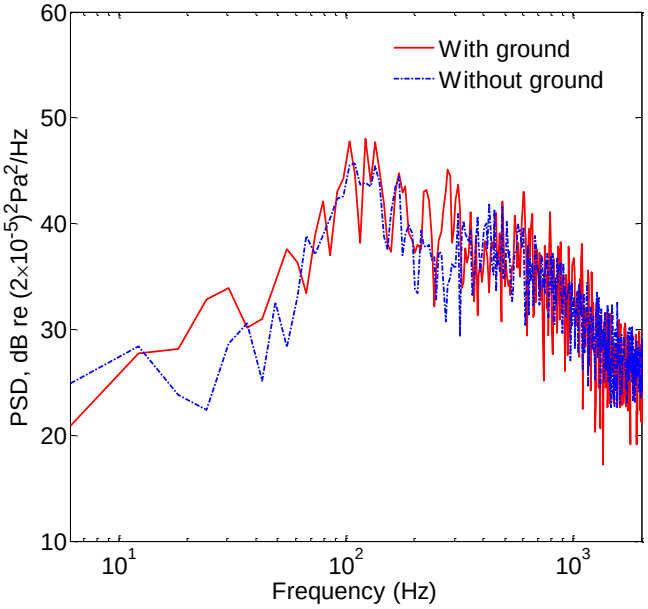

Figure 7.23: Comparison of spectra of acoustic pressure on far-field receivers (cases without fairing)

Based on the numerical simulations on the symmetrical half bogie inside the cavity, Figure 7.23 shows the spectra of the noise radiated from the wall surfaces of the half bogie at side receiver 3 as described in Figure 6.14. It is found that compared to bogie inside bogie cavity without the ground (case without the fairing), the noise level from the bogie-inside-cavity case with the ground underneath is about 1 dB higher (the OASPL below 2 kHz changes from 60.5 dB to 61.6 dB) as the stronger flow is generated there around the bogie inside the cavity as mentioned in the previous section.

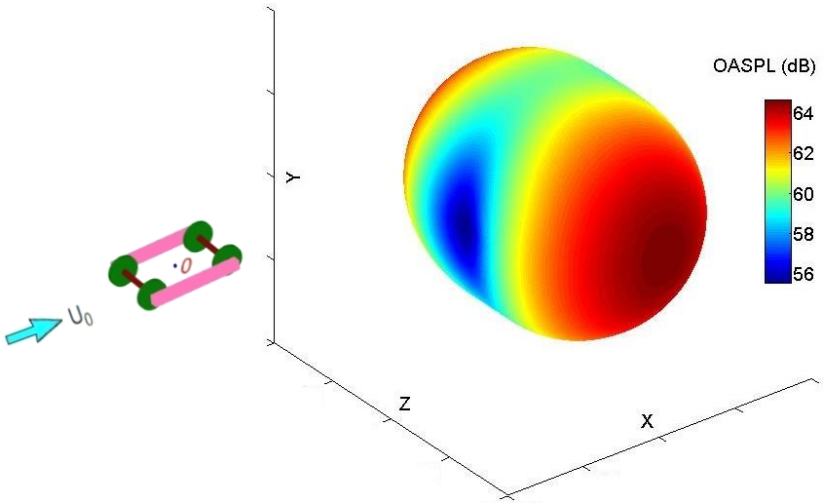

Figure 7.24: Three-dimensional noise directivity radiated from bogie surfaces inside the cavity (centre of directivity pattern corresponds to 40 dB)

Again, assuming that the near-field wall pressure fluctuations on the bogie surfaces are radiated to the free space and neglecting the ground reflections, Figure 7.24 displays the three-dimensional directivity pattern of the noise radiated from the whole bogie surfaces relative to the geometry centre of x=y=z=0 inside the bogie cavity including the effects of rotating wheelsets and moving ground on the flow. This shows that the noise directivity of the bogie exhibits a lateral dipole pattern with dominant radiation towards the trackside direction. The noise directivities in the vertical z-y and horizontal x-z planes are displayed and compared in Figure 7.25 for the two bogie-inside-cavity cases with and without the ground underneath. It is found that the noise directivity of the bogie in the two cases shows a similar lateral dipole pattern, and by comparison, the noise level is up to 2 dB higher for the case including the ground since more flow interactions are generated by the effects of rotating wheelsets and moving ground.

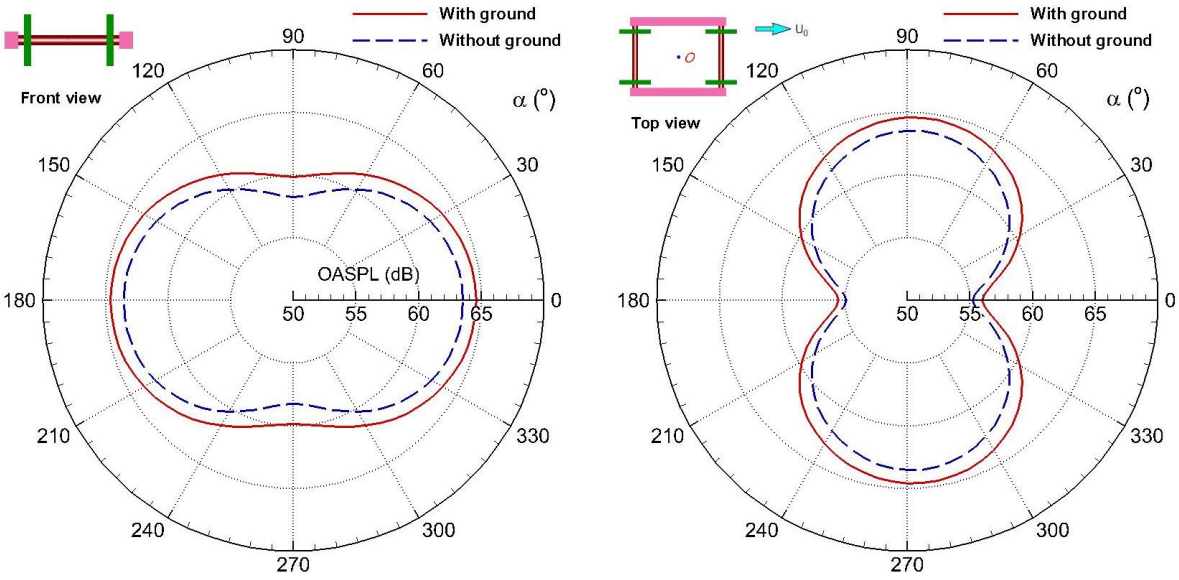

(a) Vertical *z*-*y* plane (b) Horizontal *x*-*z* plane

Figure 7.25: Two-dimensional noise directivity radiated from bogie surfaces inside the cavity (cases without fairing)

7.6 Summary

The flow behaviour and the aerodynamic noise characteristics developed from the simplified bogie inside the bogie cavity with and without a fairing have been investigated using the DDES model and the FW-H acoustic analogy method. It is found that for the current bogie-inside-cavity cases, a shear layer developed from the cavity leading edge has a strong interaction with the flow separated from the upstream bogie and cavity wall. All vortices are mixed up and convected downstream and impinge on the downstream geometries and the cavity trailing edge as well as the rear wall regions. Thus, a highly irregular and unsteady flow is generated inside the bogie cavity due to the considerably strong flow impingement and recirculation occurring there. Compared with the bogie cavity case without the fairing, the stronger flow interactions are developed around the bogie inside the cavity shielded by the fairing. Additionally, for both bogie cavity cases, the noise generated from the bogie solid surfaces alone is predicted assuming that it is radiated to the free space. Different from the isolated bogie case, noise spectra from both the front and the rear half-bogies are broadband with no distinct peak. A lateral dipole pattern of noise radiation is predicted for the bogie inside the bogie cavity with noise levels slightly higher in the bogie symmetry plane along the axle mid-span for the bogie cavity case covered by the fairing, suggesting that more

flow interactions are developed within the bogie cavity covered by fairing and thus the surface noise sources increase.

Furthermore, the flow and flow-induced noise behaviour for the bogie inside the bogie cavity with the ground underneath (case without the fairing) have been performed using the same methods as the former two bogie-inside-cavity cases. It is found that compared to the bogie-inside-cavity case having no ground underneath, a similar flow field is generated with more turbulent eddies developed inside the bogie area for the bogie-inside-cavity case with the ground underneath, and therefore, assuming the noise radiated from the bogie wall surfaces to the free space, the noise directivity of the bogie shows a lateral dipole pattern with the noise levels increased by up to 2 dB for the current case neglecting the ground reflections since the rotating wheelsets and moving ground produce more flow interactions around the geometries.

In reality, the bogie fairing and ground will change the flow field around the geometries and accordingly the noise generation and radiation. To account for these influences, a permeable surface enclosing all components should be used for noise prediction. Thus, the shielding effect by mounting a fairing around the bogie cavity region due to the change of the flow field and the influence of the noise reflection from the ground can be investigated. This will be discussed in the next chapter.

Chapter 8

Influence of Bogie Fairing and Ground on Sound Generation Based on Convective FW-H Formulation

The Ffowcs Williams–Hawkings equation has been the foundation for much of the development in the modelling of aerodynamic sound prediction over the past few decades. However, the classical FW–H equation assumes the propagation of sound waves in a quiescent medium and does not take into account the presence of a mean flow as occurs for wind-tunnel cases [114]. Thus, in the application of these formulations, the wind-tunnel problem should be transformed into a moving-observer problem where the observer is assumed to be moving at a constant speed in an environment at rest, as discussed in Section 3.2.3. If the observer remains stationary in the simulation of a wind-tunnel case, the moving mean flow should be taken into account in the computation. The calculation using the moving-medium formulation is more efficient than the solution from the moving-observer equations, even though the results are equivalent [115].

Based on the convective wave equation considering a moving medium, a surface integral formulation in the form of the FW-H equation is described in this chapter. Then, based on the convective FW–H formulation, an aerodynamic noise prediction code using the advanced time algorithm is implemented with the time-accurate flow solution on the permeable integration surface obtained from a distinct CFD simulation as input for the equivalent sources. Thereafter, the bogie fairing and ground effects on far-filed noise radiated from the train bogie area are investigated numerically.

8.1 FW-H Acoustic Analogy and Kirchhoff Approach

It is essential to mention the analytical comparison between the FW–H equation and the Kirchhoff formula for moving surfaces, as discussed by Brentner and Farassat [42,116]. It is concluded that the FW-H and Kirchhoff formulation are equivalent if the integration surface is placed in the linear source region where the input data are compatible with the wave equation. Compared with the Kirchhoff governing equation, the distinct advantage of the FW-H formula is that the source terms can be easily identified with a physical interpretation [42]. Based on the conservation laws of fluid mechanics, the FW-H equation is valid even if the integration surface is located in the nonlinear source region. As the integration surface is moved further away from the physical body, more quadrupole source contributions are accounted for by the surface integrals in the FW-H acoustic analogy. Therefore, once the volume quadrupole source is included in the noise computation, the placement restrictions of the integration surface are relaxed. However, if the integration surface is not in the linear source region, the Kirchhoff approach can lead to substantial errors which are difficult to identify.

8.2 Permeable Data Surface for FW-H Method

The use of a permeable (porous or penetrable) data surface to account for nonlinearities in the vicinity of a moving surface was proposed by Ffowcs Williams and Hawkings [40]. Many noise computations have been implemented through the application of the FW–H equation on a permeable or porous surface [117-119]. The accuracy of the permeable surface application of the FW–H equation has been demonstrated through a comparison between the acoustic pressure prediction and experimental results for a hovering rotor [116].

In noise predictions based on the classical FW-H equation, the data surface $f(\mathbf{x}, t) = 0$ has usually been assumed to coincide with a solid impenetrable surface. Then the normal velocity of the fluid is the same as the normal velocity of the surface. A relaxation of this assumption is useful as it enables noise prediction considering either physical surfaces or conveniently placed fictitious

data surfaces. As the development of an alternative but equivalent source description, Equation (2.24) is the appropriate expression for the FW–H equation with a permeable surface.

In the FW-H acoustic analogy, generally, the physical sound sources enclosed by the integral surface $f(\mathbf{x},t)=0$ are accounted for through the surface source terms. Meanwhile, any noise generated by the flow outside the surface $f(\mathbf{x},t)=0$ contributes through the quadrupole term, a volume distribution source. The volume integration in the acoustic prediction is more challenging to compute and the amount of flow-field data required for the volume integration is much larger than that for an integration over the surface surrounding the volume. If a permeable data surface enclosing most of the physical sources is used in Equation (2.24), then the surface source terms in the equation also account for the sound generated in the flow field outside the physical solid surface but inside the control data surface. Therefore, sound radiated to the far-field can be calculated from the sources on the permeable surfaces if the quadrupole volume sources outside the data surface in Equation (2.24) have a negligible contribution and can be neglected.

Once sufficiently accurate, unsteady flow-field data on the integration permeable surface are obtained from CFD simulations, the hybrid method with the coupling of the CFD dataset and the FW–H equation provides a mutually beneficial method for noise calculation: the CFD computation is only needed in the near-field sound source region while the FW–H equation provides an efficient approach to predict the sound field away from the acoustic source region, as mentioned in Section 2.3.2. Therefore, the noise prediction may be computationally efficient for complicated, nonlinear sound sources through the FW–H formulation with permeable surfaces.

8.3 Convective FW-H Equation

The convective FW–H equation for a moving source in a moving medium was first introduced in [115]. Using the convective Green's function, the convective

form of the FW–H equation considering quadrupole noise terms was developed for the moving medium case [114]. As some typos found in the main formulations in the reference [114], the convective FW–H equation for a wind-tunnel problem is derived fully in the following to understand the meaning of all terms in the formulations for developing an aerodynamic noise prediction code.

Considering the local fluid perturbation velocity $\mathbf{u}$ and a mean flow moving with constant speed $\mathbf{U}_0$, then, in the fluid field at each point the flow velocity is $\mathbf{u}+\mathbf{U}_0$. The mass continuity and conservation of momentum equations are

$$\frac{\partial \rho}{\partial t}+\frac{\partial \rho(u_i+U_{0i})}{\partial x_i}=0\,, \tag{8.1}$$

$$\frac{\partial}{\partial t}[\rho(u_i+U_{0i})]+\frac{\partial}{\partial x_j}\left[\rho(u_i+U_{0i})\left(u_j+U_{0j}\right)+(p-p_0)\delta_{ij}-\tau_{ij}\right]=0\,, \tag{8.2}$$

where $(p-p_0)$ is the gauge pressure and p_0 is the constant pressure in the undisturbed free-stream medium with speed U_0 and density ρ_0. See Section 2.2 for the definition of the other quantities.

With $\rho'=\rho-\rho_0$, $\frac{\partial \rho_0}{\partial t}=0$, $\frac{\partial U_{0i}}{\partial x_i}=0$ and $\frac{\partial(\rho_0 U_{0i})}{\partial x_i}=0$, Equation (8.1) can be written as

$$\frac{\partial \rho'}{\partial t}+\frac{\partial(\rho u_i)}{\partial x_i}+U_{0i}\frac{\partial \rho'}{\partial x_i}=0\,. \tag{8.3}$$

Then using $\frac{\partial U_{0i}}{\partial x_i}=0$, $\frac{\partial(\rho_0 U_{0i})}{\partial t}=0$ and Equation (8.3), Equation (8.2) yields

$$\frac{\partial}{\partial t}(\rho u_i)+U_{0j}\frac{\partial}{\partial x_j}(\rho u_i)+\frac{\partial}{\partial x_j}\left[\rho u_i u_j+(p-p_0)\delta_{ij}-\tau_{ij}\right]=0\,. \tag{8.4}$$

Based on the Heaviside step function $H(f)$, which is 1 outside the integral surface ($f(\mathbf{x},t)>0$) and 0 elsewhere ($f(\mathbf{x},t)<0$). The continuity equation for the entire space can be written using generalized function as following

$$H(f)\left[\frac{\partial \rho'}{\partial t}+\frac{\partial(\rho u_i)}{\partial x_i}+U_{0i}\frac{\partial \rho'}{\partial x_i}\right]=0\,. \tag{8.5}$$

Recasting the derivatives yields

$$\frac{\partial[H(f)\rho']}{\partial t}+\frac{\partial[H(f)\rho u_i]}{\partial x_i}+U_{0i}\frac{\partial[H(f)\rho']}{\partial x_i}$$

$$= H(f)\left[\frac{\partial \rho'}{\partial t} + \frac{\partial(\rho u_i)}{\partial x_i} + U_{0i}\frac{\partial \rho'}{\partial x_i}\right] + \rho'\frac{\partial[H(f)]}{\partial t} + \rho u_i\frac{\partial[H(f)]}{\partial x_i} + \rho' U_{0i}\frac{\partial[H(f)]}{\partial x_i}$$

$$= \rho'\frac{\partial[H(f)]}{\partial t} + \rho u_i\frac{\partial[H(f)]}{\partial x_i} + \rho' U_{0i}\frac{\partial[H(f)]}{\partial x_i}. \tag{8.6}$$

Utilizing the properties of generalized functions

$$\frac{\partial[H(f)]}{\partial t} = \frac{\partial f}{\partial t}\delta(f) = -v_i n_i \delta(f) = -v_n \delta(f), \tag{8.7}$$

and

$$\frac{\partial[H(f)]}{\partial x_i} = \frac{\partial f}{\partial x_i}\delta(f) = n_i \delta(f). \tag{8.8}$$

Then, Equation (8.6) can be rearranged as

$$\frac{\partial[H(f)\rho']}{\partial t} + \frac{\partial[H(f)\rho u_i]}{\partial x_i} + U_{0i}\frac{\partial[H(f)\rho']}{\partial x_i}$$

$$= \rho'[-v_i n_i \delta(f)] + \rho u_i n_i \delta(f) + \rho' U_{0i} n_i \delta(f)$$

$$= [\rho(u_i - v_i + U_{0i}) + \rho_0(v_i - U_{0i})] n_i \delta(f)$$

$$= Q_i n_i \delta(f), \tag{8.9}$$

where

$$Q_i = [\rho(u_i - v_i + U_{0i}) + \rho_0(v_i - U_{0i})]. \tag{8.10}$$

Also, the conservation of momentum equations can be written in a similar way as

$$\frac{\partial[H(f)\rho u_i]}{\partial t} + U_{0j}\frac{\partial[H(f)\rho u_i]}{\partial x_j} + c_0^2\frac{\partial[H(f)\rho']}{\partial x_i}$$

$$= \rho u_i\frac{\partial[H(f)]}{\partial t} + H(f)\left[\frac{\partial(\rho u_i)}{\partial t} + U_{0j}\frac{\partial(\rho u_i)}{\partial x_j}\right] +$$

$$U_{0j}\rho u_i\frac{\partial[H(f)]}{\partial x_j} + c_0^2\frac{\partial[H(f)\rho']}{\partial x_i}. \tag{8.11}$$

Utilizing Equations (8.4), (8.7) and (8.8), Equation (8.11) is recast as

$$\frac{\partial[H(f)\rho u_i]}{\partial t} + U_{0j}\frac{\partial[H(f)\rho u_i]}{\partial x_j} + c_0^2\frac{\partial[H(f)\rho']}{\partial x_i}$$

$$= \rho[-v_i n_i \delta(f)] - H(f)\left\{\frac{\partial}{\partial x_j}\left[\rho u_i u_j + (p - p_0)\delta_{ij} - \tau_{ij}\right]\right\} +$$

$$U_{0j}\rho u_i n_j \delta(f) + c_0^2\frac{\partial[H(f)\rho']}{\partial x_i}$$

$$= -\frac{\partial}{\partial x_j}\left\{H(f)\left[\rho u_i u_j + \langle(p - p_0) - c_0^2(\rho - \rho_0)\rangle\delta_{ij} - \tau_{ij}\right]\right\} +$$

$$\left[\rho u_i\left(u_j + U_{0j} - v_j\right) + (p - p_0)\delta_{ij} - \tau_{ij}\right] n_j \delta(f)$$

$$= -\frac{\partial}{\partial x_j}\left[H(f)T_{ij}\right] + L_{ij} n_j \delta(f)\,, \tag{8.12}$$

in which

$$T_{ij} = \rho u_i u_j + [(p - p_0) - c_0^2(\rho - \rho_0)]\delta_{ij} - \tau_{ij}\,, \tag{8.13}$$

$$L_{ij} = \rho u_i\left(u_j + U_{0j} - v_j\right) + (p - p_0)\delta_{ij} - \tau_{ij}\,. \tag{8.14}$$

The next step follows the derivation of Lighthill's equation except that the generalized derivatives are taken here. Calculating the divergence $(\partial/\partial x_i)$ of Equation (8.12), the resulting equation becomes

$$\left[\frac{\partial^2}{\partial t^2} + U_{0i}\frac{\partial^2}{\partial t \partial x_i} - c_0^2\frac{\partial^2}{\partial x_i \partial x_i}\right][H(f)\rho'] - U_{0j}\frac{\partial^2}{\partial x_i \partial x_j}[H(f)\rho u_i]$$

$$= \frac{\partial}{\partial t}[Q_i n_i \delta(f)] - \frac{\partial}{\partial x_i}\left[L_{ij} n_j \delta(f)\right] + \frac{\partial^2}{\partial x_i \partial x_j}\left[H(f)T_{ij}\right]. \tag{8.15}$$

Multiplying both sides of Equation (8.9) by U_{0j}, gives

$$U_{0j}\frac{\partial[H(f)\rho']}{\partial t} + U_{0j}\frac{\partial[H(f)\rho u_i]}{\partial x_i} + U_{0i}U_{0j}\frac{\partial[H(f)\rho']}{\partial x_i} = U_{0j}Q_i n_i \delta(f)\,. \tag{8.16}$$

Taking the divergence $\partial/\partial x_j$ of Equation (8.16), yields

$$U_{0j}\frac{\partial^2}{\partial t \partial x_j}[H(f)\rho'] + U_{0j}\frac{\partial^2}{\partial x_i \partial x_j}[H(f)\rho u_i] + U_{0i}U_{0j}\frac{\partial^2}{\partial x_i \partial x_j}[H(f)\rho']$$

$$= U_{0j}\frac{\partial}{\partial x_j}[Q_i n_i \delta(f)]\,. \tag{8.17}$$

Combining Equations (8.15) and (8.17) to eliminate the term $U_{0j}\frac{\partial^2}{\partial x_i \partial x_j}[H(f)\rho u_i]$, the inhomogeneous convective FW-H equation [114] is obtained as

$$\left[\frac{\partial^2}{\partial t^2} + 2U_{0i}\frac{\partial^2}{\partial t \partial x_i} - c_0^2\frac{\partial^2}{\partial x_i \partial x_i} + U_{0i}U_{0j}\frac{\partial^2}{\partial x_i \partial x_j}\right][H(f)\rho']$$

$$= \left(\frac{\partial}{\partial t} + U_{0j}\frac{\partial}{\partial x_j}\right)[Q_i n_i \delta(f)] - \frac{\partial}{\partial x_i}\left[L_{ij} n_j \delta(f)\right] + \frac{\partial^2}{\partial x_i \partial x_j}\left[H(f)T_{ij}\right], \tag{8.18}$$

in which, the Dirac delta function $\delta(f)$ is only non-zero on the control surface and the convective wave operator is

$$\bar{\Box}^2 = \left[\frac{\partial^2}{\partial t^2} + 2U_{0i}\frac{\partial^2}{\partial t \partial x_i} - c_0^2\frac{\partial^2}{\partial x_i \partial x_i} + U_{0i}U_{0j}\frac{\partial^2}{\partial x_i \partial x_j}\right]. \tag{8.19}$$

Similar to the classical FW-H equation, the three sources on the right-hand side of Equation (8.18) are known as the convective monopole (thickness), dipole (loading) and quadrupole terms, respectively.

8.4 Numerical Method for Solving the Convective FW-H Equation

While propagating from the source surface to the observer in a moving medium, the sound waves are convected by the mean flow velocity. Based on the Garrick triangle [120], the geometric interpretation for a source in a uniform rectilinear subsonic motion is represented in Figure 8.1. Without loss of generality, the coordinate system is chosen such that the mean flow velocity is in the positive x_1-direction, i.e. $\mathbf{u}_0 = (U_0,\ 0,\ 0)$. The source surface is described by $(\mathbf{y}, \tau_e)$ with $\mathbf{y} = (y_1,\ y_2,\ y_3)$ and the observer is described by $(\mathbf{x}, t)$ with $\mathbf{x} = (x_1,\ x_2,\ x_3)$. The moving medium is assumed to be homogeneous outside the source volume and its Mach number is M_0.

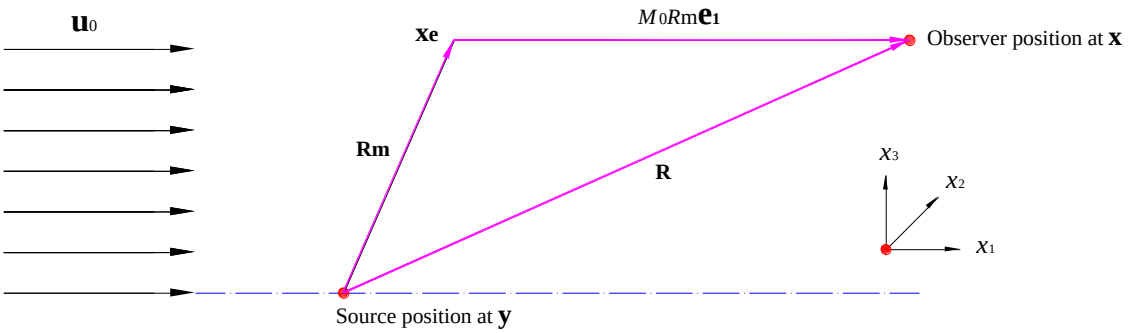

Figure 8.1: Geometric interpretation of emission

Therefore, the radiation distance from the surface point to the observer is

$$\mathbf{R} = \mathbf{x} - \mathbf{y} = (x_1 - y_1)\mathbf{e_1} + (x_2 - y_2)\mathbf{e_2} + (x_3 - y_3)\mathbf{e_3}\,, \tag{8.20}$$

and the emission vector is presented by the following form,

$$\mathbf{R}_\mathrm{m} = \mathbf{R} - \Delta t\mathbf{u}_0 = (x_1 - y_1 - M_0 R_\mathrm{m})\mathbf{e_1} + (x_2 - y_2)\mathbf{e_2} + (x_3 - y_3)\mathbf{e_3}\,, \tag{8.21}$$

in which

$$\Delta t\mathbf{u}_0 = (x_1 - y_1 - M_0 R_\mathrm{m})\mathbf{e_1}\,. \tag{8.22}$$

The norm of the emission vector is

$$|\mathbf{R}_\mathrm{m}| = R_\mathrm{m} = \sqrt{(x_1 - y_1 - M_0 R_\mathrm{m})^2 + (x_2 - y_2)^2 + (x_3 - y_3)^2}\,. \tag{8.23}$$

Since the emission distance must be positive, the valid solution of Equation (8.23) is

$$R_{\mathrm{m}} = -\frac{M_0(x_1 - y_1)}{1 - {M_0}^2} + \sqrt{\left[\frac{M_0(x_1 - y_1)}{1 - {M_0}^2}\right]^2 + \frac{(x_1 - y_1)^2 + (x_2 - y_2)^2 + (x_3 - y_3)^2}{1 - {M_0}^2}}\,. \tag{8.24}$$

It can be reformulated as

$$R_{\mathrm{m}} = \frac{R^* - M_0(x_1 - y_1)}{1 - {M_0}^2}\,, \tag{8.25}$$

in which

$$R^* = \sqrt{(x_1 - y_1)^2 + \left(1 - {M_0}^2\right)[(x_2 - y_2)^2 + (x_3 - y_3)^2]}\,. \tag{8.26}$$

The spatial derivatives of the emission distance R^* and R_{m} are $\tilde{R}_i^* = \frac{\partial R^*}{\partial x_i}$ and $\tilde{R}_i = \frac{\partial R_{\mathrm{m}}}{\partial x_i}$, which are introduced as follows:

$$\tilde{R}_1^* = \frac{x_1 - y_1}{R^*}\,, \quad \tilde{R}_2^* = \left(1 - {M_0}^2\right)\frac{x_2 - y_2}{R^*}\,, \quad \tilde{R}_3^* = \left(1 - {M_0}^2\right)\frac{x_3 - y_3}{R^*}\,, \tag{8.27}$$

$$\tilde{R}_1 = \frac{1}{1 - {M_0}^2}\left(-M_0 + \tilde{R}_1^*\right), \quad \tilde{R}_2 = \frac{x_2 - y_2}{R^*}\,, \quad \tilde{R}_3 = \frac{x_3 - y_3}{R^*}\,. \tag{8.28}$$

It should be noted that the quantities R_{m} and R^* are no longer the actual geometric distance between the source and the observer [115]. Taking into account the time delay on signal reception from emission, R_{m} represents the effective acoustic distance between the source and the observer. Moreover, with regard to the Doppler shift effect, R^* denotes the equivalent distance of the observer from the source including the amplitude decay of the acoustic signal.

Based on the definitions presented above, the three-dimensional free-space Green's function given for the convective wave equation [121] is

$$G(\mathbf{x}, t; \mathbf{y}, \tau) = \frac{\delta(\tau - t + R_{\mathrm{m}}/c_0)}{4\pi R^*}\,. \tag{8.29}$$

Then, the solution to the convective FW-H equation (8.18) may be written as

$$c_0^2 \rho'(\mathbf{x}, t) = \left(\frac{\partial}{\partial t} + U_0 \frac{\partial}{\partial x_1}\right) \int_{-\infty}^{t} \int_{\mathbb{R}^3} [Q_i n_i \delta(f)] \frac{\delta(g)}{4\pi R^*} d^3\mathbf{y} d\tau$$

$$-\frac{\partial}{\partial x_i}\int_{-\infty}^{t}\int_{\mathbb{R}^3}\left[L_{ij}n_j\delta(f)\right]\frac{\delta(g)}{4\pi R^*}d^3\mathbf{y}d\tau$$

$$+\frac{\partial^2}{\partial x_i\partial x_j}\int_{-\infty}^{t}\int_{\mathbb{R}^3}\left[H(f)T_{ij}\right]\frac{\delta(g)}{4\pi R^*}d^3\mathbf{y}d\tau\,, \tag{8.30}$$

where the limits of the integral are represented as

$$\int_{-\infty}^{t}\int_{\mathbb{R}^3}\cdots\cdots d^3\mathbf{y}d\tau=\int_{-\infty}^{t}\int_{-\infty}^{\infty}\int_{-\infty}^{\infty}\int_{-\infty}^{\infty}\cdots\cdots dy_1dy_2dy_3d\tau\,, \tag{8.31}$$

and the retarded-time variable is

$$g=\tau-t+R_{\mathrm{m}}/c_0\,. \tag{8.32}$$

Similar to the classical FW–H equation, the convective FW–H equation (8.30) has the complexity of the concurrence of time and space derivatives on the source terms, including the Dirac delta function $\delta(f)$ and Heaviside function $H(f)$. The derivations of the thickness and loading source terms for numerical implementations are described in the following while the noise contribution from the quadrupole source term outside the integration surface is neglected.

8.4.1 Thickness noise

Obtained from Equation (8.30), the thickness noise contribution is [114]

$$4\pi p_T'=\left(\frac{\partial}{\partial t}+U_0\frac{\partial}{\partial x_1}\right)\int_{-\infty}^{t}\int_{\mathbb{R}^3}\left[Q_in_i\delta(f)\right]\frac{\delta(g)}{R^*}d^3\mathbf{y}d\tau\,. \tag{8.33}$$

Generally, for problems in aeroacoustics, the surface $f(\mathbf{x},t)=0$ can be described in a coordinate frame ($\boldsymbol{\eta}$-frame) that is fixed relative to the surface. The variable $\boldsymbol{\eta}$, regardless of the motion of the surface, is the Lagrangian variable of a point on the moving surface. Once the surface motion is specified, the trajectory of each point on the surface described by a fixed $\boldsymbol{\eta}$ may then be described in space-time in the $\mathbf{y}$-frame and given by the relation

$$\mathbf{y}=\mathbf{y}(\boldsymbol{\eta},\tau)\,. \tag{8.34}$$

The inverse transformation is

$$\boldsymbol{\eta}=\boldsymbol{\eta}(\mathbf{y},\tau)\,. \tag{8.35}$$

As these transformations are isometric, Equation (8.33) can be expressed as

$$4\pi p_T'=\left(\frac{\partial}{\partial t}+U_0\frac{\partial}{\partial x_1}\right)\int_{-\infty}^{t}\int_{\mathbb{R}^3}\left[Q_in_i\delta(f)\right]\frac{\delta(g)}{R^*}d^3\boldsymbol{\eta}d\tau\,. \tag{8.36}$$

Since the calculations on temporal derivatives are more efficient than those on spatial derivatives, the spatial derivative $\partial/\partial x_1$ in Equation (8.36) should be transformed into a temporal derivative which is more suitable for numerical implementation.

As, in Equation (8.36), only the term $\delta(g)/R^*$ is related to x and t, the spatial derivative $\partial/\partial x_1$ acting on it may be converted into temporal derivative $\partial/\partial t$ as follows: taking the divergence $\partial/\partial x_i$ of Equation (8.32) gives

$$\frac{\partial g}{\partial x_i} = \frac{1}{c_0}\frac{\partial R_{\mathrm{m}}}{\partial x_i}, \tag{8.37}$$

also, taking the divergence of $\delta(g)/R^*$ yields

$$\begin{aligned}\frac{\partial}{\partial x_i}\left[\frac{\delta(g)}{R^*}\right] &= \frac{\delta'(g)}{R^*}\frac{\partial g}{\partial x_i} - \frac{\delta(g)}{R^{*2}}\frac{\partial R^*}{\partial x_i} \\ &= \frac{1}{c_0}\frac{\partial R_{\mathrm{m}}}{\partial x_i}\frac{\delta'(g)}{R^*} - \frac{\partial R^*}{\partial x_i}\frac{\delta(g)}{R^{*2}} \\ &= \frac{1}{c_0}\tilde{R}_i\frac{\delta'(g)}{R^*} - \tilde{R}_i^*\frac{\delta(g)}{R^{*2}},\end{aligned} \tag{8.38}$$

since

$$\frac{1}{c_0}\frac{\partial}{\partial t}\left[\frac{\tilde{R}_i\delta(g)}{R^*}\right] = -\frac{1}{c_0}\tilde{R}_i\frac{\delta'(g)}{R^*}, \tag{8.39}$$

then, combining Equations (8.38) and (8.39), and eliminating $\frac{1}{c_0}\tilde{R}_i\frac{\delta\prime(g)}{R^*}$, yields

$$\frac{\partial}{\partial x_i}\left[\frac{\delta(g)}{R^*}\right] = -\tilde{R}_i^*\frac{\delta(g)}{R^{*2}} - \frac{1}{c_0}\frac{\partial}{\partial t}\left[\frac{\tilde{R}_i\delta(g)}{R^*}\right], \tag{8.40}$$

and particularly,

$$\frac{\partial}{\partial x_1}\left[\frac{\delta(g)}{R^*}\right] = -\tilde{R}_1^*\frac{\delta(g)}{R^{*2}} - \frac{1}{c_0}\frac{\partial}{\partial t}\left[\frac{\tilde{R}_1\delta(g)}{R^*}\right]. \tag{8.41}$$

Based on the above formulation, Equation (8.36) may be written as

$$\begin{aligned}4\pi p_T' = &\frac{\partial}{\partial t}\int_{-\infty}^{t}\int_{\mathbb{R}^3}[Q_i n_i\delta(f)]\frac{\delta(g)}{R^*}d^3\boldsymbol{\eta}d\tau \\ &-M_0\frac{\partial}{\partial t}\int_{-\infty}^{t}\int_{\mathbb{R}^3}[Q_i n_i\delta(f)]\frac{\tilde{R}_1\delta(g)}{R^*}d^3\boldsymbol{\eta}d\tau \\ &-U_0\int_{-\infty}^{t}\int_{\mathbb{R}^3}[Q_i n_i\delta(f)]\,\tilde{R}_1^*\frac{\delta(g)}{R^{*2}}d^3\boldsymbol{\eta}d\tau\,.\end{aligned} \tag{8.42}$$

Next, the same approach is used as described in [41] to transform the variable from τ to g and the Jacobian determinant is

$$\frac{\partial g}{\partial \tau} = 1 + \frac{1}{c_0}\frac{\partial R_{\mathrm{m}}}{\partial y_i}\frac{\partial y_i}{\partial \tau} = 1 - \frac{1}{c_0}\frac{\partial y_i}{\partial \tau}\tilde{R}_i = 1 - M_r\,, \tag{8.43}$$

in which $\tilde{R}_i = -\frac{\partial R_{\mathrm{m}}}{\partial y_i}$, and, $M_r = \frac{1}{c_0}\frac{\partial y_i}{\partial \tau}\tilde{R}_i = \frac{1}{c_0}v_i\tilde{R}_i$ is the component of the source Mach number vector in the radiation direction of the observer at the emission time τ. The expression $(1 - M_r)$ is the Doppler factor which is associated with a dilatation or contraction of the observer time scale with respect to the source time scale, depending on whether the source is moving away from or towards the observer.

Some particular formulations are needed to integrate the Dirac delta functions analytically. A change of the integration variable in Equation (8.42) is carried out by using the formula

$$\int_{-\infty}^{\infty} \mathcal{L}(\tau)\delta[g(\tau)]d\tau = \sum_{n=1}^{N} \frac{\mathcal{L}}{|\partial g/\partial \tau|}(\tau_{ret}^{n})\,, \tag{8.44}$$

in which the summation is taken over all the zeros τ_{ret}^{n} of the retarded time equation $g = \tau - t + \frac{R_{\mathrm{m}}}{c_0} = 0$. This relationship may be proved by changing the integration variable in $\int_{-\infty}^{\infty}\mathcal{L}(\tau)\delta[g(\tau)]d\tau$ from τ to $g(\tau)$ and the physical explanation for this is that sound signals emitted at different times from different positions can be received at the same time.

It is noted that all terms related to the derivatives of $|\nabla f| = 1$ are cancelled out in the final results and then, the condition of $|\nabla f| = 1$ can always be satisfied on the control surface [41]; thus, the following formulation may be deduced from the integration of the Delta function [122].

$$\int_{\mathbb{R}^3} \Phi(\mathbf{x})\delta(f)\,d^3\mathbf{x} = \int_{f=0} \Phi(\mathbf{x})\,dS\,. \tag{8.45}$$

Finally, utilizing Equations (8.43), (8.44) and (8.45), Equation (8.42) can be represented as

$$4\pi p_T' = \frac{\partial}{\partial t}\int_{f=0}\left[\frac{Q_i n_i}{R^*(1-M_r)}\right]_{\tau_e} dS(\boldsymbol{\eta}) - M_0\frac{\partial}{\partial t}\int_{f=0}\left[\frac{\tilde{R}_1 Q_i n_i}{R^*(1-M_r)}\right]_{\tau_e} dS(\boldsymbol{\eta}) - U_0\int_{f=0}\left[\frac{\tilde{R}_1^* Q_i n_i}{R^{*2}(1-M_r)}\right]_{\tau_e} dS(\boldsymbol{\eta}) , \quad (8.46)$$

8.4.2 Loading noise

The loading noise contribution obtained from Equation (8.30) is [114]

$$4\pi p_L' = -\frac{\partial}{\partial x_i}\int_{-\infty}^{t}\int_{\mathbb{R}^3}\left[L_{ij}n_j\delta(f)\right]\frac{\delta(g)}{R^*}d^3\mathbf{y}d\tau , \quad (8.47)$$

in which only the term $\delta(g)/R^*$ is associated with both x and t. To improve computational efficiency, the spatial derivative $\partial/\partial \mathrm{x_i}$ should be transformed into a temporal derivative $\partial/\partial \mathrm{t}$. Based on Equation (8.40), the above equation leads to

$$4\pi p_L' = \frac{\partial}{\partial t}\int_{-\infty}^{t}\int_{\mathbb{R}^3}\frac{1}{c_0}\left[L_{ij}n_j\delta(f)\right]\frac{\tilde{R}_i\delta(g)}{R^*}d^3\mathbf{y}d\tau + \int_{-\infty}^{t}\int_{\mathbb{R}^3}\left[L_{ij}n_j\delta(f)\right]\frac{\tilde{R}_i^*\delta(g)}{R^{*2}}d^3\mathbf{y}d\tau . \quad (8.48)$$

Similar to the thickness noise source, using Equations (8.43), (8.44) and (8.45), the loading noise contribution can be reformulated as

$$4\pi p_L' = \frac{1}{c_0}\frac{\partial}{\partial t}\int_{f=0}\left[\frac{L_{ij}n_j\tilde{R}_i}{R^*(1-M_r)}\right]_{\tau_e} dS(\boldsymbol{\eta}) + \int_{f=0}\left[\frac{L_{ij}n_j\tilde{R}_i^*}{R^{*2}(1-M_r)}\right]_{\tau_e} dS(\boldsymbol{\eta}) . \quad (8.49)$$

8.4.3 Wind-tunnel case

Both the source and the observer are stationary for wind-tunnel cases. As a result, the emission distances R^*, R_{m} and their spatial derivatives $\tilde{R}_i^*$ and $\tilde{R}_i$, respectively, are constants and independent of time. The local normal vector components n_i also do not vary with time. The components of the source Mach number vector M_r are zeros. Therefore, the thickness and loading noise source terms given by Equations (8.46) and (8.49) can be simplified to

$$4\pi p_T' = \int_{f=0}\left[\left(1-M_0\tilde{R}_1\right)\frac{\dot{Q}_i n_i}{R^*} - U_0\frac{\tilde{R}_1^* Q_i n_i}{R^{*2}}\right]_{\tau_e} dS(\boldsymbol{\eta}) , \quad (8.50)$$

$$4\pi p_L' = \int_{f=0} \left[\frac{1}{c_0} \frac{\dot{L}_{ij} n_j \tilde{R}_i}{R^*} + \frac{L_{ij} n_j \tilde{R}_i^*}{R^{*2}} \right]_{\tau_e} dS(\boldsymbol{\eta}) , \tag{8.51}$$

in these equations, a dot over a variable implies temporal derivatives with respect to the source time; integrands with $1/R^*$ dependence are far-field terms and those with $1/(R^{*2})$ dependence dominate the near field.

8.5 Numerical Algorithm for Noise Prediction

If the volume (quadrupole) noise sources outside the permeable integration surface are neglected, the data input to the acoustic analogy solver are the time-dependent flow field and the geometry information on a surface mesh element (panel), provided directly from the CFD simulations. The panels can be considered as compact sources in the noise calculation for low Mach number cases since they are typically much smaller than any representative acoustic wavelength. Moreover, the panel size should be kept sufficiently small to ensure that, over the panel, the retarded time does not vary significantly and the source strength variation is approximately linear [42]. As the flow properties loaded from the CFD data are generally specified at the panel centres, a refinement of the mesh element size is needed if such midpoint values are unlikely to represent the mean value of source strength over the panel.

8.5.1 Comparison of retarded time method and advanced time approach

The distinction between the emission time and the observer time in Equation (2.24) should be noted. The contributions from each source are evaluated at the emission time. Different sources have different emission time values based on their positions relative to the observers. Therefore, the sound is emitted at different retarded times and covers different distances before reaching the receiver positions depending on the location and velocity of both the source and observer. Generally, both the retarded time method and advanced time approach (also known as the source time-dominant algorithm) may be available for the numerical implementation of Equation (2.24) and are described as follows.

In the retarded time method, the solution is evaluated in the observer time frame. The reception time is kept constant at each time step and the emission time is calculated for each source location. This approach requires the associated flow properties to be obtained using a temporal interpolation at the emission time and the flow-field variables of multiple simulation snapshots to be uploaded for each observer time step calculation. Therefore, this approach involves a large memory usage and computational cost to interpolate the time-resolved CFD results.

Alternatively, the advanced time approach uses the same formulation as the retarded time method but inverts the role of emission time and reception time: here, from the view of the source, the emission time is chosen as the primary variable to evaluate the solution [123]. Therefore, at each flow-field time step and for each source element, the time (advanced time) at which the corresponding disturbance will reach the observer is calculated. The receiver location is used to calculate the relative position between the observer and the elemental source. The source terms of Equation (2.24) are evaluated at each point in space along with the arrival time value. Thus, the acoustic signals are finally built up in the observer time frame through a summation over all the contributions computed from the integration source domain. The sound pressure history at the observers is then constructed based on the calculation evolved along the source time axis.

Compared with the retarded time method, the advanced time approach is better suited to handle large input datasets provided by time-dependent CFD solution. With no time interpolation of the input data required, the integrands are directly evaluated once the CFD input is available. This source time-dominant algorithm is intrinsically parallelizable and results in significant reduction in memory requirement [123]. In the advanced time approach, matrices of the full transient flow properties from the CFD solution data are loaded and manipulated at each computational time. All resulting contributions from source panels are then summed to give the time history of the pressure received by the observer at the proper advanced time. It is noted that as the receiver time is unequally spaced, the sound emitted at the same time by different panels on the control surface will reach the observer at different times. Therefore, for each individual source panel,

the time interpolation of the output time history of sound pressure is required to ensure that the contributions from all the control surface points are accounted for and added up at the same receiver time. Once the contributions from all points in the control surface have been calculated, the flow properties at the next source time step from the CFD data are loaded and processed.

8.5.2 Spatial interpolation

In general, a very fine surface mesh is discretized for aeroacoustic simulations and a simple first-order method is reasonably applied to perform the spatial integration over the surface elements (panels). As an example, the following generic retarded-time formulation is considered.

$$4\pi p'(\mathbf{x},t) \approx \int_{f=0} \left[\frac{Q(\mathbf{y},\tau)}{R^*(1-M_r)}\right]_{\tau_e} dS\,, \tag{8.52}$$

in which $Q(\mathbf{y},\tau)$ is the source strength. The discrete computation method corresponding to the above equation is given by

$$4\pi p'(\mathbf{x},t) \approx \sum_{i=1}^{N} \left[\frac{Q(\mathbf{y}_i,\tau_i)}{R_i^*(1-M_r)_i}\right]_{\tau_e} \Delta S_i\,, \tag{8.53}$$

where the control surface S is divided into N panels and the i refers to ith panel. The integrand is calculated at each panel centre at the retarded time [42].

It should be mentioned that a Gaussian quadrature using two-point formulae may be utilized to replace the integral evaluation at the single panel centre in Equation (8.53), and thus the increased calculation accuracy of the integrand will be achieved. Moreover, a larger number of quadrature points is needed to improve further the computation accuracy for noise prediction if the source strength variation over the panel requires it.

8.5.3 Numerical implementation

The aerodynamic noise prediction code is written in Fortran based on the convective FW-H formulation introduced above. As mentioned before, the time-dependent flow field and the geometry information on surface panels are loaded

from the CFD simulation data. For the current work, the noise contributions from source terms are computed over a fictitious, permeable data surface and thus the quadrupole source contribution inside the surface can be accounted for by the surface integrals. Since the mesh around the bodies is generated according to a grid convergence study and is sufficiently fine based on the verification of the noise predictions by the experimental measurements, the first-order method is utilized initially to perform the spatial integration over the surface elements. The advanced time approach is utilized and the source time derivative is performed using fourth-order central differences given by

$$Q'(x) = \frac{-Q(x+2\Delta t) + 8Q(x+\Delta t) - 8Q(x-\Delta t) + Q(x-2\Delta t)}{12\Delta t}, \tag{8.54}$$

where Δt is the time step of the flow field.

8.5.4 Numerical verification

The far-field noise radiated from a point monopole and a point dipole source is used to validate the noise prediction code based on the convective FW-H formulation. The harmonic velocity potentials for the point monopole and point dipole sound field in a moving medium [114,124] are given respectively as

$$\phi(\mathbf{x}, t) = \frac{A}{4\pi R^*} \exp[i\omega(t - \frac{R}{c_0})], \tag{8.55}$$

and

$$\phi(\mathbf{x}, t) = \frac{\partial}{\partial x_3}\left\{\frac{A}{4\pi R^*} \exp[i\omega(t - \frac{R}{c_0})]\right\}, \tag{8.56}$$

where R is the emission distance defined as R_{m} in Equation (8.25) and R^* is the radiation distance calculated by Equation (8.26); the non-dimensional angular frequency is $\omega l/c_0 = 4\pi/46$ and the normalized amplitude is $A/(lc_0) = 0.1$. The reference length is l which is non-dimensionalized by $L = 1m$. The source coordinate system is (x_1, x_2, x_3) and the dipole axis is aligned with the positive x_3-direction.

Assuming a mean flow U_0 (30 m/s) along the positive x_1-direction, the induced pressure, particle velocity and density are

$$p'(\mathbf{x},t) = -\rho_0\left(\frac{\partial}{\partial t} + U_0\frac{\partial}{\partial x_1}\right)\phi\,, \tag{8.57}$$

$$u(\mathbf{x},t) = \nabla\phi(\mathbf{x},t)\,, \tag{8.58}$$

$$\rho'(\mathbf{x},t) = p'(\mathbf{x},t)/c_0^2\,. \tag{8.59}$$

The real parts of pressure $p'(\mathbf{x},t)$, velocity $u(\mathbf{x},t)$ and density $\rho'(\mathbf{x},t)$ are used as the variables and evaluated analytically on the integration permeable surface as source terms. Then the far-field acoustic pressure is predicted by using the convective FW-H equation and compared with analytical calculations. The integration surface is defined as a cube that extends from $-5l$ to $5l$ in all three coordinate directions and each cube surface consists of $50l \times 50l$ evenly spaced integration panels.

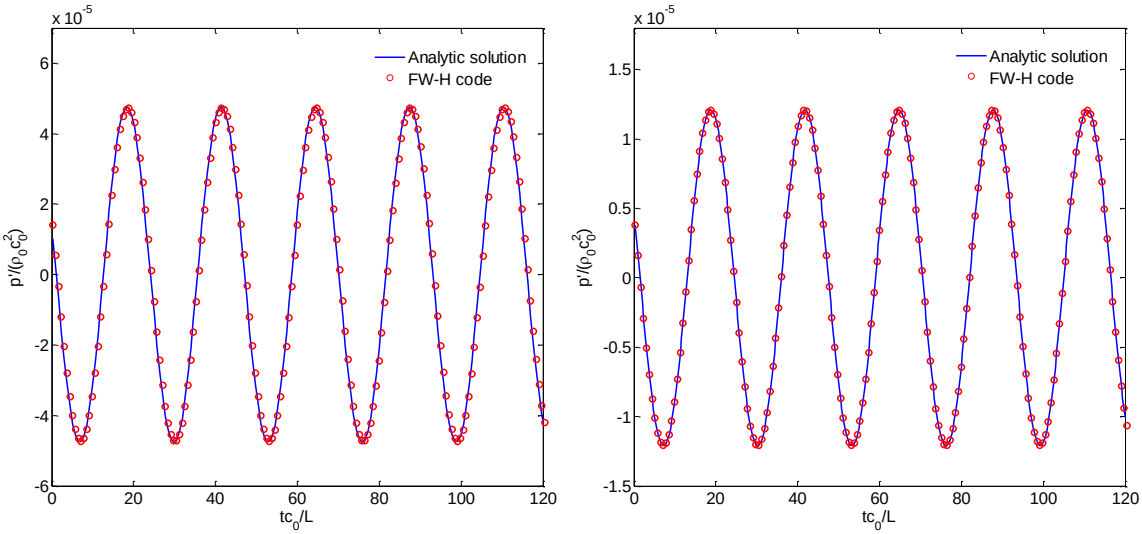

(a) Monopole source Dipole source

Figure 8.2: Comparisons of time history of sound pressure between analytical and predicted solutions

Figure 8.2 depicts the comparisons of the time history of sound pressure between the analytical solution and the numerical prediction for the monopole and dipole sources. The observer is located at $(-50l,\ 0,\ 0)$ for the monopole case and at $(0,\ 0,\ 50l)$ for the dipole case. The sound pressure is non-dimensionalized by $\rho_0 c_0^2$ and the time is non-dimensionalized by l/c_0. Furthermore, the directivity patterns of the sound radiation for the two cases are depicted in Figure 8.3, where the receivers are distributed uniformly along a circumference with a radius of $50l$ at an interval of 5º and the root-mean-square fluctuating pressure p_{rms} (=

$\left|p'(\mathbf{x},t)/\sqrt{2}\right|$, where $p'(\mathbf{x},t)$ is taken from the averaged magnitude) is displayed. Note that the directivity pattern is directional towards upstream of the sound source due to convective amplification caused by the moving medium. Based on the comparisons in Figures 8.2 and 8.3, it is found that the pressure fluctuation induced by the monopole is about four times as large in magnitude as that induced by the dipole as expected. Moreover, the time history and directivity pattern of the far-field sound pressure are in excellent agreement between the analytical solution and the numerical calculation for both monopole and dipole test cases.

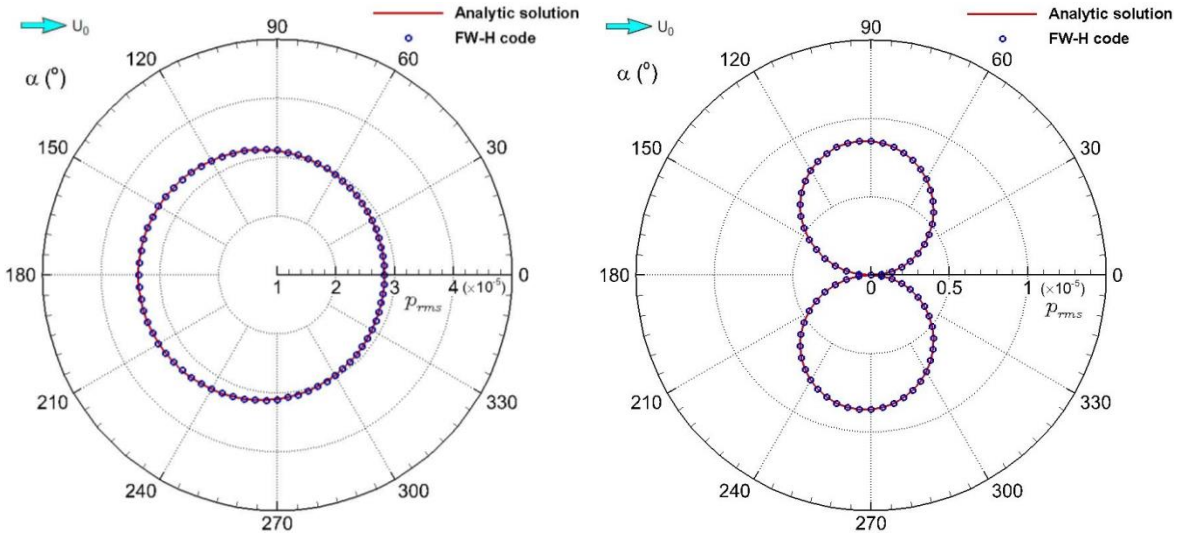

(a) Monopole source with the observer at $(-50l,\ 0,\ 0)$

(b) Dipole source with the observer at $(0,\ 0,\ 50l)$

Figure 8.3: Comparisons of noise directivity between analytical and predicted solutions

Additionally, the idealized wheel case (see Section 5.6) is used to compare the noise predictions between the solid and permeable data surfaces. Figure 8.4 sketches the wheel physical surfaces enclosed by the permeable surfaces and shows the iso-surfaces of the second invariant of the velocity gradient Q of the flow developed around the wheel. Figure 8.4(a) displays the closed permeable surfaces constituting a porous box with dimensions of $1.5D \times 1.5D \times 0.5D$ (length, height and width, where D is the wheel diameter). By removing the downstream part of the closed permeable box and extending its top, bottom and side surfaces to the end of the computational domain, an open porous box with five permeable surfaces is established as shown in Figure 8.4(b). The trackside receiver is

located 2.5 m away and 0.35 m above the wheel centre. The noise calculation using the physical solid surfaces is based on Farassat's Formulation 1A (introduced in Section 3.2.3) and the current FW-H code is applied for the noise prediction on the permeable integration surfaces for comparing the noise predictions from different methods. Generally, the compressible flow field needs to be solved and the data are applied for noise prediction in the FW-H acoustic analogy method using permeable integration surface. Considering a low Mach number flow simulated here as mentioned in Section 3.2.2 and for consistency with the calculations from the solid data surfaces, the incompressible flow data on the permeable integration surfaces are utilized for the noise predictions. Figure 8.5 displays the spectra of the noise radiated from the solid and two types of permeable surfaces. Figure 8.5(a) shows that the noise predictions from the solid and closed permeable surfaces have a good matching, especially in the frequency range between 100 Hz and 900 Hz. Compared with the results from the solid surfaces, the overall sound pressure level of noise predicted from the closed permeable surfaces is 4 dB higher within the frequency range below 10 kHz. This is because pseudo-sound is generated by the turbulent eddies in the wheel wake region passing through the porous surfaces, as indicated in Figure 8.4(a) for the downstream outflow surface. Keeping all the permeable surface further away from the geometries can reduce the pseudo-sound produced from the hydrodynamic perturbations; however, it will increase the computation cost greatly as the grids from the geometries to the permeable surface should be kept fine enough to get physically correct results. Moreover, it is found that the noise predicted from the open permeable surfaces corresponds fairly well with those from the solid and closed permeable surfaces in most of the frequency range whereas the spectrum amplitude of noise is about 20 dB higher below 200 Hz (shown in Figure 8.5b), leading to the unphysical results within this low-frequency range. This is because in the open-surface noise predictions the acoustic signals calculated do not decay properly and the computations are unbalanced, especially at low frequencies. Similar influences of the open control surface ware also observed in the noise predictions of a simplified landing gear using FW-H method [3]. As the permeable data surfaces are applied, the quadrupole sources between the solid surfaces and the porous surfaces are accounted for by the

surface integrals although its contributions are rather small at low Mach numbers [42]. Note that in an incompressible flow solver, the sound speed is effectively infinite and the acoustic propagating waves cannot be properly captured by the permeable surfaces. However, these noise signals are relatively small for the current cases at low Mach numbers.

Based on the above validation test cases, it is demonstrated that the FW-H code can be used for far-field noise prediction.

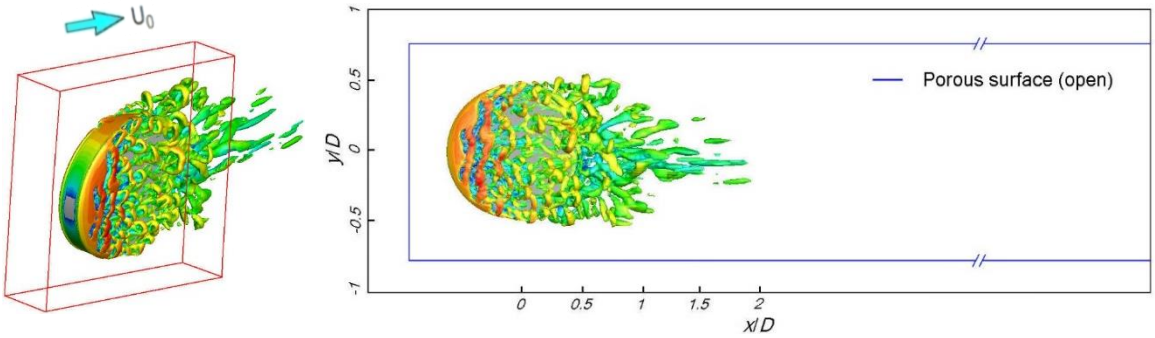

(a) Closed surfaces (b) Open surfaces

Figure 8.4: Sketches of permeable surfaces used for wheel test case

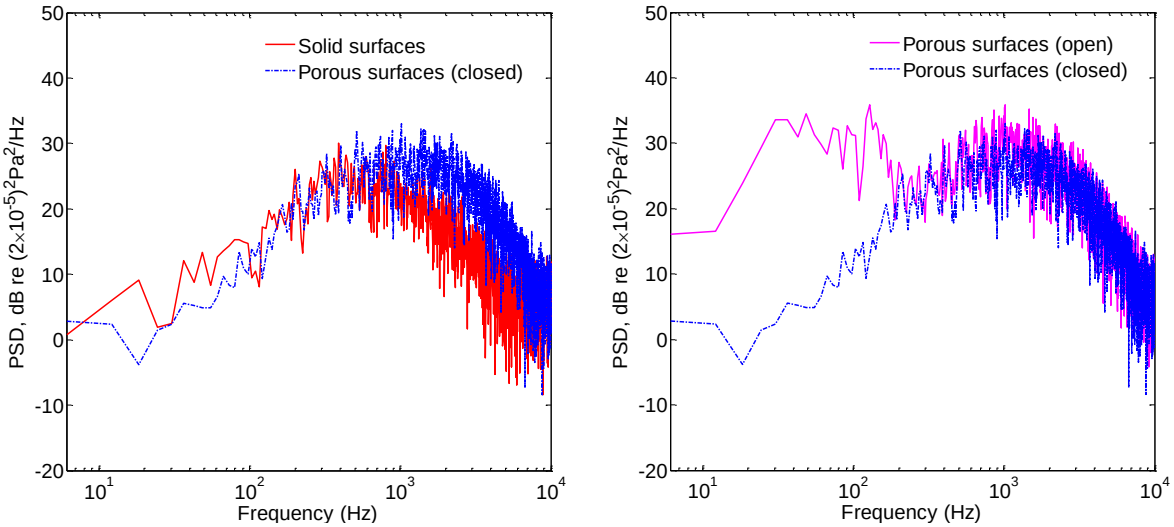

(a) Solid and closed surfaces (b) Open and closed surfaces

Figure 8.5: Comparisons of spectra of far-field sound pressure

8.6 Influence of Bogie Fairing on Sound Generation

The mesh models of the bogie-inside-cavity cases with and without the fairing have been introduced in the previous chapter. These are now used for the noise predictions using permeable data surfaces. As discussed in Section 7.4.2, the noise generated from the bogie solid surfaces alone radiated to the free space in the trackside direction is very similar in the cases without and with the fairing. Additionally, however, the noise generated inside the bogie cavity will be shielded by the cavity walls and the fairing. Moreover, additional noise will be produced by the bogie cavity flow impinging on the cavity walls. Therefore, the radiated noise is calculated using the acoustic analogy implemented on a permeable surface located at a distance from the carbody sidewall, extending over the whole height and length of the domain.

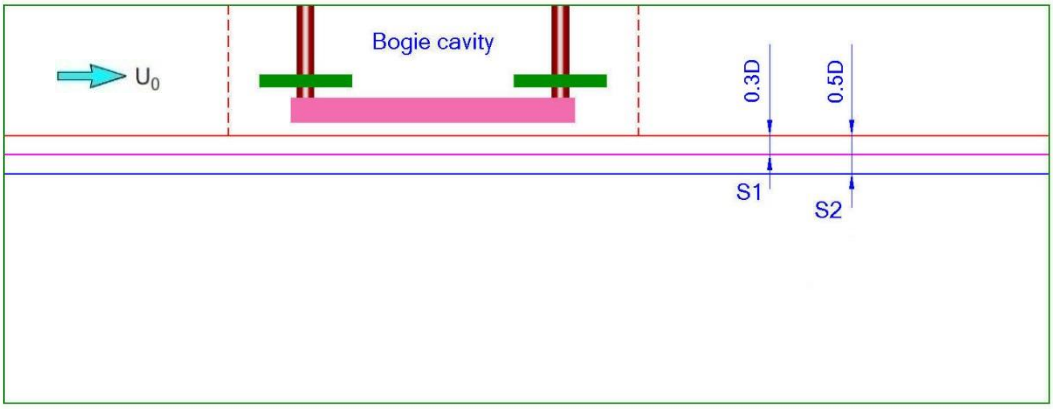

Figure 8.6: Sketch of porous surfaces used for FW-H integration (top view, not to scale)

Figure 8.6 illustrates the porous surfaces (S1 and S2) used for the FW-H integration. The gap between the porous surface (S1) and the carbody side wall is $0.3D$ (where D is the bogie cavity depth of 70 mm) and that for the porous surface S2 is $0.5D$. The mesh between the two permeable surfaces is kept fine to ensure that the flow calculations with high resolution are performed around these data surfaces. These two gap distances are chosen based on noise predictions in [125] on a two-dimensional rectangular cavity flow, where the cases of three integration lines with different distances to the cavity top wall were simulated and the numerical results from the FW-H method were in good agreement with the direct numerical simulations. In the current calculations, there are 129,666 panels on the permeable data surface for the bogie-inside-cavity case without the fairing and 128,010 panels on the permeable surface for the

case with the fairing. As the incompressible flow solver is utilized, the density remains constant; thus, the variables of pressure and three velocities in the coordinate directions on the permeable surfaces are recorded and utilized to calculate the far-field acoustic signals based on the noise prediction code as discussed in Section 8.5. Same as described in Section 7.4.1, the CFD simulations were run for 1.1 s corresponding to 17 times the flow-through time for both cases and the length of the time signal used as input for noise calculation corresponds to the last 0.52 s of the computations. Also, the PSD of the far-field noise signal is computed by Welch's method with a frequency resolution of 6 Hz.

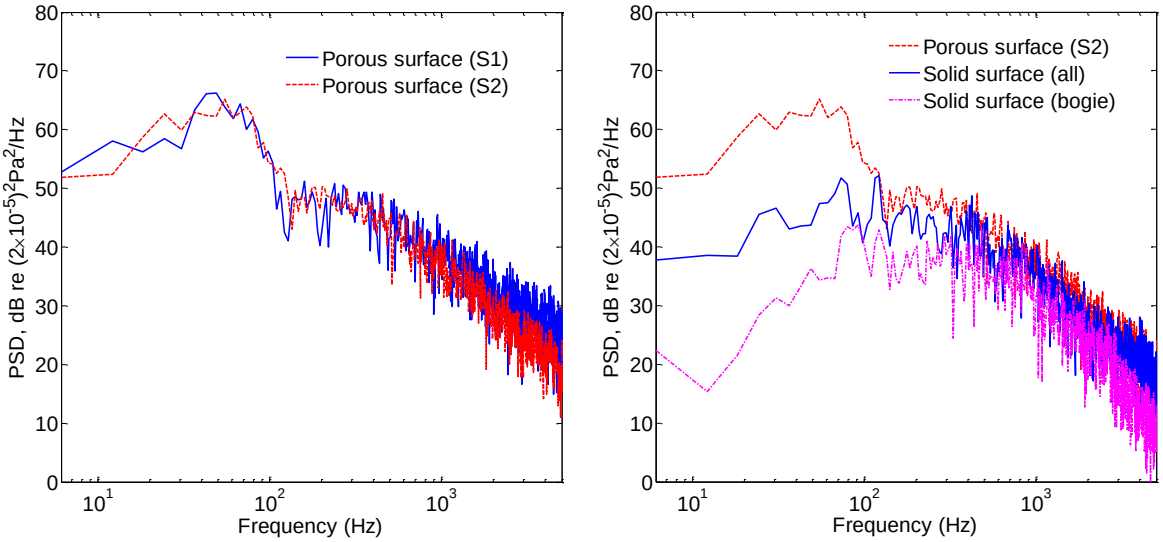

(a) Two porous surfaces (b) Porous and solid surfaces

Figure 8.7: Comparisons of far-field noise spectra in bogie cavity case without fairing

Figure 8.7 displays the comparisons of the far-field noise spectra of the bogie-inside-cavity case without the fairing based on the numerical simulations on the half bogie shown in Figure 7.1 using the permeable data surfaces in the FW-H method. The receiver is located 2.5 m away and 0.35 m above the bogie centre. This lateral distance of 2.5 m also corresponds at full scale to 25 m as used in field measurements of railway noise, e.g., in ISO 3095 [87]. Figure 8.7(a) shows that the noise predictions of the FW-H integrations on the two permeable surfaces (S1 and S2) are very similar, indicating that the influence of the placement of these two surfaces on calculating the far-field acoustic signals is negligible. By comparison, for the bogie-inside-cavity case covered by the fairing, there is no surface shape discontinuity around the bogie area on the carbody side wall, thus

the flow would be less unsteady on the side permeable surface (S1) and the difference of the noise predictions on the two surfaces (S1 and S2) is expected to be smaller. Figure 8.7(b) compares the noise predictions from permeable (S2) and solid data surfaces for bogie cavity case without the fairing. It shows that due to the noise produced from the carbody, especially the bogie cavity wall and trailing edge, the noise generated from all solid surfaces is about 6 dB higher than that from the bogie wall surfaces alone in the frequency range below 2 kHz. Moreover, compared with the noise generated from all wall surfaces, the spectrum amplitude of noise predicted by the permeable integration surfaces is around 20 dB higher below 120 Hz due to the unphysical results generated since the low-frequency acoustic signals cannot be cancelled properly in the noise calculations using open permeable surfaces, as discussed in Section 8.5.4 for the isolated wheel case. Therefore, the frequency range between 120 Hz and 2 kHz will be used for noise prediction, and within this frequency range, the noise generated from the permeable integration surface (S2) is 2.6 dB (from the permeable surface S1 is 3.1 dB) higher than that from all solid surfaces since the pseudo-sound is generated by the turbulent eddies passing through the permeable surface. The quadrupole noise generated by the turbulent flow around the geometries is also captured by the surface integrals although the quadrupole contribution is rather small for current cases at low Mach numbers. To reduce the computation cost, the permeable surface (S1) is used for the noise predictions of the subsequent bogie-inside-cavity cases.

Figure 8.8 shows the comparisons of the far-field noise predictions from the permeable surface (S1) for the bogie-inside-cavity cases without and with the fairing. Figure 8.8(a) depicts the far-field noise spectra of these two bogie-inside-cavity cases. The receiver is again located 2.5 m away and 0.35 m above the bogie centre. It is found that the spectrum level is lower for the bogie cavity case with the fairing in the frequency range between 120 Hz and 2 kHz and the corresponding OASPL is 62.9 dB, about 4 dB lower than the case without the fairing, the level of which is 67.2 dB. Figure 8.8(b) displays the noise directivity from the permeable surface for the two bogie cavity cases. The OASPL is also calculated from the PSD over the frequency range from 120 Hz to 2 kHz and the

receivers are distributed uniformly along a semicircle with 2.5 m radius from the bogie centre in the bogie horizontal central plane. Again, a lateral dipole pattern of noise radiation is predicted with noise amplitudes about 3.8-6.6 dB lower for the case with the fairing compared with the case without the fairing. Note that this noise reduction is obtained due to the change of the hydrodynamic flow field around the permeable surfaces by considering the shielding effect through mounting a fairing in the bogie cavity region and it would be different if the compressible flow were solved for noise predictions to take into account the acoustic propagation and the effects of the acoustic shielding and scattering of sound waves by the solid surfaces. However, these influences are expected to be small on noise predictions of these side receivers located in the bogie horizontal central plane for the current cases at low Mach numbers.

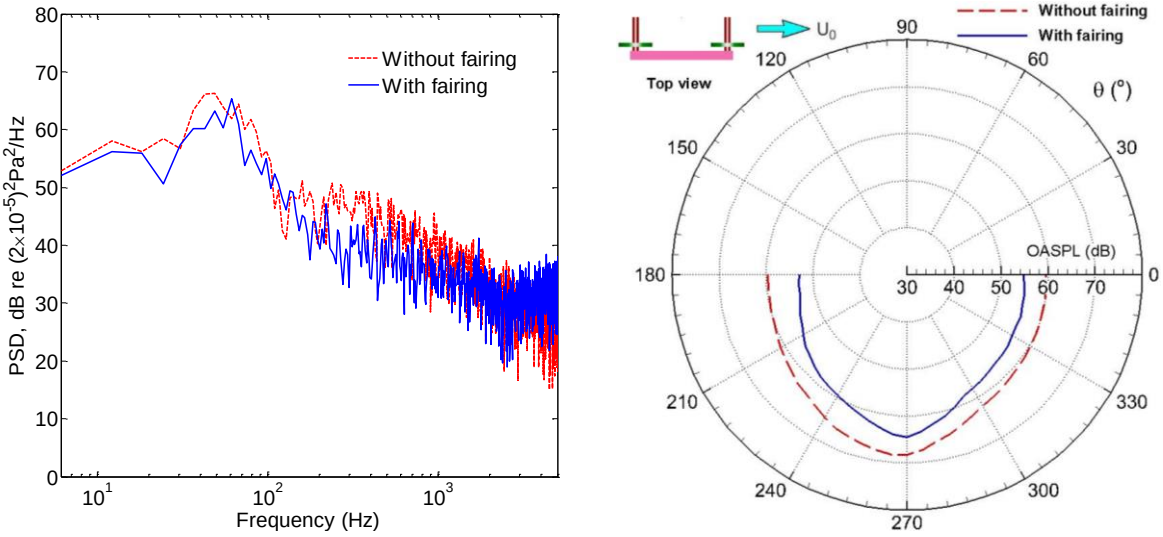

(a) Noise spectra (b) Noise directivity

Figure 8.8: Comparisons of far-field noise prediction from permeable surface (fairing effect)

8.7 Influence of Ground on Sound Generation

The porous surface (S1) in Figure 8.6 is used for the FW-H integration and there are 140,988 panels on the permeable surface for the bogie-inside-cavity case with the ground underneath. The image method is used to account for the sound reflection of the ground [126]. Assuming no sound absorption from the ground, an equivalent noise source is located symmetrically with respect to the ground

surface and generates a sound field with the same symmetry. Corresponding to the previous bogie-inside-cavity cases with and without the fairing, the frequency range between 120 Hz and 2 kHz is used for noise prediction.

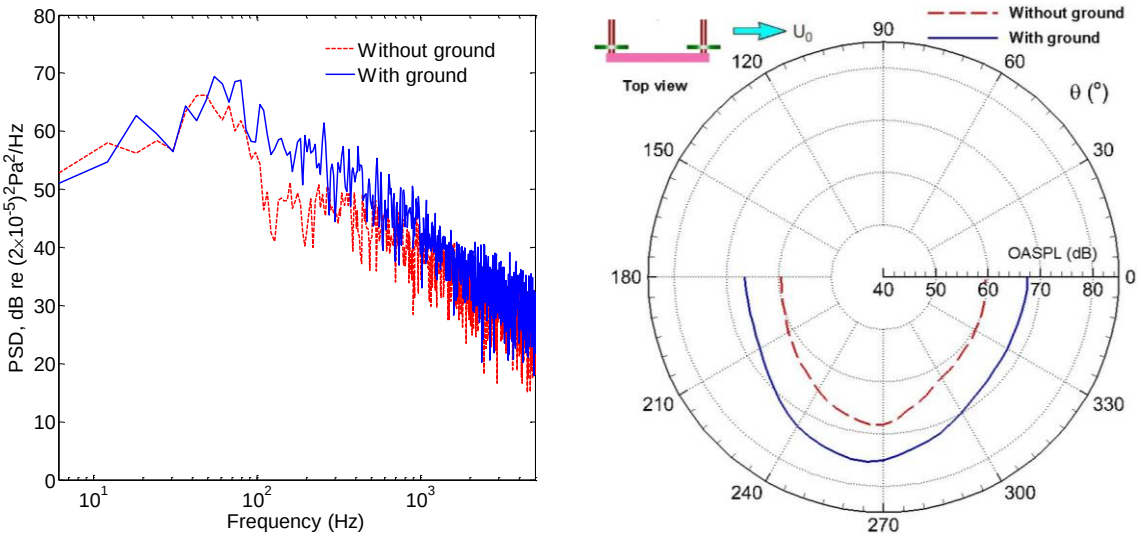

(a) Noise spectra (b) Noise directivity

Figure 8.9: Comparisons of far-field noise prediction from permeable surface (ground effect, cases without fairing)

Figure 8.9 shows the comparisons of the far-field noise predictions from the permeable surface (S1) for the cases of bogie inside the cavity with and without the ground (having no fairing) based on the corresponding flow simulation on each case. Figure 8.9(a) displays the far-field noise spectra of the two cases in which the case of without the ground is same as the case of without the fairing shown in Figure 8.8. The receiver is located 2.5 m away and 0.35 m above the bogie centre. It is found that the spectrum level is generally larger for the bogie cavity case with the ground underneath in most of the frequency range and the OASPL within the frequency range from 120 Hz to 2 kHz is 74.2 dB, 7 dB higher than the case without the ground (OASPL of 67.2 dB). Figure 8.9(b) displays the noise directivity from the permeable surfaces for the two cases with and without the ground. Again, the OASPL is calculated from the PSD over the frequency range from 120 Hz to 2 kHz and the receivers are distributed uniformly along a semicircle with 2.5 m radius from the bogie centre in the bogie horizontal central plane. A lateral dipole pattern of noise radiation is predicted with noise levels around 6-8 dB higher for the case with the ground underneath compared with the

case with no ground. This is because the moving ground and the rotating wheelsets increase the noise generation and the ground reflection effect increases the sound radiation for the case with the ground.

8.8 Summary

Based on the convective FW–H equation for the moving medium cases, an aerodynamic noise prediction code is developed using the advanced time algorithm. The validity of the code is demonstrated by the test cases. The noise generated from the point monopole and point dipole sources situated in a moving mean flow is predicted numerically and found to be in perfect agreement with the corresponding analytical solutions. Using the idealized wheel case, the noise predictions from the permeable and solid data surfaces correspond well below 1 kHz whereas at higher frequencies the noise calculated from the permeable surfaces is 4 dB larger due to the wheel wake impinging on the porous surfaces and resulting in the pseudo-sound produced from the hydrodynamic perturbations. Moreover, for all the bogie-inside-cavity cases considering the influence of the bogie fairing and ground, the noise radiated to the trackside is predicted using a side permeable integration surface close to the region of bogie cavity and parallel to the carbody side wall. Based on the cases with and without the fairing, it is found that the noise directivities have a lateral dipole pattern, and the bogie fairing is effective in reducing the noise levels in most of the frequency range and a noise reduction up to 6.6 dB is achieved for the current model case by mounting a fairing in the bogie area. Moreover, for the bogie-inside-cavity case with the ground underneath, a lateral dipole pattern of noise radiation is also predicted with noise levels around 6-8 dB higher compared with the case without the ground. Note that the current noise predictions would be different if the acoustic propagation and the effects of the acoustic shielding and scattering of sound waves by solid surfaces were calculated using the compressible flow solver. However, these influences are expected to be rather small for the current cases at low Mach numbers.

Chapter 9

Conclusions and Future Work

Aerodynamic noise becomes significant for high-speed trains and its prediction in an industrial context is difficult to achieve due to large computational resources required for unsteady numerical simulations. As one of the main aerodynamic noise sources of high-speed trains, the bogie is a complex structure containing many components with surface shape variations and discontinuities, and thus the flow developed around it is highly turbulent. Most of the researches were based on the experimental measurements to characterize the aerodynamic noise generation from the bogie area. By comparison, this study investigated numerically the aerodynamic and aeroacoustic characteristics of the flow past the scale models with increasing complexity around high-speed train bogie region. More details of the flow behaviour and the corresponding aeroacoustic mechanisms have been revealed in the train bogie area and these findings are helpful to understand the aerodynamic noise generating mechanisms of the full-scale cases from the high-speed train. This final chapter summarizes the major conclusions of this study followed by the recommendations on future work.

9.1 Conclusions

The flow behaviour and the corresponding aeroacoustic mechanisms of some main components around a high-speed train bogie region have been investigated using the DDES model and the FW-H acoustic analogy. In order to verify the numerical simulations, PIV experiments were performed in the wind tunnel to investigate the mean velocity field and the aerodynamic noise measurements were carried out in an open-jet anechoic chamber to obtain the far-field acoustic signals. The main conclusions are drawn as follows.

9.1.1 Isolated wheelset

Due to the vortex shedding and flow separation around an isolated wheelset, a complicated three-dimensional wake structure with both streamwise and spanwise vortices is developed around the isolated wheelset. Tonal noises are generated with dominant frequencies associated with the lift and drag forces and the noise directivity of a vertical dipole pattern is predicted. A slightly higher noise level is obtained considering the rotation of the wheelset. As the inflow velocity increases, the noise levels increase corresponding to an increase in the radiated sound power in proportion to the sixth power of the flow speed for a dipole sound source and the frequencies of spectral peaks increase corresponding to an invariant Strouhal number characterized by regular vortex shedding. CFD simulations and PIV measurements show that an asymmetric flow pattern is formed in the wheelset wake due to the influence from the ground effect. Compared with the idealized wheel, the noise generated from a detailed wheel is larger and more broadband due to stronger turbulent flow developed around it. By comparison, the isolated wheel (idealized wheel or detailed wheel) has a lateral dipole pattern of noise directivity and its sound radiation is generally much weaker than the noise generated from the whole wheelset.

9.1.2 Tandem wheelsets and simplified bogie

For the tandem-wheelset and simplified bogie cases, the vortices shed from the upstream geometries are convected downstream and impinge on the downstream ones, resulting in a highly turbulent wake behind the downstream geometries. For both cases, tonal noise is generated with dominant frequencies corresponding to the lift dipole due to the vortex shedding formed around the axles. A vertical dipole pattern of noise radiation is predicted for the upstream wheelset, whereas the downstream wheelset has a multi-directional directivity pattern and its sound generation is comparatively weaker. Expressed relative to the geometry centre, the noise directivity has a dipole pattern biased towards the upstream direction because the large-scale regular vortex shedding is produced from the upstream axle while the downstream geometries are submerged in the

decayed and less energetic turbulent incoming flow. Compared to the wheelsets, the noise contribution from the bogie frame is relatively small.

9.1.3 Simplified bogie inside bogie cavity

For the bogie-inside-cavity cases with and without the fairing, a shear layer developed from the cavity leading edge has a strong interaction with the flow separated from the upstream bogie and cavity wall, and thus a highly irregular and unsteady flow is generated inside the bogie cavity due to the strong flow impingement and recirculation occurring there. Compared to the bogie cavity case without the fairing, the stronger flow interactions are developed around the bogie inside the cavity covered by the fairing. The noise radiated from the bogie solid surfaces alone to the free space is assumed to compare the bogie-inside-cavity cases with and without the fairing. Results show that different from the isolated bogie case, the noise spectra are broadband with no distinct peak and a lateral dipole pattern of noise radiation is predicted for these two cases. Additionally, based on the noise predictions using the permeable integration surfaces in the FW-H method, it is found that the bogie fairing is effective in reducing noise generation and emission around the bogie area.

For the case of the bogie inside the bogie cavity with the ground underneath, a similar flow field is generated with more flow interactions developed inside the bogie region compared to the bogie-inside-cavity cases without the ground, and therefore the noise level is increased in the noise directivity of a lateral dipole pattern since the rotating wheelsets and the moving ground increase the noise generation and the ground reflection effect increases the sound radiation.

9.2 Future Work

The flow behaviour and aeroacoustic characteristics of a simplified bogie inside the bogie cavity and its isolated components have been studied. The influences of the bogie fairing and ground were discussed. It should be noted that for a full-scale bogie in reality, the Reynolds number is much higher. Moreover, the

turbulent inflow and the complex geometry will lead to complex flow structures and these will affect the noise radiated. In the industry context it is desirable to be able to predict the flow-induced noise for a detailed high-speed train at full scale with required accuracy, performing the noise assessment early in the design phase and implementing the train optimisation to improve the environment for those affected by the high-speed train noise. The future work to extend the understanding of the aerodynamic and aeroacoustic behaviour of a high-speed train is recommended as follows.

9.2.1 Aerodynamic noise predication for high-speed train in reality

The turbulent inflow conditions for high-speed train and a more detailed train configuration with more components present in reality need to be considered in the simulations to investigate the corresponding noise generating mechanisms. Moreover, the ground effects, including the rail underneath the wheels and the realistic trackbed geometry, i.e. the type of sleepers and the level of the ballast bed surface, provide a certain degree of surface roughness and will have a strong influence on the flow developed underneath a high-speed train, particularly around the bogie areas. The relative movement between the train and sleepers should be included if the detailed geometries of the sleepers are included as a boundary condition.

9.2.2 Numerical simulation and computational modelling

For the aerodynamic noise prediction code performed in this study, the Gaussian quadrature formulae with two or more integration points should be utilized to replace the integral evaluation at the single panel centre, and thus increased calculation accuracy of the integrand will be achieved. A compressible flow solver needs to be utilized for flow calculation to consider the acoustic propagation and the effects of the acoustic shielding and scattering of sound waves by the solid surfaces, which are potentially important for complex geometries with much higher inflow velocity than the current cases investigated. In reality, the high-speed trains are running along the railway lines and generally different from the wind-tunnel cases. Therefore, the by-pass noise generation from the moving train

should be calculated to include the Doppler effect. The Spalart-Allmaras turbulence model and the delayed detached-eddy simulation model have been applied throughout this research. The comparisons with the other turbulence models and the further mesh refinement implemented on the grids generated around the geometries may improve the accuracy of numerical simulations. Moreover, some non-traditional CFD methods, which are suitable to handle complex arbitrary geometries like a whole train at full scale, should be considered and compared with the conventional numerical schemes.

References

[1] C. Mellet, F. Létourneaux, F. Poisson, C. Talotte. High speed train noise emission: Latest investigation of the aerodynamic/rolling noise contribution. Journal of Sound and Vibration, 2006, 293: 535-546.

[2] W. Dobrzynski. Almost 40 years of airframe noise research: What did we achieve? Journal of Aircraft, 2010, 47(2): 353-367.

[3] P.R. Spalart, M.L. Shur, M.Kh. Strelets, A.K. Travin. Initial noise predictions for rudimentary landing gear. Journal of Sound and Vibration, 2011, 330, 4180-4195.

[4] X. Wang, Z.W. Hu, X. Zhang. Aeroacoustic effects of high-lift wing slat track and cut-out system. International Journal of Aeroacoustics, 2013, 12(3): 283-308.

[5] W. Liu, J.W. Kim, X. Zhang, D. Angland, B. Caruelle. Landing-gear noise prediction using high-order finite difference schemes. Journal of Sound and Vibration, 2013, 332: 3517-3534.

[6] B. Nebenführ, H.D. Yao, S.H. Peng, L. Davidson. Hybrid RANS/LES simulations for aerodynamic and aeroacoustic analysis of a multi-element airfoil. AIAA Paper 2013-2066, 19th AIAA/CEAS Aeroacoustics Conference, Berlin, Germany, 2013.

[7] R. Fattah, Z.W. Hu, D. Angland. Aeroacoustics of a landing gear door. AIAA Paper 2013-2259, 19th AIAA/CEAS Aeroacoustics Conference, Berlin, Germany, 2013.

[8] L.S. Hedges, A.K. Travin, P.R. Spalart. Detached-eddy simulations over a simplified landing gear. Journal of Fluids Engineering, 2002, 124(2): 413-423.

[9] D.J. Thompson. Railway noise and vibration: mechanisms, modelling and means of control. Elsevier, Oxford, UK, 2008.

[10] C. Talotte, P.E. Gautier, D.J. Thompson, C. Hanson. Identification, modelling and reduction potential of railway noise sources: a critical survey. Journal of Sound and Vibration, 2003, 267: 447-468.

[11] C. Talotte. Aerodynamic noise: a critical survey. Journal of Sound and Vibration, 2000, 231(3): 549-562.

[12] F. Poisson. Railway noise generated by high-speed trains. Proceedings of the 11th International Workshop on Railway Noise, Uddevalla, Sweden, 2013.

[13] D.J. Thompson, C.J.C. Jones. Review of the modelling of wheel/rail noise generation, Journal of Sound and Vibration, 2000, 231: 519-536.

[14] C.J. Baker. A review of train aerodynamics Part 1-Fundamentals. The Aeronautical Journal, 2014, 118: 201-228.

[15] C.J. Baker. A review of train aerodynamics Part 2-Applications. The Aeronautical Journal, 2014, 118: 345-382.

[16] H. Hemida, C. J. Baker, G. Gao. The calculation of train slipstreams using large-eddy simulation. Proceedings of the Institution of Mechanical Engineers Part F: Journal of Rail and Rapid Transit, 2014, 228: 25-36.

[17] H. Hemida, S. Krajnovic. LES study of the influence of the nose shape and yaw angles on flow structures around trains. Journal of Wind Engineering and Industrial Aerodynamics, 2010, 98: 34-46.

[18] M. Jönsson, J. Haff, H. Richard, S. Loose, A. Orellano. PIV investigation of the flow field underneath a generic high-speed train configuration. Euromech Colloquium 509, Vehicle Aerodynamics, External Aerodynamics of Railway Vehicles, Trucks, Buses and Cars, Berlin, Germany, 2009.

[19] J.A. Schetz. Aerodynamics of high speed trains. Annual Review of Fluid Mechanics, 2001, 33: 371-414.

[20] C.J. Baker. Flow and dispersion in ground vehicle wakes. Journal of Fluids and Structures, 2001, 15: 1031-1060.

[21] N. Frémion, N. Vincent, M. Jacob, G. Robert, A. Louisot, S. Guerrand. Aerodynamic noise radiated by the intercoach spacing and the bogie of a high-speed train. Journal of Sound and Vibration, 2000, 231(3): 577-593.

[22] K. Nagakura. Localization of aerodynamic noise sources of Shinkansen trains. Journal of Sound and Vibration, 2006, 293: 547-556.

[23] Hee-Min Noh, Sunghoon Choi, Sukyoon Hong, Seog-Won Kim. Investigation of noise sources in high-speed trains. Proceedings of the Institution of Mechanical Engineers Part F: Journal of Rail and Rapid Transit, 2013, 0: 1-16.

[24] F. Poisson, P.E. Gautier, F. Létourneaux. Noise sources for high-speed trains: A review of results in the TGV case. Noise and Vibration Mitigation for Rail Transportation Systems, Notes on Numerical Fluid Mechanics and Multidisciplinary Design, 2008, 99: 71-77.

[25] A. Lauterbach, K. Ehrenfried, S. Kröber, T. Ahlefeldt, S. Loose. Microphone array measurements on high-speed trains in wind tunnels. 3rd Berlin Beamforming Conference, Berlin, Germany, 2010.

[26] E. Le Dévéhat, C. Talotte, A. Dugardin. Aerodynamic noise reduction using a CFD approach based on the prediction of the turbulence production area. MIRA International Conference on Vehicle Aerodynamics, Coventry, UK, 1996.

[27] E. Masson, N. Paradot, E. Allain. The numerical prediction of the aerodynamic noise of the TGV POS high-speed train power. Proceedings of the 10th International Workshop on Railway Noise, Nagahama, Japan, 2010: 457-464.

[28] M. Meskine, F. Pérot, M.S. Kim, D. M. Freed, S. Senthooran, Z. Sugiyama, F. Polidoro, S. Gautier. Community noise prediction of digital high speed train using LBM. AIAA Paper 2013-2015, 19th AIAA/CEAS Aeroacoustics Conference, Berlin, Germany, 2013.

[29] Y. Wakabayashi, T. Kurita, H. Yamada, M. Horiuchi. Noise measurement results of Shinkansen high-speed test train. Noise and Vibration Mitigation

for Rail Transportation Systems, Proceedings of the 9th International Workshop on Railway Noise, Munich, Germany, 2007.

[30] M. Ikeda, T. Mitsumoji, T. Sueki, T. Takaishi. Aerodynamic noise reduction of a pantograph by shape-smoothing of panhead and its support and by the surface covering with porous material. Proceedings of the 10th International Workshop on Railway Noise, Nagahama, Japan, 2010: 441-448.

[31] M. Jacob, V. Gradoz, A. Louisot, D. Juvé, S. Guerrand. Comparison of sound radiated by shallow cavities and backward steps. AIAA Congress. Seattle, USA, 1999.

[32] C. Noger, J.C. Patrat, J. Peube, J.L. Peube. Aeroacoustical study of the TGV pantograph recess. Journal of Sound and Vibration, 2000, 231: 563-575.

[33] M. Hassan, L. Labraga, L. Keirsbulck. Aero-acoustic oscillations inside large deep cavities. 16th Australasian Fluid Mechanics Conference, Gold Coast, Australia, 2007.

[34] A. Torii, J. Ito. Development of the series 700 Shinkansen train-set, improvement of noise level. Proceedings of World Congress on Railway Research 1999, Tokyo, Japan, 1999.

[35] N. Yamazaki, T. Takaishi. Wind tunnel tests on reduction of aeroacoustic noise from car gaps and bogie section. Quarterly Report of RTRI, 2007, 48(4): 229-235.

[36] B. Schulte-Werning, C. Heine, G. Matschke. Unsteady wake characteristics of high-speed trains. PAMM Proceedings Applied Maths and Mechanics, 2003, 2: 332-333.

[37] L.M. Cleon, A. Willaime. Aero-acoustic optimisation of the fans and cooling circuit on SNCF's X 72500 Railcar. Journal of Sound and Vibration, 2000, 231(3): 925-933.

[38] M.J. Lighthill. On sound generation aerodynamically. I. General theory. Proceedings of the Royal Society of London, Series A, Mathematical and Physical Sciences, 1952, 211(1107): 564-587.

[39] N. Curle. The influence of solid boundaries upon aerodynamic sound. Proceedings of the Royal Society of London, Series A, Mathematical and Physical Sciences, 1955, 231(1187): 505-514.

[40] J.E. Ffowcs Williams, D.L. Hawkings. Sound radiation from turbulence and surfaces in arbitrary motion. Philosophical Transactions of the Royal Society of London, 1969, 342: 264-321.

[41] F. Farassat. Derivation of Formulations 1 and 1A of Farassat. NASA/TM-214853, 2007.

[42] K.S. Brentner, F. Farassat. Modelling aerodynamically generated sound of helicopter rotors. Progress in Aerospace Sciences, 2003, 39: 83-120.

[43] M.S. Howe. Theory of vortex sound. Cambridge University Press, UK, 2003.

[44] A. Powell. Theory of vortex sound. Journal of the Acoustical Society of America, 1964, 36: 177-195.

[45] T. Coloniusa, S.K. Lele. Computational aeroacoustics: progress on nonlinear problems of sound generation. Progress in Aerospace Sciences, 2004, 40: 345-416.

[46] G. Gabard, R.J. Astley. Theoretical model for sound radiation from annular jet pipes: far- and near-field solutions. Journal of Fluid Mechanics, 2006, 549: 315-341.

[47] V.L. Wells, R.A. Renaut. Computing aerodynamicallygenerated noise. Annual Review of Fluid Mechanics, 1997, 29: 161-199.

[48] C.K.W. Tam. Computational Aeroacoustics: An overview of computational challenges and applications. International Journal of Computational Fluid Dynamics, 2004, 18 (6): 547-567.

[49] Z.W. Hu, C.L. Morfey, N.D. Sandham. Sound radiation from a turbulent boundary layer. Physics of Fluids, 2006, 18: 161098101-4.

[50] P.R. Spalart. Stratergies for turbulence modelling and simulations. Int. J. Heat Fluid Flow, 2000, 21: 161-168.

[51] G. Iaccarino, A. Ooi, P.A. Durbin, M. Behnia. Reynolds averaged simulation of unsteady separated flow. International Journal of Heat and Fluid Flow, 2003, 24: 147-156.

[52] P.R. Spalart, W.H. Jou, M.Kh. Strelets, S.R. Allmaras. Comments on the feasibility of LES for wings, and on a hybrid RANS/LES approach. First AFOSR International Conference on DNS/LES. In advances in DNS/LES, C. Liu & Z. Liu, Greyden Press, Columbus, OH, 1997.

[53] G. Constantinescu, M. Chapelet, K.D. Squires. Turbulence modelling applied to flow over a sphere. AIAA Journal, 2003, 41(9): 1733-1742.

[54] E. Achenbach. Experiments on the flow past spheres at very high Reynolds number. Journal of fluid mechanics, 1972, 54(3): 565-575.

[55] B. Lazos. Mean flow around the inline wheels of four-wheel landing gear. AIAA Journal, 2002, 40(2): 193-198.

[56] S. Morton, J. Forsythe, K. Squires, K. Wurtzler. Assessment of unstructured grids for detached-eddy simulations of high Reynolds number separated flows. 8th ISGG Conference, Honolulu, 2002.

[57] S. Succi. The lattice Boltzmann equation for fluid dynamics and beyond. Oxford University Press, UK, 2013.

[58] S. Chen, G. Doolen. Lattice Boltzmann method for fluid flows. Annual Review of Fluid Mechanics, 1998, 30: 329-364.

[59] R.M. Fink. Airframe noise prediction method. Technical report 77-29, FAARD, 1979.

[60] M.G. Smith, L.C. Chow. Prediction method for aerodynamic noise from aircraft landing gear. AIAA Paper 1998-2228, 1998.

[61] M.G. Smith, L.C. Chow. Validation of prediction model for aerodynamic noise from aircraft landing gear. AIAA Paper 2002-2581, 2002.

[62] Y.P. Guo, K.J. Yamamoto, R.W. Stoker. An empirical model for landing gear noise prediction. AIAA Paper 2004-2888, 2004.

[63] D.J. Thompson, M.G. Smith, F. Coudret. Application of a component-based approach to modelling the aerodynamic noise from high-speed trains.

Proceedings of the 10th International Workshop on Railway Noise, Nagahama, Japan, 2010: 449-456.

[64] E. Latorre Iglesias, D.J. Thompson, M.G. Smith. Component-based model for aerodynamic noise of high-speed trains. Proceedings of the 11th International Workshop on Railway Noise, Uddevalla, Sweden, 2013.

[65] M. Jönsson, J. Haff, H. Richard, S. Loose, A. Orellano. PIV investigation of the flow field underneath a generic high-speed train configuration. Euromech colloquium 509, Vehicle Aerodynamics, External Aerodynamics of Railway Vehicles, Trucks, Buses and Cars, Berlin, Germany, 2009.

[66] B.S. Lazos. Mean flow features around the inline wheels of a four-wheel landing gear. AIAA Journal, 2002, 40(2):193-198.

[67] H.H. Heller, W.M. Dobrzynski. Sound radiation from aircraft wheel-well/landing gear configurations. Journal of Aircraft, 1977, 14(8):768-774.

[68] T.J. Mueller. Aeroacoustic Measurements. Springer-Verlag, 2002.

[69] T. Kitagawa, K. Nagakura. Aerodynamic noise generated by Shinkansen cars. Journal of Sound and Vibration, 2000, 231(3): 913-924.

[70] P. Nelson. Source identification and location, Chapter 3 in Advanced Applications of Acoustics, Noise and Vibration. In: F.J. Fahy and J.G. Walker (eds.). Spon Press, London, 2004.

[71] J. Piet, G. Elias. Airframe noise source localization using a microphone array. AIAA Paper 97-1643, 1997.

[72] S.M. Jaeger, N.J. Burnside, P.T. Soderman, W.C. Horne, K.D. James. Array assessment of an isolated, 26%-scale, high-fidelity landing gear. AIAA Paper 2002-2410, 2002.

[73] R.W. Stoker, Y. Guo, C. Streett, N.J. Burnside. Airframe noise source location of a 777 aircraft in flight and comparisons with a past model-scale test. AIAA Paper 2003-3232, 2003.

[74] M.C. Remillieux. Aeroacoustic study of a model-scale landing gear in a semi-anechoic wind tunnel. MSc thesis, Virginia Polytechnic Institute and State University, 2007.

[75] OpenFOAM, http://www.openfoam.com (accessed on September 8, 2013).

[76] B.Y. Wang, G.C. Zha. A general sub-domain boundary mapping procedure for structured grid CFD parallel computation. AIAA Paper 2007-4432, 2007.

[77] V.N. Vatsa, D.P. Lockard, M.R. Khorrami. Application of FUN3D solver for aeroacoustics simulation of a nose landing gear configuration. AIAA Paper 2011-2820, 2011.

[78] Pointwise. Gridgen version 15 manual, 2009.

[79] P.R. Spalart. Detached-eddy simulation. Annual Review of Fluid Mechanics, 2009, 41:181-202.

[80] M.L. Shur, P.R. Spalart, M.Kh. Strelets, A.K. Travin. Detached-eddy simulation of an airfoil at high angle of attack. In 4th Int. Symposium on Eng. Turb. Modelling and Experiments, Corsica, France, 1999.

[81] P.R. Spalart, S.R. Allmaras. A one-equation turbulence model for aerodynamic flows. AIAA Paper 92-0439, 1992.

[82] J. Dacles-Mariani, G.G. Zilliac, J.S. Chow, P. Bradshaw. Numerical/experimental study of a wing tip vortex in the near field. AIAA Journal, 1995, 33(9):1561-1568.

[83] P.R. Spalart, S. Deck, M. L. Shur, K. D. Squires, M. Kh. Strelets, A.K. Travin. A new version of detached-eddy simulation, resistant to ambiguous grid densities. Theoretical and Computational Fluid Dynamics, 2006, 20:181-195.

[84] Y. Ueno, T. Nagata, A. Ochi, K. Hayama. Aeroacoustic analysis of the rudimentary landing gear using octree unstructured grid with boundary-fitted layer. 18th AIAA/CEAS Aeroacoustics Conference, Colorado Springs, US, 2012.

[85] P.D. Welch. The use of fast Fourier transform for the estimation of power spectra: a method based on time averaging over short, modified periodograms. IEEE Trans. Audio Electroacoustics, Vol. AU-15: 70-73, 1967.

[86] Z.W. Hu, C.L. Morfey, N.D. Sandham. Wall pressure and shear stress spectra from direct numerical simulations of channel flow. AIAA Journal, 2006, 44(7): 1541-1549.

[87] International Standard ISO 3095: Acoustics-Railway applications-Measurement of noise emitted by railbound vehicles. 2013.

[88] I. Afgan, C. Moulinec, R. Prosser, D. Laurence. Large eddy simulation of turbulent flow for wall mounted cantilever cylinders of aspect ratio 6 and 10. International Journal of Heat and Fluid Flow, 2007, 28: 561-574.

[89] K.D. Squires, V. Krishnan, J.R. Forsythe. Prediction of the flow over a circular cylinder at high Reynolds number using detached-eddy simulation. Journal of Wind Engineering and Industrial Aerodynamics, 2008, 96: 1528-1536.

[90] T. Nishino, G.T. Roberts, X. Zhang. Unsteady RANS and detached-eddy simulations of flow around a circular cylinder in ground effect. Journal of Fluids and Structures, 2008, 24: 18-33.

[91] D.H. Yeo, N.P. Jones. Investigation on 3-D characteristics of flow around a yawed and inclined circular cylinder. Journal of Wind Engineering and Industrial Aerodynamics, 2008, 96: 1947-1960.

[92] R.M. Orselli, J.R. Meneghini, F. Saltara. Two and three-dimensional simulation of sound generated by flow around a circular cylinder. 15th AIAA/CEAS Aeroacoustics Conference, Miami, Florida, 2009.

[93] W.F. King, E. Pfizenmaier. An experimental study of sound generated by flows around cylinders of different cross-section. Journal of Sound and Vibration, 2009, 328: 318-337.

[94] B. Greschner, F. Thiele, M.C. Jacob, D. Casalino. Prediction of sound generated by a rod-airfoil configuration using EASM DES and the generalised Lighthill/FW-H analogy. Computers & Fluids, 2008, 261: 402-413.

[95] A. Roshko. Experiments on the flow past a circular cylinder at very high Reynolds number. Journal of Fluid Mechanics, 1961, 10: 345-356.

[96] S.E. Kim. Large eddy simulation of turbulent flow past a circular cylinder in subcritical regime. 44th AIAA Aerospace Science Meeting and Exhibit, Reno, NV, 2006.

[97] C. Norberg. Fluctuating lift on a circular cylinder: review and new measurements. J. Fluids and Structures, 2002, 17: 57-96.

[98] A.K. Travin, M.L. Shur, M.Kh. Strelets, P.R. Spalart. Detached-eddy simulations past a circular cylinder. Flow, Turbulence and Combustion, 2000, 63: 293-313.

[99] J. Jeong, F. Hussain. On the identification of a vortex. J. Fluid Mech., 1995, 285: 69-94.

[100] Y. Dubief, F. Delcayre. On coherent-vortex identification in turbulence. Journal of Turbulence, 2000, 1: 1-22.

[101] M. Braza, R. Perrin, Y. Hoarau. Turbulence properties in the cylinder wake at high Reynolds numbers. Journal of Fluids and Structures, 2006, 22: 757-771.

[102] C. Mockett, R. Perrin, T. Reimann, M. Braza, F. Thiele. Analysis of detached-eddy simulation for the flow around a circular cylinder with reference to PIV data. Flow Turbulence Combust, 2010, 85: 167-180.

[103] V.N. Vatsa, D.P. Lockard. Assessment of hybrid RANS/LES turbulence models for aeroacoustics applications. 16th AIAA/CEAS Aeroacoustics Conference, Stockholm, Sweden, 2010.

[104] I. Hasegawa, S. Uchida. Railway technology today: Braking systems. Japan Railway & Transport Review, 1999, 20: 52-59.

[105] H. Sakamoto, K. Hirakawa. Fracture analysis and material improvement of brake discs. JSME International Journal, 2005, 48: 458-464.

[106] M.M. Zdravkovich. Flow around circular cylinders. Vol I: Fundamentals. Oxford University Press, 1997.

[107] T.P. Chong, P.F. Joseph, P.O.A.L. Davies. Design and performance of an open-jet wind tunnel for aero-acoustic measurement. Applied Acoustics, 2009, 70: 605-614.

[108] D.J. Moreau, C.J. Doolan. The flow-induced sound of a wall-mounted finite length cylinder with circular and square cross-section. AIAA Paper 2013-2205, 19th AIAA/CEAS Aeroacoustics Conference, Berlin, Germany, 2013.

[109] Y. Zhou, M.W. Yiu. Flow structure, momentum and heat transport in a two-tandem-cylinder wake. Journal of Fluid Mechanics, 2006, 548: 17-48.

[110] D. Sumner. Two circular cylinders in cross-flow: A review. Journal of Fluids and Structures, 2010, 26: 849-899.

[111] <https://info.aiaa.org/tac/ASG/FDTC/DG/BECAN_files_/Workshop_June_2010_Final_problem_Statements/Contact_Information.pdf> (accessed on April 16, 2013).

[112] <https://info.aiaa.org/tac/ASG/FDTC/DG/BECAN_files_/BANCII.htm> (accessed on June 22, 2013).

[113] D.P. Lockard. Summary of the tandem cylinder solutions from the benchmark problems for airframe noise computations-I workshop. AIAA Paper 2011-0353, 2011.

[114] A. Najafi-Yazdi, G.A. Brès, L. Mongeau. An acoustic analogy formulation for moving sources in uniformly moving media. Proceedings of the Royal Society of London, Series A, 2011, 467: 144-165.

[115] V.L. Wells, A.Y. Han. Acoustics of a moving source in a moving medium with application to propeller noise. Journal of Sound and Vibration, 1995, 184(4): 651-663.

[116] K.S. Brentner, F. Farassat. An analytical comparison of the acoustic analogy and Kirchhoff formulation for moving surfaces. AIAA Journal, 1998, 36: 1379-1386.

[117] P. di Francescantonio. A new boundary integral formulation for the prediction of sound radiation. Journal of Sound and Vibration, 1997, 202: 491-509.

[118] A.R. Pilon, A.S. Lyrintzis. Integral methods for computational aeroacoustics. AIAA Paper 97-0020, 1997.

[119] J. Prieur, G. Rahier. Comparison of Ffowcs Williams-Hawkings and Kirchhoff rotor noise calculations. AIAA Paper 98-2376, 1998.

[120] I.E. Garrick, E.W. Watkins. A theoretical study of the effect of forward speed on the free-space sound-pressure field around propellers. NASA/TM-79844, 1954.

[121] D. Blokhintsev. Acoustics of a nonhomogeneous moving medium. NASA/TM-1399, 1956.

[122] F. Farassat. The Kirchhoff Formulas for Moving Surfaces in Aeroacoustics-The Subsonic and Supersonic Cases. NASA /TM-110285, 1996.

[123] D. Casalino. An advanced time approach for acoustic analogy predictions. Journal of Sound and Vibration, 2003, 261: 583-612.

[124] D.P. Lockard. A comparison of Ffowcs Williams-Hawkings solvers for airframe noise applications. AIAA Paper 2002-2580, 8th AIAA/CEAS Aeroacoustics Conference and Exhibition, Breckenridge, Colorado, 2002.

[125] X. Gloerfelt, C. Bailly, D. Juvé. Direct computation of the noise radiated by a subsonic cavity flow and application of integral methods. Journal of Sound and Vibration, 2003, 266: 119-146.

[126] A. P. Dowling, J. E. Ffowcs Williams. Sound and Sources of Sound. Horwood Publishing, Westergate, 1983.